ParisTech
INSTITUT DES SCIENCES ET TECHNOLOGIES
PARIS INSTITUTE OF TECHNOLOGY

MINES ParisTech

École doctorale n° 432 : Science des Métiers de l'Ingénieur

Doctorat ParisTech

T H È S E

pour obtenir le grade de docteur délivré par

l'École nationale supérieure des mines de Paris

Spécialité " Sciences et Génie des Matériaux "

présentée et soutenue publiquement par

Delphine RECHE

Le 18 mars 2011

Relations entre microstructure et aptitude au pliage des aciers à effet TRIP pour application automobile

Relations between microstructure and bendability on TRIP-aided steels for automotive products

Thèse confidentielle jusqu'au 31 janvier 2014

Directeur de thèse : **Anne-Françoise GOURGUES-LORENZON**
Co-encadrement de la thèse : **Thierry STUREL**

Jury

Mme Sandrine THUILLIER, Professeur, Université de Bretagne Sud	Président
M. Michel BRUNET, Professeur, INSA Lyon	Rapporteur
M. Paul VAN HOUTTE, Professeur, Katholieke Universiteit Leuven, Belgique	Rapporteur
Mme Véronique AUBIN, Professeur, Ecole Centrale	Examinateur
Mme Anne-Françoise GOURGUES-LORENZON, Professeur, Mines Paris Tech	Examinateur
M. Thierry STUREL, Ingénieur de recherche, ArcelorMittal Global R&D	Examinateur
M. Jacques BESSON, Directeur de recherche CNRS, Mines Paris Tech	Examinateur

T H È S E

MINES ParisTech
Centre des Matériaux
B.P. 87 - 91003 EVRY Cedex

Relations between microstructure and bendability on TRIP-aided steels for automotive products

Abstract

In order to limit fuel consumption, automotive industries push the steelmakers to develop thinner sheets with higher strength. Ultra High Strength Steels (UHSS) such as low alloy TRIP (TRansformation Induced Plasticity)-aided steels enable to get complex shapes for automotive parts. However, understanding the formability of these steels appears to be complex and involves a detailed study of failure mechanisms during forming tests. Therefore, links between microstructural features, in particularly banded structures, and formability were investigated in order to better predict the bending ability of steels as a function of their microstructure. In this study, four low alloy TRIP-aided steels exhibiting different bending performances were characterized using both air and stretch bending tests. From scanning electron and light microscopy observations, cracks initiate from the outer surface or from just below in air-bending, but from the central segregation bands in stretch bending. Fracture surfaces after bending tests are ductile and damage mainly appears by ferrite/martensite interface decohesion and occasionally as microcracks within martensite islands. An original procedure based on thickness-reduced specimens, with various locations of the main hard band within the specimen thickness, was set up. It enabled to propose a relationship between cracking, local thickness of hard band and local strain during air-bending. In order to develop a local fracture criterion that could be used for any bending test, stress and strain fields were computed by numerical simulation of the two bending tests. For that purpose, an experimental database including tensile tests on smooth and notched samples as well as shear tests was established. Material parameters of constitutive equations, accounting for anisotropic elasto-plastic behaviour with mixed hardening, were determined from this database. Finite element simulation of both bending tests associated with a ductile damage criterion made it possible to satisfactorily predict strain fields, bending load-displacement curves and fracture angle. The possibility of using simplifying assumptions in the model (such as an isotropic flow criterion, pure isotropic hardening, two-dimensional assumptions and simplified boundary conditions) is also discussed.

Keywords: Ultra High Strength Steels, TRIP-aided steels, microstructure, damage mechanisms, air-bending test, stretch bending test, finite-element simulation.

Relation entre microstructure et aptitude au pliage des aciers à effet TRIP pour application automobile

Résumé

Pour limiter la consommation des véhicules, les industries automobiles demandent aux aciéristes de développer des aciers de plus en plus fins avec des hautes résistances. Les aciers très haute résistance (THR) comme les aciers TRIP (TRansformation Induced Plasticity) permettent d'effectuer des pièces automobiles aux formes complexes. Néanmoins, le compréhension des mécanismes de mise en forme de ces aciers n'est pas simple et implique une étude détaillée des mécanismes de rupture apparaissant durant la mise en forme. Ainsi, les liens entre les paramètres microstructuraux, en particulier les structures en bandes, et la mise en forme ont été étudiés pour obtenir une meilleure prédiction de la capacité en pliage des aciers en fonction de leur microstructure. Dans cette étude, quatre aciers TRIP présentant des performances en pliage différentes ont été caractérisés à la fois en pliage en V et en pliage sous traction. A partir d'observations au microscope optique et à balayage, nous avons démontré que les fissures s'initiaient à partir de la surface ou juste en dessous en pliage en V alors qu'elles s'initiaient au niveau de la ségrégation centrale en pliage sous traction. Les surfaces de rupture après pliage sont ductiles et l'endommagement apparait principalement par décohésion de l'interface ferrite/martensite et occasionnellement par rupture des ilots martensitiques. Une procédure originale basée sur des échantillons rectifiés présentant la bande de ségrégation à différents endroits dans l'épaisseur a été établi. Ce travail a permis de proposer une relation entre l'épaisseur d'une bande, son endommagement et sa déformation locale atteinte pendant un test de pliage en V. Pour développer un critère de rupture pour ces tests de pliage, les champs de contrainte et déformation ont été calculés par simulation numérique pour ces deux tests. Pour ce faire, une base de données expérimentale incluant des tests de traction sur éprouvettes lisses et entaillées et des tests de cisaillement a été établie. La loi de comportement du matériau a été déterminée à partir de cette base expérimentale et présente un comportement élasto-plastique anisotrope avec écrouissage mixte. La simulation numérique des deux essais de pliage associée à un critère d'endommagement a permis de prédire de manière satisfaisante les champs de déformation, les courbes force/déplacement ainsi les angles de rupture. La possibilité d'utiliser des modèles simplifiés (tels qu'un critère d'écoulement isotrope, un écrouissage purement isotrope, des calculs en 2D et des conditions aux limites simplifiées) a également été discuté.

Mots clés: Aciers Très Haute Résistance, aciers TRIP, microstructure, mécanismes d'endommagement, test de pliage en V, test de pliage sous traction, simulation numérique par éléments-finis.

Remerciements

Au terme des ces trois années de thèse, le temps est venu de présenter mes remerciements à toutes les personnes qui ont contribué à cette aventure scientifique et humaine. Sans leur aide efficace et leur soutien précieux, ce manuscrit n'aurait pas abouti à ce qu'il est aujourd'hui.

Je remercie vivement tous les membres de mon jury pour le temps consacré à la lecture de mon manuscrit et pour leurs précieux conseils. Un grand merci à Paul Van Houtte et Michel Brunet qui ont accepté d'être rapporteurs de ces travaux ainsi qu'à Sandrine Thuillier et Véronique Aubin, les examinatrices de mon jury. Leurs remarques pertinentes m'ont permis d'améliorer la qualité de ce travail.

Cette thèse a été menée en collaboration avec le Centre des Matériaux (CdM) de l'Ecole des Mines de Paris et ArcelorMittal Global R&D. Ainsi, je tiens ainsi à remercier Esteban Busso, directeur du CdM, de m'avoir accueillie dans cet environnement technique et humain de qualité. Je remercie également Michel Babbit de m'avoir reçue au Centre Auto ainsi que Messieurs Alain Carmet, Philippe Hein et Martin Munier qui m'ont permis d'évoluer et de m'intégrer très rapidement au sein des équipes "MBIWS" puis "AUP²".

Pour reprendre un ordre plus chronologique, je suis très reconnaissante à Isabelle Boul d'avoir lancé cette thèse à la suite de mon stage de fin d'études, de m'avoir fait confiance et de m'avoir donné le goût de la recherche et plus particulièrement celui de la mise en forme.

Je tiens maintenant à remercier sincèrement Anne-Françoise Gourgues-Lorenzon qui a dirigé cette thèse et m'a si bien accompagnée durant ces trois années. Un grand merci pour ta disponibilité, ton écoute et implication malgré la distance, la rigueur et les méthodes de travail que tu m'as apportées mais aussi pour toutes ces relectures méticuleuse d'articles ou de chapitres en temps imposé.

Je remercie mon encadrant chez ArcelorMittal, Thierry Sturel, de m'avoir accompagnée pendant cette thèse. Merci pour ta confiance et ton soutien au cours de cette aventure. Je te remercie également pour ta disponibilité, tes conseils et l'autonomie que tu m'as laissée tout au long de cette thèse.

Un grand merci également à Jacques Besson. Vous avez hérité d'une énième thésarde alors que vous en aviez déjà beaucoup mais grâce à vous, j'ai pu découvrir les terres inconnues de la simulation numérique. Avant cette thèse, je n'avais jamais utilisé les éléments finis, alors merci pour votre patience, pour les explications sur ces modèles complexes et pour toutes les réponses aux problèmes que j'ai pu rencontrer sur ZéBuLon.

Ayant passé un an au Centre des matériaux et deux chez ArcelorMittal, je vais d'abord remercier mes collègues d'Evry puis ceux de Maizières, en espérant n'oublier personnes (si c'est le cas, je leur présente par avance mes excuses).

Je souhaiterai tout d'abord remercier les chercheurs et techniciens qui m'ont aidé au cours de cette thèse. Merci à toutes les personnes de l'atelier, Christophe, Jean-Pierre, René, Georges, Michel pour l'usinage des éprouvettes ainsi que pour celui du montage du pliage

sous traction. Merci Odile de m'avoir aidée dans mes recherches bibliographiques. Merci également aux personnes de l'informatique, Greg et Olivier mais aussi aux personnes du service administratif. Merci Daniel pour les essais de RX. Merci Anne et Maria de m'avoir initiée au MEB et un grand merci également à Nicole pour les manips de nanoindentations qui étaient loin d'être une partie de plaisir…Merci également à Abdennour de m'avoir aidée à dessiner sous Inventor mais aussi de m'avoir formée à l'utilisation des différentes machines du bocal. Merci également à M. Pineau pour les discussions sur des problèmes métallurgiques ou autres.

Cette aventure aurait sans doute été moins agréable sans la présence de l'ensemble des thésards et autres personnes du CdM qui m'ont accueillie au cours de cette année à Evry et où entraide et bonne humeur ont permis un travail efficace. Merci Djamel pour tous les renseignements sur la mécanique, sur Linux ou encore sur Zébulon.
Pika…que dire de la morphomath, merci d'avoir été présent à chaque moment, pour ton écoute, ton soutien, tes conseils, et pour tout le reste. Merci également pour le roller dans les rues parisiennes...
Clémence, ma grande amie, sans toi, Evry n'aurait surement pas été pareil. Merci pour tout ce que tu as fait pour moi, pour ton écoute, tes encouragements. Merci également pour le prêt de ton clic-clac car sans toi mes aller-retour à Evry n'auraient sans doute pas été aussi sympa.
Florence, merci également pour ton écoute et tes encouragements surtout en fin de thèse. Je te souhaite bon courage pour la suite dans ton nouveau travail et félicitation à la première "Docteur" de notre promo.
Angel, merci de m'avoir fait découvrir "le pantalon" et merci pour l'hébergement après les thèses sur Paris. Bonne continuation.
Julie, merci de m'avoir initié à Zébulon et m'avoir appris à jouer avec les lignes de codes car au début ce n'était vraiment pas simple. Bon courage pour la suite et j'espère que tu es venue à bout de ces fameux aciers TWIP.
Je vais maintenant remercier tous les autres thésards ou autres personnes avec qui j'ai pu partager du travail, des rires, des sorties, etc…merci Yohann pour ta terrasse, merci Julien d'avoir été présent pendant cette année et d'avoir fait le petit bout de chemin entre le CdM et le 407. Un grand merci également à Tony, Guillaume, Thomas, Cédric, Bahram, Sophie, Vlad, Guilhem, la grande Julie, Jianqiang, Nikolai, Fabrice, Steeve, Clara, Laurent, Florine, Greg, Aurélie, Thomas….à qui je souhaite une grande réussite.

Je souhaiterais maintenant remercier mes collègues d'ArcelorMittal. Je vais tout d'abord remercier les ingénieurs et techniciens qui m'ont formée et aidée pour les différents essais que j'ai eu à effectuer…parmi eux, Grégory pour les essais de RX, Aurélien pour les manips de sigmamétrie, Stéphane pour les manips avec le logiciel Aramis et Nathalie et Rémi pour les observations métallographiques de la fin de thèse. Je souhaiterai également remercier tout le service métallo de m'avoir formée, aidée et conseillée quand j'avais des problèmes d'attaques ou d'observations. Merci également à toutes les personnes d'AUP² avec qui j'ai pu travailler et en particulier le service mise en forme.
Merci à Germain, Max et Flo (mon parrain) de m'avoir appris différents tests de mise en forme et de m'avoir accueillie dans votre bureau. Merci également à Nico, Rémi, Cyril, Benoît et Dominique pour l'aide et les conseils que vous m'avez apportés. Xavier, je te remercie également pour tes conseils sur la simulation numérique et ton aide sur des problèmes pas toujours simples à résoudre.
Merci également à toutes les autres personnes des deux autres services (soudage et fatigue) pour votre soutien et encouragements tout au long de cette thèse…Bastien, Michel, Rémi

(bon courage pour la fin de ta thèse), Marina, Bernard, Adrien, Mathieu, Daniel, Nora, Irina, les deux Dom, Agatha, Nathalie, Tarik, Jérôme, Stéphanie, Florent (bon courage également pour cette dernière année de thèse), etc. Je remercie aussi Rachel et Danielle, les secrétaires de mon service ainsi que Sabine Fogel pour les recherches bibliographiques.
Merci beaucoup Jonas, Pape et Perrine de m'avoir incluse dans vos réunions de projet et pour l'aide précieuse que vous m'avez apportée sur ces sacrés aciers TRIP !
Un grand merci également à toi, Olivier, pour ton implication, ton dynamisme, tes idées nouvelles et pour tous les conseils au cours de ces trois années.
Alain, je ne trouverai sans doute pas tous les mots mais je souhaite te remercier sincèrement pour ta grande disponibilité que ce soit pendant mon stage ou pendant ma thèse. Merci pour tous les conseils avisés ainsi que pour ton implication qui m'ont été d'une aide précieuse.

Cette aventure n'aurait pas été possible sans certaines rencontres et notamment les personnes qui sont plus que de simples collègues…je pense naturellement à des personnes de la team NCIS…Julie, Nico, Savine, Mike, etc merci pour tout ce que vous m'avez apporté au cours ce ces années, merci d'avoir été là et de m'avoir remonté le moral dans les moments de doute. Je vous souhaite bonne continuation (une meilleure santé) et une belle réussite pour la suite.
Je souhaiterais maintenant remercier mes coéquipiers de volley-ball et amis…merci à vous toutes et tous. Un grand merci à Sophie, Anne, Claire, Pat, Manu, Jean, DD, Sam, Julien, et Rémi pour tout ce que vous avez fait. Un petit message pour toi Sophie, continue comme ça, la vue est belle en haut de cette montagne. Grâce à vous, les séances de volley m'ont permis de décompresser et même si j'avais des difficultés à dépasser le filet, j'ai toujours beaucoup aimé jouer avec vous…que ce soit le mardi soir ou en matchs. Merci également à vous tous pour les sorties, les rires, la danse et pour les encouragements tout au long de cette thèse.
Merci également à tous mes amis de prépa, de Montpellier ou d'ailleurs pour ces retrouvailles au cours de ces trois ans et pour votre soutien.
Enfin, je souhaiterais remercier toutes les personnes qui ont fait le déplacement à Paris le jour de ma soutenance.

Mes dernières lignes iront à ma famille qui m'a toujours soutenue. Merci à mes parents et ma sœur d'avoir toujours cru en moi et de m'avoir apporté un grand réconfort. Sabine, crois en toi et en tes rêves…tu pourras faire des choses magnifiques alors garde ton cap et continue comme ça. Bon courage pour ces nouvelles aventures qui t'attendent.
Enfin mes derniers mots seront pour toi, Stéphane. Je te remercie tendrement de m'épauler et de m'aider tous les jours depuis six ans. Merci pour ton amour et ton soutien sans pareil. Sans toi, je ne serai sûrement pas en train de terminer ce manuscrit. Je te souhaite bon courage pour tes nouvelles aventures en terre inconnue…

Table of content

Introduction

Ultra High Strength Steels (UHSS) for automotive application

In the Kyoto protocol, it was decided to reduce greenhouse gases emissions. Private cars are responsible for more than 10% of CO_2 emissions in the European Union.
For that purpose, European, Japanese and Korean automotive industries engage themselves to reduce CO_2 emissions down to 120g/km before 2012.
Ultra High Strength Steels (UHSS) are thus developed and used to decrease vehicle weight but formability issues can be encountered with these new steels.

Ultra High Strength Steels in automotive industry

Current environmental concerns require that greenhouse gases and CO_2 emissions have to be decreased. Therefore, European standards impose to the automotive industry a reduction of vehicle fuel consumption and CO_2 emissions. To achieve these requirements, automotive industries have to use thinner sheets with higher strength and equivalent or improved functional properties.
In this industrial context, steelworkers develop and propose nowadays thin sheets as Ultra High Strength Steels (UHSS) which are very advantageous to reduce the vehicle weight by keeping a high strength. They are commonly used in automotive body in white (BIW) to make safety and structural parts such as bumper reinforcements and intrusion beams (Figure 1).

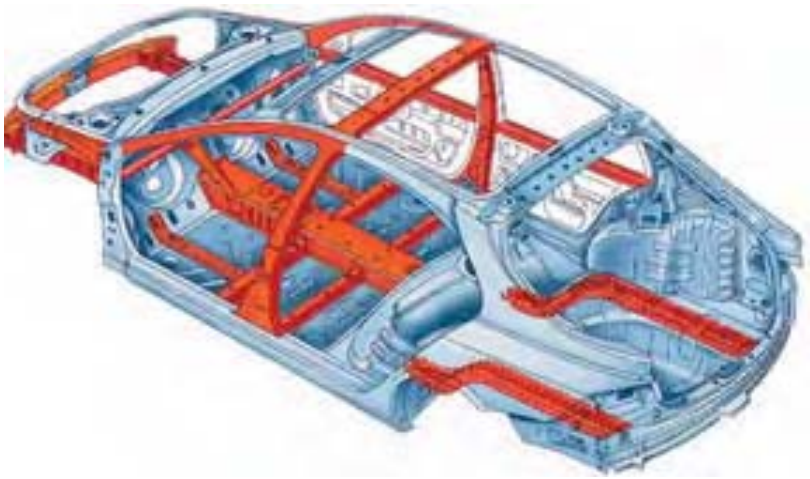

Figure 1. Typical applications of high strength steels for crash resistance

UHSS make reference to three main steel families:

- Dual phase (DP) steels: composed of hard phases (martensite or martensite / bainite) dispersed in a soft pure ferrite matrix. The combination of high strength and ductility and the capacity for strain hardening lead to excellent fatigue properties and good energy absorption characteristics, making these steels suitable for structural and reinforcement components, such as longitudinal beams and cross-members.

- TRIP (TRansformation Induced Plasticity) steels: composed of a ductile ferrite matrix containing small islands of hard bainite and retained austenite. Transformation of the austenite into martensite during deformation causes significant strain hardening and delays the onset of necking, providing high ductility.

- Multiphase (MP) steels: with extremely fine microstructures, consisting of ferrite / bainite or precipitation-hardened bainite or mixture of bainite and martensite. They have excellent combination of high strength and ductility, high YS (Yield Strength), good formability and good resistance spot weldability. These grades are particularly suited for automobile safety components requiring good impact resistance, such as bumper beams and door reinforcements.

The main quality of these steels is to offer a good compromise between strength and ductility (Figure 2). In this graph, it is clearly seen that TRIP steels offer the best compromise between the tensile strength and the fracture elongation. Thus, these steels are potentially very attractive for the automobile industry.
Indeed, they differ from conventional steels by their remarkable combination of high strength and ductility, resulting from their particular microstructure. The strain hardening capacity of TRIP steels is considerable, ensuring efficient strain redistribution during forming and hence good drawability, combined with very high yield strength in the finished component.
Due to their high energy absorption capacity and good fatigue strength, TRIP steels are particularly used for structural and safety components such as longitudinal beams, mid-post reinforcements, etc.

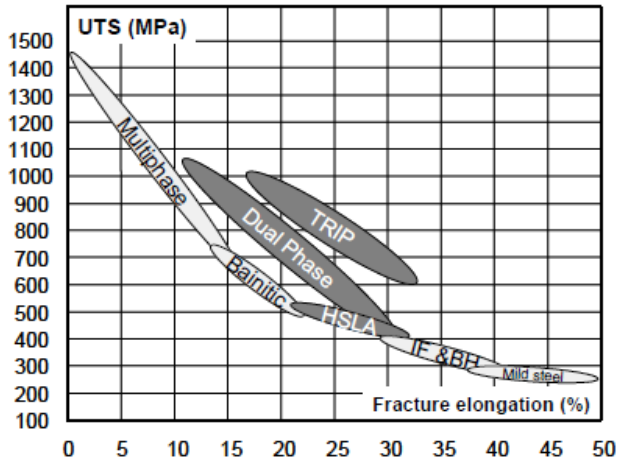

Figure 2. Ultimate tensile strength and fracture elongation for main steel product families

Metallurgical route for TRIP steels production

Figure 3 illustrates the metallurgical route for TRIP steels processing. After the steelmaking step, the first step corresponds to the continuous casting. Then, from the slab state, there are 3 main steps: first the hot rolling, secondly the coiling and finally the cold rolling. After cold rolling, the material is significantly strain hardened and the annealing cycle (Figure 4) is designed to recrystallize the grain and produce a TRIP grade that meets the specifications targeted by the final customer. This step is done so as to restore enough ductility for the automotive part forming. This annealing cycle corresponds to the heat treatment of the TRIP studied (with a galvanization).
During heating and soaking between Ac_1 and Ac_3, the microstructure recrystallizes from initial ferrite+pearlite microstructure yielding at the end of the soaking a microstructure made of approximately 60% of ferrite and 40% of austenite. Such distribution depends on the soaking temperature. The higher the latter, the more initial austenite is formed.
Then, a slight cooling from 30 to 60°C/s is performed during which nucleation, growth and coarsening of ferrite appears. This cooling shall be fast enough to avoid pearlite formation.
In order to stabilize austenite phase thanks to its carbon enrichment, a isothermal holding in the bainitic region is carried out. In addition, austenite is transformed into bainite during this holding. Note that this bainite formed is carbide-free due to the presence of Al and Si.

After this step, the steel is hot dip galvanized (liquid Zn at 460°C) before going through a furnace in order to form the galvannealed GA coating (Zn-Fe alloy).
The final cooling can lead to a transformation of the austenite into martensite especially in the mid-thickness area which is enriched in C and Mn. At the end of annealing, retained austenite is still present (between 8 and 20%).

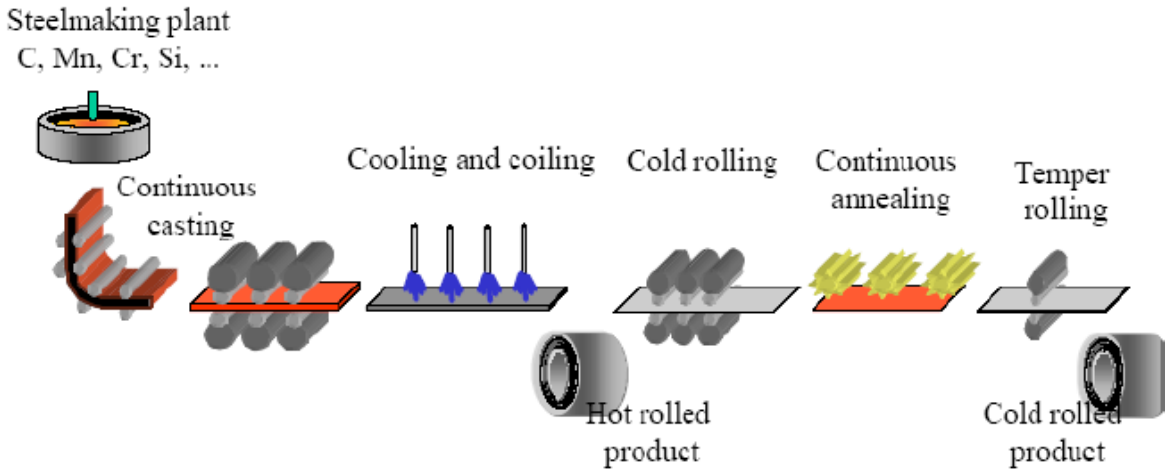

Figure 3. Production of TRIP steels

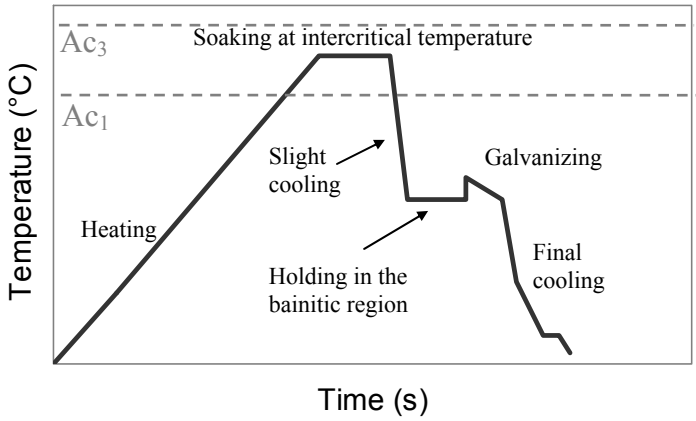

Figure 4. TRIP steels heat treatment

Sheet formability by stamping

In automotive industry, most of parts are stamped to be given their final shape. Stamping process differs according to the part shape and several stampings (less or more complex) are sometimes necessary to obtain the final automotive part.
However, on new TRIP steel grades with increasing mechanical properties, cracking can occur on radii during stamping (Figure 5). Connecting steel formability with standard mechanical properties seems insufficient and the significance of many relationships is not obvious. It is thus necessary to take the microstructure of these materials into account to study in more detail the bendability of these steels.

Figure 5. Bumper beam with a large crack along the radius after stamping

Scope of the research

To enlarge the use of UHSS in automotive body as structural parts, good knowledge and experience must be developed regarding their formability.
During the development of these products, every limit in terms of in-use properties has to be known and characterizations are necessary to help and lead metallurgical development of new grades. Therefore, understanding the formability of UHSS for automotive applications involves a detailed study of failure mechanisms during forming tests.

The aim of this work is to study the relationships between the microstructure and the bendability of UHSS.
TRIP steels can generally be stamped more easily than other UHSS. In addition, these steels are developed to be able to perform more complex automotive parts than it is possible with DP steels for example. Therefore, it is necessary to get deeper information and to study the bendability of TRIP steels in more detail. In this study, four TRIP-aided steels exhibiting various bending performances and various microstructures were used. For this work, two bending tests were considered: air-bending and stretch bending.

The main objectives of this project are:
- To investigate the link between microstructure and damage during bending.
- To quantitatively investigate, in the particular case of the low alloy TRIP-aided steels, the main microstructural parameter controlling failure in bending conditions.
- To build a design tool enabling metallurgical engineers to rather easily test new ways of metallurgical improvement of UHSS regarding bending performances.

This manuscript is divided into four chapters.

The first chapter is devoted to a literature survey on both bendability, TRIP steels and the origin of the micro and macrosegregations. Then, using scanning electron and light microscopy, a first microstructural characterization of the four studied materials is given. Finally, based on tensile and bending tests, a mechanical analysis of the four steels is proposed.

After this state-of-the-art survey and after a short presentation of the four TRIP-aided steels studied, the approach of this study is explained in more detail. The outline of the three other chapters will thus be given at the end of the first chapter.

Aciers très haute résistance pour application automobile

Les exigences environnementales actuelles requièrent que les émissions de gaz à effet de serre et de CO_2 soient réduites. A cet effet, des normes européennes imposent aux constructeurs automobiles une réduction de la consommation des véhicules ainsi qu'une diminution des émissions de CO_2. Pour atteindre ces exigences, les industries automobiles doivent utiliser des tôles plus fines avec des résistances plus élevées et des propriétés d'usage équivalentes ou améliorées. C'est dans ce contexte industriel que les aciéristes développent et proposent des aciers Très Haute Résistance (THR) qui ont l'avantage de réduire le poids des véhicules tout en gardant une haute résistance. Ces aciers sont couramment utilisés dans la caisse en blanc (squelette structurel de la voiture) pour les pièces de structure et de sécurité telles que les poutres de renfort ou les poutres de pare-choc (Figure 1).

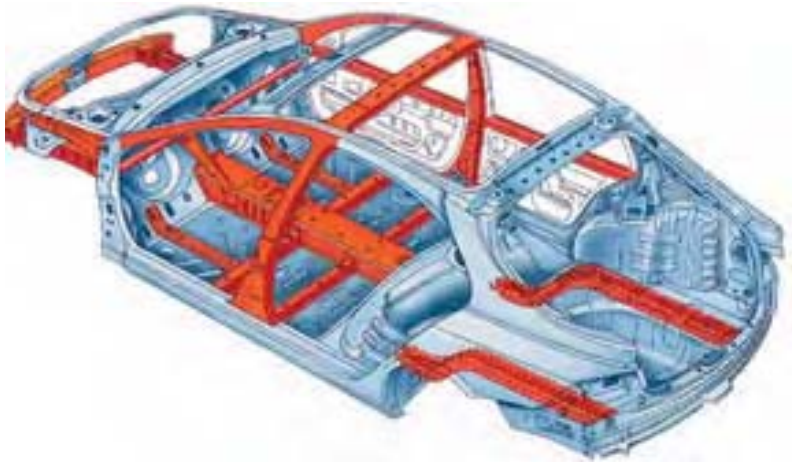

Figure 1. Application des aciers très haute résistance

Les aciers très haute résistance regroupent trois grandes familles :

- Dual Phase (DP): aciers composés de phases dures (martensite ou martensite/bainite) dispersées dans une matrice ductile de ferrite. La combinaison haute résistance/ductilité et la forte capacité d'écrouissage font de ces aciers des candidats très fiables pour des pièces de structures ou de renforts tels que les longerons ou les traverses.

- TRIP (TRansformation Induced Plasticity): aciers composés d'une matrice ductile de ferrite contenant des petits îlots de bainite et d'austénite résiduelle. Ces aciers offrent un potentiel de durcissement supplémentaire par rapport aux DP grâce à la possibilité d'activer la transformation martensitique de l'austénite au cours de la déformation. Leur grande ductilité en font également des aciers de choix pour les pièces de structures ou de sécurité.

- Multiphase (MP): ces aciers ont une structure ferrito-bainitique très fine ou une structure bainitique durcie par des précipités ou alors une structure bainite-martensite. Ces aciers ont un bon compromis résistance/ductilité, une haute limite élastique "Re", de bonnes caractéristiques de formage et une très bonne soudabilité par points. Ces aciers sont utilisés pour des pièces automobiles de sécurité destinées à la résistance aux chocs tels que longerons ou les renforts de portières.

La principale qualité des ces aciers est d'offrir un bon compromis entre résistance et ductilité (Figure 2). Dans ce graphique, nous pouvons constater que les aciers TRIP offrent un meilleur compromis entre résistance en traction et allongement à rupture. C'est pour cette raison que ces aciers sont très demandés par l'industrie automobile.
En effet, ils diffèrent des aciers conventionnels de part leur remarquable combinaison résistance/ductilité, résultant de leurs microstructures. La capacité d'écrouissage des TRIP est considérable, assurant une distribution de la déformation efficace pendant leur mise en forme. En raison de leur forte capacité d'absorption des chocs et de leur bonne résistance à la fatigue, les aciers TRIP sont particulièrement utilisés pour des pièces de structures et de sécurité tels que les traverses, les longerons, les renforts, etc.

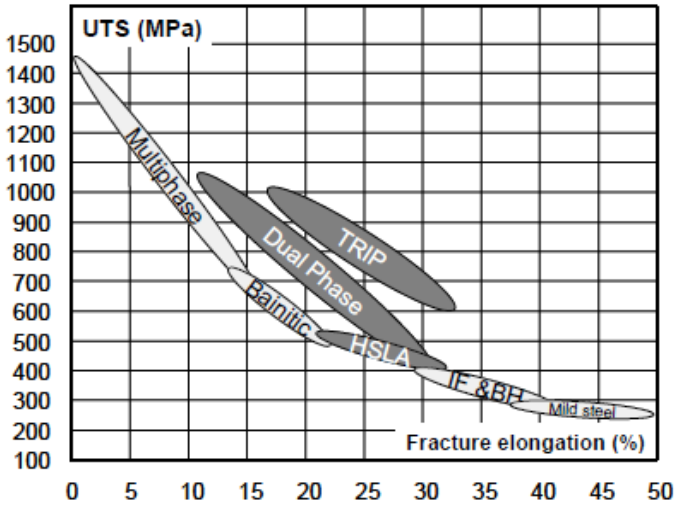

Figure 2. Résistance en traction en fonction de l'allongement à rupture pour différentes familles d'aciers

Route métallurgique des aciers TRIP

La figure 3 illustre la route métallurgique des aciers TRIP. Après la coulée continue, la brame va suivre trois étapes : le laminage à chaud, le bobinage et enfin le laminage à froid. Après le laminage à froid, le matériau s'est durci donc le recuit (Figure 4) va permettre de recristalliser les grains et de produire des aciers TRIP ayant les propriétés demandées par les clients. Cette étape permet de restaurer une certaine ductilité nécessaire pour la mise en forme des tôles. Le cycle de recuit illustré à la Figure 4 correspond à celui des TRIP étudiés (avec un passage à la galvanisation). Pendant le chauffage et le maintien entre Ac_1 et Ac_3, la microstructure initialement ferrito/perlitique est recristallisée pour atteindre à la fin du maintien une microstructure composée d'environ 60 % de ferrite et 40 % d'austénite. Cette distribution dépend de la température de maintien et plus elle est élevée, plus la quantité d'austénite formée est importante.
Cette étape est suivi par un refroidissement entre 30 et 60°C/s assurant germination, croissance et grossissement de la ferrite. Ce refroidissement doit être assez rapide pour éviter la formation de perlite.
Pour stabiliser l'austénite grâce à son enrichissement en carbone, un maintien isotherme dans la région bainitique est effectué. Lors de cette étape, une partie de l'austénite est transformée en bainite. Il faut noter qu'en présence d'aluminium et de silicium, la bainite formée est sans Fe_3C.

Après cette étape, l'acier est trempé dans un bain de Zn à 460°C avant d'entrer dans un four pour former le revêtement GA (alliage Zn-Fe).
Le refroidissement final entraîne une transformation partielle de l'austénite en martensite, surtout à mi-épaisseur qui est particulièrement enrichie en C et Mn. A la fin de ce recuit, l'austénite restante est appelée austénite résiduelle et représente 8 à 20 % de l'acier.

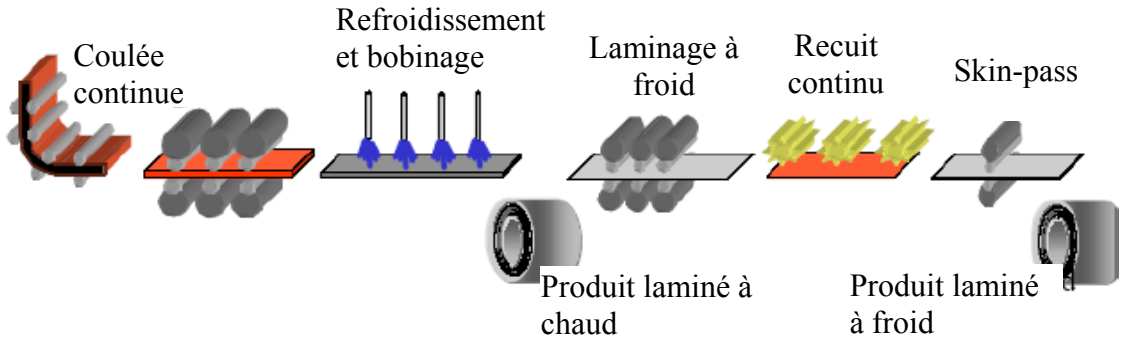

Figure 3. Production des aciers TRIP

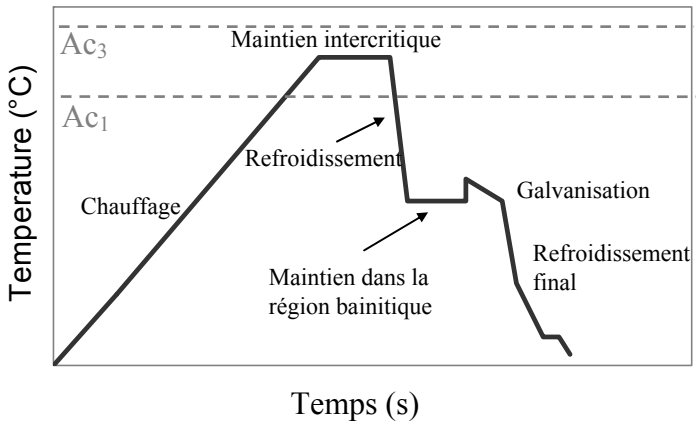

Figure 4. Traitement thermique des aciers TRIP

Mise en forme des tôles par emboutissage

Dans l'industrie automobile, la plupart des pièces sont embouties pour leur donner leur forme finale. En fonction de la pièce désirée, le procédé d'emboutissage varie et il est parfois nécessaire d'effectuer plusieurs emboutissages pour obtenir des pièces automobiles avec des formes plus ou moins complexes.
Cependant, sur les nouveaux grades d'aciers TRIP ayant des propriétés mécaniques de plus en plus élevées, des fissures apparaissent sur les rayons des pièces embouties (Figure 5). Relier les propriétés de mise en forme des aciers avec leurs propriétés mécaniques classiques semblent maintenant insuffisant.
Il est donc nécessaire de prendre en compte la microstructure de ces aciers pour étudier plus précisément leur comportement en pliage.

Figure 5. Poutre de pare-choc fissurée au niveau d'un pli après emboutissage

Problématique et démarche de l'étude

Pour élargir l'utilisation des aciers THR pour les pièces de structure, les limites des propriétés en mise en forme doivent être connues et une caractérisation est nécessaire pour aider au développement de ces nouveaux grades d'aciers. Ainsi, la compréhension de la mise en forme des aciers THR pour application automobile implique une étude détaillée des mécanismes d'endommagement pendant les essais de mise en forme.

Le but de ce travail est donc d'étudier les relations entre microstructure et capacité au pliage des aciers THR.
Les aciers TRIP peuvent généralement être emboutis plus facilement que les autres aciers. De plus, ils sont développés dans le but d'effectuer des pièces aux formes très complexes. Il est ainsi nécessaire d'étudier plus particulièrement ces aciers. Dans cette étude, quatre aciers TRIP présentant des performances en pliage différentes et des microstructures variées ont été utilisés. Deux tests de pliage ont particulièrement été étudiés : le pliage en V et le pliage sous traction.

Les principaux objectifs de ce projet sont:

- *Effectuer les liens entre microstructure et endommagement pendant les tests de pliage.*
- *Etudier d'une manière quantitative, dans le cas particulier des aciers TRIP, le principal paramètre microstructural qui contrôle la fissuration en pliage.*
- *Proposer un outil permettant aux ingénieurs métallurgistes de tester d'une manière simple des voies d'amélioration métallurgique des aciers THR vis à vis de leur performance en pliage.*

Ce manuscrit est constitué de quatre chapitres:

Le premier chapitre est consacré à l'état de l'art concernant à la fois le pliage, les aciers TRIP ainsi que l'origine des micro et macroségrégations. Dans une deuxième étape, une caractérisation à la fois microstructurale et mécanique des quatre aciers étudiés est effectuée.

Après cet état de l'art et une présentation rapide des quatre matériaux de l'étude, il sera possible d'expliquer plus en détail l'approche de cette étude. La démarche des trois autres chapitres sera donnée à la fin du premier chapitre.

Chapter 1

Characterization of the bendability of TRIP steels

In the following part, a literature survey on bending tests and a short presentation of TRIP steels was given.
Four TRIP steels were chosen in this study to investigate and characterize their bendability.
No clear correlation between bendability and both usual mechanical properties and microstructural features have been observed.
Therefore, it is necessary to develop a more detailed mechanical / microstructural analysis of failure in bending.

Table of contents

I. Literature survey

I.A. Bendability of sheet metals

The formability of sheet metals often refers to the limit of strain or stress states up to which the forming process is accomplished successfully.
It is very difficult, however, to find suitable strain limit for sheet bending operations. The bending limit could be defined as the amount of strain that initiates a crack at the outer surface of the bending zone, from which a minimum bending radius is deduced. It is affected by many testing and material parameters, such as the tool geometry, bending procedure, material properties, sheet thickness and the surface or edge condition of the sheet. Note that information provided in this part is the more precise as possible. When information is missing, it is mean that all data were not mentioned in the various studies.

Bending tests can be classified in three categories: simple bending, stretch bending and draw-bending. The two last categories correspond to bending under tension and differ from the first test where bending is applied without tension. It is important to distinguish pure bending by appliance of a torque on both sides from 3 points bending which induces both pure bending and a little tension.

1. Impact of specimen dimension and mode of preparation

One of the most significant parameters for this type of test is the surface state of cut edges. Indeed, the blanking process creates a section with three areas: a rollover (edge rounding), a sheared zone and a fracture zone (including the burr), Figure I.1.
The last one is generally the most problematic as it may introduce lot of incipient damage which will further develop under a stress field. Moreover, strain hardening due to cutting will increase the hardness of the material over a significant depth, reducing locally ductility.

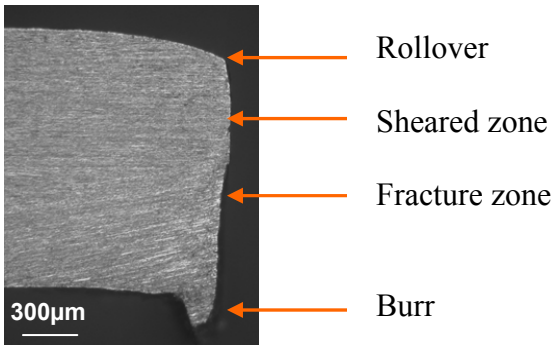

Figure I.1 : Cut edge of a dual phase steel sheet (cross-section micro light optical micrograph) (Dalloz et al., 2007).

To perform a bending test, it is necessary, before any other operation, to grind the surface of the edges. Indeed, the bending test is considered as valid (no artefact due to specimen preparation) only if edge effect is negligible. This means that a crack should start from the middle of sample width and not from the edge.
In addition, the sample width has a non-negligible influence on the allowed minimal bend. It is easier to bend samples with decreasing width because the necessary stress to bend the

sample will be lower. Moreover, a very wide sample leads to plane strain field whereas for a narrow one, the stress state is closer to uniaxial tension.

A study done on a copper-alloyed material shows that the minimal bending radius can be doubled if sample width increases from one to ten times the material thickness (Figure I.2). This tendency becomes blurred for higher values of width. We can also imagine that this dependency on specimen width should vary according to the ductility of material (Determe, 1998).

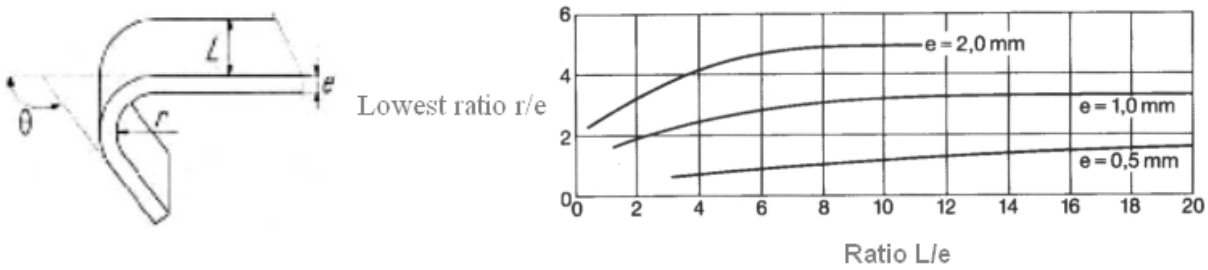

Figure I.2: Minimum bending radius evolution according to sample width for copper alloys ($CuFe_2P$) with various values of thickness (Determe, 1998).

2. Impact of microstructure

The first cause of material damage is generally the presence of internal inhomogeneities. For steels, we can distinguish various categories of defects, which are:
- Inclusions
- Microstructural heterogeneities.

Col (2010) showed that in presence of manganese sulphides (MnS), the bendability of a steel sheet may be lowered due to the initiation of a crack at this type of inclusion (Figure I.3). The material in this picture is a hot rolled mild steel of 1.5mm thickness.

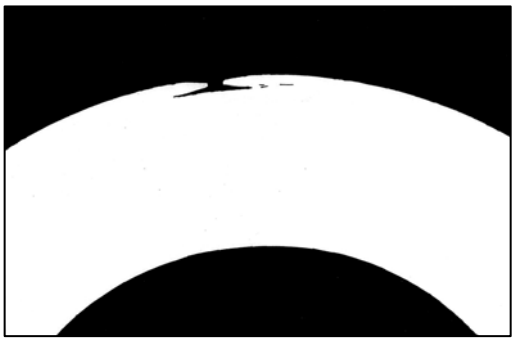

Figure I.3. Crack due to a MnS on a wheel rim element (Col, 2010).

Such inhomogeneities can induce heterogeneous behaviour. Their location and orientation, often elongated along the rolling direction, favour crack development along the transverse direction. This can explain differences in bending behaviour noticed between rolling and transverse directions (Figure I.4). Indeed, sheet bend along transverse direction has generally a lower bendability. This effect was observed by Leu et al. (1997) where a poor bendability was noticed on transverse bent specimens.

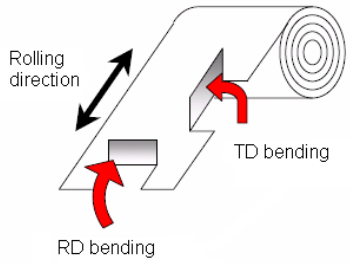

Figure I.4 : Bend orientation with respect to the coil (Determe, 1998).

Yamazaki et al. (1995) showed that the bendability of UHSS with a tensile strength higher than 780MPa correlates better with microstructural homogeneity than with total elongation. In their study, they evaluated the bendability of steels by placing a specimen over a 90° V-block, forcing a punch of specified tip radius into the specimen, and measuring the minimum bending radius at which the specimen did not crack. Before bending, they performed hardness measurements on various sheets with various levels of microstructural homogeneity. Rockwell hardness was measured at five points with 2mm intervals from the surface of sheet specimens, and its standard deviation was taken as a microstructural homogeneity index. The minimum bending radius does not correlate at all with the total elongation in tension but fits quite well with the microstructural homogeneity index (Figure I.5). In their study, they measured the strain distribution of the bend surface and showed that higher strains were found for ferritic areas while lower strains were measured for martensitic areas. In addition, cracks are initiated at the boundary between high-strain portions and low-strain portions, i.e. between the hard and soft phases.

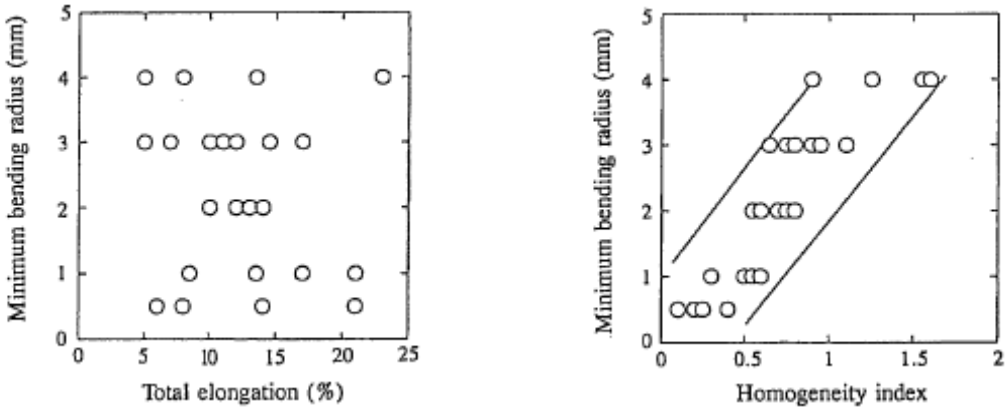

Figure I.5. Bending radius vs. total elongation and microstructural homogeneity index (Yamazaki et al., 1995).

Nagataki et al. (1994) worked on bendability of UHSS with fully martensitic structure having tensile strength ranging from 1100 to 1650 MPa and a thickness of 1.4mm. They showed that the microstructure should be refined and homogenized for the improvement of bendability.

From a few years, health and cleanliness of steels have been improved. This induces a decreasing of inclusions into steels. Moreover with the increase use of UHSS, inclusions still have an influence on the bendability but heterogeneities of microstructure (difference between hard and soft phases in multiphase steels for example) seem to have the most important role on the bendability of materials.

3. Relationships between bendability and other In Use Properties

Mechanical properties such as yield strength, tensile strength, strain hardening, reduction of area in tensile test, etc can be tentatively used to characterize the formability of a sheet. However, these values are not the most reliable parameters to predict the bendability of sheets.

To investigate pure bending of anisotropic sheet metals, Leu et al. (1997) proposed a simplified approach to identify the bending instability using the "maximum bending moment" concept, with the incorporation of the normal anisotropic R-value (defined as the ratio of the transverse plastic strain in the plane of the sheet to the plastic strain through the thickness) and the strain hardening exponent "n". The value of R is given by the following averaging: $R = (R_0 + 2\ R_{45} + R_{90}) / 4$ where R_0, R_{45} and R_{90} are the Lankford coefficients at 0°, 45° and 90° with respect to the rolling direction of the sheet.
They showed that the springback is almost proportional to the normal anisotropic value R and decreases sharply with decreasing strain hardening exponent "*n*". Concerning pure bending, the authors have shown that the minimum bending radius is proportional to the sheet thickness and decreases with the normal anisotropy "R" and the strain hardening exponent "*n*". However, this trend was not confirmed by Yamazaki et al. (1995) who showed that the minimum bending radius was not correlated with the strain hardening exponent. In this paper, sheet was bent on a 90° V-block contrary to Leu's study where pure bending was assumed.

Datsko et al. (1960) predicted the minimum bending radius for several materials (magnesium, aluminium, 1018 steel, cast-iron and titanium), from the reduction of area determined by a standard tensile test. They assumed that the fracture strain in the outer fibre of a bending specimen equals the one in tensile test specimens. The material assumed to be homogeneous, isotropic and the sheet was assumed to be bent in plane strain conditions. In their paper, they determined several equations allowing linking the R_{min} (smallest radius that a material can withstand without cracking) to the *Ra%* (reduction of area) with various location of the neutral fibre. In their study, three-point bending test was used to determine the minimum bending angle as well as another bending method which provided similar results.

In case where the neutral fibre coincides with the mid-thickness the following equation can be used:

$$\frac{R}{t} = \frac{50}{Ra\%} - 1 \qquad (1)$$

According to the authors, this equation is only valid for $Ra\% < 20$.

When there is a shift in the neutral fibre, the equation (2) is chosen:

$$\frac{R}{t} = \frac{60}{Ra\%} - 1 \qquad (2)$$

The Forming limit curve (FLC) can also be used to predict the bendability of a material. For example, Sriram et al. (2003) performed stretch bending tests on various steels such as skin panel steels (BH210, BH280, IF) and structural steels (HSLA350, DP600, TRIP600,

DP800, DP980) with thicknesses ranging from 0.6mm to 1.8mm. Strains were measured in the failed samples both in the unsupported sidewall region and on the punch nose and compared with the corresponding achievable limit strain determined by the empirical FLC. These authors introduced a new element to define the stretch bending ability of UHSS within a wide range of *R/t* ratios and introduced a new concept called "stretch bendability index". The purpose of the index is to isolate the stretching influence from coupled stretch-bend condition. This index represents the ability of the material to withstand stretching in the presence of severe bending.

The stretch bendability index is expressed as a ratio: *A / B* (Figure I.6). *B* is the limit strain (from FLC) for a given strain path and *A* is the maximum major hoop strain in the unsupported sidewall region for a given *R/t* ratio when the failure occurs at the punch nose. The maximum achievable value of the stretch bendability index is 1.

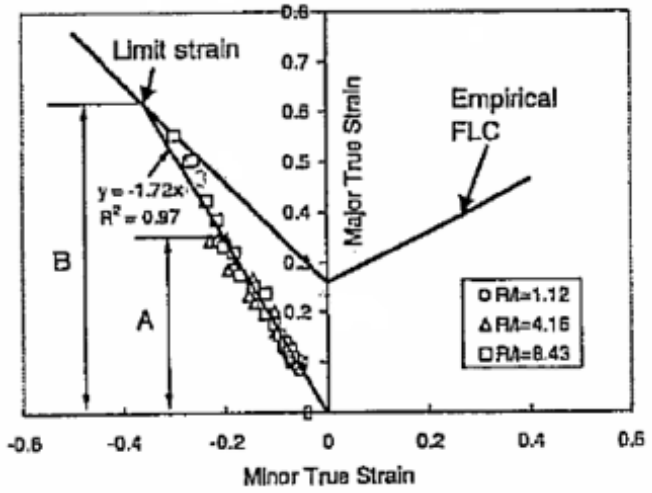

Figure I.6. Strain path and stretch bendability index (SBI) for 0.93mm BH210 specimens (Sriram et al., 2003).

In Figure I.7, it is noticed that the *R/t* value for a stretch bendability index (SBI) of 1 represents the critical *R/t* ratio $(R/t)_c$ for stretch bending for a given steel grade. For *R/t* ratios below $(R/t)_c$, bending severity limits achievable formability. For *R/t* ratios higher than $(R/t)_c$, the effect of bending on the achievable formability is minimal.

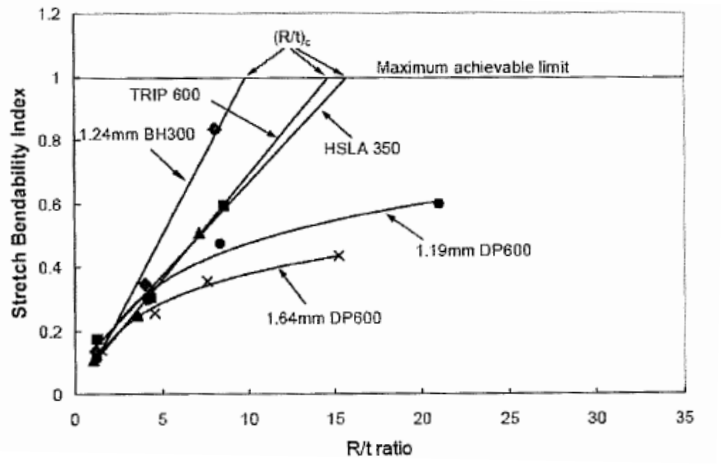

Figure I.7. SBI as a function of *R/t* ratio for some structural steels (Sriram et al., 2003).

4. Failure modes

a. Simple bending

In their work, Nagataki et al. (1994) observed fracture surfaces of specimens tempered at 400°C after bending with an inside radius close to 0 mm. They showed that fracture in bending occurs by shear mode crack propagation followed by void nucleation. Steninger et al. (1982) worked on steels with tensile strength ranging from 240 to 390 MPa and a thickness of 5 mm. They performed V-bending tests on these specimens and observed cracks on outer surfaces of the specimens. Fracture propagated along shear bands and voids expanded preferentially along the shear direction.

Chien et al. (2004) reviewed two most commonly found failure modes: necking (which involves void nucleation, growth and coalescence) and shear localization. The bendability of aluminium sheets was investigated with the shear localization mode. For example, the pictures of three samples bent with three different radii are shown in Figure I.8.
Note that there is a high indentation of the punch especially for specimen bent with lower punches (radii of 0.3mm and 0.4mm).

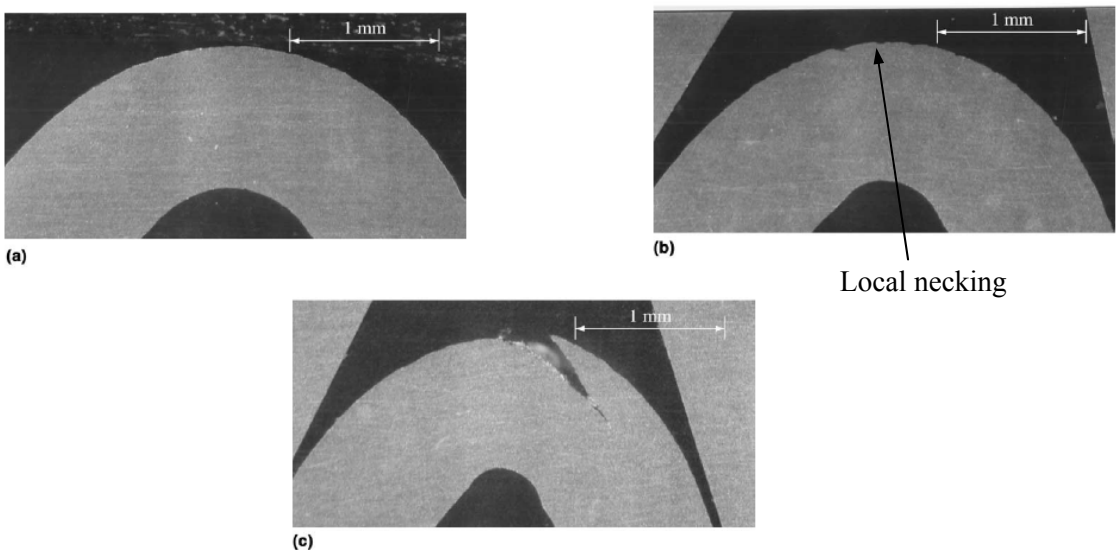

Figure I.8. Cross-sections of AA6111 specimens (aluminium sheet) with an initial thickness of 1mm. These specimens were subjected to bending in a semi-guided wrap-bend test with bending radii of: (a) 0.6 mm, (b) 0.4 mm and (c) 0.3mm (Chien et al., 2004).

Vallellano et al. (2008) analysed the effect of strain gradient in stretch bending on the failure of metal sheets. Depending on the severity on the gradient, two kinds of failure are expected: a necking-controlled failure and a fracture-controlled failure. They showed that the sheet failure is controlled by the ability of the less strained fibres (inner fibres) to neck. This idea is consistent with the work reported by Tharrett and Stoughton (2003). In fact, they observed necking on the sheet when the strain on the concave side of the sheet reached the in-plane forming limit strain. A conservative failure criterion is to assume that the sheet fails once the outer fibre fails. This criterion is obviously not new and has been successfully checked in a variety of bending operations (Ragab and Saleh, 2005).

b. Stretch bending

Demeri (1981) performed stretch bending tests on several steels (AK steels with tensile strength of 300MPa, HSLA-F50 and DP 80 with tensile strength of 680MPa) and on one aluminium sheet (2036-T4) with thicknesses ranging from 0.5mm to 2.5mm in order to determine the influence of material and geometrical variables on sheet metal formability. Data obtained are curves relating the punch radius "*R*", the sheet thickness "*t*" to the height of the configuration at failure "*H*" (cf. Figure I.9 for AK steels).
For AK steel, fracture location depends on three factors: (i) punch radius, (ii) sheet thickness and (iii) transverse constraints. The curves obtained for the various materials could be divided into two regions:

i) predominantly stretching for values of $(R/t) > 20$
ii) predominantly bending for values of $(R/t) < 20$.

Indeed, for most of steel grades, failure moved from the punch contact region to the unsupported sidewall with increasing the *R/t* ratio.

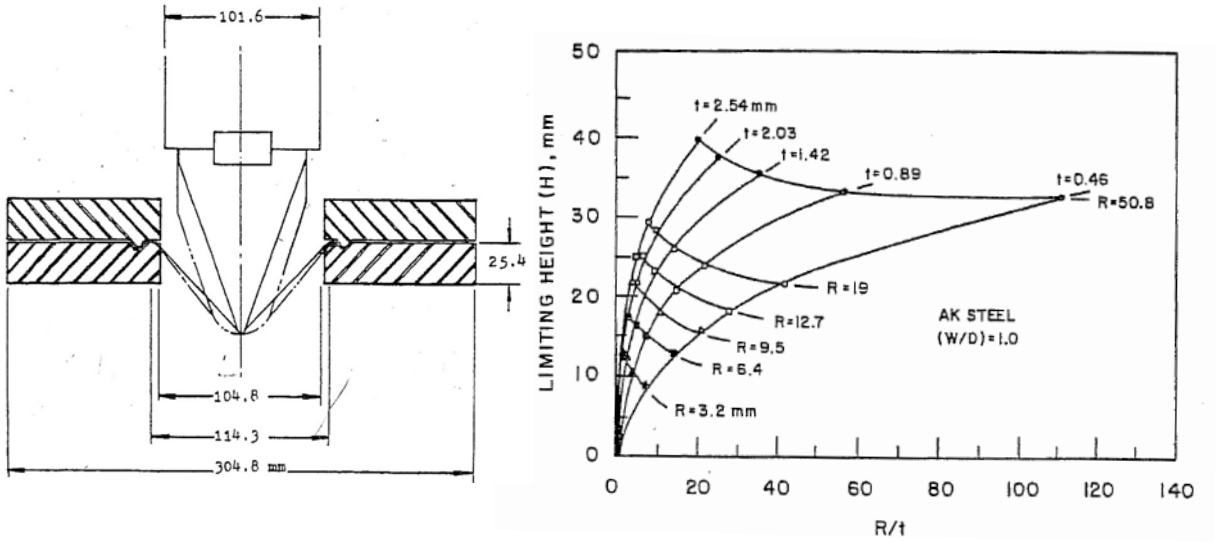

Figure I.9. (a) Stretch bent test, (b) Bendability curves for AK steel sheets (Demeri, 1981).

Damborg (1998) used another type of stretch bending test to determine the stretch bendability of sheets. For that purpose, he carried out tests on two steels: HSLA (550 MPa, 1.5mm) and DQSK (Draw Quality Silicon Killed with 365MPa and 1.5mm thickness) and one aluminium alloy (Al 6022-T4 with 330MPa and 0.9mm thickness) with various punch radii and various tension loads (Figure I.10). Thanks to this test, he also noticed the two possible fracture modes in stretch bending: bending or stretching fracture (Figure I.10).

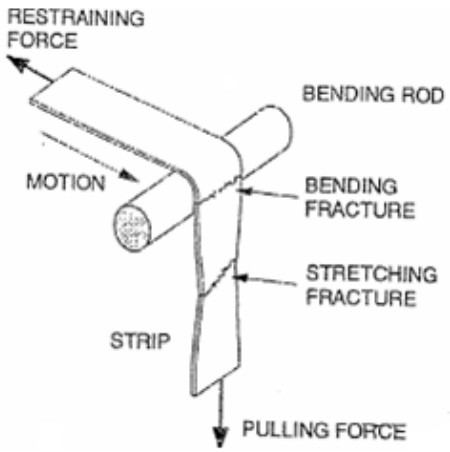

Figure I.10. Schematics of a bending under tension test, illustrating the typical location of the bending and stretching fracture (Damborg, 1998).

Sriram et al. (2003) found similar results in stretch bending (Figure I.11) except for some DP steels where, even for for high R/t ratios, failure did not move from the punch nose to the sidewall. In other words, DP steels were found to be more sensitive to bending fracture (with respect to stretching fracture) than the other steels. According to the authors, the different behaviour of DP steels is not clearly understood. They assumed that steel processing, chemistry and distribution of martensite may influence its forming behaviour.

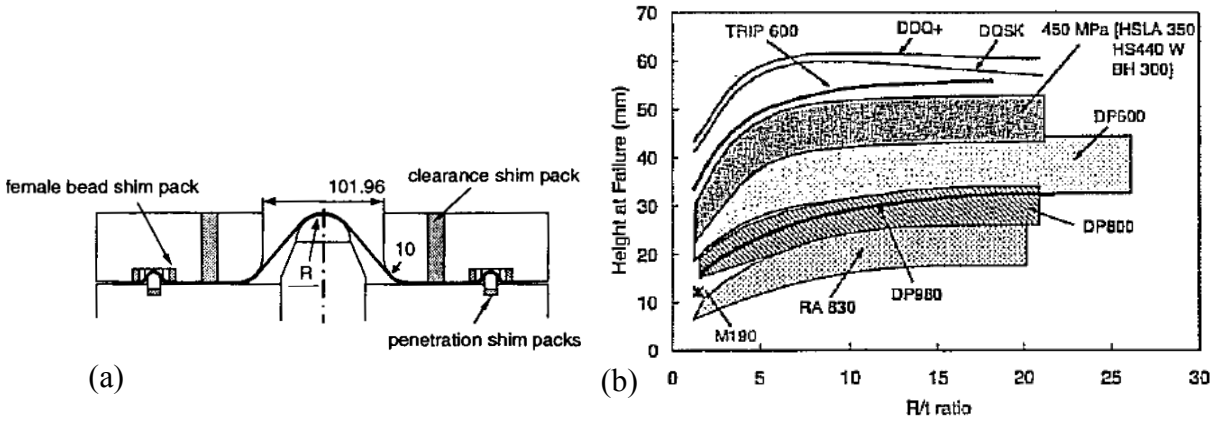

Figure I.11. (a) Stretch bending device, (b) Height at failure as a function of *R/t* ratio for structural steels in stretch bending (Sriram et al., 2003).

To summarize, in simple bending, cracks seem to initiate from the surface (on the bent nose) and propagate along shear direction. This will be discussed in the following parts.
In addition, from the above mentioned results, the height at failure during a stretch bending test can be expressed as a function of *R/t*. Moreover, several authors claimed that above a critical ratio $(R/t)_c$, failures move from the punch nose to the sidewall, which means that above $(R/t)_c$, stretching is predominant over bending.

5. Mechanical description of the bending tests

a. Analytical models

To simulate as well as possible what happens in material during bending, the stress and strain distributions have to be known within the bent specimen.

During bending solicitation, strain goes from elastic to plastic modes until fracture. During the elastic stage, stress repartition is homogeneous with:
- a zero value at neutral fibre
- a compression stress next to inner radius
- a tensile stress next to outer radius

Beranger et al. (1994) demonstrates that in pure bending, the neutral fibre is exactly at mid-thickness (Figure I.12a). When tension appears in bending and in presence of friction, this assumption is not true and thus the neutral fibre moves within the material due to thickness reduction of sheet steel (Figure I.12b).

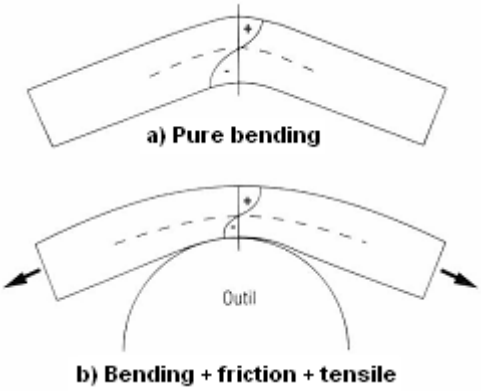

Figure I.12 : Stress distribution: a) pure bending b) bending + friction + tensile (Beranger et al., 1994).

In simple bending, without applied tension, and where the radius of curvature is more than several times the sheet thickness, the neutral fibre approximately coincides with the mid-thickness (Figure I.13) so that the axial strain ε can be given by the following equation:

$$\varepsilon(y) = \ln(1 + \frac{y}{R_0}) \tag{3}$$

Where R_0 corresponds to the radius at mid-thickness and y is the distance from the mid-thickness.

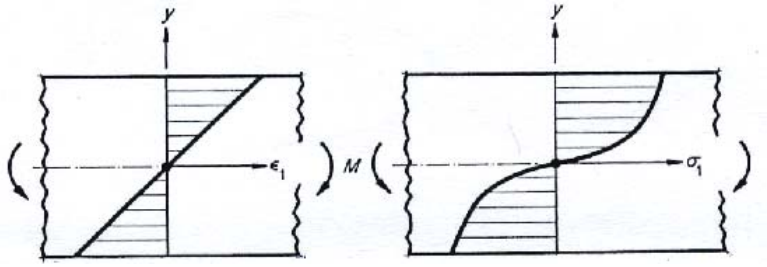

Figure I.13: Strain and stress distribution for a material in pure bending that obeys the relation $\sigma_1 = k\varepsilon_1^n$ (Marciniak and Duncan, 1992).

In various studies (Chakrabarty et al., 2000; Chakrabarty et al., 2001, Livatyali et al., 2003; Quach et al., 2004; Ragab et al., 2005), the true bending strain was defined as equation (3).

However, other authors developed more accurate equations to determine the bending strain. For example, Zhang et al. (1998) used the following equation:

$$\varepsilon = \varepsilon_0 + \frac{1}{2}\ln(1 + \frac{2y}{R_0}e^{-\varepsilon_0}) \tag{4}$$

where ε_0 is the strain at the neutral fibre. When the neutral fibre is undeformed, the value ε_0 becomes equal to zero. In this case, equations (3) and (4) can be approximated by the same following value:

$$\varepsilon \approx \frac{y}{R_0} \tag{5}$$

Wu et al. (2006) defined the bending strain at the outer fibre with the following equation:

$$\varepsilon = \ln\left(1 + \frac{\frac{t}{R_0}}{2\left(1 + \frac{t}{R_0}\right)}\right) \tag{6}$$

Lemoine et al. (2009) compared the reliability of these formulas and showed that they are all equivalent till a ratio thickness / bending radius equal to 0.1. For t/R > 0.1, significant difference appear between these formulas (with y = t / 2, i.e. at the outer surface).

Analytical and semi-analytical models have been widely adopted in the study of bending process (Leu, 1997; Zhang et al., 1998; Chakrabarty et al., 2000 and 2001; Quach et al., 2004 and Ragab et al., 2005). Unfortunately, these models are generally used with significant simplifications and simple constitutive equations laws (i.e. without damage) and thus, the accuracy of the results are considerably affected. Therefore to avoid these problems and to increase the accuracy of these models, finite-element simulation is needed.

b. Need of numerical simulation to predict the bendability of sheet

The understanding and development of bending mechanics are aimed at obtaining important information for industrial applications: (i) springback prediction to determine accurately the final dimensions of bent parts, (ii) bendability and fracture prediction, (iii) estimation of the bending force reached during these tests and (iv) contact issues between punch and sheet. As the fracture in bending is a localized phenomenon, it is intended to model very accurately this test to access to strain and stress fields. Therefore, the numerical simulation thanks to a finite-element method is generally used to model precisely bending tests.

Only few numerical works can be found in literature concerning the modelling of bending tests and prediction of fracture. Most finite-element simulations of bending tests focused

on the prediction of springback (Date et al., 1999; Gan and Wagoner, 2004). In order to correctly predict bendability and fracture in bending tests, it is necessary to include a damage criterion in the model and to select a suitable one, accurate knowledge of damage mechanisms is essential. In the case of sheet-metal forming, a lot of authors studied the mechanisms leading to final failure and proposed their own models.
The formability approaches can be classified in three main families: (i) Forming Limit Diagrams (FLD) approaches which are based on strain fields and dedicated to sheet metal forming (Keeler and Backofen, 1964; Goodwin, 1968) (ii) coupled damage approaches and (iii) uncoupled damage approaches.

For many sheet forming processed, the FLD has been used for the evaluation of failure. Laukonis and Ghosh (1978) and Graf and Hosford (1993) showed that FLD are only valid with proportional strain path. However, for bending tests, the stress/strain state changes continuously and so the strain path does not stay constant. In order to solve this issue, other failure criterions were used.
Considering coupled damage approaches, damage evolution is considered within the elastoplastic material law and fracture is then fulfilled when the damage variable reaches a critical value. Gurson (1977) was one of those who develop a ductile damage macroscopic constitutive law based on microvoid growth. Its model was largely used and extended in the literature (Tvergaard, 1982; Tvergaard and Needleman, 1984). The Gurson model is the first micromechanical model for ductile fracture which introduces a strong coupling between deformation and damage. It is derived from an analysis similar to the one performed by Rice & Tracey (1969) for an isolated void. Other scientists as Lemaitre (1985) also developed damage formulation fully coupled with the behaviour laws of elasto-plasticity.
Eventually, uncoupled damage approaches also named “fracture criterion” are used as soon as the failure is fulfilled when the stress and/or the strain state reaches a critical value

To model forming tests including failure criterion, several finite-element analysis exist in the literature (Table I.1). The main aim of these numerical simulations generally consisted in the prediction of bendability, failure location and estimation of the stress and strain fields. Note that most of the authors used an isotropic hardening law with either an anisotropic yield criterion (Hill generally) or an isotropic criterion (Von Mises). According to the authors who chose a mixed (isotropic+kinematic) hardening law, results were well predicted and best results were obtained than with an isotropic hardening law.

Material	Thick.	Forming tests	2D/3D	Constitutive equation	Failure criterion	Main results	Reference
2024-O aluminium alloy	1.02mm	air bending in U or V-shape	2D: Plane strain	Isotropic hardening + Hill	No fracture criterion	Springback prediction	Wang et al. 1993
mild steel	0.67mm	deep drawing test	3D	Isotropic hardening + Hill	Extension of Gurson-Tvergaard model	Prediction of localized necking and damage	Brunet et al. 1996
mild steel & high strength steel	1.2mm and 1.4mm	Cyclic 3-point bending test	3D	(i) isotropic (ii) kinematic (iii) mixed hardening + Von Mises	No fracture criterion	Best prediction of the bendability with mixed hardening	Zhao and Lee 2002
0.6% carbon steel (780MPa)	3mm	air bending test	3D	Isotropic hardening + Von Mises	Rice and Tracey	Prediction of damage evolution and F/d curve	Hambli et al. 2004
HSLA 500	4mm	wiping-die bending test	3D	Isotropic hardening + Von Mises	Lemaitre	Prediction of stress	Bahloul et al. 2006
Orthotropic thin sheet		Hydrobulging test	3D	Mixed hardening + Hill	continuum damage mechanics	Prediction of fracture location	Saanouni and Badreddine 2007
HSLA	4mm	wiping-die bending test	3D	Isotropic hardening + Von Mises	Lemaitre	Prediction of failure and load	Mkaddem and Bahloul 2007
galvanized BH220	1mm	Nakazima test	3D	Isotropic hardening + Von Mises	GTN	Prediction of local crack initiation	Uthaisangsuk et al. 2008
DP980		draw bend test	3D	Isotropic hardening + Von Mises	No fracture criterion	Prediction of failure and F/d curves	Kim et al. 2009
DP600	1.2mm	Nakazima test	3D	Isotropic hardening + Barlat	Gologanu model	Prediction of failure, F/d curves and strain fields	Falkinger et al. 2010
DP780	1mm	stretch bending test	(i)3D, (ii)plane strain and (iii)shell elements	Isotropic hardening + Hill	MMC fracture model	Prediction of failure, F/d curves and strain and stress fields (best agreement with 3D)	Luo et Wierzbicki 2010
DP600	4mm	pure bending test	2D: plane strain	Mixed hardening + Hill	extended Gurson model	Prediction of bendability	Bettaieb et al. 2010

Table I.1. Studies dealing with numerical simulations of various forming tests.

6. Summary

To conclude on this part, it was first noticed that several parameters can influence the bendability of steels (mechanical properties, microstructure, tools, etc…) making difficult the understanding of formability issue. Among them, microstructural parameters, in particular heterogeneities, seem to have a key role in bending operation.
Secondly, it was shown that, in bending tests, failure propagate by a shear mode and seem to initiate from the outer surface in air-bending test and appear either at the punch nose or in the sidewall in stretch bending tests depending on the bending conditions.
Finally, it is highlighted that finite-element numerical simulation is an efficient tool to accurately relate global bending performance to mechanical behaviour and predict failure mechanisms at microstructural scale. It was shown that a mixed hardening law coupled with anisotropic criterion provides the best combination to accurately predict bendability. Almost analyses were carried out with a coupled damage approach and most of them used 3D modelling except for simple bending test where 2D simulation with plane strain condition was sufficient.

I.B. TRIP steels

1. Definition

Low alloy TRIP-aided steels (which will be termed "TRIP steels" throughout this manuscript for the sake of simplicity) are composed of a ductile ferrite matrix containing small islands of hard bainite, martensite and retained austenite. Transformation of retained austenite into martensite during deformation causes significant strain hardening and delays the onset of necking, providing high ductility. It is the "TRansformation Induced Plasticity" (TRIP) effect that forms the basis of the exceptional properties of the TRIP steels.

These steels differ from conventional steels by their remarkable combination of high strength and ductility, resulting from their particular microstructures. The hardening capacity of the TRIP steels is considerable, ensuring efficient strain redistribution during forming and hence good drawability, combined with very high yield strength in the finished component.

Due to their high energy absorption capacity, TRIP steels are principally used for structural and safety automotive parts such as longitudinal beams, seat structures, etc.

2. Processing of TRIP steels

It was shown (Rigsbee and van der Arend, 1977; Speich and Miller, 1979) that retained austenite contained in Dual Phase steel permits the improvement of their mechanical properties.

If austenite is stable enough, the mechanical strength and the ductility are increased. The stabilization is performed after the intercritical annealing. During the bainitic transformation, austenite is supersaturated in carbon, ensuring its stability.

In order to obtain a multiphased structure with retained austenite, the thermal cycle used for DP steel is modified by introducing holding in the bainitic domain (Matsumura et al., 1987). Figure I.14 illustrates heat cycles for cold rolled DP steels (a) and TRIP steels (b).

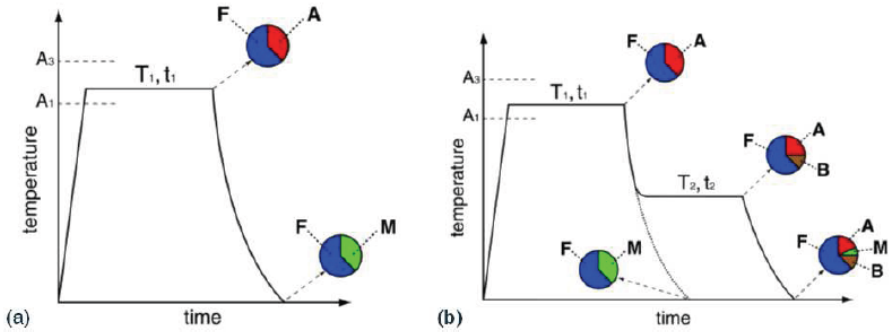

Figure I.14. Heat treatment cycle and microstructures (a) DP steels (b) TRIP steels. F: ferrite; A: austenite; B: bainite; M: martensite (Matsumura et al., 1987).

The evolution of the microstructure during the TRIP steel process is shown in Figure I.15 with:

(i) ferrite and austenite during the intercritical annealing

(ii) austenite decomposition and ferrite nucleation at grain boundary

(iii) ferrite, bainite and retained austenite: during and after the bainitic holding in a range of temperature between 350 and 500°C.

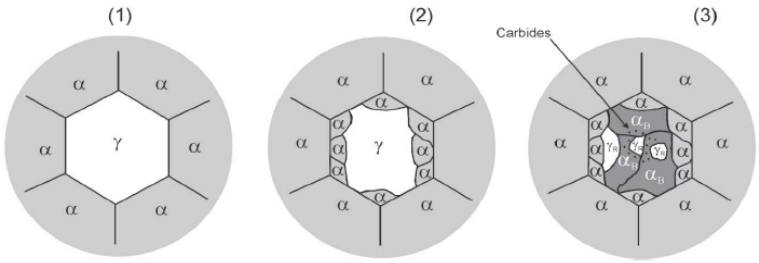

Figure I.15. Microstructure formation during the thermal cycle. α = ferrite, α_b = bainite, γ = austenite, γ_r= retained austenite (Ohlert et al., 2002).

At room temperature, the microstructure of these TRIP steels is composed of ferrite, bainite, retained austenite and sometimes martensite. A typical microstructure of a TRIP steel by SEM is shown in Figure I.16.

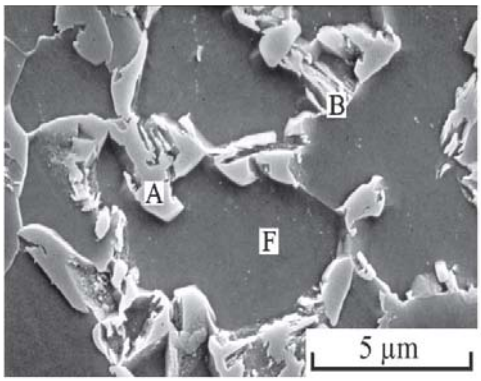

Figure I.16. Typical microstructure of a TRIP steel by SEM. F = ferrite, A = retained austenite and B = bainite (Jacques et al., 2002).

3. Role of retained austenite

In the case of DP steel, mechanical properties are mainly due to the interaction between a hard phase (martensite) and a soft phase (ferrite). For TRIP steels, the progressive transformation of retained austenite into martensite, coupled with the multiphased microstructure are the factors responsible for their mechanical properties.

Destabilization of retained austenite can be caused by plastic deformation (Pickering, 1992). This transformation induced by mechanical loading improves the mechanical properties of low-alloy TRIP steels with dispersed retained austenite islands (Haidemenopoulos et al., 1989; Jacques, 1998).

Retained austenite influences the mechanical properties thanks to both its stability and its distribution: too instable retained austenite is transformed into martensite too early, so that necking cannot be efficiently delayed. On the contrary, if the retained austenite is too stable, the martensitic transformation does not occur and the positive effect on delaying necking is cancelled. Therefore, austenite should have the right good stability to ensure progressive martensitic transformation during straining.

In addition, the repartition of retained austenite must be homogeneous in the part before the deformation. Indeed, the mechanically induced martensitic transformation improves strength and ductility by both composite strengthening resulting from the progressive increase in the amount of hard martensite, and dislocation strengthening of the ferrite matrix as a consequence of the transformation strain accompanying the martensitic transformation (Jacques et al., 2001).

4. Influence of the alloying elements

The present study focuses on the low alloy TRIP-aided steel family, and more particularly the Mn-Al-Si family. Effects of alloying elements have been largely studied. Some authors speak about the role of carbon to stabilize austenite (Tsukatani et al., 1991; Sakuma et al., 1991), other ones about the silicon or manganese contents (Pichler and Stiaszny, 1999; Baik et al., 2000; Kim et al., 2001; Lee et al., 2002; Mahieu et al., 2002) to obtain a multiphased microstructure and to improve the mechanical properties of the material. Effects of various alloying elements can be summarized as:

Carbon stabilizes austenite by decreasing transformation temperatures Ms (martensite start) and Mf (martensite finish).

Manganese is an austenite stabilizer. By delaying ferritic and pearlitic transformations, it promotes the formation of retained austenite. It is also used to harden the material by solid solution strengthening and to refine the ferritic structure. Additionally, pronounced banding may occur in steels containing big amount of manganese (Kim et al., 2001). Banding is attributed to the inter-dendritic segregation of solute manganese during solidification of ingot/slab from liquid steel (Bastien, 1957).

Silicon inhibits the cementite formation during the bainitic transformation and causes the stabilization of austenite thanks to the carbon rejected from the bainitic ferrite formed during isothermal holding at low temperatures. As manganese, it can be used to harden the material by solid solution strengthening.
However, one of its drawbacks is its tendency to segregate and therefore to lead to heterogeneous properties. Moreover, it decreases the welding ability and has a deleterious effect during the hot dip galvanizing of the sheet.
To avoid the drawbacks of high Si additions, lots of authors investigated the possibility to partly replace Si by other elements such as P or Al (Gallagher et al., 2002; Chen et al., 1989; Barbel et al., 2002; De Meyer et al., 1999, Girault et al., 2001). Addition of one of these elements does not seem to affect final mechanical properties. For example, Traint et al. (2002) showed that addition of P and more particularly of Al help to form more stable retained austenite.

Aluminium is a strong ferrite stabilizer, as Si, it inhibits the formation of Fe_3C as it is not soluble in this element. Hence, the most suitable element which can readily provide the same effects as Si is Aluminum. As a matter of fact, up to 1.5%, Aluminum shall not affect coatability adversely (Mintz, 2001; Maki et al., 2003).

Molybdenum is a solid solution strengthener of ferrite and retards pearlite formation. It is also known to increase hardenability and retained austenite fraction but has the drawback to be expensive.

Finally, as for Dual Phase steels, final mechanical properties of TRIP steels can be improved by adding micro-alloying elements such as Ti, Nb or V (Kim et al., 2002; Bai et al., 1998; Pereloma et al., 1999). These elements are principally used to harden the material by solid solution or by precipitation but they are also used to modify phase transformations by acting both on thermodynamic equilibrium and on transformation kinetics.

5. Martensitic transformation

It is a diffusionless transformation which implies the same chemical composition for the austenite and martensite phases.
This transformation corresponds to an austenite shearing which leads to a shape change and a volume increase. This highest volume leads to stress concentration around the newly formed martensite islands. To approach 100% of martensite from retained austenite, it is necessary to cool until a temperature lower than M_f. For cooling temperature between M_s and M_f, martensitic transformation will be therefore only partial.

Several authors tried to give an empirical formula for M_s calculation as a function of the chemical composition (Beranger et al., 1994). The use of such equations is often restricted to a category of steels. For example, for low alloy TRIP steels, the following equation is proposed (Andrews, 1965):

$$M_s(°C) = 539 - 423 \cdot C - 30.4 \cdot Mn - 7.5 \cdot Si + 30 \cdot Al \ \text{(in wt\%)} \quad (7)$$

In fact, the M_s temperature is also a function of other factors such as previous transformations or strain state in retained austenite.
According to the stress or the strain state, various retained austenite transformation mechanisms can be involved in a TRIP steel (Lee et al., 2003). Indeed, mechanical properties that Lee et al. (2003) have obtained in uniaxial tension depend on the amount of retained austenite. On the contrary, the formability in equibiaxial stress is controlled by the stability of retained austenite. The strain rate is also an influent parameter.

6. Microstructure heterogeneities

As mentioned previously, microstructural parameters could have an influence on bendability. TRIP steels have a very good combination of high strength and ductility due to the progressive transformation of retained austenite into martensite. However, the repartition of the phases in the material (especially retained austenite distribution) has an influence on mechanical properties. When this repartition is heterogeneous, this could be detrimental. For example, when retained austenite islands are linked by each others, banded structures are formed and this alignment could have an influence on the bendability. Therefore, these microstructure heterogeneities should have to be taken into account more precisely. Hence, in order to understand the influence of banded structures, the following part will deal with their origin.

I.C. Banded structures formation

Banded structures appear during the cooling after the hot rolling. They are not formed during the solidification of the steel but it is a consequence of the micro and macrosegregations.

1. Solidification of steel in continuous casting

Micro and macrosegregations are formed during the solidification of steels in continuous casting (Figure I.17). Segregation can be defined as heterogeneity of the composition in the as-cast product after complete solidification.
Two different kind of segregation must be distinguished:

- The microsegregation is a variation of composition at the dendritic scale, in the order of 10 to 100µm.
- The macrosegregation is a variation of composition at the product scale, in the order of few mm.

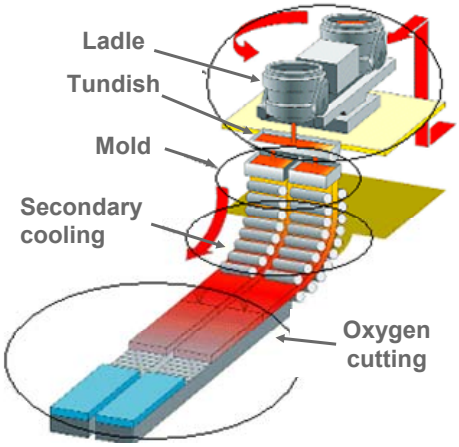

Figure I.17: Continuous casting.

Figure I.18 summarizes the formation mechanisms of solidification structures and segregation in continuous cast steel products (Didier and Bobadilla, 2008).

- At the first step of solidification, a solid shell is formed in the mold. The growth of the solid shell is columnar.

- In a second step, the liquid in the center of the slab becomes undercooled and equiaxed dendrites nucleate and grow in the liquid. These dendrites slowly settle due to the density difference between the liquid and the solid.

- When the number of equiaxed dendrites ahead of the columnar front becomes too important, the growth of the columnar zone is stopped. The width of the central equiaxed zone and of the columnar zone is then fixed. The solidification continues through the growth of the central equiaxed grains. The interdendritic liquid can move between the dendrites arms.

- At the end of solidification, the deformations of the solid skeleton of the mushy zone due to bulging and shrinkage lead to segregated interdendritic liquid motion and to the formation of macrosegregated zones.

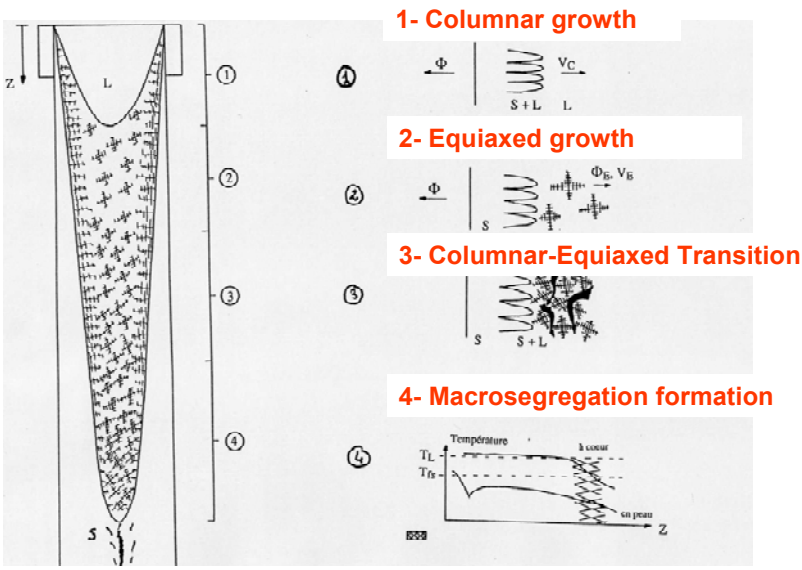

Figure I.18: Solidification of continuously cast products (Didier and Bobadilla, 2008).

After the solidification, the slab has the structure shown in Figure I.19. Two areas can be distinguished:

- Two columnar zones where dendrites are oriented in the perpendicular direction of casting.
- An equiaxed zone with thinner dendrites, at mid-thickness of the product.

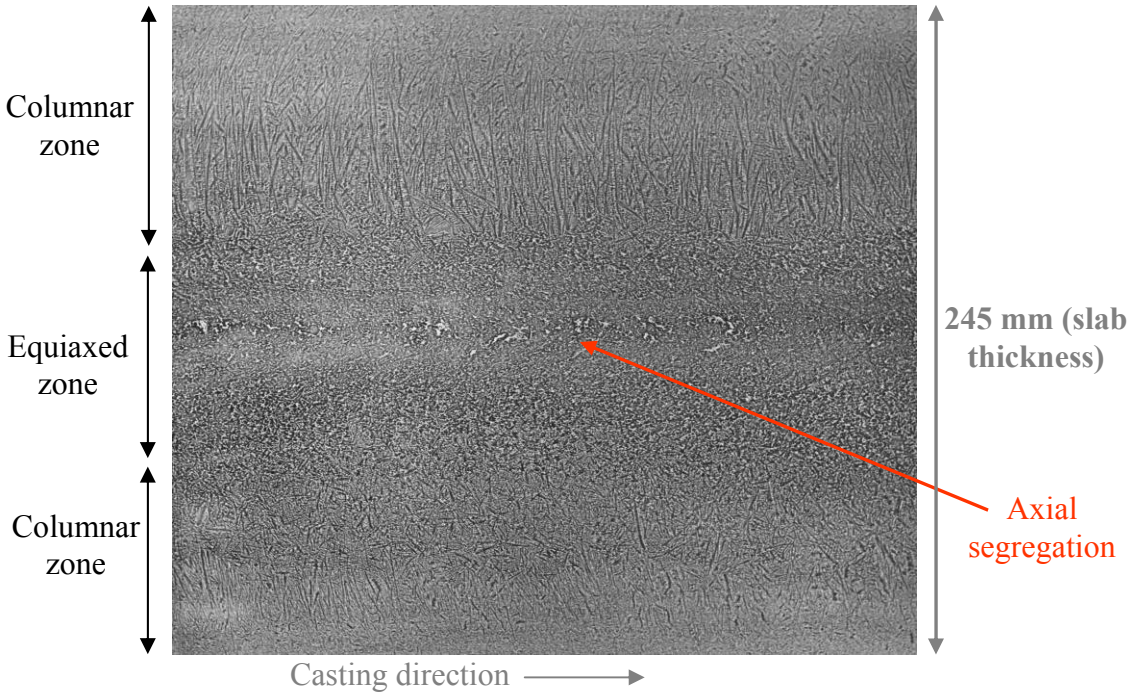

Figure I.19: Solidification structure (Bobadilla, 2008).

2. Microsegregation formation (Bobadilla et al., 2009)

The microsegregation that results from solute redistribution (C, Mn, Si, P, S…) during dendritic solidification leads to variation in the solute concentration between the center and the outside of a dendrite arm.

In as-cast product, because the dendritic microstructure size (primary and secondary arm spacing) increases from the skin to the core of the product, the level of microsegregation increases from the skin to the center part of the slab.

The elements with low diffusion coefficient (Mn, Si, Cr, Ni, Mo…) show high microsegregation level at the end of solidification. This is due to the fact that very few solute redistribution can occur in the solid phase during the solidification. Figure I.20 illustrates a Mn content map from the skin to the mid-thickness of the slab. Note that the dendrites arms regions correspond to the lowest content of Mn (in blue) while the highest concentrations of Mn are observed in the interdendritic region (in red). In addition, the highest Mn content is observed at-mid-thickness, this means that microsegregations will principally appear in this area.

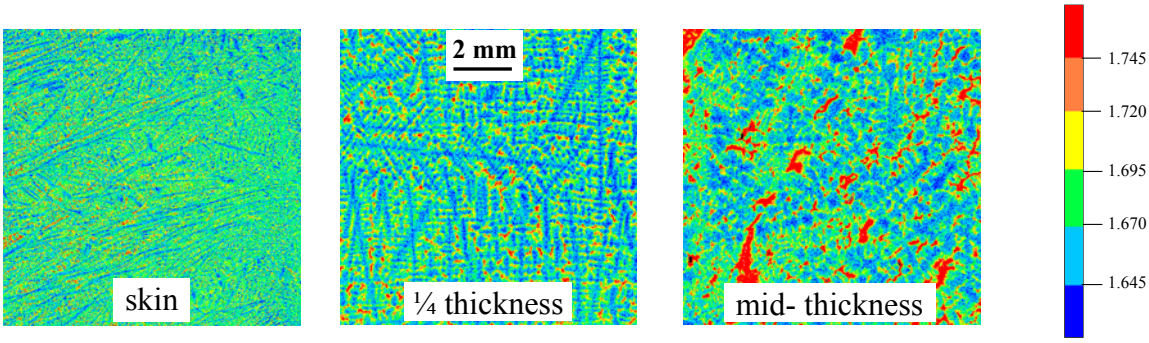

Figure I.20: Mn content for three locations on a slab through the thickness. TRIP800 steel (Bobadilla, 2003).

In as-cast product, the microsegregation level depends on the chemical composition of the steels: it increases with carbon, manganese, phosphorus content and so on… In order to get low microsegregation level it is necessary to refine the dendritic microstructure i.e. to decrease the dendrite spacing.

3. Macrosegregation formation

The mechanisms of macrosegregation formation on flat products during continuous casting are explained by segregated liquid flowing to the center of the slabs at the end of solidification (Didier and Bobadilla, 2008). Two factors will lead to interdendritic liquid motion during the continuous casting of flat products (Figure I.21):

- Bulging of the slabs between the rolls during casting lead to periodic expansion and compression of the central mushy zone. This periodic deformation of the solid skeleton of the mushy zone leads to segregated interdendritic liquid motion and increases the formation of macrosegregation.
- Shrinkage will lead to a local depression at the end of solidification. This depression will create movements of the segregated interdendritic liquid which will be sucked up in the center of the slab.

The last interdendritic liquid, which is rich in alloying elements due to the microsegregation, solidifies in the center of the slabs and forms the axial macrosegregation.

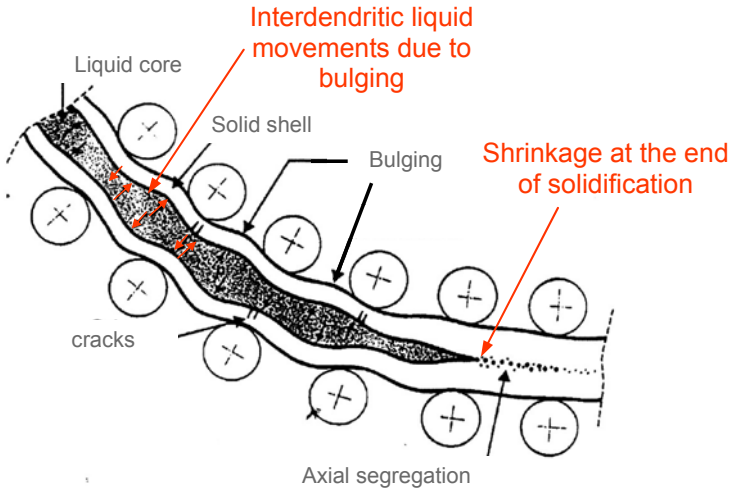

Figure I.21: Mechanisms of macrosegregation formation. Note that bulging is enhanced on the scheme (Didier and Bobadilla, 2008).

4. Banded structures formation (Didier and Bobadilla, 2008)

The theory of the formation of banded structures is illustrated in Figure I.22 (Thompson and Howell, 1992).

Banded structure formation depends on the spatial distribution of substitutionnal elements (Mn, Si) resulting of the remaining segregation from solidification. During hot-rolling, the microsegregated zones rich in Mn formed during the solidification are spread over the rolling direction (Figure I.22a). The temperature at the end of rolling is generally around 800 to 900°C. The steel is fully austenitic in this temperature range. All the structure is austenitic with higher amount of Mn in the segregated zones.
During cooling, the ferrite phase first appears in regions which are the poorest in Mn and for which the transformation temperature for austenite into ferrite is higher (Figure I.22b).
As cooling progresses, the ferrite grains grow in the Mn-poor regions and carbon is rejected into the remaining austenite phase, so that the carbon content in the segregated zone increases (Figure I.22c). When the temperature reaches the eutectoid temperature, pearlite is formed by simultaneous precipitation of ferrite and cementite in the segregated zones which are rich in carbon. The final structure obtained is composed of ferrite grains (in white) in the former intradendritic zones and of pearlite (in black) in the former interdendritic regions (Figure I.22d).

This oriented structure called “banded structure” is responsible for an anisotropy of the mechanical properties of the steel.

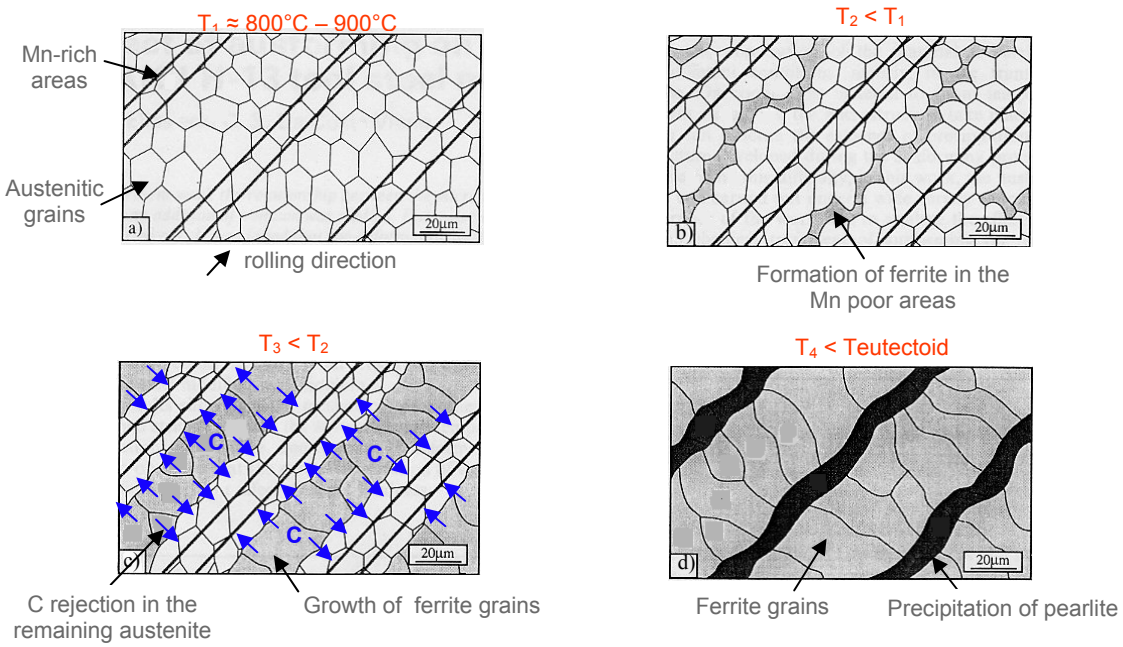

Figure I.22. Banded structure formation (Thompson and Howell, 1992).

5. Parameters allowing to control micro and macrosegregation

For a given steel grade, the main continuous casting parameters to control macrosegregation and microsegregation are:

- Superheating
- Casting speed
- Secondary cooling
- Soft reduction

For metallurgists, the superheat is the temperature of the liquid steel measured in the mold subtracted by the value of the liquidus. A high superheat is characterized by a thick central segregation band and thinner segregation bands around it. A low superheat is characterized by many thick bands in the center of the hot rolled sheet.
The major way used to control the macrosegregation during the continuous casting of flat products is the soft reduction (Figure I.23). Soft reduction is applied at the end of solidification of the continuous cast product. The principle is to reduce the thickness of the product by a few mm near the end of solidification in order to avoid the interdendritic liquid motion in the mushy zone responsible for axial macrosegregation.

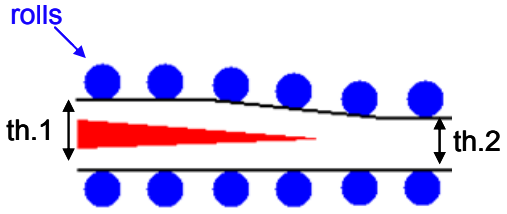

Figure I.23: Soft reduction principle from thickness th.1 down to thickness th.2 at the end of the solidification.

Steps following the continuous casting as the reheating of slabs or the rolling and coiling also have an influence on microsegregation and macrosegregation.

- Slabs furnace: slab reheating reduces the intensity of microsegregation (especially in the skin of the product) but does not reduce the intensity of axial macrosegregation.

- Rolling: hot rolling does not affect the intensity of microsegregation and macrosegregation but elongate them strongly.

- Coiling: the coiling temperature impacts on structural banding, is more important than the superheat and must be as low as possible. Indeed, a low coiling temperature means a higher cooling rate (run out table) before coiling and then less time for carbon diffusion: less banded structure.

6. Summary

Figure I.24 illustrates the effects of (a) the superheat on the slab structure and (b) the coiling temperature on the banded structures after hot rolling.

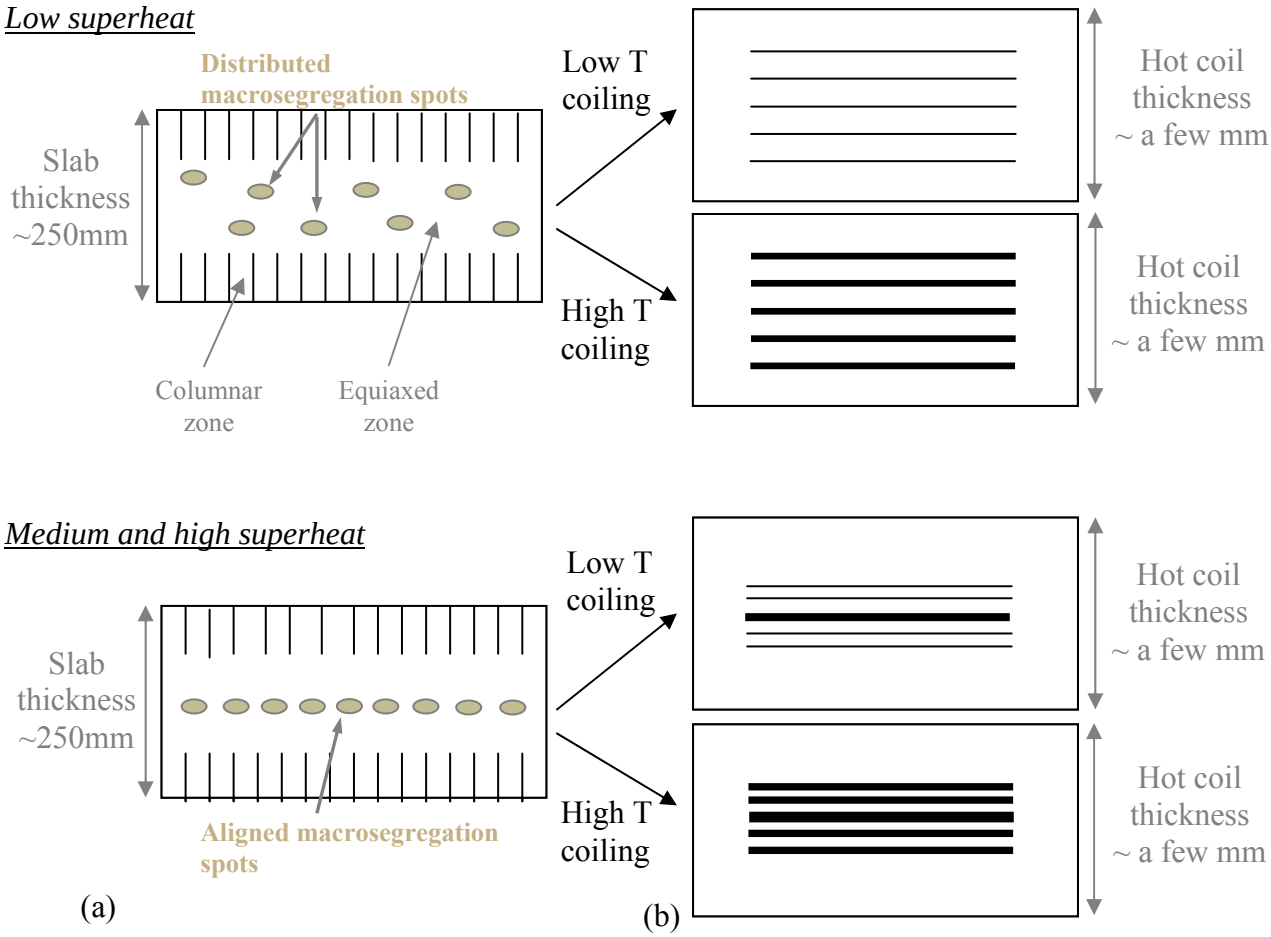

Figure I.24: (a) Superheat effect on the slab structure before hot rolling and (b) temperature coiling effect on the banded structures after hot rolling.

II. Microstructural characterization of the four TRIP-aided steels studied

Four TRIP steels were chosen for this study. Steel 1, Steel 3 and Steel 4 have a thickness of 1.6mm while Steel 2 which come from the same casting as Steel 1 has a thickness of 2mm. All four steels were provided in the galvannealed (GA) state. These materials provide different microstructures and various bending performances. They were thus chosen to check the effect of the microstructure on their bendabilities.

II.A. Chemical composition and phase morphology

Chemical compositions and microstructures at third-thickness (rolling direction) are respectively reported in Table I.2 and Figure I.25. Figure I.26 shows mid-thickness microstructures both along rolling and transverse directions for the four TRIP steels. As Steel 1 and Steel 2 come from the same casting, they have the same chemical composition. Differences with the two other materials are in fact very slight except for the Al+Si content.

	C	Mn	Si + Al	P + Mo + Ti +Cr +Ni
Steel 1	216	1673	1480	194
Steel 2	Same composition as Steel 1			
Steel 3	219	1694	1614	209
Steel 4	225	1663	1554	214

Table I.2. Chemical composition of the TRIP steels (x 0.001 wt%)

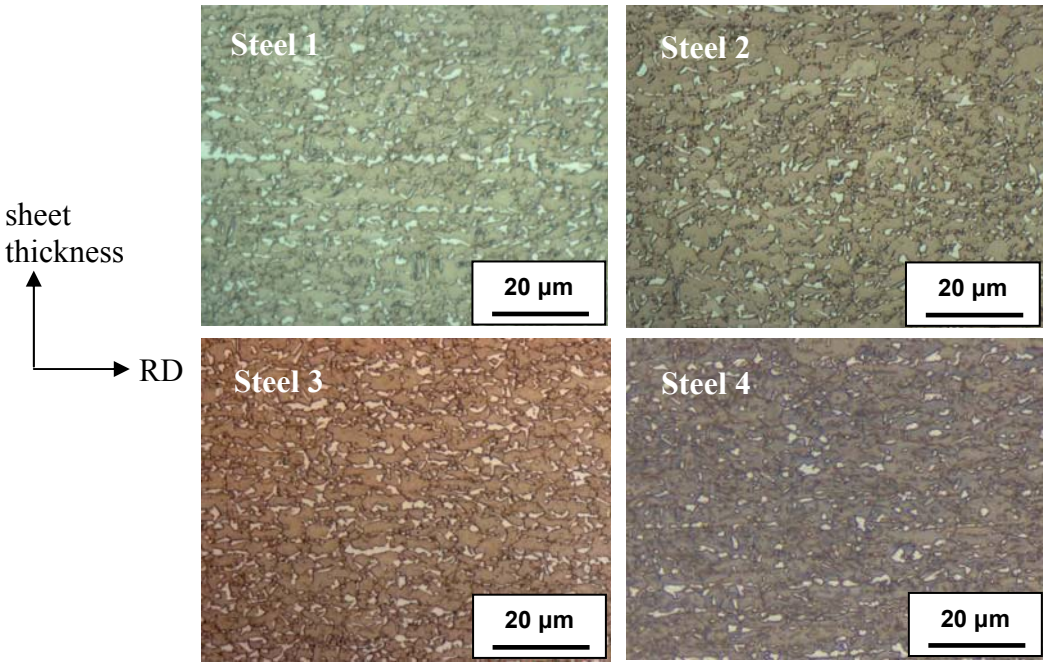

Figure I.25. Light optical micrographs of the four TRIP steels along rolling direction, LePera etching, third-thickness microstructure.

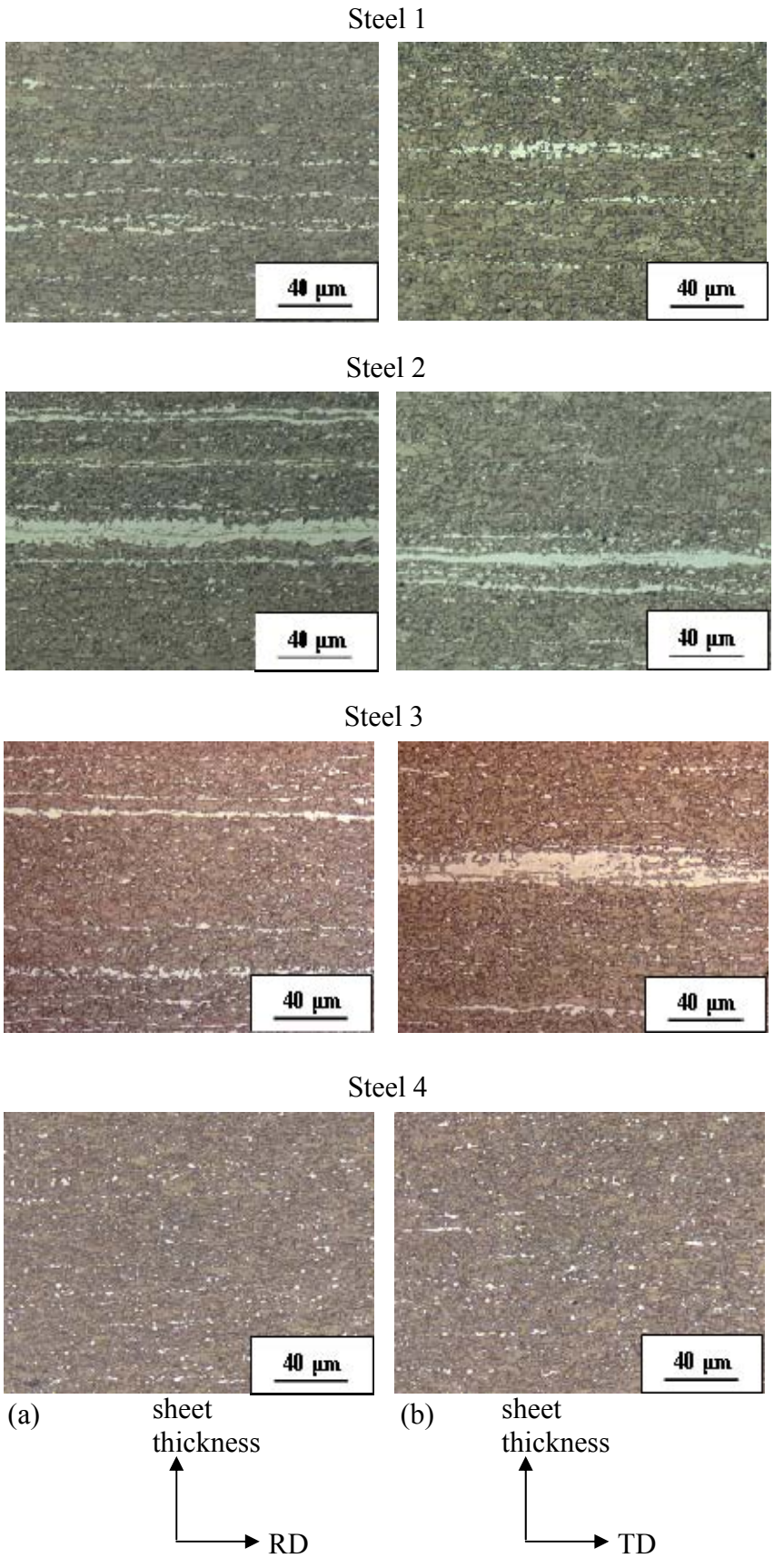

Figure I.26. Light optical micrographs of the four TRIP steel. Mid-thickness microstructures, LePera etching (a) along rolling direction and (b) along transverse direction.

Microstructures of the four steels were observed by light microscopy after a LePera etching (Appendix 1). It is noticed that:

- Martensite/austenite (M/A) islands appear in white.
- Ferrite appears in brown.
- M/A are present in micrographs as 2-5µm islands linked by thin bands of smaller islands.
- All steels except Steel 4 have a central segregation band at mid-thickness. This band has a thickness ranging between 2 and 20µm for the four steels studied. In addition, from various cross-sections observations carried out on steels, this band is found to be heterogeneous both with its presence and with its thickness along the sheet.
- This central segregation is thicker for Steel 2 and Steel 3.
- In addition, this band differs along rolling and transverse direction. This band is more pronounced along transverse direction than along rolling direction for Steel 3.
- Central segregation is composed mainly of martensite and occasionally on austenite.
- Concerning banded structures, they are thinner (often < 2µm) and are mainly present in the vicinity of the mid-thickness and occasionally close to the surface.

Note that these cross-sections observations are not appropriated to estimate the shape of the central segregation band in 3D. From these observations, hard segregation bands seem to be present as layer with variable thickness along the sheet. Similarly, it is difficult to evaluate the shape of M/A islands in 3D. They could be connected with each other and may play an important role on the cracking in bending.

In order to determine the M/A islands content in each steel, light microscopy observations were performed at third-thickness. After a Klemm colorant etching (Appendix 1), the M/A islands appear in white. Figure I.27 illustrates results obtained after etching with and without threshold.
Table I.3 provides the amount of M/A islands for each steel. Note that their contents are very similar and ranging between 17 and 20%. In order to determine if the islands are more austenitic or more martensitic, retained austenite measurements are also carried out (see next part).

Material	% M/A islands
Steel 1	18%
Steel 2	17%
Steel 3	19%
Steel 4	20%

Table I.3. M/A islands quantification for the four steels studied.

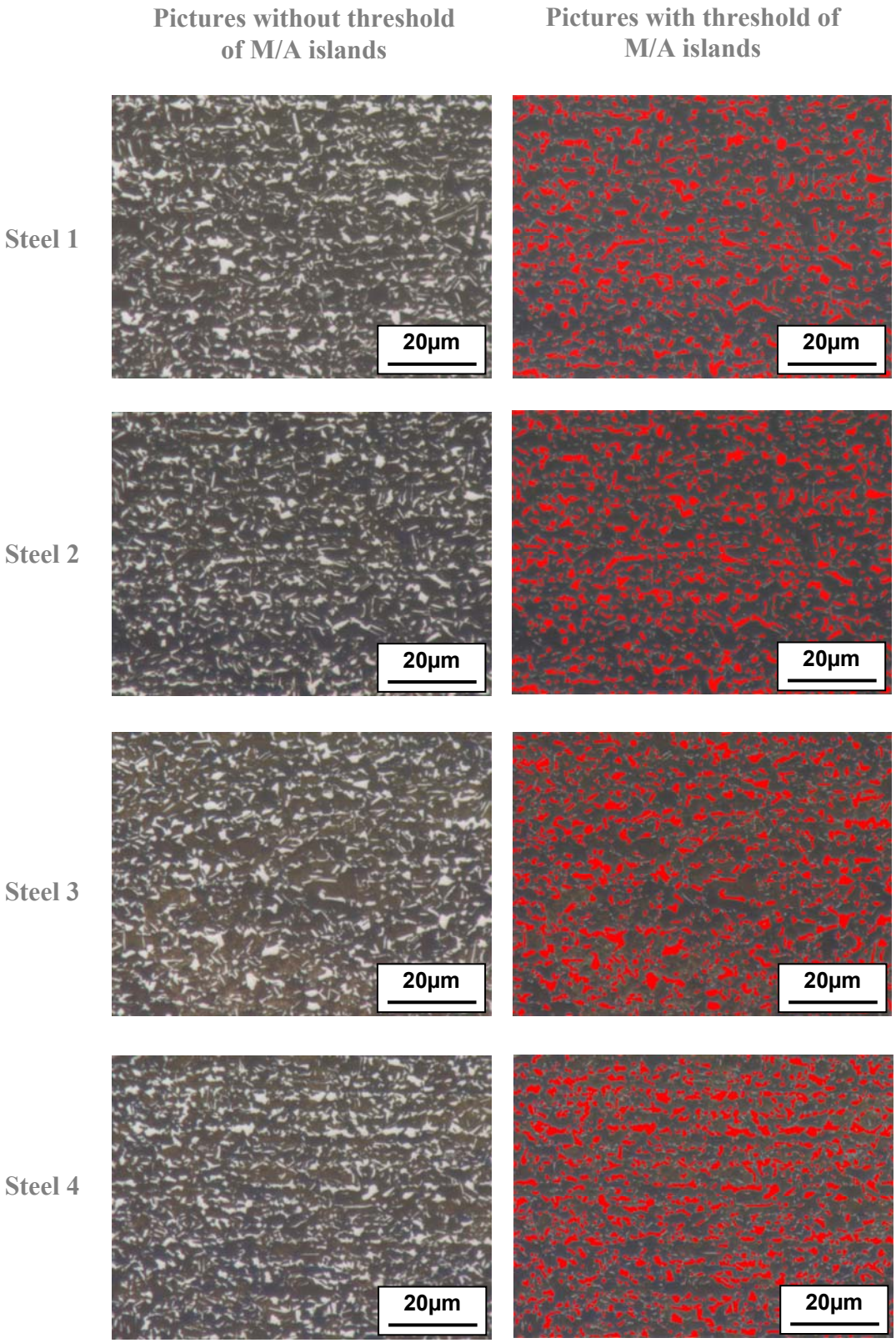

Figure I.27. Quantification of M/A islands in the four TRIP-aided steels.

II.B. Determination of the retained austenite content

In one study (Jacques et al., 2009), measurements of retained austenite in several multiphase TRIP steels (~1mm) were carried out by comparing six different techniques (light microscopy, X-ray diffraction, EBSD, magnetic saturation, thermal diffusivity and laser ultrasonics). According to these measurements, a large variability of the estimated retained austenite contents has been observed. Among these techniques, light microscopy and EBSD systematically brought larger and smaller amounts of retained austenite respectively and X-ray diffraction and magnetic saturation are shown to be the most common methods for retained austenite measurements.

The main drawback of X-ray diffraction (XRD) method is that the analysis is carried out on the first few microns below the sample surface. Therefore, this technique cannot be used to determine retained austenite content in steels which have a heterogeneous repartition of phases through the specimen.

Magnetic measurements are also widely used and one of their advantages is that measurements are conducted on the bulk. Austenite being paramagnetic contrary to other steel's constituents, the saturation magnetization of the sample can be linked on the amount of retained austenite. Hence, the transformation of retained austenite into martensite corresponds to a transformation of a paramagnetic phase into a ferromagnetic phase. Although this method is easily usable, it has the drawback to be destructive compared to XRD measurements.
Other techniques are also used to determine the amount of retained austenite. Among them, the Mössbauer spectroscopy (Ladriere and He, 1986; Jacques, 1998) and neutron diffraction (Huang et al., 2002; Reed et al., 1998) can be mentioned. However, these methods require specific experimental means and their use was outside the scope of the present study.

1. XRD measurements

In this study, XRD measurements were carried out to determine the retained austenite content in each of the selected materials in the as-received conditions. Details of this experiment are given in Appendix 1. The peaks used to measure respectively the amount of ferrite and austenite are (200), (211), (220) and (200), (220), (311).
In order to investigate the transformation of retained austenite into martensite, measurements were performed on as-received materials (flat samples containing austenite) and on bent specimens for three steels (Figure I.26).
It is found that the amount of retained austenite in the as-received material is 8% for Steel 1, 10% for Steel 2, 16% for Steel 3 and 15% for Steel 4. Steel 1 and Steel 2 have very low amount of retained austenite. The difference between the M/A islands content obtained after light microscopy and the retained austenite amount measured by XRD is the martensite amount. Steel 1 and 2 have the highest martensite content with respectively 10% and 7%. Steel 3 and 4 have the lowest martensite content with respectively 3% and 5%. This result is in agreement with the mechanical properties because Steel 1 and 2 have the highest tensile strengths.

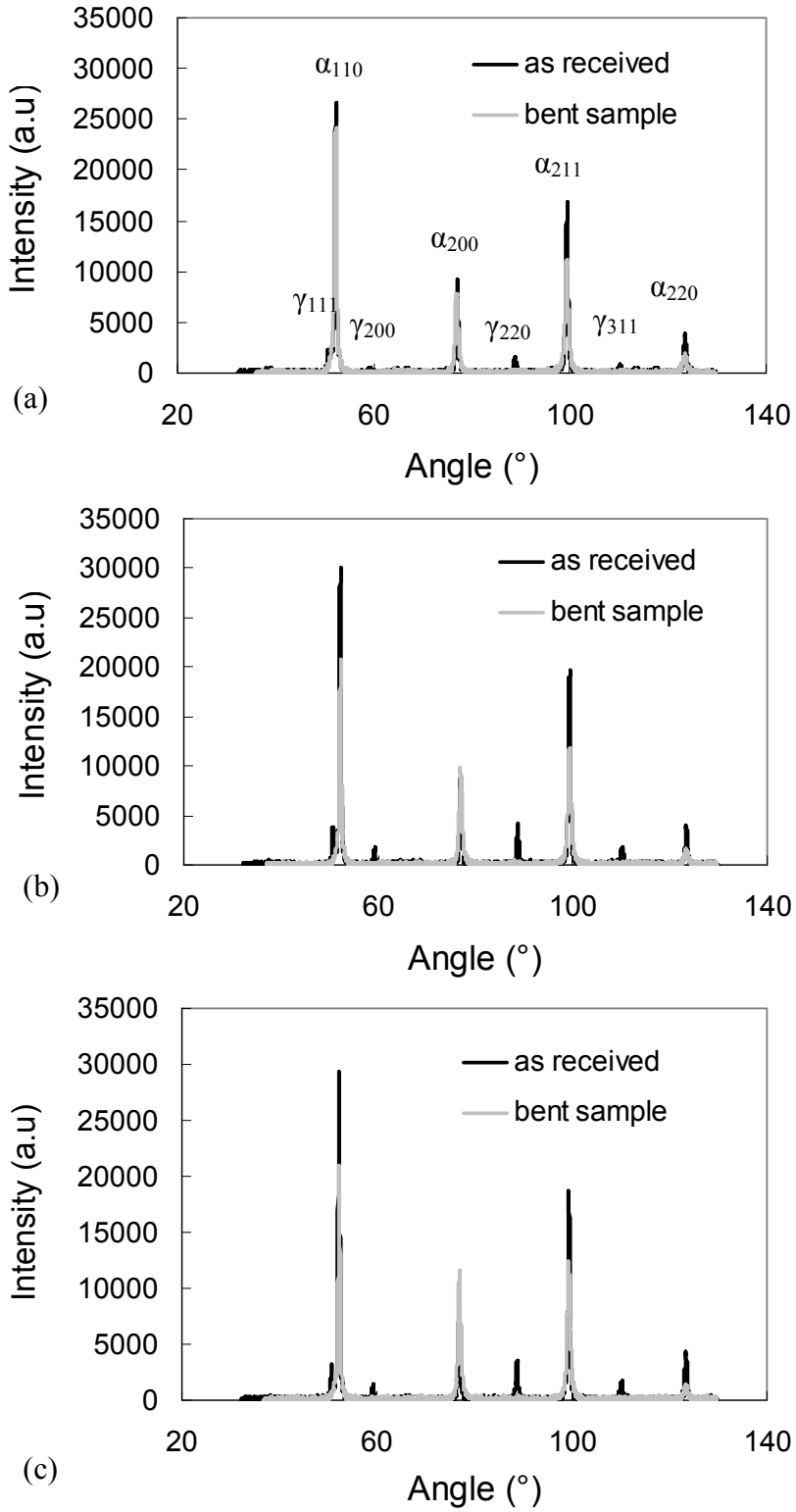

Figure I.28. XRD measurements both on as-received and bent specimens along RD-TD plane. 2θ scale. (a) Steel 1, (b) Steel 3, (c) Steel 4.

It is noticed from Figure I.28 that austenite peaks have disappeared with the bent sample. This means that the austenite has been transformed into martensite during bending (just below the surface – outer fibre – tensile area).

2. Magnetic measurements

Concerning magnetic measurements, sigmametry method was used. This technique consists in measuring the saturation magnetization of specimens with and without austenite. More details about the measurement are given in Appendix 1.

Although with this method, the whole thickness specimen is analysed, similar results to XRD measurements are obtained for as-received materials except for Steel 1 which has a higher value of retained austenite with this method. Indeed, Steel 1, Steel 3 and Steel 4 have respectively 12%, 16% and 13% of retained austenite. The difference between XRD and magnetic measurements for Steel 1 is not well understood and could be due to an heterogeneous repartition of retained austenite into the sample. For bent samples, retained austenite was still detected (nearly 5% for all steels). This difference is due to the location of measurements (over a few microns beyond the outer surface in the tension deformed area for XRD versus all the thickness for magnetic measurements). So, it is possible to conclude that a significant part of retained austenite is totally transformed into martensite during bending. Indeed, the area which is less deformed has surely retained austenite which was not transformed into martensite.

The carbon content in retained austenite was also determined for the steels investigated, from the 2θ XRD plots.
Several authors proposed equations linking the austenite cell parameter, a_γ (a_γ in nm), to alloy element content (in wt%):

$$a_\gamma = 0.3555 + 0.0044.C \quad \text{(Roberts, 1953)} \tag{8}$$

$$a_\gamma = 0.3573 + 0.0033.C \quad \text{(Ridley et al., 1969)} \tag{9}$$

$$a_\gamma = 0.3553 + 0.000095.Mn + 0.00056.Al + 0.00006.Cr + 0.000474.C \quad \text{(Cheng et al., 1990)} \tag{10}$$

The last expression is the most suitable one for TRIP steels. It yields to the following carbon content (%) in retained austenite:

- 1.15 % for Steel 1
- 1.12 % for Steel 2
- 1.18 % for Steel 3
- 1.17 % for Steel 4

As a conclusion, all steels have similar carbon content in retained austenite i.e. close to 1.15%. These values are in good agreement with the ones found in the literature. For example, Sugimoto et al. (2002) calculated a C content in retained austenite ranging between 1.10% and 1.20% for TRIP having about 10% of retained austenite and 0.2 C (wt%). Srivastava et al. (2007) obtained a concentration of carbon in retained austenite of 0.82% for their TRIP steels. This lowest value can be due to the difference in tensile strength: 600MPa for their steels and highest strength for our TRIP-aided steels. Girault et al. (1998) found a C content in retained austenite of 1.05% and 1.2% for two TRIP steels having respectively 0.11% and 0.27% C amount.

II.C. Nanohardness of ferrite matrix and secondary phases

Nanoindentation measurements were carried out on the three TRIP steels with a thickness of 1.6mm. This technique consists in indenting the material with a slight depth and to monitor the penetration evolution as a function of the applied load in order to determine the local mechanical properties at the surface of the material. Additional details on this technique are given in Appendix 1.

The nanohardness tests were coupled with an Atomic Force Microscope (AFM) allowing locating the area to indent before testing.
An example of loading/unloading curves of Steel 1 both for M/A islands in the vicinity of the mid-thickness and the ferritic matrix is shown in Figure I.29.

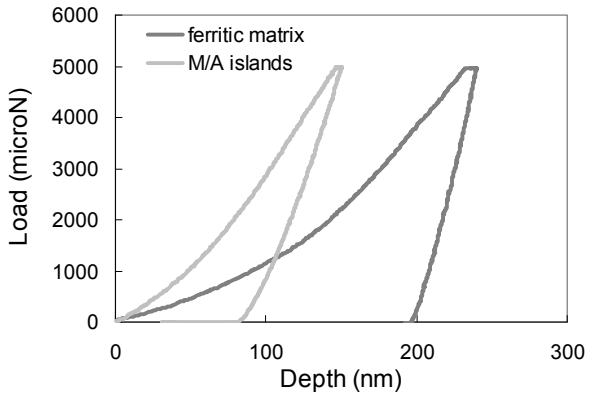

Figure I.29. Loading/ unloading cycle for Steel 1.

Figure I.30 shows two AFM pictures of a M/A island before and after nanohardness measurements.

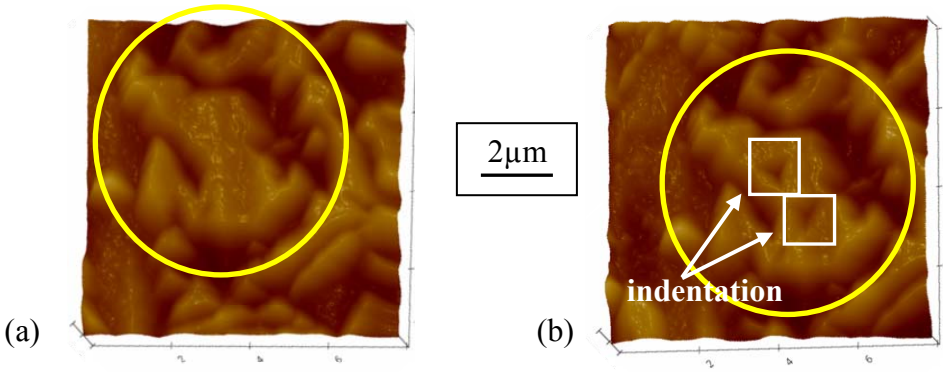

Figure I.30. AFM observations. M/A island is surrounded with yellow circle. (a) Island before the indentation, (b) island after indentation with two prints surrounded with white squares.

Scanning electron microscopy was also used to have a better image resolution to measure the size of indents. For example, Figure I.31 shows two observations with indentations on the central segregation band (a) and in the ferritic matrix (b). As expected, the print on the softer matrix is larger than the ones within the central segregation band and the size of indents is much smaller than the size of phases, at least in the plane of view.

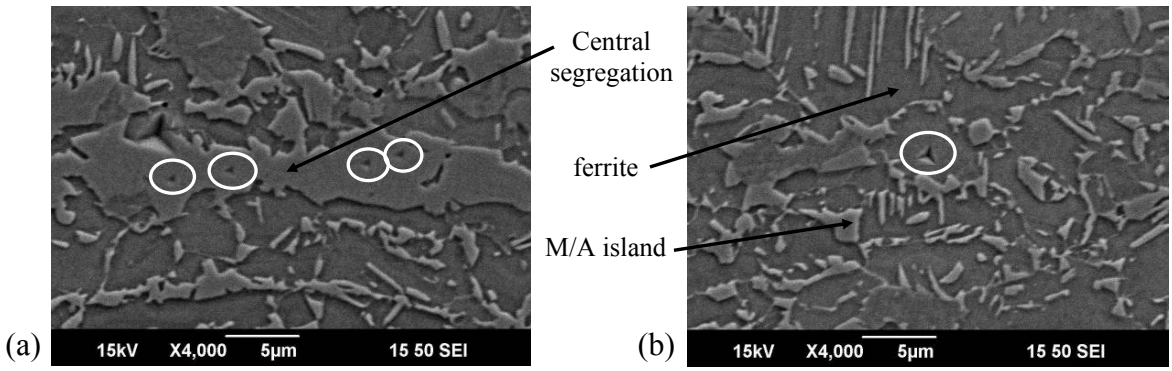

Figure I.31. SEM observations after nanohardness measurements on Steel 3. Prints are surrounding in white. (a) on the central segregation band, (b) in the ferritic matrix.

Five nanohardness measurements carried out for the three steels both on ferritic matrix and M/A islands close to the mid-thickness are reported in Figure I.32.

Similar ferritic matrix nanohardness is noticed for all TRIP steels, while the nanohardness of M/A islands in the vicinity of the mid-thickness is slightly different for the three steels. The ferrite nanohardness value is in very good agreement with the ones found by Jacques et al. (2007) and Furnémont et al. (2002) where they measured a nanohardness of about 5GPa. In these studies, the austenite and the martensite were found to have a nanohardness of respectively 11 and 17GPa. The values of the M/A islands close to the mid-thickness for the three steels are in this range. The difference between the three steels could be due to the nature of the island, i.e. mainly austenitic for Steel 1 and 4 and mainly martensitic for Steel 3. In addition, this steel is also the most segregated one among the three materials.

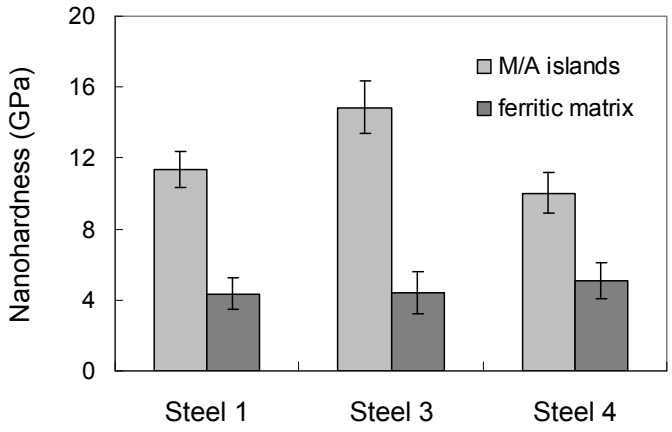

Figure I.32. Nanohardness measurements for the three TRIP steels both for the M/A islands in the vicinity of the mid-thickness and for the ferritic matrix.

II.D. Summary

Table I.4 provides a summary of the microstructural properties of the four studied materials. Their microstructures are very different as well as the behaviour of each phase (content, distribution, nanohardness, etc). These different behaviours could have a role during bending tests.

	Microstructure homogeneity	Central segregation	Retained austenite (DRX)	Martensite content	Nanohardness (GPa) Ferrite	MA islands
Steel 1	Medium	Medium (<5µm)	8%	10%	4.1	11
Steel 2	Low	High (<20µm)	10%	7%	/	
Steel 3	Medium	High (<20µm)	16%	3%	4.3	15
Steel 4	High	Low (< 2µm)	15%	5%	5.5	10

Table I.4. Summary of the microstructural properties of the four TRIP studied.

III. Mechanical characterization of the four TRIP-aided steels studied

A knowledge of the mechanical properties is essential for a practical application of any steel. The aim of this section is to give a full analysis of the mechanical behaviour of the studied TRIP steels both in tensile tests and in bending tests. All experimental procedures and specimen dimensions are described in Appendix 2.

III.A. Tensile properties at room temperature

Tensile tests have been performed on ISO specimens 20x80 along each direction under load line displacement control at an initial strain rate of $2.5.10^{-4}$ s^{-1}. The longitudinal strain was monitored with an extensometer of 80mm in gauge length. Engineering stress/strain curves along transverse direction of each TRIP steel are shown in Figure I.33 and Table I.5 summarizes their mechanical properties.

According to their mechanical behaviours, the four chosen steel sheets can be separated in two families. Steel 1 and Steel 2 have similar mechanical properties with high tensile strength and medium fracture elongations and the two other ones Steel 3 and Steel 4 are more ductile but present a yield point elongation (~0.4%) that might play a role at the beginning of bending tests. The main difference between Steel 1 and Steel 2 is the lower total elongation of Steel 2 compared to that of Steel 1.

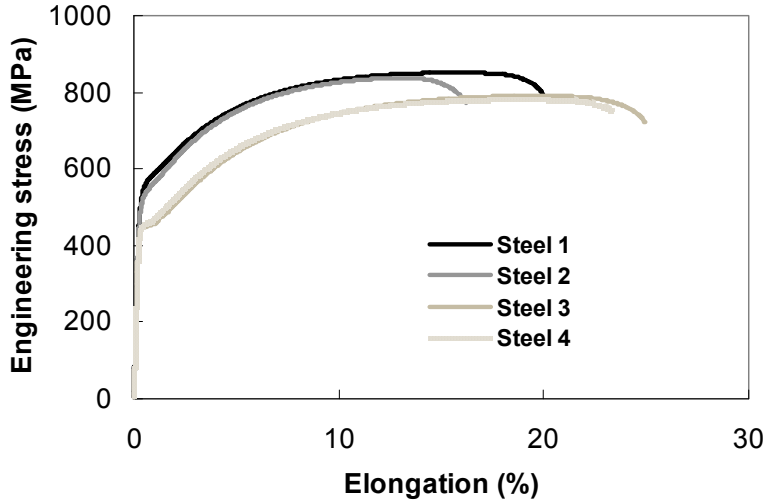

Figure I.33. Engineering stress / strain curves along TD for the four TRIP steels.

Note that fracture surface of tensile specimen are ductile with dimples and fractures appear at 45° within the thickness as it is reported in Figure I.34.

Figure I.34. Broken tensile specimen with a 45° fracture through the thickness.

	Direction	0.2% proof stress (MPa)	Tensile Strength (MPa)	Uniform elongation (%)	Total elongation (%)
Steel 1 (1.6mm)	RD	467	866	15.0	20.0
	TD	546	851	15.0	19.2
Steel 2 (2mm)	RD	464	816	16.6	22.9
	TD	521	834	13.6	17.0
Steel 3 (1.6mm)	RD	426	795	19.7	25.5
	TD	448	790	19.2	24.5
Steel 4 (1.6mm)	RD	433	764	20.0	27.2
	TD	451	782	18.2	22.8

Table I.5. Room temperature tensile properties of the four TRIP steels along rolling (RD) and transverse (TD) directions (ISO 20x80mm tensile specimens).

III.B. Air-bending properties

This test is the most commonly used for bending because it is the most simple one and easy one to set up. With this test, it is possible to determine the maximum bending angle for a specified bending radius. It is important to underline that the inner radius (of the bent sample) does not exactly correspond to the punch radius. This test is carried out on a universal tensile machine (Figure I.35). Various punches are available (radius from 0.1 to 15 mm). Samples have to be ground before trials to avoid cracks starting from edges (Dalloz et al., 2007). The dimensions of the samples are 50x100mm with full thickness. This test is carried out without lubrication.

(a) 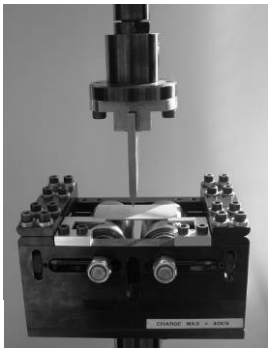 (b) 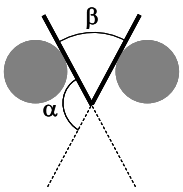

α: bending angle
β: angle of the bend
(c) 

Figure I.35 : (a) Air-bending device, (b) schematic and (c) bent specimens.

For this study, air-bending tests were performed on the four TRIP steels. Five samples along each direction (rolling and transverse) were bent for Steel 1, 3 and 4 while Steel 2 was only bent along transverse direction as it is the most detrimental one (Table I.6). For this test, the punch used has a radius of 0.1mm. Tests are interrupted as soon as the first crack was considered to appear at the bend nose. As a criterion to stop the test, an automatic method based on the load/displacement curve was used. As soon as the load decreases, it is considered that a microcrack had appeared. The test is usually stopped after 5 to 10% decrease of the load. To check whether the specimen is cracked or not, a magnifying glass is used.

The angle of the bend (β) of each sample was measured thanks to a protractor (after unloading and thus specimen springback) in order to compare the steels with each other. The bending angle (α) is then deduced. Finally, based on the five tests results, an average and its standard deviation are calculated.

	Steel 1		Steel 2		Steel 3		Steel 4	
	RD	TD	RD	TD	RD	TD	RD	TD
Sample 1	51	63	No data	62	Bending until the limit of the machine without cracking (~15°)		Bending until the limit of the machine without cracking (~15°)	
Sample 2	34	61		59				
Sample 3	34	66		58				
Sample 4	22	55		56				
Sample 5	22	64		58				
β angle (°)	33	62		59	<15	<15	<15	<15
α angle(°)	**147**	**118**		**121**	**>165**	**>165**	**>165**	**>165**
Stand. dev.	11.9	4.2		2.2	0	0	0	0

Table I.6. Air-bending results.

From Figure I.36, it is possible to note that:

- Due to the limit of the machine, it was not possible to bend Steels 3 and 4 specimens above 165°. As no crack was observed on them, it is not possible to use this test to compare their bendability.

- Steels 3 and 4 have a better bendability than the two other ones.

- Steel 1 and Steel 2 which have similar mechanical properties, also present equivalent air-bending behaviour along TD.

- There is a high anisotropy when comparing bending angles along rolling or transverse directions (Steel 1). It is clearly noticed that Steel 1 has best bendability along rolling direction. This confirms study of Leu et al. (1997) where a poor bendability was noticed on transverse bent specimens.

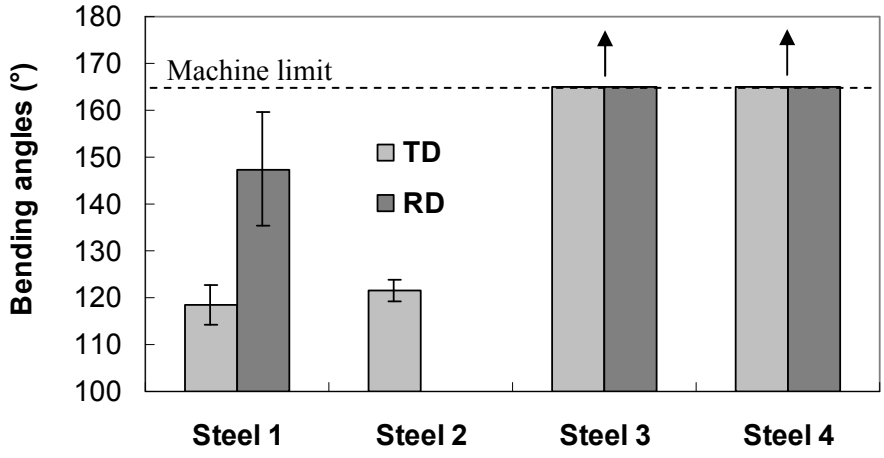

Figure I.36. Air-bending results for each TRIP steel.

III.C. Stretch bending properties

In the automotive industry, many parts are stamped, and some more complex forming paths than simple bending have to be encountered. Stretch bending is one of them. As for the Erichsen test, the stretch bending test consists in clamping blanks of a sample between a die and a blank-holder. This test makes it possible to determine failure heights for various values of punch radius, *R*, and then rank material formability for various *R/t* ratios (*t* being the sheet thickness). It is also possible to evaluate the failure mode which seems to move from punch region to sidewall for high punch radii, depending on the bendability of material.

As for the air-bending test, five samples (size: 50x250mm) along each of the rolling and transverse direction were bent for Steel 1, 3 and 4 and Steel 2 was only bent along transverse direction. For the stretch bending test, three punch radii (R = 2, 4, 6mm) were tested and there is a lubrication between the sheet and the punch. In this test, grease and a Teflon film were laid on the punch radius to improve the friction between specimen and tool.

As this test is very unstable, it is carried out with a hydraulic press and thus implies a lot of stored energy, it is thus impossible to interrupt it as soon as a micro-crack appears in the sample (Figure I.38). Therefore, the test was only stopped once the sample was broken in two parts. To compare steels, the bending angle (α) was determined for each sample after failure (equivalent to failure height). This angle was measured with a protractor by reproaching the two broken parts of the specimens. Finally, an average and a standard deviation are given for the five samples. Figure I.38 shows two stretch bent specimens (A: with a punch radius of 6mm, B: with a punch radius of 2mm).

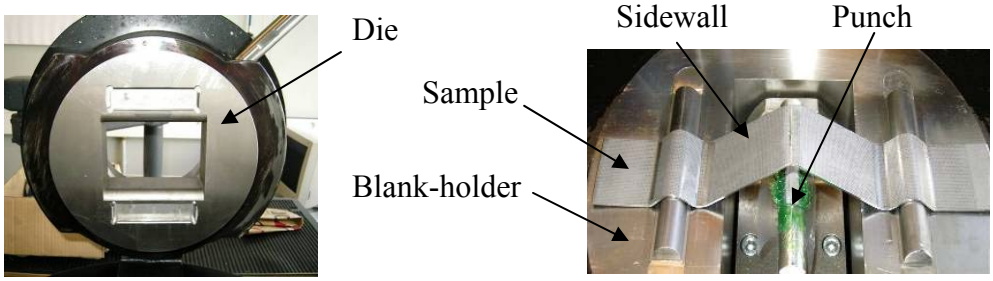

Figure I.37 : Stretch bending device

Figure I.38: Picture of two stretch bent samples (A: punch radius = 6mm, B: punch radius = 2mm).

Figure I.39 shows bending angles obtained after fracture for each steel and for the three punch radii (2, 4 and 6mm) along rolling and transverse directions, except for Steel 2 which was only bent along the transverse direction.

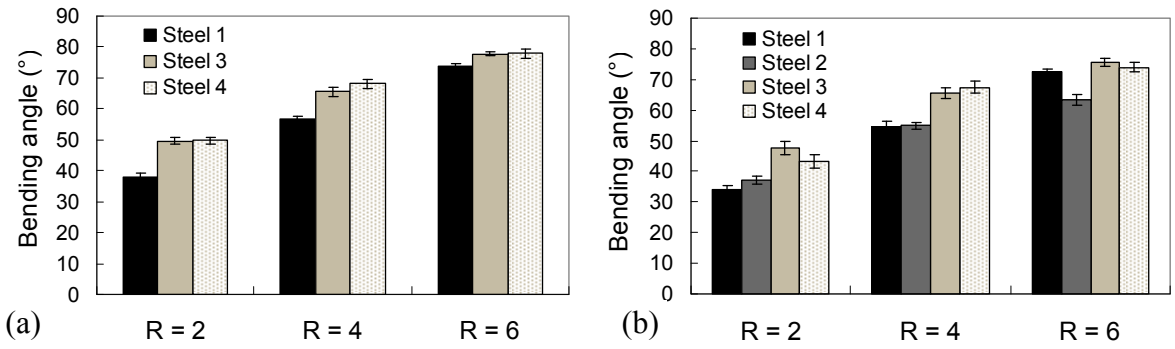

Figure I.39. Stretch bending results: (a) along rolling direction, (b) along transverse direction.

From Figure I.39, it is reported that for a punch radius of 6mm, Steel 1, Steel 3 and Steel 4 have similar bending behaviour and Steel 2 has a lower bending angle than the three other steels along transverse direction. For lower punch radii (2 and 4mm), Steel 1 and 2 have lowest bendability than the two other ones.
Regarding the fracture locations, all steels broke on the punch nose for punch radii of 2 and 4mm while for higher radius (6mm), Steels 3 and 4 have their cracks located in the sidewall and not at the punch nose. For the 6mm punch radius, Steel 1 and 2 broke at the punch nose. It is in agreement with studies discussed in part I.A. for which high values of *R/t*, lead to shift of the crack from the punch nose to the sidewall.
Thus, to summarize, Steel 1 and 2 have lowest ability compared to Steel 3 and 4 in stretch bending for all punch radii.

In order to overcome instability issues due to the previous machine, a new device was designed (Appendix A2) to be able to stop the test at various steps to get non propagating cracks. This device enables to investigate damage mechanisms more accurately and cross-sectional observations of stretch bent specimens will be shown in Chapter 3. The device used is a conventional servohydraulic testing machine Instron (load cells: 250 kN and 50 kN) which makes it possible to apply very low displacement rates (0.05mm/s instead of 0.5mm/s with the hydraulic press). The new device is shown in Figure I.40a and the bent specimen is presented in Figure I.40b. With this tool, only a punch with a radius of 4mm was used and the dimension of the samples was 40x180mm for further tests.

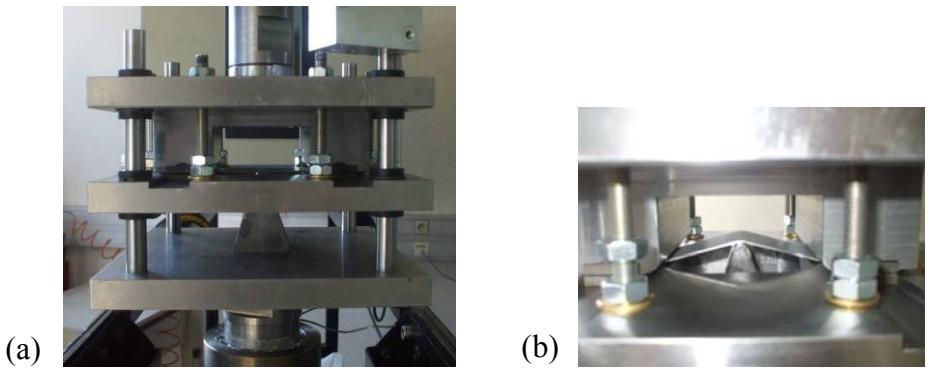

Figure I.40. (a) Stretch bending tool after machining, (b) sheet bent under tension.

III.D. Summary

Firstly, Steel 1 and 2 have the lowest bendability compared to Steel 3 and 4 as well as in air-bending than in stretch bending tests. However, the lowest bendability of the two first steels compared with the two other ones is more visible in air-bending where bending angles differences are more pronounced.

In addition, note that stretch bending angles are clearly lower compared to the air-bending ones. This result was expected because the stretch bending test is more severe than the air-bending one due to the stretching imposed. It is thus necessary to use these two bending tests to obtain comprehensive database on both bending tests and represent the most accurately the various forming modes appearing during parts stamping.

IV. Summary of Chapter 1

This chapter provided a literature survey on bendability and gives a short presentation on TRIP-aided steels. In addition, the origin of the banded structures was explained in the last part of this literature review. Finally, a microstructural and mechanical analysis was carried out on the four TRIP-aided steels studied. This chapter intended both to fix the background of this study and to highlight the most relevant findings related to this PhD work.

From the state of the art, it was noticed that several parameters can influence the bendability of steels such as mechanical properties, microstructure, tools, etc…making difficult the understanding of formability issues. It seems clear that higher tensile strength decreases the bendability of materials. However, at this stage, it is not possible to affirm what is the role of each microstructural parameter such as the central segregation, the banded structures, the retained austenite content and the nanohardness of various phases. The link between the microstructure and bendability is not well known and has to be improved to investigate more accurately damage mechanisms.

Available published data on mechanical analysis of bending tests were presented in this chapter. These data are summarized in section I.5. and more particularly in Table I.1.
Among these studies, most of them used an isotropic hardening law to simulate forming tests and either a Von Mises or a Hill yield criterion was chosen to account for the anisotropy. Studies with a mixed hardening rule exhibited more accurate results than with purely isotropic one. Almost modelling was associated with a coupled damage approach to predict fracture in bending and simulations were carried out mainly in 3D and occasionally in 2D.

Finally, from first characterizations conducted on the four steels studied, it appears that Steel 1 and 2 have the lowest bendability compared to Steel 3 and 4 but no clear relationship with their microstructures was noticed. Therefore, complementary analyses are necessary to describe more precisely the relationship between bendability and microstructure.

V. Choice of the materials and approach used in the present study

V.A. Choice of the materials

In order to investigate damage mechanisms and relationship between microstructure and bendability, the four TRIP-aided steels were studied both with air and stretch bending tests. As Steel 1 and Steel 2 have the lowest bendability, they were investigated in more detail. The microstructure of Steel 2 is less homogeneous than that of Steel 1 and it exhibits more hard segregated bands. In order to determine the influence of hard segregation bands as a function of their locations through the thickness, Steel 2, which is the thickest material, was used. Surface machining was carried out in order to artificially move the central segregation from the mid-thickness and to obtain thickness-reduced specimens with various locations of the main hard band.

In order to conduct a comprehensive mechanical analysis of both bending tests, constitutive equations of Steel 1 was established and then the simulation of both air and stretch bending tests was carried out.
In addition, air-bending test simulations were also performed on thickness-reduced Steel 2 in order to investigate more severe loading conditions (bending angle up to 180° and thinner material). For that purpose, as Steel 2 has a mechanical behaviour very close to Steel 1, constitutive equations of Steel 1 were used to model air-bending on Steel 2.

V.B. Outline of the next three chapters

A full mechanical analysis of the air-bending test is reported in the second chapter. For that purpose, constitutive equations of Steel 1 were first determined and then modelling of the air-bending test without damage was carried out thanks to finite element simulation. The modelling of air-bending test of thickness-reduced Steel 2 specimens up to 180° is also presented in this chapter.

The third chapter addresses investigation of damage mechanisms after both tensile and bending tests. Observations and understanding of damage mechanisms linked to the microstructure are reported. The influence of the segregated bands on air-bending ability is investigated and a relationship between damage, band thickness and local strain is proposed.

Finally, a comparison between stretch bending and air-bending tests is carried out in chapter 4. Modelling of these two tests including damage development was performed using finite element simulation.

Résumé du Chapitre 1

Ce chapitre établit à la fois une étude bibliographique ainsi qu'une présentation sommaire des aciers TRIP étudiés. L'origine des structures en bandes a été détaillée dans la dernière partie de cette étude bibliographique. Une analyse à la fois microstructurale et mécanique a été réalisée sur les aciers de l'étude à la fin de ce chapitre. Les objectifs de ce chapitre ont été d'une part de fixer le contexte de l'étude et d'autre part de mentionner les résultats les plus significatifs disponibles dans la littérature en relation avec les travaux de cette thèse.

A partir de cet état de l'art, il a été démontré que divers paramètres tels les propriétés mécaniques, la microstructure, les outils, etc. peuvent avoir une influence sur la capacité en pliage des aciers. Il semble clair qu'une résistance en traction élevée diminue l'aptitude au pliage d'un acier. Néanmoins, cette étude n'a pas permis de dégager le rôle de chacun des paramètres microstructuraux tels que la ségrégation centrale, les structures en bandes, le taux d'austénite résiduelle et la dureté des phases. Les liens entre la microstructure et l'aptitude au pliage des aciers ne sont pas vraiment connus et nécessitent d'être améliorés pour étudier d'une manière précise les mécanismes d'endommagement.

Les données disponibles dans la littérature portant sur l'analyse mécanique des tests de pliage ont été présentées dans ce chapitre. Elles sont synthétisées dans la partie I.5 et plus particulièrement dans le tableau I.1.
Parmi ces études, la plupart des auteurs ont modélisé des essais de mise en forme avec soit un critère d'écoulement isotrope de Von Mises, soit un critère anisotrope de Bron Besson. De plus, les simulations numériques réalisées avec un écrouissage mixte ont permis d'obtenir de meilleurs résultats que celles effectuées avec un écrouissage purement isotrope. La plupart d'entre-elles ont inclus l'endommagement dans leurs modèles pour prédire la rupture en pliage et ces modélisations ont principalement été conduites en 3D et occasionnellement en 2D.

Enfin, à partir des premières caractérisations réalisées sur les quatre aciers de l'étude, nous avons montré que les aciers nommées "acier 1" et "acier 2" ont la plus faible aptitude au pliage comparé aux deux autres aciers mais nous n'avons pas relevé de relation directe avec leurs microstructures. Des analyses complémentaires sont donc nécessaires pour décrire de manière précise les relations entre microstructure et aptitude au pliage.

Chapter 2

Mechanical analysis of Steel 1 and air-bending test modelling

An experimental database including tensile tests on smooth and notched samples as well as shear tests was established to determine the constitutive equations of Steel 1. These constitutive equations enabled to simulate both air and stretch bending tests. In a journal paper, finite element simulation of air-bending tests has been conducted first on Steel 1 and then on thickness-reduced Steel 2 to investigate other bending conditions. This modelling made it possible to satisfactorily predict stress and strain fields and bending load-displacement curves. The constitutive equations accounted for anisotropic elasto-plastic behaviour with mixed hardening in this article. The possibility of using simplifying assumptions in the model (such as an isotropic flow criterion, pure isotropic hardening, two-dimensional assumptions and simplified boundary conditions) was also discussed in complementary data of this article.

Regarding the model, three cases were investigated: (i) an anisotropic Bron-Besson model with mixed isotropic/kinematic hardening (article), (ii) a Bron Besson yield criterion with a purely isotropic hardening (article + complementary data) and (iii) a Von Mises yield criterion with mixed hardening (complementary data).

Table of contents

I. Global analysis of the air-bending test

This part is based on a journal paper which has been submitted for publication to *International Journal of Mechanical Sciences* in May 2011. The text of this article is reproduced below.

Analysis of the air-bending test using finite-element simulation: Application to steel sheets

D. Rèche [1), 2)], J. Besson [1)], T. Sturel [2)], X. Lemoine [2)], A.F. Gourgues-Lorenzon [1)]

[1)] *MINES ParisTech, Centre des Matériaux, CNRS UMR 7633, BP 87 91003 Evry Cedex, France*
[2)] *ArcelorMittal Global R&D, Voie Romaine, BP 30320, 57283 Maizières-lès-Metz Cedex, France*

Corresponding author: Delphine Rèche: delphine.reche@arcelormittal.com
Tel: 0033 3 87 70 48 01
Fax: 0033 3 87 70 47 14
ArcelorMittal Global R&D, Voie Romaine, BP 30320, 57283 Maizières-lès-Metz Cedex, France

Abstract

A full mechanical analysis of the air-bending test was performed in order to determine the stress and strain fields involved in this test. Two low alloy TRIP-aided steels and two bending conditions were considered: the first one is commonly used to test the bending ability (sheet thickness 1.6mm, bending angle up to 150°) whereas the second one involves fairly different loading conditions (sheet thickness 0.75mm, bending angle up to 180°). Constitutive equations were determined from tensile and shearing tests to accurately represent the flow behaviour of the sheet during both bending and unloading.
Predictions from the two-dimensional simulation of air-bending were in good agreement with all experimental measurements (load vs. displacement curves, hardness and strain field measurements of bent then unloaded specimens). While neither using three-dimensional simulations nor representing the contact between punch and sheet were necessary, an anisotropic yield criterion with both isotropic and kinematic contributions to hardening is required. In particular, accounting for kinematic hardening is necessary for the correct simulation of air-bending of a prestrained material. The strain path experienced by the material both at the apex and close to the initial mid-thickness is then discussed. This method can be applied to assess local mechanical loading, prestrain effects and possibility of damage development to any high strength steel grade.

Keywords

Ultrahigh strength steels, TRIP steels, air-bending, constitutive equations, finite element simulation.

1. Introduction

Advanced high strength steels (AHSSs) have been more and more intensively used in recent years in the automotive industry for weight and cost reduction as well as for crash performance improvement. However, a drop of formability might be experienced under severe conditions, in particular forming modes such as bending.
Bending is one of the most frequently used sheet-forming operations in the automotive industry to produce structural and safety parts such as bumper beams and lateral reinforcement beams. Development and optimisation of bending operations for a given steel sheet requires the knowledge of its strength and of its bendability, which is generally defined as the ratio of the minimum bending radius that can be achieved without failure, to the sheet thickness. In the particular case of AHSSs, due to their high strength, localized fracture might occur and affect the bendability.

The minimum bending radius can be given in various ways. Datsko and Yang [1] predicted the minimum bending radius for a specific material, from the reduction of area in uniaxial tension. Leu [2] studied sheet metal and showed that the minimum bending radius is proportional to the sheet thickness and decreases with increasing the Lankford coefficient "r" ratio. In addition, a large strain hardening exponent was reported to favour low minimum bending radius and to delay strain localisation and thus it was expected to increase the fracture strain [2]. This trend was not in agreement with the study of Yamazaki et al. [3] who worked on ultra high strength steels and showed that the minimum radius was not correlated with the strain-hardening exponent.

The mechanical analysis of bending of metallic sheets focused on the prediction of springback after removing the tooling. Among them, Nilsson et al. [4] used a finite element method to predict the springback in V-die bending. Li et al. [5] showed that the hardening model in the material constitutive equations directly affects the accuracy of springback predictions. In their particular case, the best accuracy was found with an elasto-plastic power-exponent hardening rule. Gan and Wagoner [6] developed a method for the design of sheet metal forming dies to produce a specified part shape, by taking springback into account. Eggertsen and Mattiasson [7] showed the importance of the choice of both hardening constitutive equations and yield criterion to get a good accuracy of springback prediction. To the authors' knowledge, no finite element analysis focussed on the stress and strain fields through the specimen thickness. Only analytical and semi-analytical models were used to this aim. Although these models can save computation time, they often require simplifying assumptions which can affect the accuracy of the results. For example, some authors such as Chakrabarty et al. [8], Chakrabarty et al. [9] and Ragab and Saleh [10] assumed that there is no variation of the specimen thickness during bending. As will be shown in the present paper, such assumptions are not fulfilled in the case of air-bending of AHSSs, so that a more accurate mechanical analysis is required to investigate stress and strain fields in the whole air-bending specimen. That is why finite-element method was used to study successfully bending tests. Little work has been done in the past to give a full mechanical analysis of the air-bending test. Zhao and Lee [11] simulated

three-point bending of two types of sheet metals: mild and high strength steels with plane-strain hypothesis by using three constitutive equations involving (i) isotropic hardening, (ii) kinematic hardening or (iii) a combination of both. They showed that a combination of isotropic and non linear kinematic hardening accurately predicts the load-displacement curve. Wang et al. [12] showed that such numerical simulation can be carried out in plane-strain conditions. In their modelling they assumed an isotropic hardening rule and also that all bent fibres had the same curvature centre. In the following, it will be shown that this assumption is not true. Hambli et al. [13] simulated the air-bending test assuming a 3D elastic-plastic model with a Mises criterion, an isotropic hardening law coupled with a damage criterion. Thuillier et al. [14] characterized the mechanical behaviour of an aluminium thin sheet. They used the GTN model to predict the ductile rupture in bending. In addition, they chose a purely isotropic hardening rule and a Von Mises yield criterion in their work. To the authors' knowledge, no study has reported yet simulation of the air-bending test after tensile prestraining and with a kinematic contribution to hardening.

In order to predict the effect of microstructural non-homogeneity such as a central hard band or banded structures on the bendability of AHSSs, a local fracture criterion must be developed. This requires accurate assessment of the stress and strain fields that develop during bending. The purpose of the present study was to build a methodology for the mechanical analysis of the air-bending test, based on the finite element analysis technique, and to apply it to the case of low alloy transformation-induced plasticity (TRIP)-aided steels. The results are intended to be used to derive a fracture criterion in air-bending for this family of steels.
The complexity of the model that has to be used was thoroughly analysed, by considering the need of including (i) plastic yield anisotropy, (ii) accurate description of the contact between the sheet and the tools, (iii) 3D formulation of the problem, (iv) both isotropic and kinematic contributions to hardening. Following a preliminary mechanical analysis of the test that gave the requirements for relevant constitutive equation determination, an experimental database was built to identify constitutive equation parameters on a sound and relevant basis. Finite element simulation of the air-bending tests was then performed and validated against all available experimental measurements. The influence of tensile prestraining before air-bending was also addressed.

2. Materials and experimental methods

2.1. Materials

The present study focused on two cold rolled TRIP-aided steels of different thickness (1.6 and 2mm) but from the same heat (C~0.2 wt%, Mn~1.6 wt%, Al+Si~1.5 wt%) and with similar mechanical properties (Table 1), in particular along the transverse direction, which was also the bending direction mainly used in the present study. In order to investigate bending of a thin sheet and to be able to reach high fracture strain, modelling was also performed with a bending up to 180° on thickness-reduced specimens of Steel 2. This steel was previously used in Rèche et al. [15] to investigate the role of hard bands where the central hardest band was artificially shifted to various locations in the sheet thickness in order to obtain a "model material". To keep a sufficient specimen thickness for air-bending test, the thicker base material (Steel 2) was used. Surface machining followed by chemical polishing made it possible to investigate the bending behaviour of various specimens (the central hard band being shifted away from the mid-thickness) by reducing the thickness

from 2mm down to 0.75mm. The model was first validated with conventional bending conditions (Steel 1) and then with more severe ones (thickness-reduced Steel 2). In the following, only full-thickness Steel 1 and thickness-reduced Steel 2 are considered.

	0.2% proof stress (MPa)	Tensile strength (MPa)	niform longation (%)	Fracture elongation (%)
Steel 1 (1.6mm)				
RD	467	866	5.0	20.0
TD	546	851	5.0	19.2
Steel 2 (2mm)				
RD	464	816	6.6	22.9
TD	521	834	3.6	17.0

Table 1: Room temperature tensile properties of Steel 1 and Steel 2 (all in full thickness) along rolling (RD) and transverse (TD) directions (ISO 20x80mm tensile specimens)

2.2. Characterisation of the mechanical behaviour

2.2.1. Air-bending tests

Air-bending tests were carried out at room temperature using a universal tensile machine and 50x100mm specimens. The load and punch displacement were continuously measured. Two rotary rolls (in grey in Figure 1a) and various punches were used. The tests were performed without lubrication. The spacing between either roll and the punch was equal to the thickness of the considered sheet + a small gap of 0.1mm, i.e., 1.7mm for Steel 1 and 0.85mm for thickness-reduced Steel 2. Before the tests, specimen edges were ground to avoid premature failure that could be due to cutting edge-induced damage effects sometimes encountered in AHSSs [16]. For Steel 1, five specimens were tested along both RD and TD with a punch radius of 0.1mm. Note that, in this case, the bending angle, α, was limited to 150° due to the punch wedge (30°, see Figure 1b). A thinner punch developed for that purpose was used to bend thickness-reduced Steel 2 along TD (Figure 1c). This punch enabled to reach a bending angle, α, up to 180°. Therefore, with thickness-reduced Steel 2 and this punch, higher strains can be reached at the end of the test but provided that the hard bands were sufficiently far from the outer surface, no cracking occurred even under these very severe bending conditions.
The evolution of strain fields during air-bending of Steel 1 and Steel 2 was analysed in three dimensions with Aramis software [17] using a maximum allowable strain of 100%. Two CCD cameras allowed monitoring surface deformation thanks to a speckle laid on the surface of the specimen. Strain fields were then computed using digital image correlation. The acquisition frequency was 2 images per mm of punch displacement, i.e. about 52 images for air-bending of Steel 1.

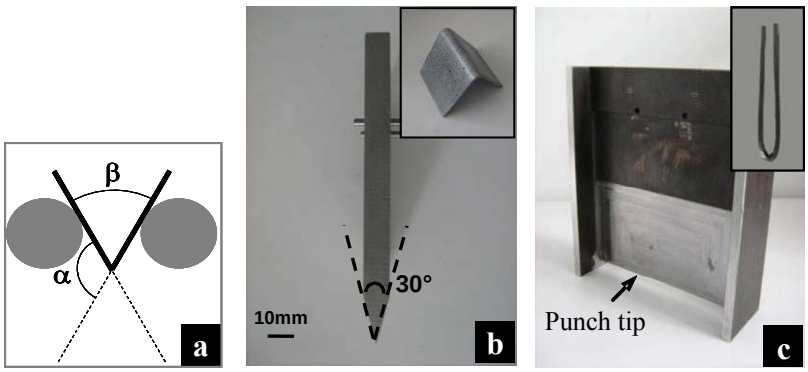

Figure 1: (a) schematics of the air-bending test with α = bending angle, (b) punch with radius = 0.1mm, punch thickness = 10mm and (inlet) a bent sample, (c) thin punch with side stiffeners and radius = 0.4mm, punch thickness = 0.8mm and (inlet) a 180° bent sample.

As a first approximation, the maximal strain reached at the outer surface after air-bending was determined thanks to a simple analytical formula. Marciniak and Duncan [18] proposed the following equation:

$$\varepsilon = \ln(1 + y / R) \tag{1}$$

where y is the distance between a bent fibre and mid-thickness and R is the bending radius at mid-thickness. In the present case, to assess the strain at the outer surface, this equation could be rewritten as:

$$\varepsilon = \ln(1 + t /(2R_i + t)) \tag{2}$$

where t is the initial thickness and R_i is the inner radius of the bent specimen.

The initial thickness of the Steel 1 specimen was equal to 1.6mm and the inner radius profile (curvature radius of inner fibre) was measured manually by determination of the contour of the sheet in polished cross-sections to be equal to 2.05mm (average of three specimens with very low experimental scatter) for a bending angle of 118° (TD sample). Hence, for these bending conditions, the maximum hoop strain (at the outer surface) was estimated to be 0.25. Due to the very low bend radius of thickness-reduced Steel 2 bent up to 180°, this formula was not valid. No first estimation for this maximal strain could thus be given. Finite element simulation was required to give a valid assessment of the hoop strain in such bending conditions.

2.2.2. Experimental database dedicated to FE simulation of the bending test

To determine constitutive equations to be used in the FE simulations of bending, tensile tests on smooth samples along RD, TD and 45° directions were performed at room temperature to evaluate isotropic hardening as well as strength and strain anisotropy of the material. The tensile specimens had a gauge area of W_0=12mm in width and 64mm (see Fig. 2a) in length and the initial elongation rate was 10^{-4} s^{-1}. Elongation was measured using an axial extensometer with a L_0 = 12mm gage length. A second extensometer was used to measure the reduction in width of the specimen (ΔW) to evaluate the corresponding Lankford coefficient ("r" ratio). In the following (ΔL) denotes the axial displacement measured with the extensometer.

U-Notched tensile (NT) specimens (18x100mm with one full thickness notches of radius 2mm on either edge and width of the remaining ligament = 10mm, see Fig. 2c) cut along TD, RD and 45° directions were also tested in tension at room temperature to reach higher local strains (up to 0.40), necessary to accurately model the air-bending test (see section 2.2.1.). These specimens were also used to investigate the effect of stress multi-axiality on plastic yielding. The prescribed notch opening rate was 0.5mm.min^{-1}.

In-plane reverse shear tests (100x30mm specimens with a gauge part of 4.5mm in height) were also carried out along RD under a prescribed loading rate of 0.05 kN.s^{-1} in order to assess the Bauschinger effect and to determine the kinematic contribution (if any) to hardening at high strains.

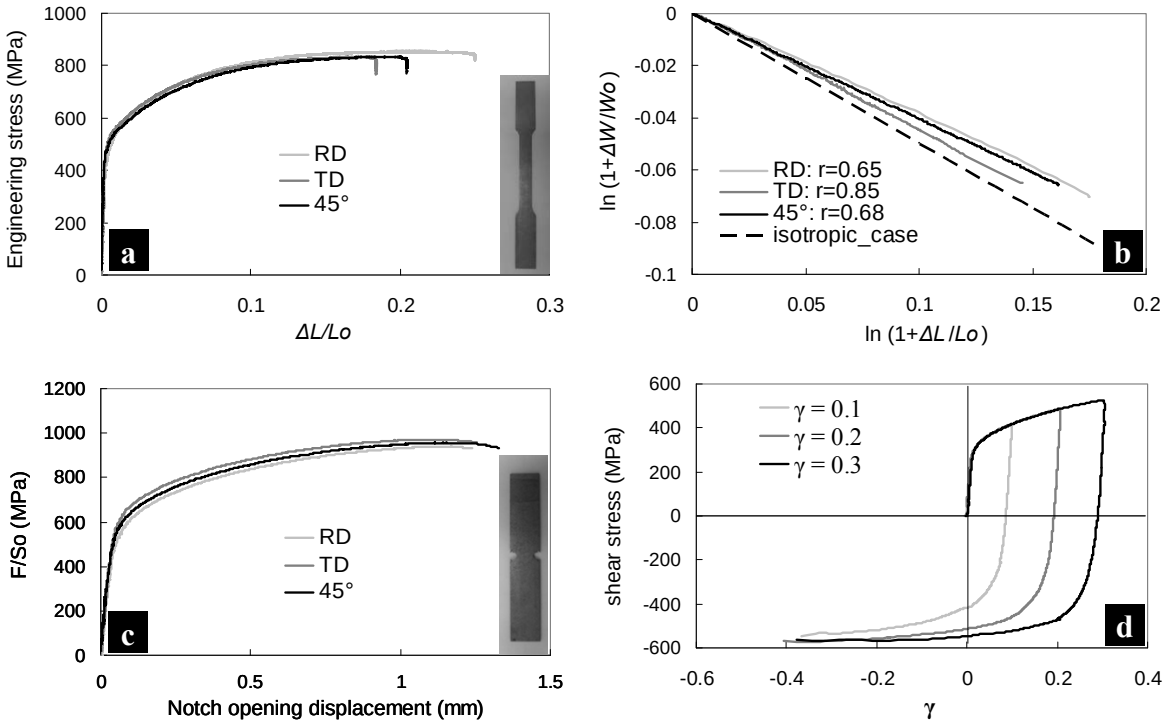

Figure 2: (a) Engineering tensile stress-strain curves, (b) strain anisotropy (smooth tensile specimens), (c) Tensile curves on NT specimens where F is the load and So is the initial cross section between notch roots, (d) cyclic shear curves along RD. γ corresponds to the ratio between the horizontal displacement and the specimen width = 4.5mm.

Figure 2a shows that the tensile response is almost isotropic. However, the "r" ratio (figure 2b) was significantly lower than 1 (between 0.65 and 0.85) yet with small differences between loading directions. Slight stress anisotropy was observed for notched specimens (Figure 2c). The three shearing tests evidenced a strong Bauschinger effect (Figure 2d), so that constitutive equations should include both isotropic and kinematic contributions to hardening to accurately describe the mechanical behaviour of the material, especially in the case where bending after prestraining has to be modelled.

3. Determination of constitutive equations for Steel 1

For the low alloy TRIP-aided steels considered here, although microstructural inhomogeneity and microstructural instability affect the local strain behaviour, the phase transformation of retained austenite into martensite was not explicitly taken into account in the model. The material was considered as a homogeneous medium and the effect of phase transformation on the yield behaviour was implicitly taken into account in the model parameters.

3.1. Constitutive equations

For rolled sheets, it has been proposed [19] to use the Hill quadratic yield criterion [20] together with mixed isotropic/kinematic hardening. However this criterion can hardly represent both stress and strain anisotropy so that more complex yield functions have been proposed in literature. Barlat et al. [21] developed an anisotropic criterion that is more appropriated for aluminium alloys. This yield function was further extended by Karafillis and Boyce [22] and Bron and Besson [23]. In their model, they used 16 material parameters to represent a complex yield surface and the convexity was proved. These complex yield surfaces have principally been used assuming pure isotropic hardening. Recently, some authors used anisotropic yield criteria coupled with a mixed isotropic/kinematic hardening. For example, Eggertsen and Mattiasson [24] modelled the bending / unbending behaviour with various anisotropic yield criteria including a contribution of kinematic hardening. They demonstrated that the model with purely isotropic hardening yielded to poorer prediction of the load-displacement curves than the one with a model including mixed hardening. Williams et al. [25] used a non-linear isotropic/kinematic hardening model associated with the Yld2000-2d anisotropic model developed by Barlat et al. [26] and Yoon et al. [27] to predict the axial crush response of hydroformed aluminium alloy tubes. Vladimirov et al. [28] used a non-linear isotropic and kinematic hardening associated with an anisotropic Hill yield criterion to model sheet metal forming such as deep drawing tests.

In the present study, according to the experimental results, an anisotropic yield criterion coupled with kinematic+isotropic hardening was used as in [29]. In order to represent kinematic hardening, a back stress $\underline{X}$ was introduced [30]. The yield surface was expressed using the difference ($\underline{B}$) (i.e. effective stress), between the Cauchy stress, $\underline{\sigma}$, and the back stress: $\underline{B} = \underline{\sigma} - \underline{X}$. In order to account for anisotropic plastic yielding, it was necessary to use an anisotropic scalar measure of stress to define the yield surface. The model proposed by Bron and Besson [23] was used in the following.

For any symmetric second order tensor, $\underline{T}$, the anisotropic scalar measure (T_E) of $\underline{T}$ is defined as:

$$T_E(\underline{T}) = \left(\sum_{k=1}^{K} \alpha_k \left(T_{Ek} \right)^a \right)^{1/a} \tag{3}$$

In practice, only two functions ($K = 2$) were used. α_k are positive coefficients with a sum equal to 1, i.e. $\alpha_1 = \alpha$ and $\alpha_2 = 1 - \alpha$ in the present case. The function $T_E(\underline{T})$ is positive and homogeneous of degree 1. T_{Ek} are secondary anisotropic scalar measures. One first defines two modified deviators:

$$\underline{T}_k = \underline{\underline{L}}_k : \underline{T}\,,\ k = 1,\ 2 \quad \text{(equivalent to } T_{ij}^k = L_{ijkl}^k T_{kl}\text{)} \tag{4}$$

where the fourth order tensor $\underline{\underline{L}}_k$ is expressed as follows using Voigt notations:

$$\underline{\underline{L}}_k = \begin{pmatrix} \frac{1}{3}\left(C_{LL}^k + C_{SS}^k\right) & -\frac{1}{3}C_{SS}^k & -\frac{1}{3}C_{LL}^k & 0 & 0 & 0 \\ -\frac{1}{3}C_{SS}^k & \frac{1}{3}\left(C_{SS}^k + C_{TT}^k\right) & -\frac{1}{3}C_{TT}^k & 0 & 0 & 0 \\ -\frac{1}{3}C_{LL}^k & -\frac{1}{3}C_{TT}^k & \frac{1}{3}\left(C_{LL}^k + C_{TT}^k\right) & 0 & 0 & 0 \\ 0 & 0 & 0 & C_{TL}^k & 0 & 0 \\ 0 & 0 & 0 & 0 & C_{LS}^k & 0 \\ 0 & 0 & 0 & 0 & 0 & C_{ST}^k \end{pmatrix} \tag{5}$$

The eigenvalues T_k^i of $\underline{T}_k$ are then computed: $T_k^1 \geq T_k^2 \geq T_k^3$. T_{E1} and T_{E2} are respectively computed as:

$$T_{E1} = \left[\frac{1}{2}\left(\left|T_1^2 - T_1^3\right|^{b_1} + \left|T_1^3 - T_1^1\right|^{b_1} + \left|T_1^1 - T_1^2\right|^{b_1}\right)\right]^{1/b_1} \tag{6}$$

$$T_{E2} = \left[\frac{3^{b_2}}{2^{b_2} + 2}\left(\left|T_2^1\right|^{b_2} + \left|T_2^2\right|^{b_2} + \left|T_2^3\right|^{b_2}\right)\right]^{1/b_2} \tag{7}$$

a, b_1, b_2 and α are four material parameters that influence the shape of the yield surface and $c_{IJ}^{1,2}$ $(I, J = L, T, S)$ parameters control yield anisotropy. The model used in the present study was simplified by assuming $a = b_1 = b_2$.

As mechanical tests were performed along in-plane directions, coefficients corresponding to shear along the thickness direction could not be adjusted. It was therefore assumed that $c_{ST}^{1,2} = c_{LS}^{1,2} = 1$. Following these simplifications, 10 out of a total of 16 parameters had to be optimised to represent yield anisotropy.

The yield surface was then expressed by:

$$\phi = B_E - R(p) \text{ with } B_E = T_E(\underline{B}) \tag{8}$$

In Eq. 8, p is the cumulative plastic strain and R is the current flow stress. Plastic flow was then computed using the normality rule as:

$$\dot{\underline{\varepsilon}}_p = \dot{p}\frac{\partial B_E}{\partial \underline{\sigma}} \tag{9}$$

Where $\dot{p}$ is the plastic multiplier such that $\dot{\underline{\varepsilon}}_p : \underline{B} = \dot{p}B_E$ (equivalent to $\dot{\varepsilon}_{p_{ij}} B_{ij} = \dot{p}B_E$)

Non-linear (Armstrong–Frederick type) kinematic hardening was included in the model using two back-stresses [19] to accurately represent experimental data. Their evolutionary equations are given by:

$$\underline{X} = \underline{X}_1 + \underline{X}_2 \text{ with } \dot{\underline{X}}_1 = \frac{2}{3}C_1\dot{\underline{\varepsilon}}_p - \dot{p}D_1\underline{X}_1 \text{ and } \dot{\underline{X}}_2 = \frac{2}{3}C_2\dot{\underline{\varepsilon}}_p - \dot{p}D_2\underline{X}_2 \quad . \tag{10}$$

where C_1, D_1, C_2 and D_2 are material parameters. Finally an additive form for the $R(p)$ function (isotropic hardening) was chosen as:

$$R(p) = R_0 + Hp + Q\left(1 - \exp\left(-bp\right)\right) \tag{11}$$

Isotropic strain hardening is principally given by the exponential term at low strains and by the linear term at high strains. This hardening law was also successfully used by Thuillier et al. [31] to model bending tests.
The model thus included two non-linear kinematic hardening variables (involving four material parameters: C_1, D_1, C_2, D_2), one non-linear isotropic hardening variable (involving two material parameters: Q, b) and one linear isotropic hardening variable (involving one material parameter: H). The use of a linear variable was found to be mandatory to account for large strains experienced both during tension of notched specimens and during bending. R_0 corresponds to the initial value of the yield stress.

3.2. Finite element simulation procedure

The in-house finite element software Zset [32] was used to simulate all mechanical tests. A fully implicit integration scheme was used to integrate the material constitutive equations. All calculations were done using an updated Lagrangian formulation with linear brick elements using selective integration (finite strain B-bar method, [33]). Tensile tests on smooth specimens were simulated up to (experimental) necking using one volume element. Notched (NT) and shearing specimens were analysed using 3D FE simulation; corresponding meshes are shown in Figure 3. In addition to usual symmetry conditions, displacements were prescribed over the AB segment along direction 2 for notched tensile specimens (Figure 3a) and along direction 1 for the shear specimens (Figure 3b).

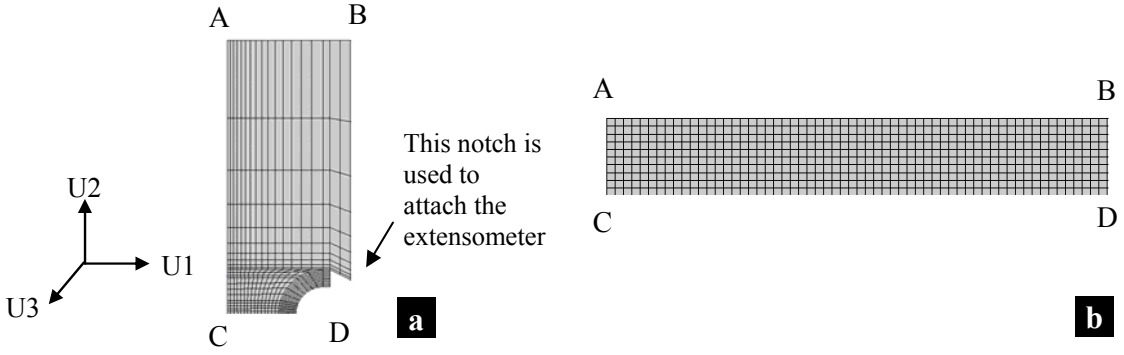

Figure 3: two-dimensional view of (a) meshing of the NT specimen (1/8 of the specimen due to symmetry with smallest element size = 130 x 150 x 800 µm close to the U-shaped notch) and (b) meshing of the shearing specimen (1/2 specimen with element size = 500 x 450 x 800 µm)

3.3. Identification of model parameters

In a first step, the yield criterion parameters were determined. To this purpose, a first approximation of strain hardening had to be made. In this first step, it was considered to be purely isotropic (there were little changes in loading path in the tests considered here). The

value of R_0 was set to 499 MPa. The Von Mises yield criterion was used to optimize isotropic strain hardening parameters thanks to tensile tests on smooth and notched samples along all directions. Then, the parameters of the Bron Besson yield criterion were identified. The values of a and α influence the shape of the yield surface. $c_{I,J=L,T}^{k=1,2}$ parameters were optimised from tensile tests on smooth and notched samples (RD, TD, 45°) by including experimental data on strain anisotropy i.e. measurements of "r" ratio.
In a second step, hardening parameters were determined. To this aim, isotropic hardening parameters had to be modified and C_i and D_i (i=1, 2) coefficients were optimized from shearing tests.
All model parameters were optimized using the optimizer integrated in the in-house finite element software Zset with the simplex algorithm.

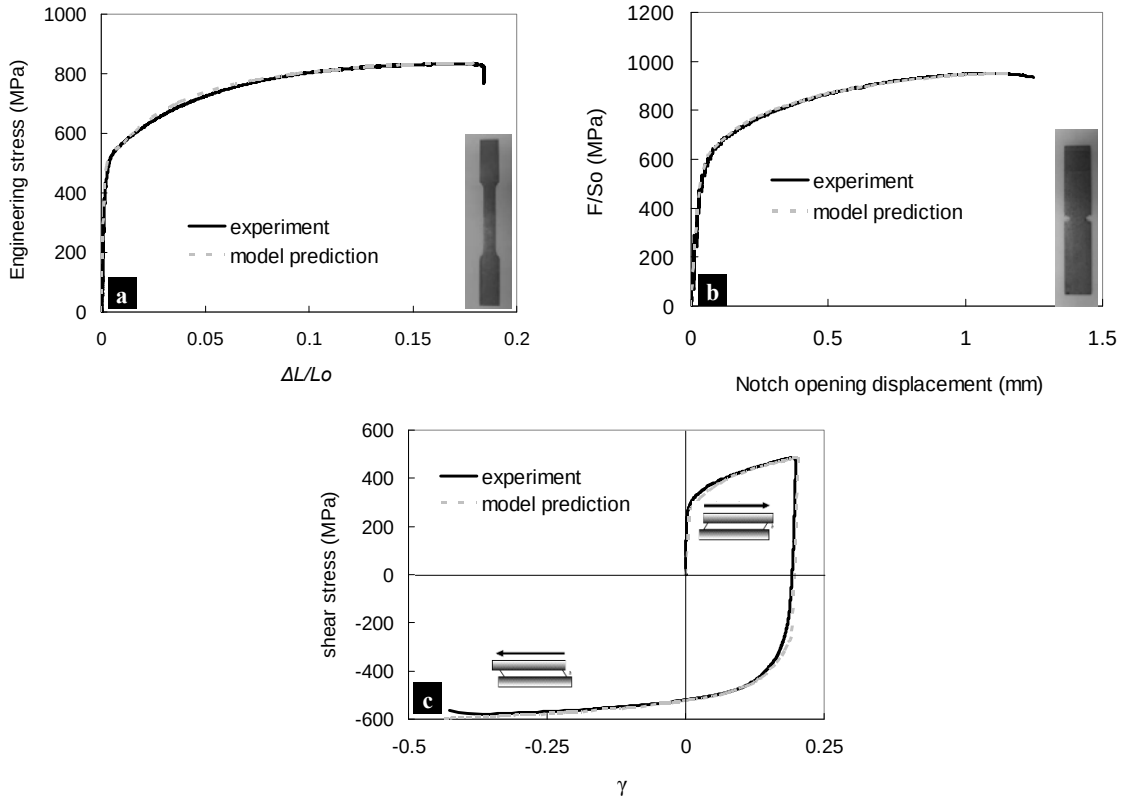

Figure 4: Experiment vs. model predictions for Steel 1: tensile curves (a: smooth and b: NT specimens tested along TD) and c: cyclic shearing curves along RD.

The model together with the optimized set of material parameters (Table 2) well reproduced tensile and reverse shearing curves (Figure 4). Note that $c_{TT,LL,SS,TL}^{k=1,2}$ parameters were close to 1, consistently with the slight anisotropy of the material. From numerical simulations, the local amount of strain reached 0.40 during tension on NT specimens and shear tests. The corresponding strain range was thus wide enough to encompass values that were expected to be reached during the air-bending test (max. 0.25 for Steel 1, see Section 2.2.1). The same hypothesis remained to be validated for Steel 2 using finite element calculations (see below).

Elastic properties	$E = 210\ GPa,\ \nu = 0.3$
Isotropic hardening	$R_0 = 499\ MPa, H = 110\ MPa$
	$b = 8.4,\ Q = 382\ MPa$
Kinematic hardening	$C_1 = 718\ MPa,\ D_1 = 9.4$
	$C_2 = 9900\ MPa,\ D_2 = 66.7$
Plastic anisotropy	$a = 6.1,\ \alpha = 0.55$
	$c_{TT}^1 = 0.99, c_{LL}^1 = 0.96, c_{SS}^1 = 0.92, c_{TL}^1 = 1.14, c_{LS}^1 = c_{ST}^1 = 1$
	$c_{TT}^2 = 0.99, c_{LL}^2 = 1.04, c_{SS}^2 = 1.17, c_{TL}^2 = 1.04, c_{LS}^2 = c_{ST}^2 = 1$

Table 2: Optimized material parameters for constitutive equations (Steel 1)

4. Full mechanical analysis of the air-bending test

4.1. Mechanical analysis of the bending test in usual conditions (Steel 1)

4.1.1. Numerical representation of the test

As air-bending tests are more severe along TD because cracking usually occurs earlier than along RD (at least in AHSSs), only simulation of air-bending along TD was carried out for Steel 1.
As no variation in specimen width was experimentally detected during and after the air-bending test, a plane strain assumption was considered to be reasonable in numerical simulations of the test and was first used. Only one half of the specimen and punch and one roll were meshed (Figure 5) due to symmetry conditions. The size of smallest elements was about 25 x 50 µm just next to the punch (i.e. there were 32 elements along the sheet thickness). For 3D simulations, 5 elements were considered along the specimen width. Finite element simulations were performed for the same displacement range as for experiments.
Tooling (punch + rolls) was assumed to behave elastically with a Young's modulus of 210 GPa and a Poisson ratio of 0.3. Two contact zones were considered:

- Between the sheet and the rolls: as rolls rotated almost freely during the test, friction could be neglected. Consequently, rolls were fixed and the corresponding friction coefficient was set to 0.

- Between the sheet and the punch: the contact area was first fully represented in the mesh. It was shown after modelling that only four nodes of the 2D mesh of the sheet were in contact with the punch (half meshing). In 3D, this corresponds to four lines of nodes along the direction of the sample width. Two conditions were then compared:
  (i) full representation of the punch (see Figure 5) assuming a Coulomb condition with various values of the friction coefficient between the punch and the sheet.
  (ii) prescribed vertical displacement on the four nodes in 2D (four lines of nodes in 3D) close to the symmetry axis.

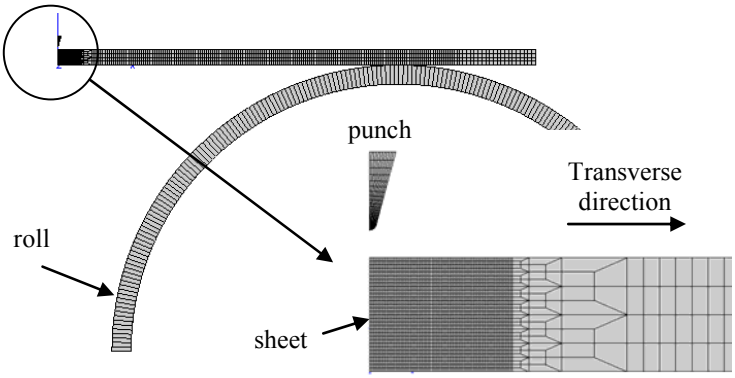

Figure 5: Meshing of the air-bending test

In the following, the "reference" calculations conditions denote a 2D plane strain assumption, a mesh with 32 elements in the sheet thickness and boundary conditions (i).

4.1.2. Modelling results

Very good agreement between experimental curves and 2D model predictions was obtained except at the end of the curve where the decrease in load was slightly underestimated by the model (Figure 6). In fact, crack initiation and stable crack propagation occurred during this stage of the test [15] and the damage-free model not expected to be able to describe this.

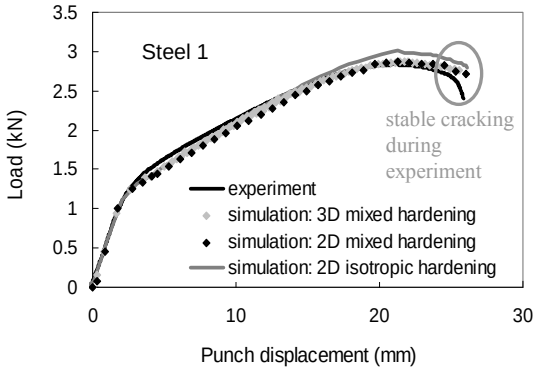

Figure 6: Experimental and predicted load vs. displacement curves both in 2D and 3D with a mixed isotropic/kinematic hardening rule (boundary condition (ii)) and in 2D with an isotropic hardening rule (boundary condition (i)).

Hardness measurements were carried out through the thickness on cross-sections of bent specimens of Steel 1. The softest area (i.e. that had experienced less work hardening) was considered as "the neutral fibre" after bending and unloading. The location of the minimum cumulated plastic strain predicted after bending and then unloading by simulation well corresponded to the (experimentally measured) softest region, at about 850µm from the outer surface (Figure 7). Due to stretching of the outer part of the specimen and compression of its inner part, the neutral fibre did not stay at mid-thickness and shifted toward the inner surface. Furthermore, the material next to the mid-thickness,

initially in the compressive zone, was moved to the other side of the "neutral fibre" i.e. was eventually pulled in tension during the bending test.

The minimum value of hardness measured on bent samples was very close to the hardness of the undeformed material. This correlated well with the simulation results which showed that the minimum value of the cumulated plastic strain was very low (~0.015) after the end of the test.

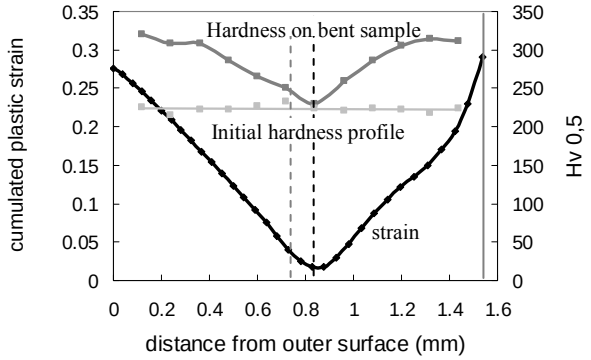

Figure 7: Evolution of the cumulative plastic strain *p* predicted using the "reference" calculation conditions, hardness through the thickness of bent + unloaded specimen and initial hardness profile. The "neutral fibre" was shifted from the mid-thickness of the sheet toward the inner surface (initial compressive zone). The dashed black line and the dashed grey line respectively represent "the neutral fibre" and the mid-thickness in the updated geometry. The vertical grey line represents the inner surface after thickness reduction due to bending.

The radius of curvature at the outer surface, at the end of the test (point A in Figure 8a) on bent then unloaded specimens was experimentally determined from metallographic observations to be 3.84mm. This value very well agreed with model predictions (also after unloading: 3.92mm). Note that this radius did not exactly correspond to the sum of the inner radius and the thickness of the sheet (i.e. 2.05 + 1.6mm). This difference was due to the fact that the centres of curvature were not the same for inner and outer skin of the specimen. This was mainly due to the high level of plastic strain that was locally reached during the test. Thus, even for moderately severe bending conditions used for Steel 1, the analytical formulae (Eq. 2) and the analytical approach from Ben Bettaieb et al. [34] could only be used as a first approximation. However, the value predicted from Eq. 2 (0.25) was in fair agreement with model prediction (~0.27). In more detail, experimental measurement of strain fields very well agreed with model predictions, both concerning the evolution of maximum principal strain at the apex and the strain gradient perpendicularly to the apex (Figure 8b). Consequently, the model together with reference calculation conditions accurately predicted all experimental data concerning this air-bending test.

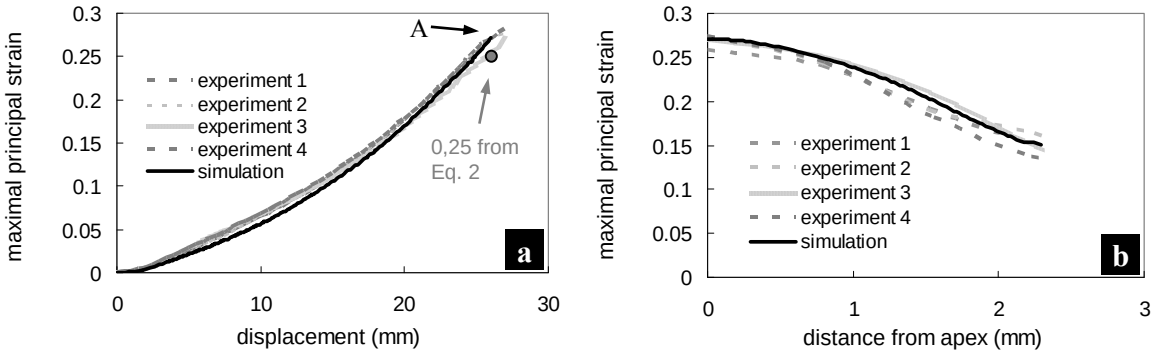

Figure 8: Evolution of strain during the air-bending test. Strain field measurements vs. model prediction (reference calculation conditions).
(a) Evolution of a material point taken at the apex. The grey point corresponds to the value given by equation (2) in section 2.2.1, (b) Strain along a line perpendicular to the apex (point A in (a)). Curvilinear abscissa in mm.

4.2. Effects of meshing and boundary conditions

To investigate the effects of the numerical representation of the test, simulations were first carried out by using boundary conditions (i) with two different friction coefficients between the sheet and the punch. As no lubrication was used during the test between the punch and the sheet specimen, a high friction coefficient was first assumed (0.25) according to Gieck [35], Muller [36] and Stöcker et al. [37] who gave friction coefficients values between 0.20 and 0.30 for two steels without lubrication. However, the actual value of the friction coefficient was not known and the value of 0.25 was also tentatively replaced by a lower one (0.1). Similar results were obtained by using both values so that the value of 0.25 was kept for the rest of the 2D calculations with boundary condition (i). In addition, similar results were obtained by replacing the punch by prescribing the displacement nodes located just below the tool (boundary conditions (ii)).
Additional 3D calculations were then carried out, using boundary conditions (ii) to limit the number of elements. The load-displacement curves predicted using 2D and 3D calculations were almost identical (Figure 6), which indicated that a 2D calculation was sufficient for modelling the air-bending test.

To summarize, this sensitivity study made it possible to perform accurate modelling of this air-bending test using a 2D calculation with the plane strain hypothesis. The friction coefficient between the sheet and the punch had little influence in the range investigated. Moreover, the punch could be replaced by prescribed displacement of the four nodes closest to the symmetry axis.

4.3. Role of kinematic hardening

4.3.1. Effect on the global response

To check whether it was actually necessary to take kinematic hardening into account in air-bending test even without prestraining, purely isotropic hardening was alternatively assumed. It was represented by the following equation:

$$R'(p) = R_0 + H'p + Q'\left(1 - \exp\left(-b'p\right)\right) \quad (13)$$

The initial value R_0 (i.e. 499 MPa) was kept and the values of parameters H', Q' and b' were optimized on a tensile test on smooth specimen along TD. The initial Bron Besson parameters (given in Table 2) were also used in these constitutive equations. After optimization, H', Q' and b' were respectively set to 800 MPa, 393 MPa and 23. While these parameters were determined from a test along a specific direction, they can still be used with acceptable accuracy for loading along other directions. From Figure 6, the load vs. punch displacement curve was not as well predicted by assuming purely isotropic hardening as by assuming mixed hardening. In fact, the isotropic hardening rule led to an overestimation of the load compared to the mixed hardening rule.

4.3.2. Effect on springback

In the literature, Geng and Wagoner [38] and Eggertsen and Mattiasson [24] reported that taking kinematic hardening into account improved the prediction of springback after unloading compared to using a purely isotropic hardening rule. In the present study, one test was interrupted by unloading after a prescribed punch displacement of 20mm (corresponding to a bending angle α = 88°, to avoid any damage development in this specimen). The load/displacement curve was well represented up to this value of punch displacement assuming either mixed or pure isotropic hardening: both models predicted an angle equal to 89°. After unloading, the bending angle was measured to 78°, to be compared to 79° using mixed hardening and 81° using isotropic hardening. The agreement was therefore slightly better with mixed hardening. However, the difference was rather small, so that this air-bending test did not appear as an appropriate tool to study the influence of the hardening rule on the prediction of springback effects.

4.3.3. Effect on the global response after prestraining

In industrial stamping, some regions of the sheet blanks may have already been deformed before bending. It seems therefore necessary to investigate the influence of prior straining on the subsequent behaviour in air-bending. For this purpose, uniaxial tensile tests were carried out along TD using Steel 1 up to an elongation of 10%. Then, air-bending specimens (using the same geometry as before) were cut from the gauge part of the prestrained tensile specimens and tested in air-bending until microcracking, in the same conditions as previously described. FE simulation of this test was performed in the "reference" conditions but assuming either mixed or purely isotropic hardening. The reduction in thickness which occurred during prestraining was taken into account in the model. The corresponding curves are given in Figure 9. With a purely isotropic hardening, the yield stress was largely overestimated, while the first half of the curve was very satisfactorily described using the mixed hardening rule. At the end of the test, both curves were almost superimposed and overestimated the experimental one. This was attributed to the fact that the model did not account for damage development in the material [15]. Straining prior to bending affected the bendability of the sheet (i.e. damage developed earlier than in the bending specimens that had not been previously strained). Cracking was observed for lower values of punch displacement after 10% of prestraining than for the as-received material. This was consistent with the work of Friedman and Luckey [39] on aluminium alloys.

The true strain reached at the outer surface at microcracking for the as-received material was evaluated to be 0.27 with the model prediction. If the amount of true strain introduced by tensile prestraining is subtracted from this value, one gets a value of true strain equal to 0.175. The punch displacement yielding that value in the as-received material was found to be equal to 20.5 mm. This value was in very good agreement with the punch displacement at microcracking of the prestrained specimen (Figure 9). This means that, for the particular case of tensile prestraining along the same direction as that of hoop strain applied during bending, the effect of prestraining can be satisfactorily predicted by a critical cumulative plastic strain criterion. However, due to the kinematic contribution to hardening, (i) the load-displacement curve can only be predicted with the mixed hardening rule and (ii) this simple result can be extended neither to prestraining along other directions nor to other prestraining conditions.

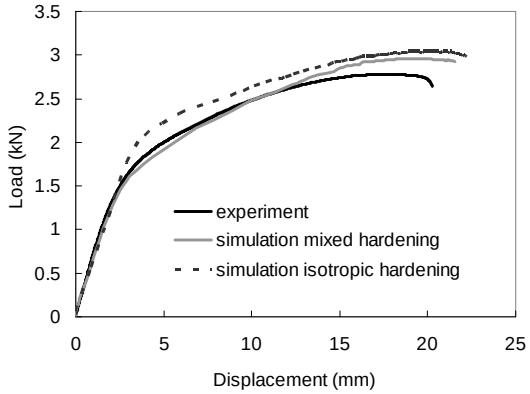

Figure 9: Experimental and predicted load / punch displacement curves of a prestrained and then air-bent specimen. Model predictions assuming either purely isotropic or mixed hardening rules are respectively represented with a dotted grey line and a continuous grey line.

4.3.4. Effect on local stress-strain paths

The evolution of hoop stress vs. hoop strain is plotted in Figure 10 for various nodes located slightly below the mid-thickness (toward the inner surface) along the symmetry axis. At the beginning of the test, all considered nodes were located in the compressive zone but some of them were eventually loaded in tension (consistently with Figure 7) after a slight compressive plastic strain. This loading path confirmed that using kinematic hardening was necessary to accurately represent the local stress/strain path next to the mid-thickness.

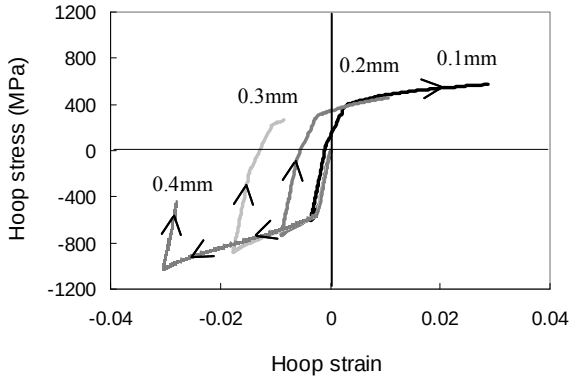

Figure 10: Loading paths for various nodes initially next to the mid-thickness, along the symmetry axis. The nodes were initially located at distances from mid-thickness of, respectively, 0.1, 0.2, 0.3, and 0.4mm toward the inner surface.

To summarize, integration of kinematic hardening in the constitutive equations slightly improved the accuracy of the global response in terms of load vs. punch displacement curves as well as the prediction of springback. In case of non-proportional loading paths (as for prestraining before air-bending), kinematic hardening is needed to accurately predict the global response. Finally, to accurately predict local stress and strain path next to the mid-thickness of the sheet, kinematic hardening is also required.

4.4. Using the model to assess local stress and strain fields during air-bending

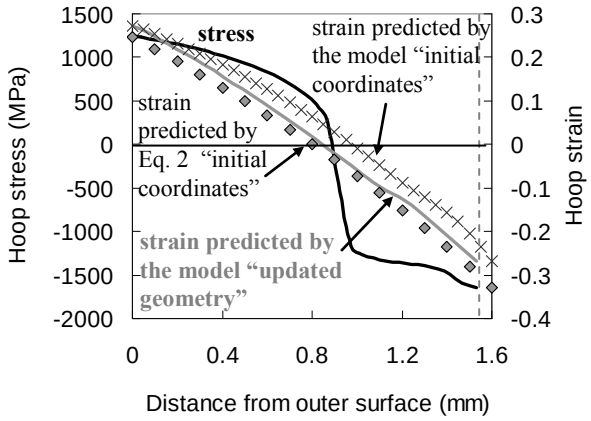

Figure 11: Hoop stress (black line) and hoop strain (grey line) predicted by the model in the updated geometry, along the symmetry axis, for a punch displacement of 26mm (end of the test), before unloading. For comparison purposes, the corresponding hoop strains predicted by Eq. 2 (grey diamonds) and predicted by the model (grey crosses) are also represented in the initial coordinates (undeformed state), Steel 1. The inner surface in the updated geometry is represented by the vertical dashed grey line.

Calculation of the strain using Eq. 2 yielded a maximal value close to 0.25, in close agreement between the value given with both model prediction and Aramis measurements (0.27). The difference between these values was due to an approximation made with the analytical formula. The latter only applied when the neutral fibre stays at the mid-thickness, which was not the case with the present bending conditions. Regarding the strain gradient given by the model prediction and by Eq. 2 in the initial coordinates (i.e. no decrease in thickness was taken into account), different curves were obtained and the analytical formula clearly underestimated the strain with respect to the numerical prediction (Figure 11). It is therefore necessary to account for the change in the sheet thickness to well predict stress and even strain fields.
As tensile tests on notched specimens were performed up to a local strain of 0.4, it can be concluded that the numerical simulation of the air-bending tests carried out on Steel 1 was actually performed with constitutive equation parameters that were identified in a relevant range of stress and strain states.

4.5. Application to the mechanical analysis of a more severe air-bending test on a thinner sheet (Steel 2)

The model was then applied to thickness-reduced Steel 2 under severe bending conditions (i.e. up to 180° bending). As Steel 1 and 2 had the same heat treatment, the same chemical

composition and similar mechanical behaviour, the same constitutive equations and parameters were used as for Steel 1. The plane strain hypothesis was also used in this case as no variation in the sample width was observed after bending. Continuous experimental strain measurements were not made possible because rolls were too close to the specimen to allow recording the strain evolution with the two cameras. The only way to obtain such information was to take one picture of the specimen before the test and one of the deformed specimen after bending and unloading. Thus, only the strain field after the end of the test was accessed experimentally.

4.5.1. Mesh and boundary conditions

As previously, only one half of the specimen and punch and one roll were meshed. These calculations were performed with 32 elements in the thickness and the size of smallest elements was about 31 x 23µm just in front of the punch (close to the apex). The tools (punch + rolls) were assumed as previously to behave elastically. Here, the punch radius was equal to 0.4mm and the friction coefficient between sheet and punch was set to 0.25 as for air-bending test on Steel 1. As the punch diameter was similar to the sheet thickness, only boundary condition (i) was used, i.e. the punch was not replaced by prescribed node displacement. As for Steel 1, the friction coefficient between sheet and rolls was set to zero.

4.5.2. Mechanical analysis

Experimental and predicted load vs. punch displacement curves were in good agreement (Figure 12a) in the first part of the test (punch displacement up to 15mm). The change in slope (after a punch displacement of about 15mm) was qualitatively well predicted but still quantitatively underestimated. In fact, the maximum strain achieved during this test is higher than 0.4 so that constitutive equations are used here beyond the strain range used for parameter identification. The discrepancy at the end of the test could also be due to the difficulty to well represent the contact conditions for such severe bending test up to 180°. Indeed, at the end of the test, friction between the sheet and the rolls might have occurred as the contact area increased. In addition, the contact between the sheet and the punch moved from its initial location (Figure 12b). At the end of the test, the inner radius of the bent specimens was smaller than the punch radius. This phenomenon underlined the difficulty to perform such calculations because of contact issues.

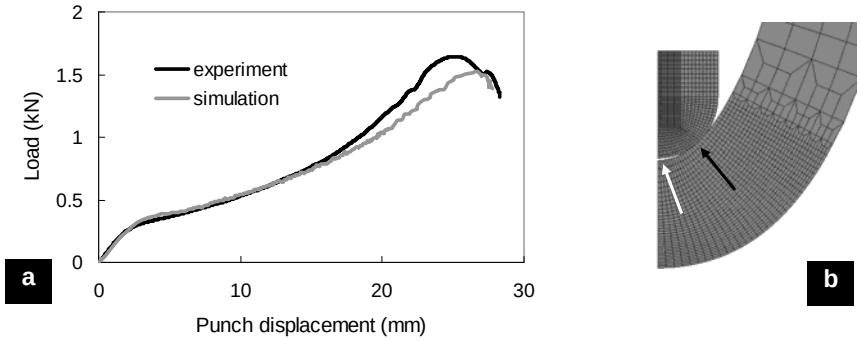

Figure 12: (a) Load vs. punch displacement curves for experiment and 2D simulation for a 180° bending angle, (b) The contact area between punch and sheet has moved during the test. Initial contact is illustrated with white arrow and final contact is showed with a black arrow.

The strain gradient (section taken perpendicularly to the apex) after bending up to 180° and then unloading is represented in Figure 13. The model prediction was in good agreement with experiments in view of the experimental scatter. As for Steel 1, external and internal radii measured on bent specimens were compared to model predictions, both after unloading. Very good agreement was observed between the two values respectively of the outer radius (1.14mm from experimental measurements vs. 1.17mm from model predictions) and of the inner radius (0.32mm from experimental measurements vs. 0.33 mm from model predictions).

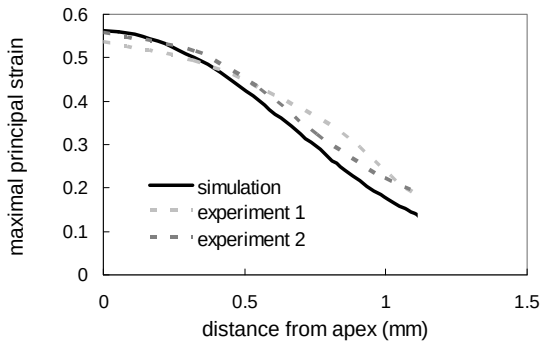

Figure 13: Evolution of the major strain at outer surface after bending up to 180° followed by unloading. Experimental values (strain field measurements vs. model predictions). Section taken perpendicularly to the apex at the end of the test. Curvilinear abscissa in mm along the outer surface.

Good correlation was also found between through-thickness hardness measurements and model prediction of cumulative plastic strain (Figure 14), so that the location of the "neutral fibre" was well predicted by the model. The slight difference in location of the neutral fibre was probably due to the difficulty to perform hardness measurements through such a thin material. Moreover, the minimum value of hardness measured on the bent specimen was significantly higher (by about 40 $HV_{0.3}$) than the hardness of the as-received material. This correlated well with finite element results which indicated a minimum cumulated plastic strain equal to 0.13 in this case (compared to 0,015 for Steel 1). The evolution of hoop stress vs. hoop strain was plotted in Figure 14b for various nodes located slightly below the mid-thickness (toward the inner surface) along the symmetry axis as for bending of Steel 1. At the beginning of the test, all considered nodes were located in the compressive zone but some of them were eventually loaded in tension after a slight compressive plastic strain. Here, it was clearly necessary to take the kinematic contribution to hardening into account to accurately represent the local stress/strain path next to the mid-thickness. Although the prediction of the load/displacement curve was not in very good agreement with experimental data at the end of the test, the numerical simulation was considered to correctly predict the available database, making it possible to estimate strain and stress fields.

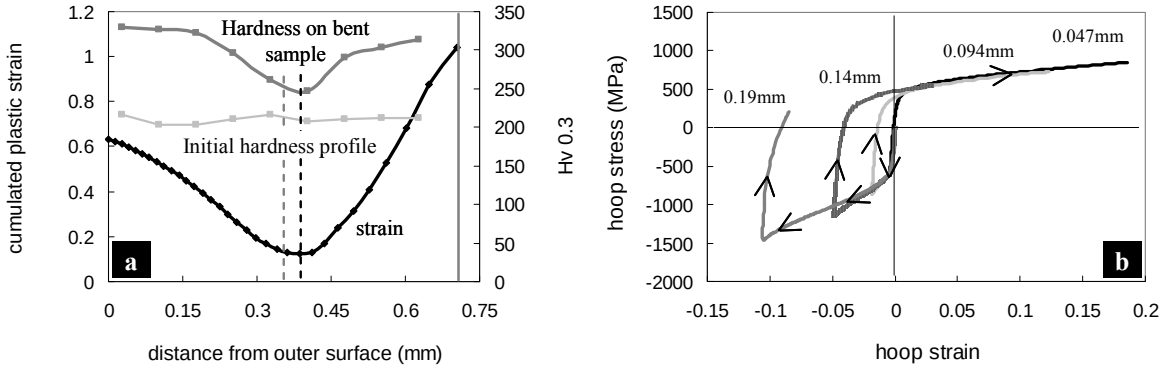

Figure 14: (a) Evolution of cumulative plastic strain and hardness through the thickness on a specimen bent up to 180° and initial hardness profile. The neutral fibre shifted from mid-thickness of the sheet toward the inner surface, i.e., the initial compressive zone. The dashed black line and the dashed grey line respectively represent the neutral fibre and the mid-thickness in the updated geometry. The continuous vertical grey line represents the inner surface (thickness reduction).
(b) Loading paths for various nodes initially next to the mid-thickness along the symmetry axis. The nodes were initially located at distances from mid-thickness of, respectively, 0.047, 0.094, 0.14, and 0.19mm toward the inner surface.

4.5.3. Local stress and strain fields during air-bending of the thin specimens

Very high values of the hoop stress (1320MPa) and of the hoop strain (0.56) were predicted at the end of the test by the model (Figure 15a). Note that unlike in air-bending of Steel 1, thickness-reduced Steel 2 did not crack, except as soon as hard bands were located close to the outer surface [15]. Internal damage was observed through the thickness after air-bending of Steel 2 but no microcracking was observed at the outer surface. The very low thickness of this material could possibly explain this result. This bending test involved very high strain levels with a significant gradient through the thickness. In particular, the node initially at mid-thickness underwent a total hoop strain close to 0.28 at the end of the test (Figure 15b). Moreover, the increase in stress, in the compressive area, with increasing distance from the outer surface was due to the shift of the contact region between the sheet and the punch (Figure 12b).

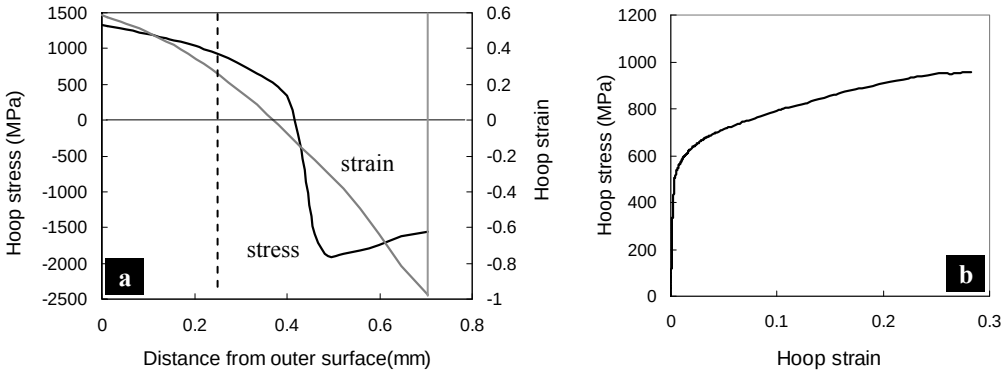

Figure 15: (a) Hoop stress (black line) and hoop strain (grey line) along the symmetry axis for a 180° bending (thickness-reduced Steel 2). The location of material initially at mid-thickness is represented by the vertical dashed line (0.23mm from outer surface). The inner surface is represented by the vertical grey line (thickness reduction), (b) hoop stress vs. hoop strain evolution for the node initially at mid-thickness.

5. Summary and concluding remarks

In order to carry out a realistic simulation of air-bending tests, a comprehensive experimental database (including tensile tests on smooth and notched samples and shear tests) was established for the considered low alloy TRIP steels. Using this database, material constitutive equations accounting for anisotropic elasto-plastic behaviour with mixed isotropic/kinematic hardening was determined. Using such material description allowed good prediction of load vs. displacement curves obtained during air-bending tests.

Numerical simulation of the air-bending test showed the following results:

(i) The friction coefficient between the sheet and the punch has no influence (in the investigated range: 0.1 vs. 0.25) in conventional bending conditions.

(ii) The test can be satisfactorily modelled by considering fixed rolls and perfect sliding conditions between the sheet and the rolls.

(iii) Both two air-bending tests considered here involve plane strain conditions.

(iv) When using a very sharp punch (compared to the sheet thickness), there is no need to explicitly model the contact between the sheet and the punch. It can be replaced by prescribed node displacement of the sheet in the vicinity of the symmetry axis.

(v) A slight shift of the neutral fibre (defined by the minimum cumulated plastic strain) from the mid-thickness toward the compressive area was predicted, in agreement with experimental observations. This implies that the whole sheet thickness undergoes plasticity for sufficiently large bending angles.

(vi) Although kinematic hardening appears to have little effect on the load/displacement curves and on the prediction of springback, the material close to the sheet centre undergoes initial compression followed by reverse plasticity in tension. Kinematic hardening should thus be taken into account to predict the strain path next to the initial mid-thickness, especially for severe bending.

(vii) Kinematic hardening should be taken into account in case of changes in loading path e.g. by tensile prestraining prior to air-bending.

Acknowledgements

The authors are grateful for the financial support provided by ArcelorMittal Global R&D. The authors also thank O. Bouaziz and A. Col for their valuable comments and S. Douchamps for measurements performed with the Aramis facility.

References

[1] J. Datsko, C.T. Yang, Correlation of bendability of materials with their tensile properties, J. Eng. Ind. 82 (1960) 309-314.

[2] D.K. Leu, A simplified approach for evaluating bendability and springback in plastic bending of anisotropic sheet metals, J. Mater. Process. Technol. 66 (1997) 9-17.

[3] K. Yamazaki, Y. Mizuyama, M. Oka, Y. Tokunaga, Influence of microstructure on bendability of ultrahigh-strength steel sheet, Journal of the Japan Society for Technology of Plasticity 36 (1995) 973-978.

[4] A. Nilsson, L. Melin, C. Magnusson, Finite-element simulation of V-die bending: a comparison with experimental results, J. Mater. Process. Technol. 65 (1997) 52-58.

[5] X. Li, Y. Yang, Y., Wang, J. Bao, S. Li, Effect of the material hardening mode on the springback simulation accuracy of V-free bending, J. Mater. Process. Technol. 123 (2002) 209-211.

[6] W. Gan, R.H. Wagoner, Die design method for sheet springback, Int. J. Mech. Sci. 46 (2004) 1097-1113.

[7] P.A. Eggertsen, K. Mattiasson, On constitutive modelling for springback analysis, Int. J. Mech. Sci. 52 (2010) 804-818.

[8] J. Chakrabarty, W.B. Lee, K.C. Chan, An analysis of the plane-strain bending of an orthotropic sheet in the elastic/plastic range, J. Mater. Process. Technol. 104 (2000) 48-52.

[9] J. Chakrabarty, W.B. Lee, K.C. Chan, An exact solution for the elastic/plastic bending of anisotropic sheet metal under conditions of plane strain, Int. J. Mech. Sci. 43 (2001) 1871-1880.

[10] A.R. Ragab, C.A. Saleh, Evaluation of bendability of sheet metals using void coalescence models, Mater. Sci. Eng. A. 395 (2005) 102-109.

[11] K.M. Zhao, J.K. Lee, Finite element analysis of the three-point bending of sheet metals, J. Mater. Process. Technol. 122 (2002) 6-11.

[12] C. Wang, G. Kinzel, T. Altan, Mathematical modeling of plane strain bending of sheet and plate, J. Mater. Process. Technol. 39 (1993) 279-304.
[13] R. Hambli, A. Mkaddem, A. Potiron, Finite element damage modeling in bending processes, J. Mater. Process. Technol. 147 (2004), 302-310.

[14] S. Thuillier, N. Le Maoût, P.Y. Manach, Bending limit prediction of an aluminium thin sheet, Int. J. Mater. Form. 3 (2010) 223-226.

[15] D. Rèche, T. Sturel, O. Bouaziz, A. Col., A.F. Gourgues-Lorenzon, Damage development in low allow TRIP-aided steels during air-bending, Mater. Sci. Eng. A 528 (2011) 5241-5250.

[16] A. Dalloz, J. Besson, A.F. Gourgues-Lorenzon, T. Sturel, A. Pineau, Effect of shear cutting on ductility of a dual phase steel, Eng. Fract. Mech. 76 (2009) 1411-1424.

[17] Aramis, Optical 3D deformation analysis software developed by GOM GmbH, http://www.gom.com/3d-software/aramis-software.html.

[18] Z. Marciniak, J.L. Duncan, Bending. The Mechanics of Sheet Metal Forming, first edition, A.Arnold, 1992, pp. 68-99.

[19] J.L. Chaboche, A review of some plasticity and viscoplasticity constitutive theories, Int. J. Plast. 24 (2008) 1642-1693.

[20] R. Hill, A theory of the yielding and plastic flow of anisotropic metals. Proc. Royal Soc. London, A193, 1948, pp. 281-297.

[21] F. Barlat, D.J. Lege, J.C. Brem, A six component yield function for anisotropic materials, Int. J. Plast. 7 (1991) 693-712.

[22] A.P. Karafillis, M.C. Boyce, A general anisotropic yield criterion using bounds and a transformation weighting tensor, J. Mech. Phy. Solid. 41 (1993) 1859-1886.

[23] F. Bron, J. Besson, A yield function for anisotropy materials. Application to aluminium alloys, Int. J. Plast. 20 (2004) 937-963.

[24] P.A. Eggertsen, K. Mattiasson, On the modelling of the bending-unbending behaviour for accurate springback predictions, Int. J. Mech. Sci. 51 (2009) 547-563.

[25] B.W. Williams, C.H.M. Simha, N. Abedrabbo, R. Mayer, M.J. Worswick, Effect of anisotropy, kinematic hardening and strain-rate sensitivity on the predicted axial crush response of hydroformed aluminium alloy tubes, Int. J. Impact Eng. 37 (2010) 652-661.

[26] F. Barlat, J.C. Brem, J.W. Yoon, K. Chung, R.E. Dick, D.J. Lege, F. Pourboghrat, S.H. Choi, E. Chu, Plane stress yield function for aluminum alloy sheets - Part 1: Theory, Int. J. Plast. 19 (2003) 1297-1319.

[27] J. Yoon, F. Barlat, R.E. Dick, K. Chung, T.J. Kang, Plane stress yield function for aluminum alloy sheets - Part II: FE formulation and its implementation, Int. J. Plast. 20 (2004) 495-522.

[28] I.N. Vladimirov, M.P. Pietryga, S. Reese, Anisotropic finite elastoplasticity with nonlinear kinematic and isotropic hardening and application to sheet metal forming, Int. J. Plast. 26 (2010) 659-687.

[29] Y. Shinohara, Y. Madi, J. Besson, A combined phenomenological model for the representation of anisotropic hardening behaviour in high strength steel line pipes, Eur. J. Mech. A Solids. 29 (2010) 917-927.

[30] J.L. Chaboche, Constitutive equations for cyclic plasticity and cyclic viscoplasticity. Int. J. Plast. 5 (1989), 247-302.

[31] S. Thuillier, N. Le Maoût, P.Y. Manach, Influence of ductile damage on the bending behaviour of aluminium alloy thin sheets, Materials and Design 32 (2011) 2049-2057.

[32] J. Besson, R. Foerch, Large scale object-oriented finite element code design, Comput. Meth. Appl. Mech. Eng. 142 (1997) 165-187.

[33] B. Moran, M. Ortiz, C.F. Shih, Formulation of implicit finite-element methods for multiplicative finite deformation plasticity, Int. J. Numer. Meth. Eng. 29 (1990) 483-514.

[34] M. Ben Bettaieb, X. Lemoine, L. Duchêne, A.M. Habraken, Simulation of the bending process of hardening metallic sheets using damage model. Part I: Theoretical development and numerical implementation, Mater. Sci. Eng. A. 528 (2010) 434-441.

[35] K. Gieck, Technical formulary, 10th Edition française, Dunod (In French), 1997.

[36] J. Muller, General mechanics formulary, 17th Edition, Paillart, 2000, p.147 (In French).

[37] H. Stöcker, F. Jundt, G. Guillaume, Physics, 2nd Edition, Dunod, 2007, p.253 (In French).

[38] L. Geng, R.H. Wagoner, Role of plastic anisotropy and its evolution on springback, Int. J. Mech. Sci. 44 (2002) 123-148.

[39] P.A. Friedman, S.G. Luckey, Failure of Al-Mg-Si alloys in bending, Practical Failure Analysis, ASM Inter. 1 (2002) 33-42.

II. Complementary data for model predictions

II.A. Experimental database

Constitutive equation parameters of Steel 1 have been determined by fitting model predictions to experimental results, i.e. tensile tests on smooth and notched samples and shear tests. In section I, only simulations along the transverse direction were given for tensile tests. In the following, simulations along the three directions (rolling, transverse and 45°) are shown (Figure II.1).
For the following curves, a Bron Besson yield criterion coupled with a mixed isotropic/kinematic hardening was used as in section I.

Note that the model is in good agreement with all experimental curves. The rolling direction is slightly overestimated with the simulation compared to the experiment for tensile tests on notched specimens while the simulation along 45° direction slightly underestimates the experiment at the end of the test for tensile tests both on smooth and notched samples. Finally, the prediction along transverse direction perfectly fit with experiments. This is in this direction that air and stretch bending tests were carried out.

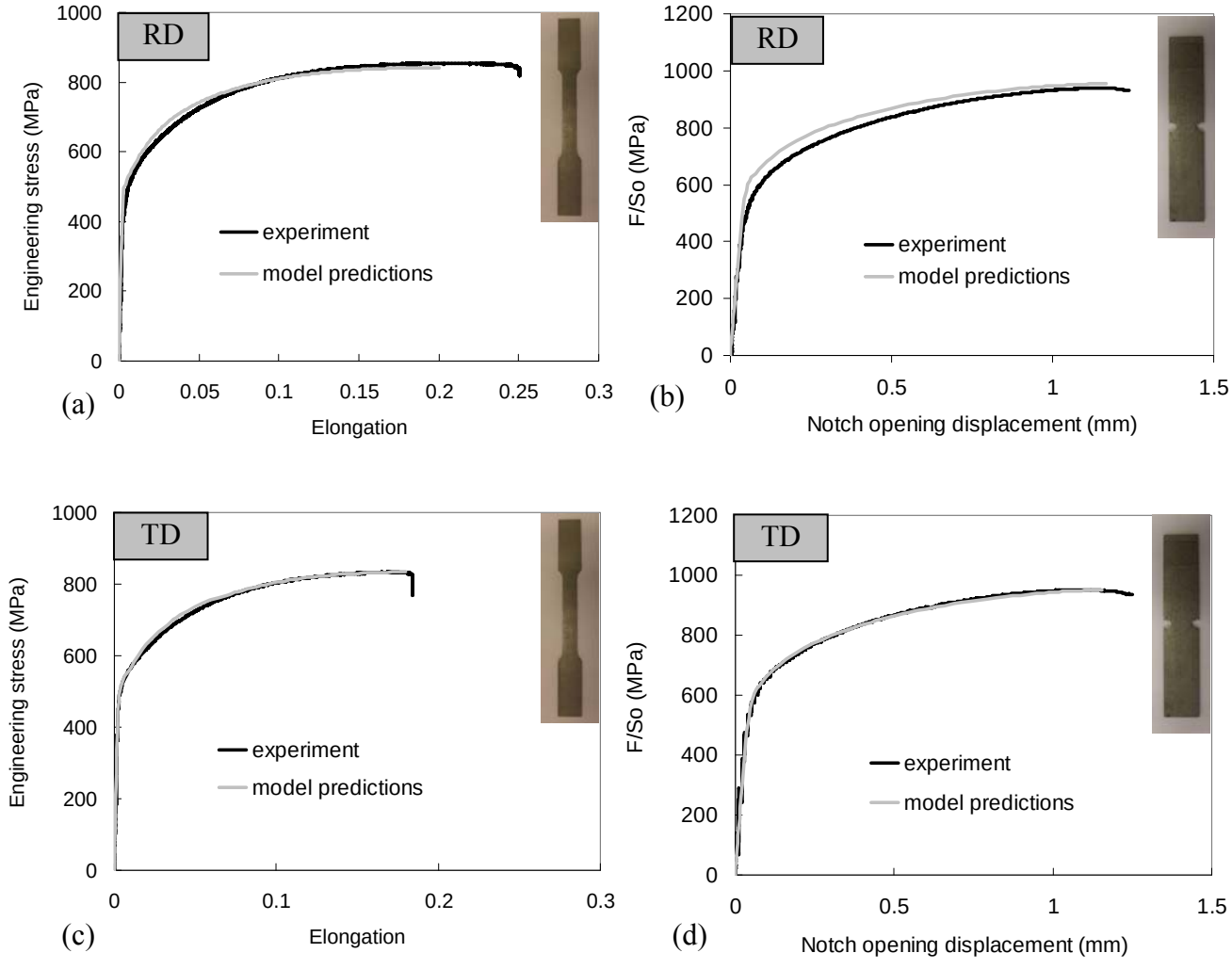

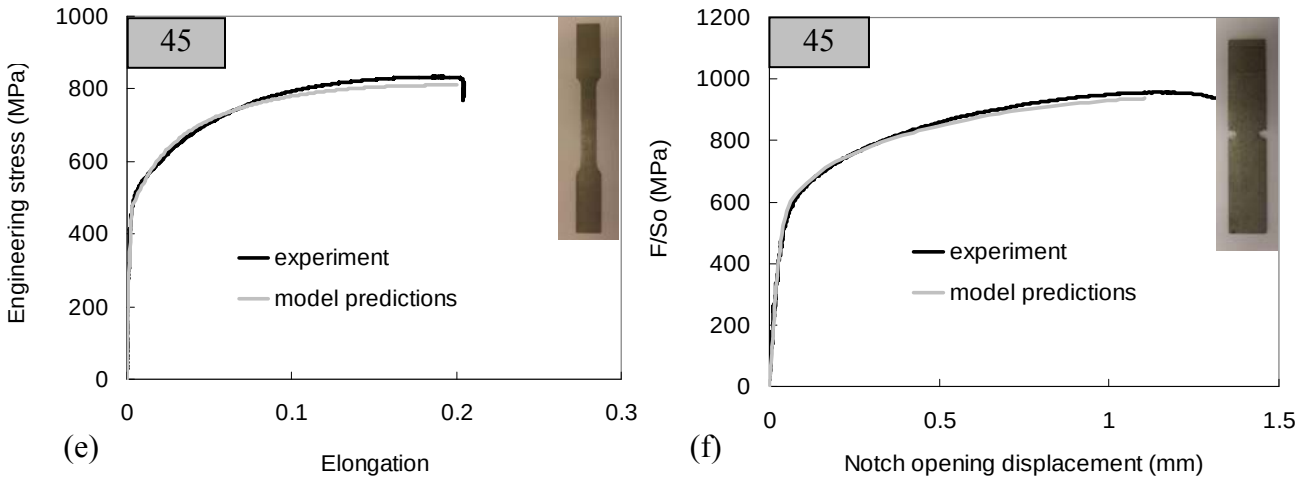

Figure II.1. Experiment vs. model predictions for Steel 1. Bron Besson yield criterion and mixed isotropic/kinematic hardening. Tensile curves on smooth and notched specimens. Engineering tensile stress-strain curves along (a) rolling, (c) transverse and (e) 45° directions. Tensile curves on notched specimens along (b) rolling, (d) transverse and (f) 45° directions where F is the load and So is the initial cross section.

Shear tests were also carried out to determine constitutive equations of Steel 1. In section I, only simulation curve for $\gamma_{max} = 0.2$ was shown. Figure II.2 illustrates both experimental curves and model predictions for $\gamma_{max} = 0.1$, 0.2 and 0.3.

To summarize, there is very good agreement between all simulated and experimental curves along the three directions for all tests (tensile and shear tests). This is due to the use of both an anisotropic yield criterion (Bron-Besson equations) and mixed isotropic/kinematic hardening rules, as will be explained in more detail in the following.

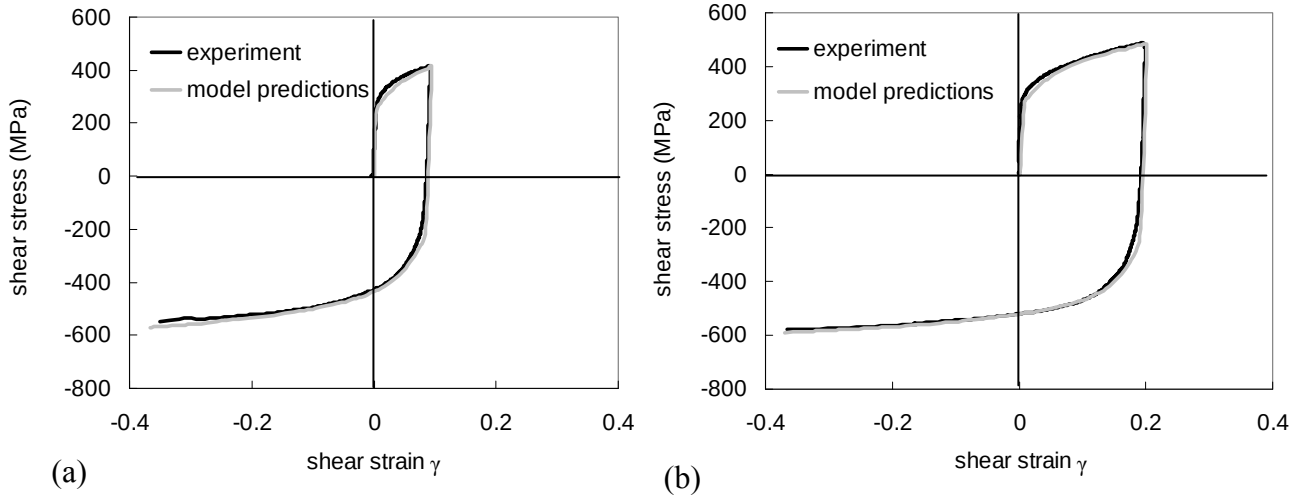

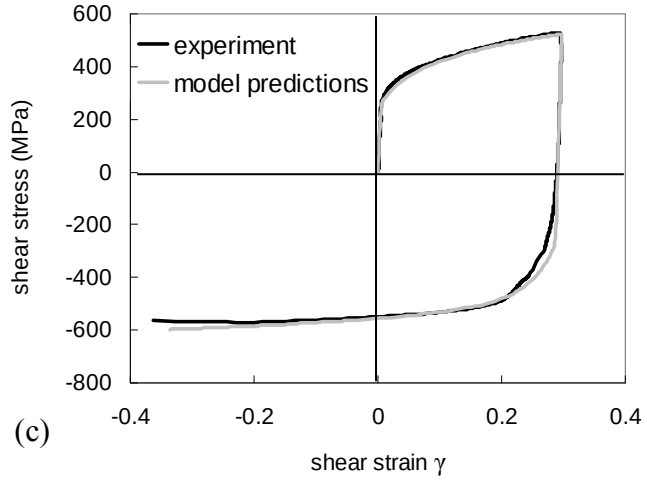

Figure II.2. Experimental vs. predicted curves for Steel 1. Cyclic shear curves (a) $\gamma_{max} = 0.1$, (b) $\gamma_{max} = 0.2$ and (c) $\gamma_{max} = 0.3$.

II.B. Comparison with predictions by other models assuming either Von Mises isotropic yield criterion or isotropic hardening rule

The model presented in section I included both a mixed isotropic and kinematic hardening with an anisotropic yield criterion. In this section, a comparison with other models is carried out. Simulations were first performed assuming a Von Mises yield criterion and a mixed hardening rule. Then, model predictions with a Bron Besson yield criterion and a purely isotropic hardening rule were quantified.

1. Constitutive equations accounting for a mixed hardening and a Von Mises yield criterion

In this part, the model assumes an isotropic Von Mises yield criterion instead of an anisotropic Bron Besson yield criterion and a mixed hardening rule. Figure II.3 and 4 illustrate both the predicted and the experimental curves along the three directions for smooth and notched tensile specimens.

Although the difference is small, experiments are better simulated with the Bron Besson yield criterion than with the Von Mises one and the curves simulated with the Von Mises criterion systematically overestimate stresses compared to predictions from the Bron Besson yield criterion. In fact, 45° direction simulations for tensile test on smooth specimens are not well predicted with the Von Mises yield criterion. The two other directions are closer to the experimental curves. Regarding tensile tests on notched specimens, the rolling direction is the worse predicted with Von Mises yield criterion but this is in agreement with predicted curves given by the Bron Besson yield criterion.

a. Tensile tests on smooth specimens along the three directions

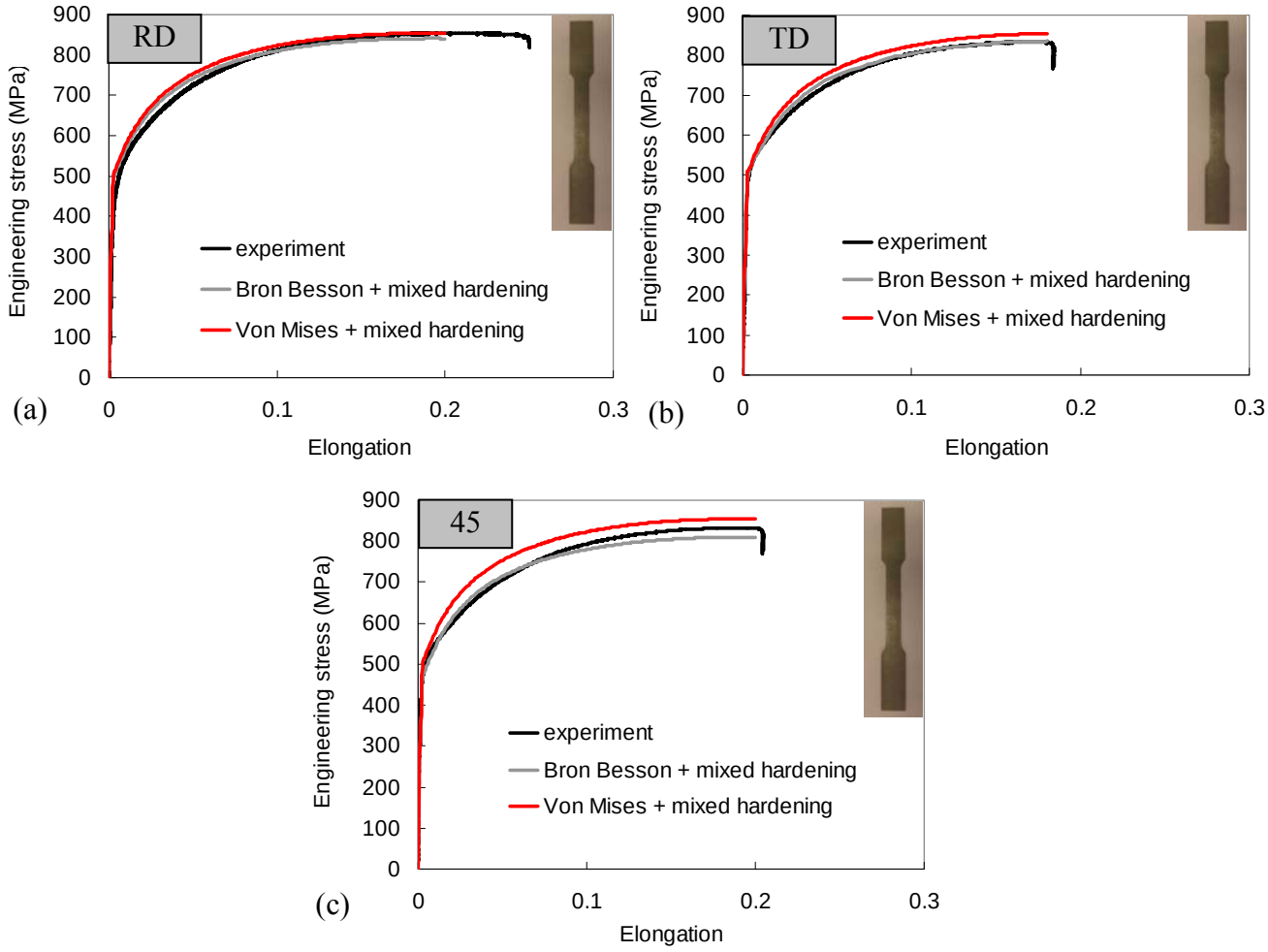

Figure II.3. Experiment vs. model predictions for Steel 1 both with a Von Mises (red curves) and a Bron Besson (grey curves) yield criterion. Mixed isotropic/kinematic hardening rule. Engineering tensile stress-strain curves along (a) rolling, (b) transverse and (c) 45° directions.

b. Tensile tests on notched specimens along the three directions

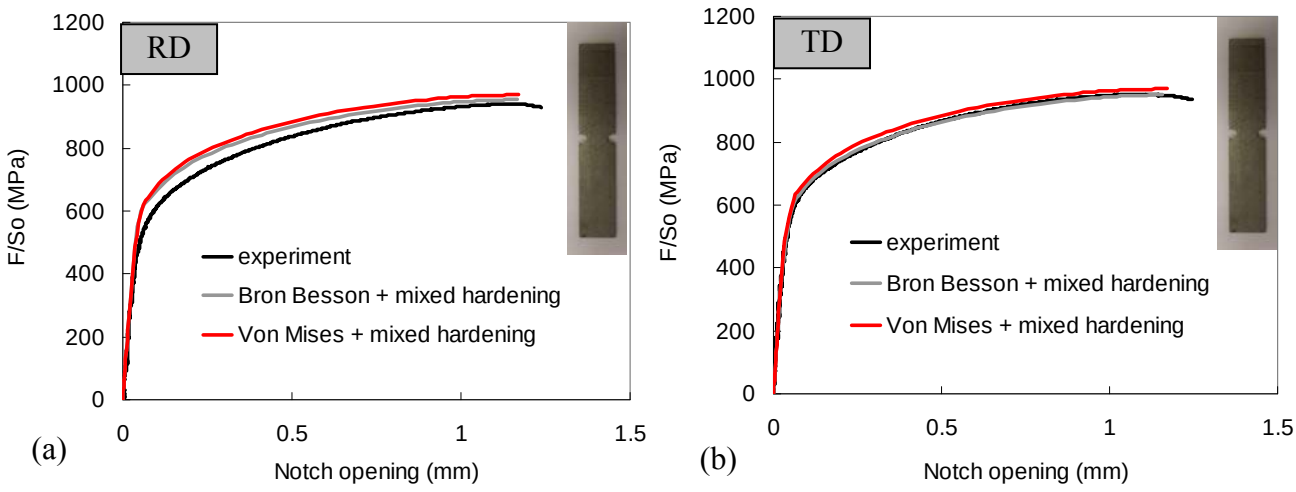

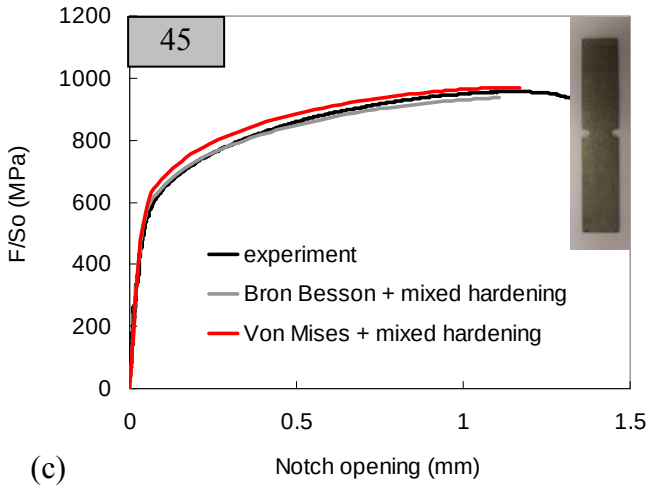

Figure II.4. Experiment vs. model predictions for Steel 1 both with a Von Mises (red curves) and a Bron Besson (grey curves) yield criterion. Mixed isotropic/kinematic hardening rule. Tensile curves on notched specimens along (a) rolling, (b) transverse and (c) 45° directions where F is the load and So is the initial cross section.

c. Cyclic shear tests

In Figure II.5, it is clearly noticed that experiments are better modelled with a Bron Besson yield criterion than with the Von Mises one. Note that during shearing, the Von Mises yield criterion overestimates the stress for the three values of maximum shear strain. For reverse shearing, this phenomenon is also noticed, despite the use of the same mixed isotropic/kinematic hardening rules. In fact, only the yield stress in compression is underestimated, experimental and predicted curves being parallel in the plastic part of the reverse shear curve.

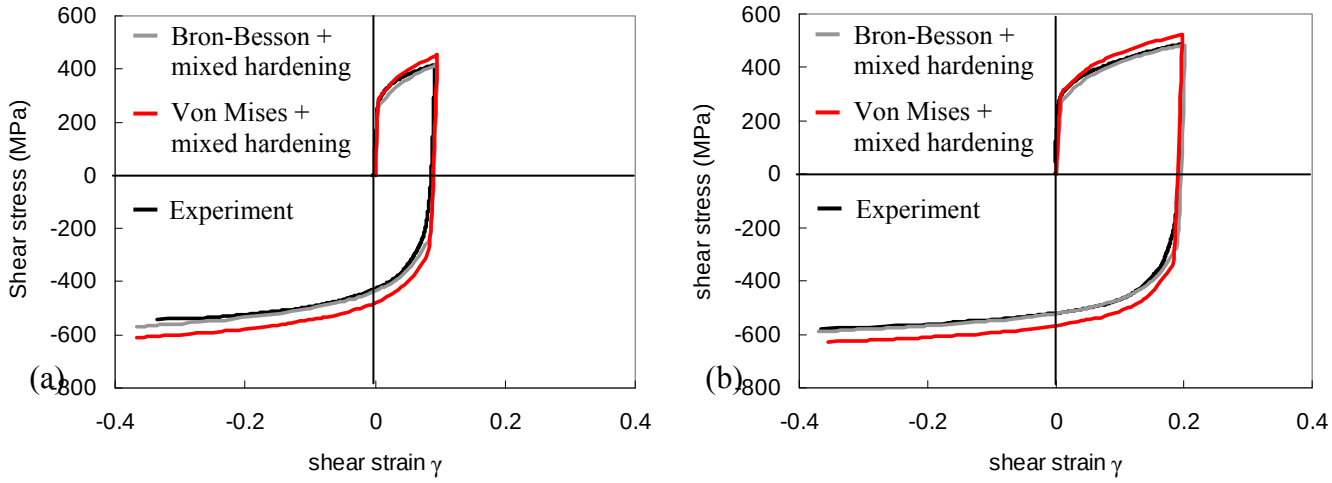

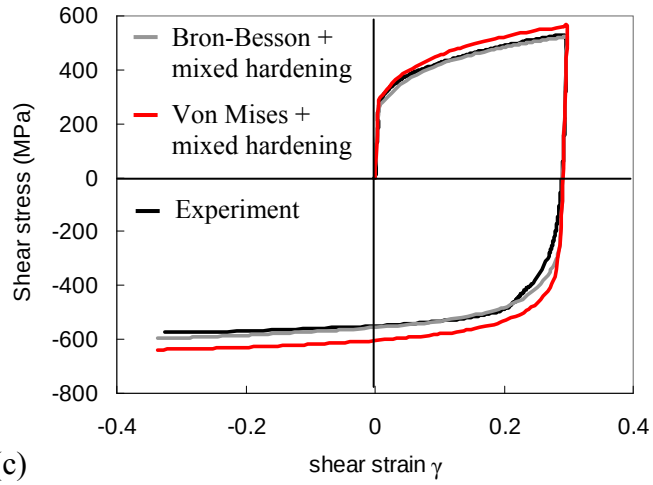

Figure II.5. Experiment vs. model predictions for Steel 1 both with a Von Mises (red curves) and a Bron Besson (grey curves) yield criterion. Mixed isotropic/kinematic hardening rule. Cyclic shearing curves (a) $\gamma_{max} = 0.1$ and (b) $\gamma_{max} = 0.2$ and (c) $\gamma_{max} = 0.3$.

d. Summary: effect of the yield criterion (with mixed hardening rule)

With simulations of tensile tests on both smooth and notched specimens, it is noticed that similar curves are obtained with the Bron Besson or with the Von Mises yield criterion. For the cyclic shear tests, the difference is more significant between the two model predictions. Therefore, it seems clear that the Bron Besson yield criterion is the more appropriated and the more accurate criterion for shear tests. For tensile tests, the choice of the yield criterion is not discriminatory. In section III, model predictions with a Von Mises criterion and a mixed hardening will be given for the air-bending test. However, based on these results, it is expected to not have a real impact on the air bending test simulation.

2. Constitutive equations accounting for a purely isotropic hardening and a Bron-Besson yield criterion

In order to determine the influence accounting for kinematic hardening on the accuracy of model prediction, purely isotropic hardening combined with the Bron Besson yield criterion was used. Note that Bron Besson yield criterion parameters defined in section I are used in this model The isotropic hardening parameters were optimized on the tensile curve on smooth specimen along the transverse direction (Figure II.6b). The new hardening rule equation is described by the following equation:

$$R(p) = R_0' + H' p + Q'\left(1 - \exp\left(-b' p\right)\right) \quad (1)$$

where p is the cumulative plastic strain (calculated with the Bron Besson yield criterion) and with R_0' = 499 MPa, H' = 800MPa, Q' = 393MPa and b' = 23.

With these new constitutive equations, the entire database was modelled. Figure II.6 and 7 illustrate both the model predictions and the experimental curves along the three directions for smooth and notched tensile specimens. It is noticed that both model predictions with either the mixed or purely isotropic hardening rules are similar for all curves except for

smooth and notched specimens along the 45° direction for which the simulation is more accurate with the Bron Besson model.

a. Tensile tests on smooth specimens along the three directions

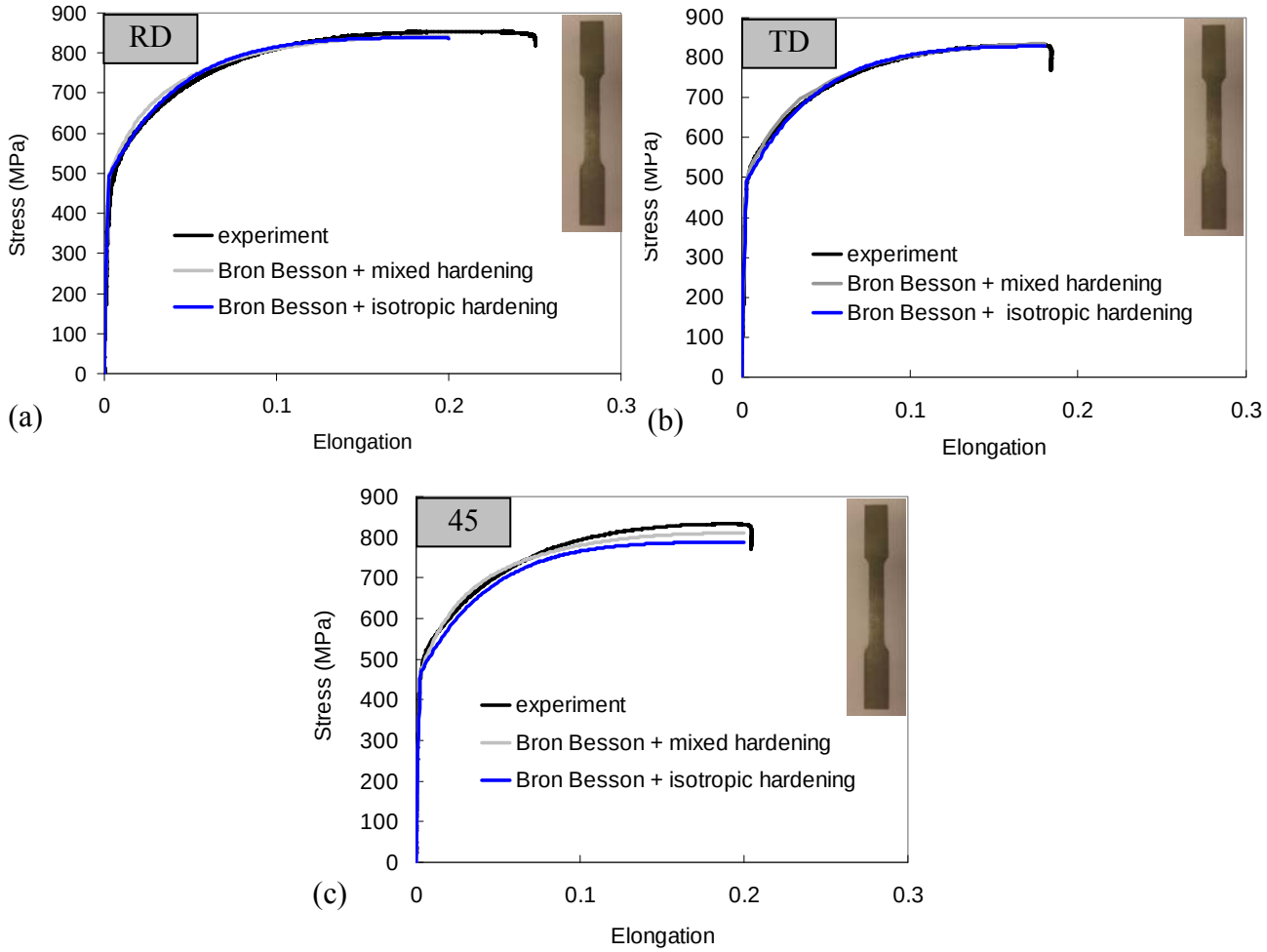

Figure II.6. Experiment vs. model predictions for Steel 1 both with a purely isotropic hardening (blue curves) and a mixed hardening (grey curves). Bron Besson yield criterion (same parameters for both models). Engineering tensile stress-strain curves along (a) rolling, (b) transverse and (c) 45° directions.

b. Tensile tests on notched specimens along the three directions

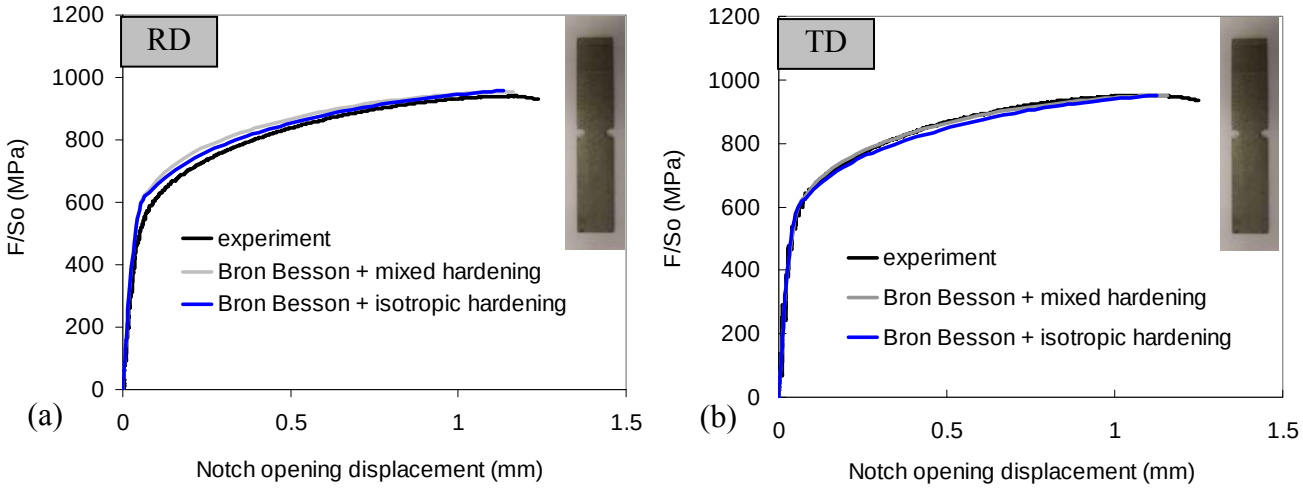

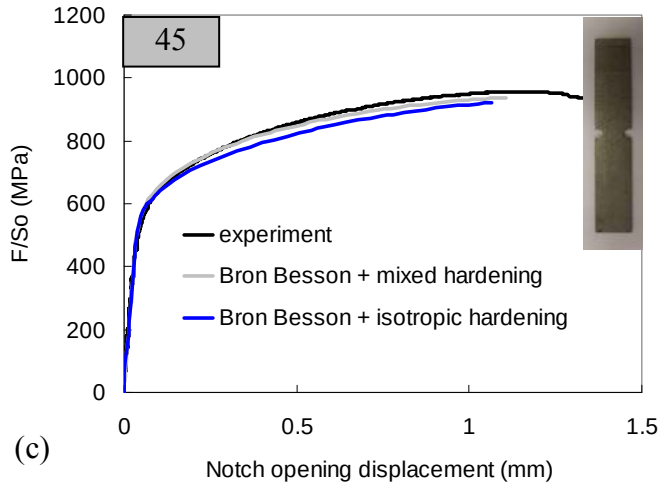

Figure II.7. Experiment vs. model predictions for Steel 1 both with a purely isotropic hardening (blue curves) and a mixed hardening (grey curves). Bron Besson yield criterion (same parameters for both models). Tensile curves on notched specimens along (a) rolling, (b) transverse and (c) 45° directions where F is the load and So is the initial cross section.

c. Cyclic shear tests

Shear tests were also modelled with a purely isotropic hardening law for γ_{max} = 0.1, 0.2 and 0.3. In Figure II.8, it is clearly noticed that experiments are better modelled with a mixed isotropic + kinematic hardening than with purely isotropic hardening. Indeed, for the shearing, simulated blue curves (purely isotropic hardening) underestimate the experiments (black curves). As expected, without kinematic hardening the reverse shearing is poorly represented because the Bauschinger effect is not taken into account.

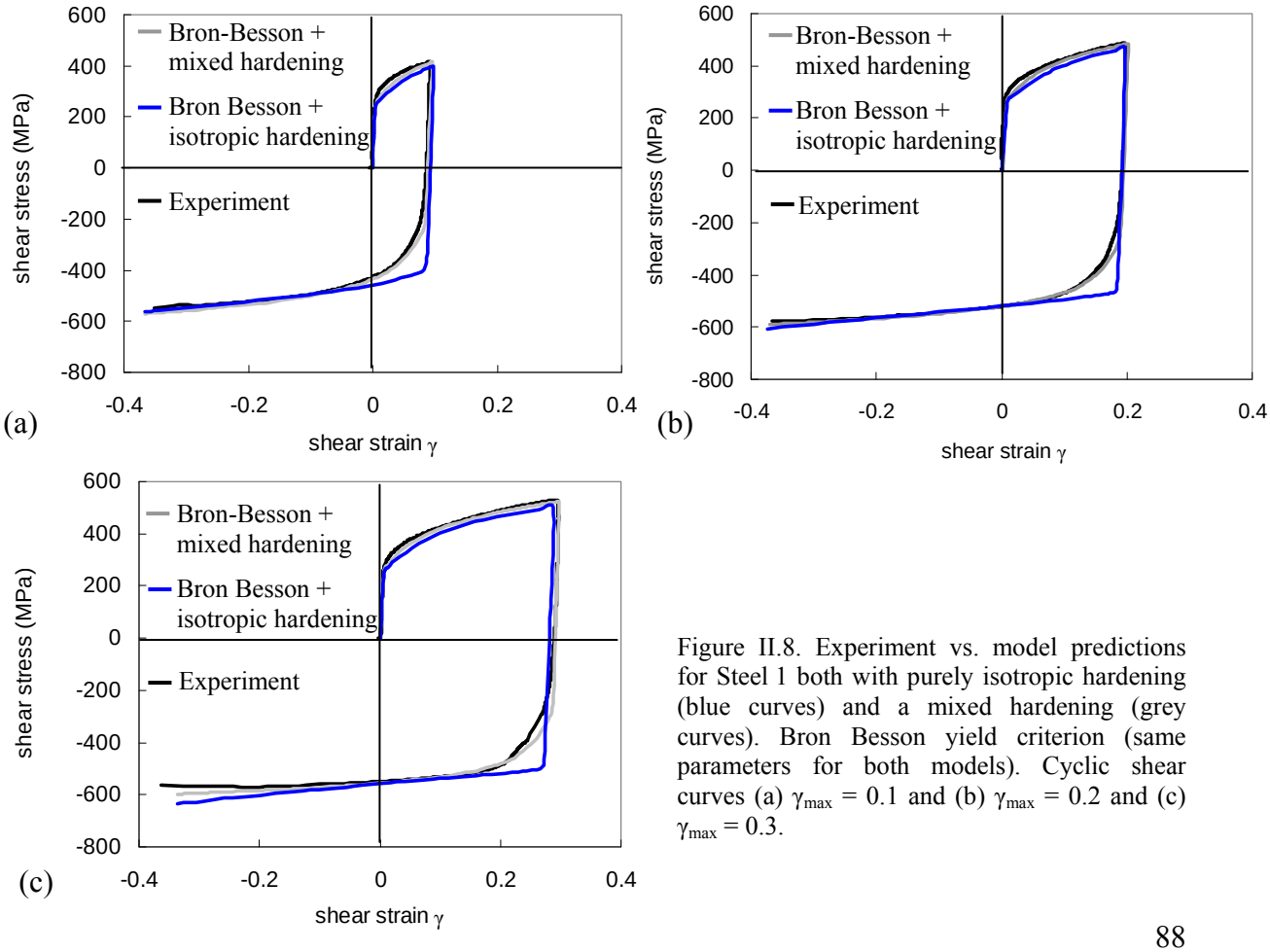

Figure II.8. Experiment vs. model predictions for Steel 1 both with purely isotropic hardening (blue curves) and a mixed hardening (grey curves). Bron Besson yield criterion (same parameters for both models). Cyclic shear curves (a) γ_{max} = 0.1 and (b) γ_{max} = 0.2 and (c) γ_{max} = 0.3.

d. Summary: effect of the hardening rule by using the Bron Besson yield criterion

With simulations of tensile tests both on smooth and notched specimens, it is noticed that similar curves are obtained both with a mixed hardening and with a purely isotropic hardening. Regarding the cyclic shear tests, the difference is well visible between predictions from the two models. As the material shows a Bauschinger effect, these tests cannot be satisfactorily modelled without any kinematic contribution in the hardening rule. Therefore, it seems clear that for these tests on this material, mixed hardening is more appropriate and yields more accurate predictions than purely isotropic hardening rule. The effect of a purely isotropic hardening on the air-bending test has been investigated on section I and will be shown in section III with the model assuming a Von Mises yield criterion.

3. Partial conclusion

In this section, three models were compared (Table 7):

<table>
<tr><td colspan="2" rowspan="2"></td><td colspan="2">Isotropic hardening law</td></tr>
<tr><td>YES</td><td>NO</td></tr>
<tr><td rowspan="2">Yield isotropic criterion</td><td>YES</td><td>/</td><td>Von Mises + mixed hardening:

→ Bauschinger effect is taken into account.
→ Stresses are overestimated.
→ Calculations are rather fast.
→ In air bending test, the load is overestimated (see next section).</td></tr>
<tr><td>NO</td><td>Bron Besson + purely isotropic hardening

→ Tensile tests on notched or smooth specimens are in good agreement with experiments.
→ Bauschinger effect is not taken into account.
→ In air-bending test, the load is overestimated.</td><td>Bron Besson + mixed hardening

→ Tensile tests on notched and smooth specimens are in very good agreement with experiments.
→ Bauschinger effect is taken into account.
→ Air-bending test prediction is in very good agreement with experimental curve.</td></tr>
</table>

Table 7. Comparison of the three models.

Based on these results, it seems clear that a yield anisotropic criterion with mixed isotropic/kinematic hardening rules have to be taken into account to well predict the whole experimental database. In addition, to predict air-bending tests with accuracy, this model is also required.

III. Influence of simulation conditions of the air-bending test

In this section, it is intended to study the influence of the mesh as well as the air-bending test boundary conditions. In addition, the choice of the model for air-bending test predictions is discussed at the end of this part.

III.A. Influence of meshing conditions

In order to determine the influence of the mesh, four calculations were performed with various numbers of elements across the thickness close to the punch. The refined mesh in the vicinity of the punch was chosen to be equal to 2mm. The size of the smallest element along the transverse direction is constant and equal to 25µm for the four meshes. The four cases studied were:

(i) 8 elements across the sheet thickness (i.e. 200µm elements size)
(ii) 16 elements across the sheet thickness (i.e. 100µm elements size)
(iii) 32 elements across the sheet thickness (i.e. 50µm elements size)
(iv) 64 elements across the sheet thickness (i.e. 25µm elements size)

In agreement with section I, this parametric study is carried out in 2D (plane strain assumption), with the Bron Besson yield criterion and mixed isotropic/kinematic hardening rules. In addition, calculations were carried out with the punch and a friction coefficient of 0.25. The corresponding meshes are illustrated in Figure II.9.

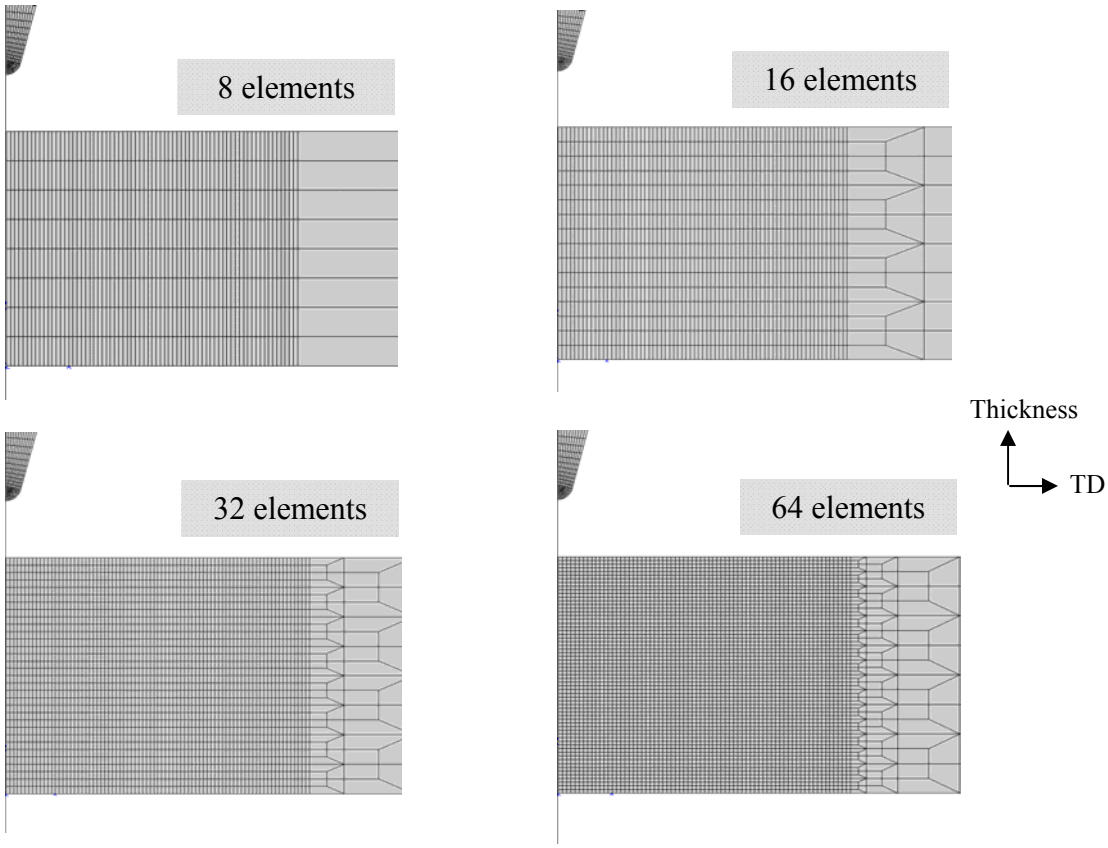

Figure II.9. Four meshes with various numbers of elements across the thickness. Total thickness = 1.6mm.

Figure II.10a illustrates load / displacement curves for four meshing (8 to 64 elements in the thickness). Similar curves are obtained for the four simulations, meaning that the number of elements across the thickness do not change the global response of the load / displacement curve. Hoop stress and hoop strain distributions across the thickness at the end of the test are illustrated in Figure II.10b. Strain and stress fields maps calculated using each of the four meshes are respectively given in Figure II.11 and Figure II.12.

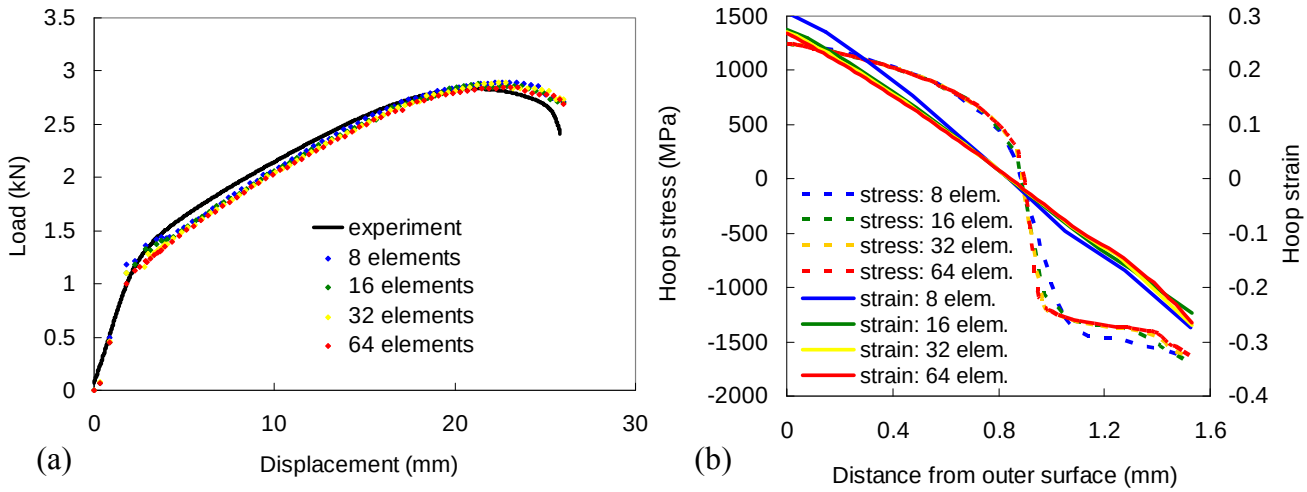

Figure II.10. (a) Influence of the mesh on the load / displacement curves. Calculations with the Bron Besson yield criterion, mixed isotropic/kinematic hardening rules. (b) Influence of the mesh on the hoop stress and hoop strain distributions across the thickness at the end of the test (i.e. for a punch displacement of 26mm).

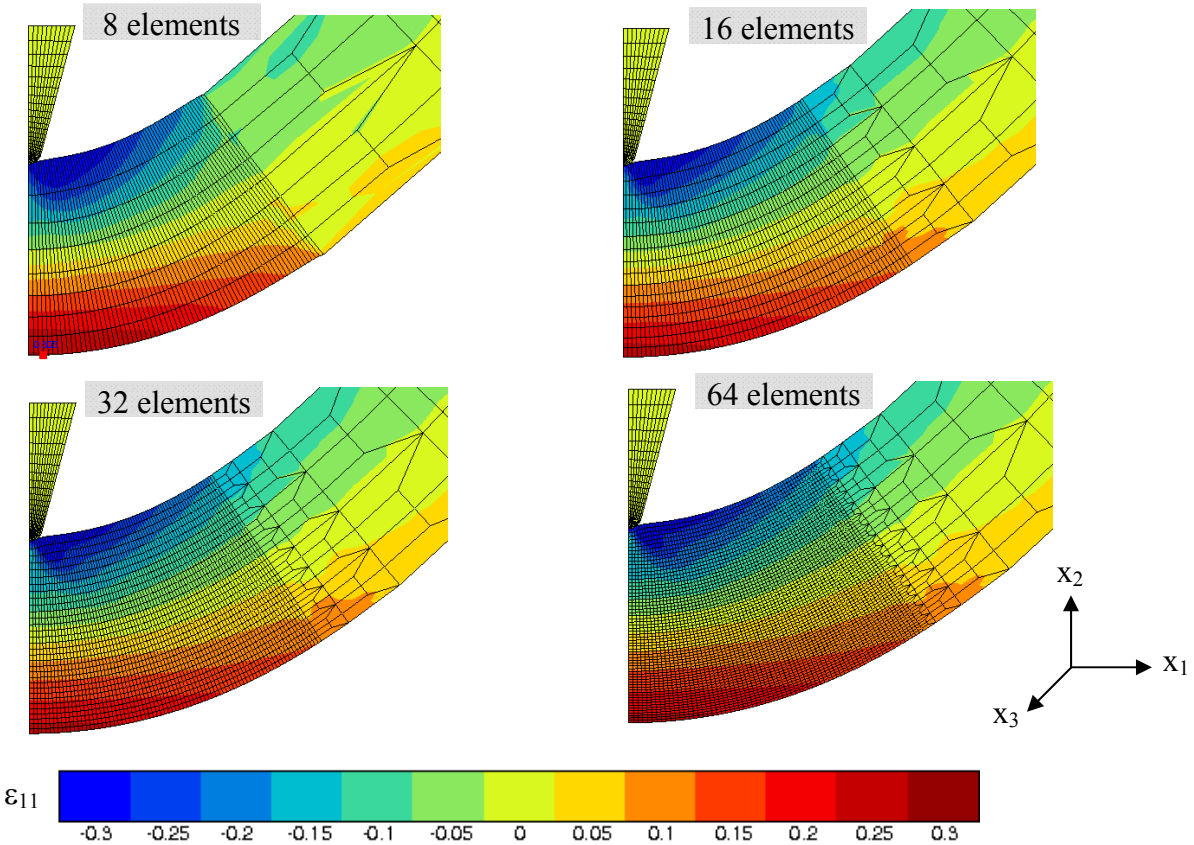

Figure II.11. Strain field after bending of Steel 1. ε_{11} map for the four simulations (8 to 64 elements across the thickness) taken at the end of the test (i.e. for a punch displacement of 26mm).

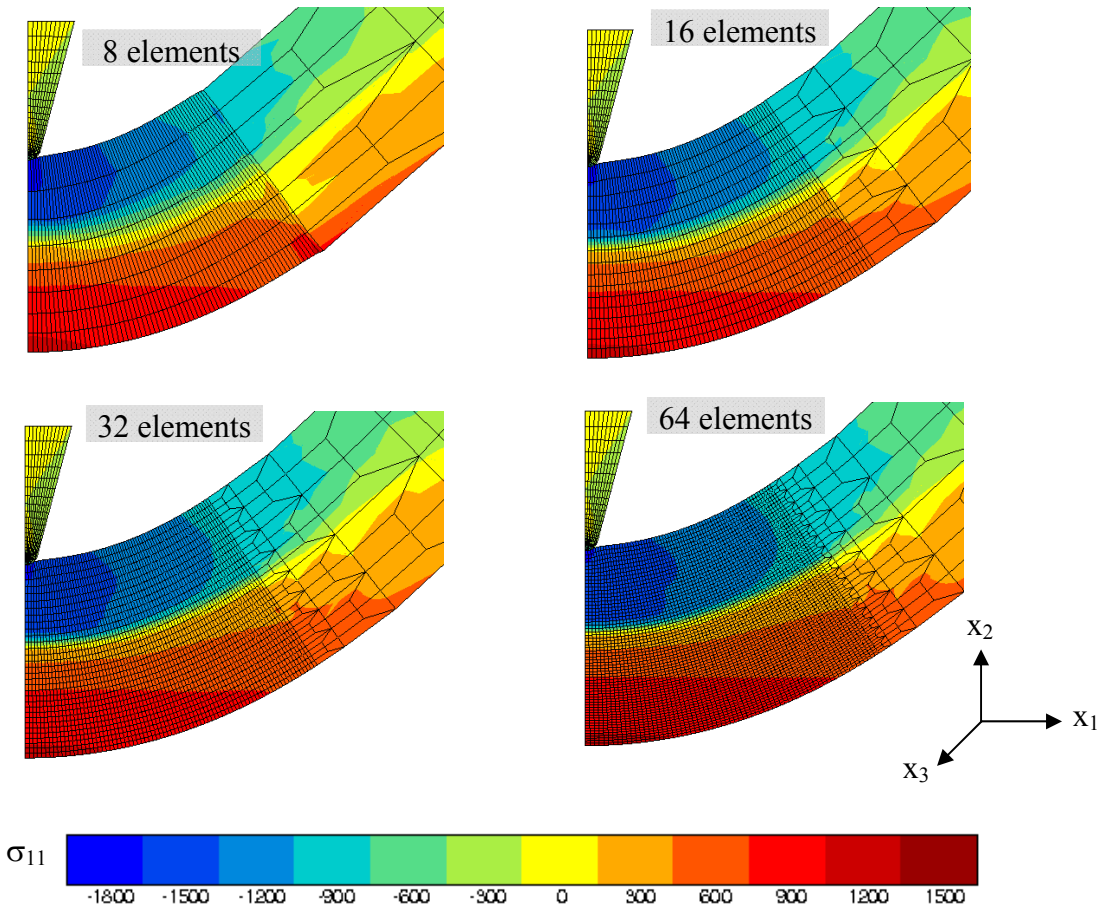

Figure II.12. Stress field after bending of Steel 1. σ_{11} map for the four simulations (8 to 64 elements across the thickness) taken at the end of the test (i.e. for a punch displacement of 26mm).

Regarding stress and strain fields as a function of the local meshing size, it seems clear that with 8 elements in the thickness, the stress and strain gradients are not well represented. With 16 elements across the thickness, the accuracy is rather good. In addition, it is reasonable to say that with 32 or 64 elements across the thickness, the stress and strain distributions are very close. Thus, calculations could be performed with 16 or 32 elements across the thickness to keep a good compromise between a good accuracy and a limited elements number. Nevertheless, in Chapter IV, it is intended to include damage in the model to simulate air-bending test. Therefore, it was decided to perform all simulations with 32 elements across the thickness to get a better accuracy.

III.B. Influence of the boundary conditions

1. Influence of the friction coefficient

As mentioned in section I, air-bending tests were carried out without lubrication. Thus, a high friction coefficient was first assumed ($\mu = 0.25$). As the actual friction coefficient between the sheet and the punch was not known, a lower value ($\mu = 0.1$) was also tested. Note that same conditions were kept (i.e. 32 elements across the thickness and Bron Besson yield criterion with mixed hardening rules). The corresponding curves are

illustrated in Figure II.13a and b. The load / displacement simulated curves (Figure II.13a) are similar, meaning that the friction coefficient between the sheet and the punch has no influence in this configuration. Same results are obtained regarding the evolution of the hoop stress and hoop strain (Figure II.13b) where no difference between μ=0.25 and μ=0.1 were noticed. Note that with a higher punch radius, the friction coefficient may have an influence.

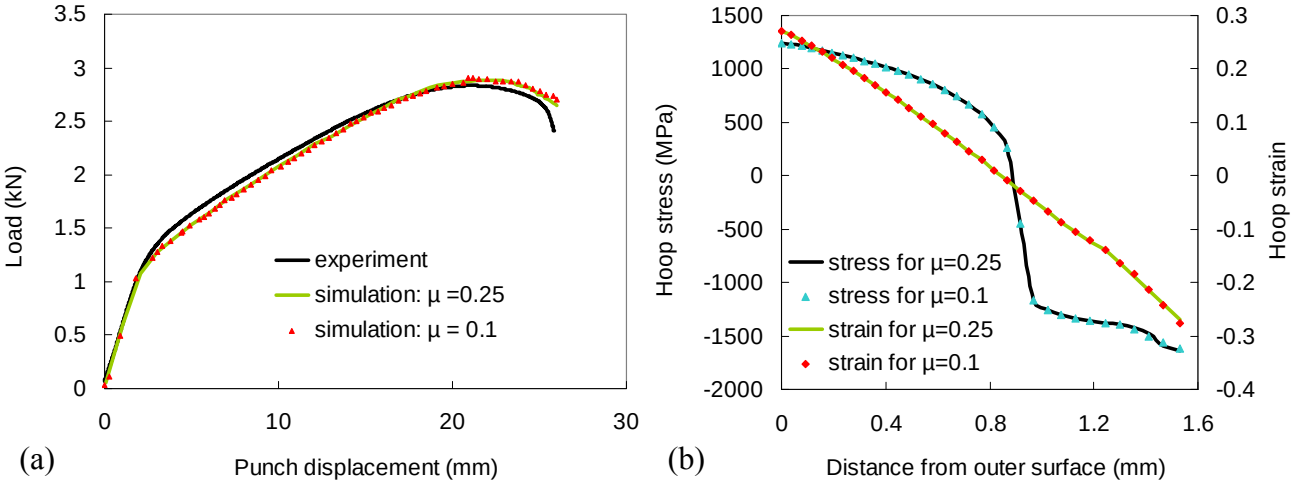

Figure II.13. Influence of the friction coefficient on the air-bending test with μ = 0.25 and μ = 0.1 (a) experimental and predicted load / displacement curves, (b) hoop stress and hoop strain distributions for both friction coefficients at the end of the test (i.e. a punch displacement of 26mm).

This result was expecting regarding more precisely the contact between the sheet and the punch (Figure II.14). Indeed, due to its tight shape, the punch is in contact with only four nodes, that is why the friction coefficient has no influence in this case.

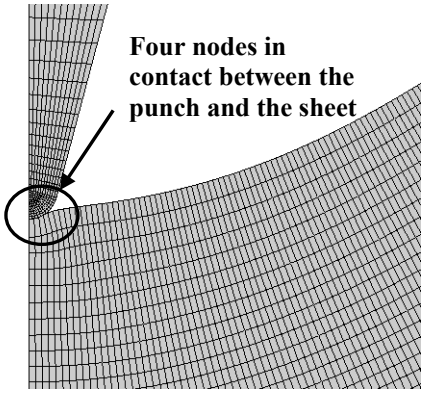

Figure II.14. Zoom on the contact between the sheet and the punch. Only four nodes of the sheet are in contact with the tool.

2. Influence of the punch

Based on previous observations, simulation was also conducted by replacing the punch with prescribed displacement of the nodes located just under the punch (Figure II.14). Here also, calculations were carried out in 2D with 32 elements across the thickness and with a

Bron Besson yield criterion and mixed hardening rules. The corresponding curves are shown in Figure II.15a and b. Regarding the load / displacement curves (Figure II.15a), a similar behaviour is noticed with simulations with or without the punch. Figure II.15b illustrates same results because hoop stress and hoop strain have similar distributions across the sheet thickness with or without the punch. These conclusions are only valid because the punch radius is very small (R = 0.1mm) i.e. because the contact area between the punch and the sheet is very small: the inner radius of the sheet after the end of the bending (2.05mm) is much higher than the punch radius itself. This is due to both the punch geometry, the sheet thickness and the constitutive behaviour of the sheet material. In case of a larger punch or of much thinner sheet (such as thickness-reduced Steel 2), the punch could not be replaced by prescribed nodes displacement.

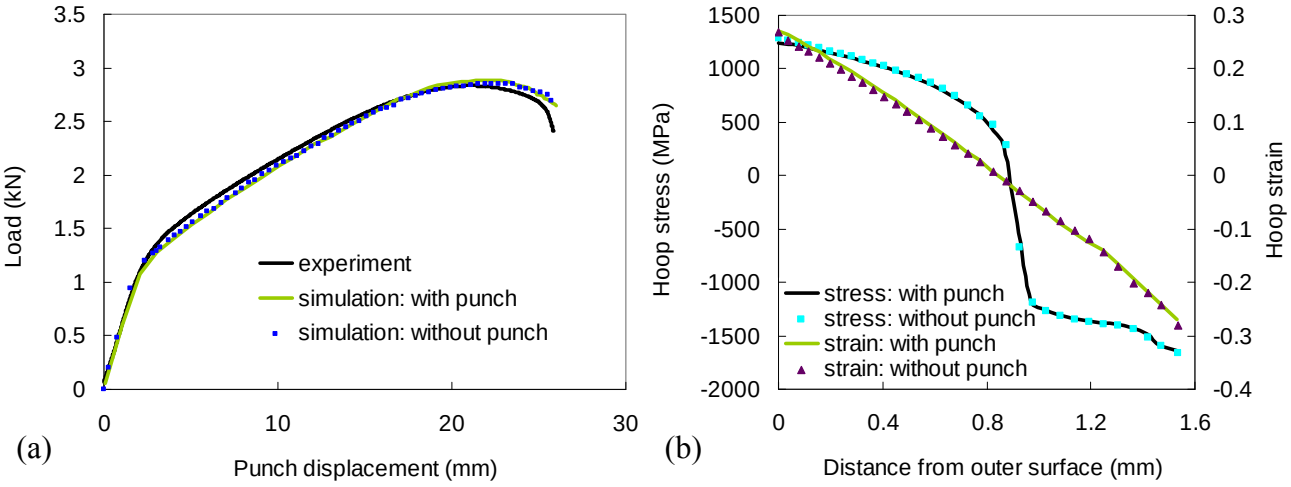

Figure II.15. Influence of the punch on the air-bending test. (a) experimental and predicted load / displacement curves with and without the punch, (b) hoop stress and hoop strain distributions across the thickness both with and without the punch at the end of the test (i.e. a punch displacement of 26mm).

III.C. Influence of the constitutive equations on the model predictions for the air-bending test

In section I, air-bending tests on Steel 1 were carried out in 2D with 32 elements across the thickness and with a Bron Besson yield criterion associated with mixed isotropic/kinematic hardening rules. In this part, it is intended to compare these results with the ones found with (i) an isotropic yield Von Mises criterion and (ii) a purely isotropic hardening rule. All these calculations were also performed assuming plane strain hypothesis (2D) with 32 elements across the thickness.

The air-bending test was first modelled assuming a Von Mises yield criterion instead of a Bron Besson anisotropic criterion (Figure II.16). Then, the mixed hardening law was replaced by a purely isotropic one (Figure II.17). As observed in part II.B.1, the Von Mises yield criterion overestimates the load and is less accurate than the modelling with the Bron Besson one (Figure II.16a). Regarding the hoop stress and strain distributions (Figure II.16b), the yield criterion has no influence except for the points located close to the inner surface. Indeed, hoop stress and hoop strain have lower values with the Von Mises yield criterion in the compressive part than with the Bron Besson yield criterion.

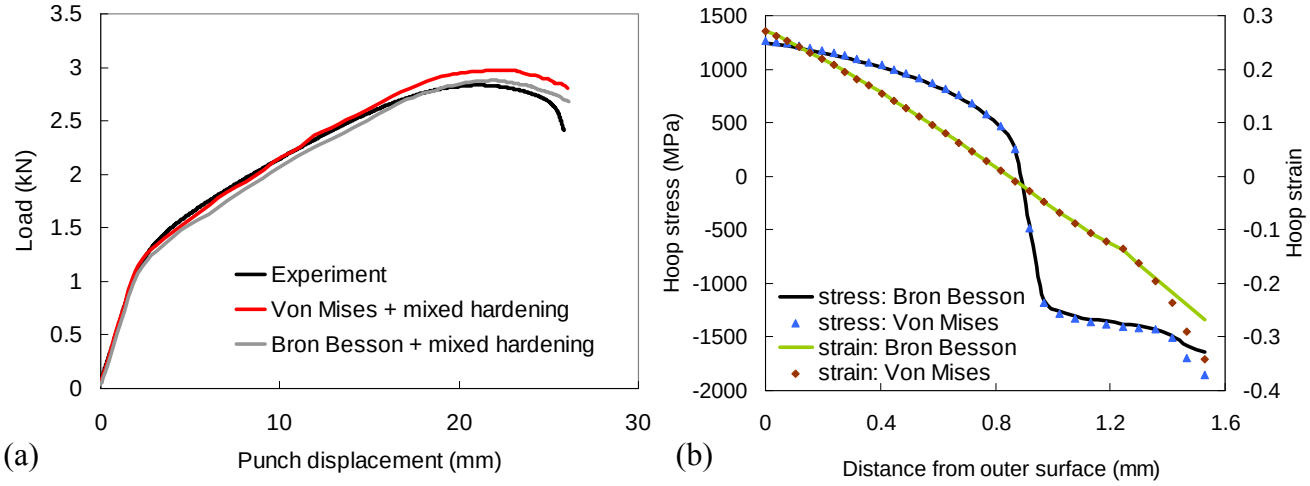

Figure II.16. (a) Load / displacement curves for the air-bending test. Black, grey and red curves respectively correspond to experiment, model predictions with a mixed hardening law and a Bron Besson yield criterion (as in section I) and model predictions with a mixed hardening law and a Von Mises yield criterion. (b) Hoop stress and hoop strain distributions across the thickness both with a Bron Besson and a Von Mises yield criterions at the end of test (i.e. a punch displacement of 26mm).

Figure II.17a showed that similar load / displacement curves are obtained until a displacement of about 10mm with both a mixed and a purely isotropic hardening rule. After this displacement, the load is also overestimated with the isotropic hardening rule compared to the mixed hardening one. Regarding the hoop stress and strain distributions (Figure II.17b), the hardening rule has no influence except for the points located close to the inner surface. Indeed, hoop stress and hoop strain have lower values with the purely isotropic hardening rule in the compressive area than with the mixed hardening rule.

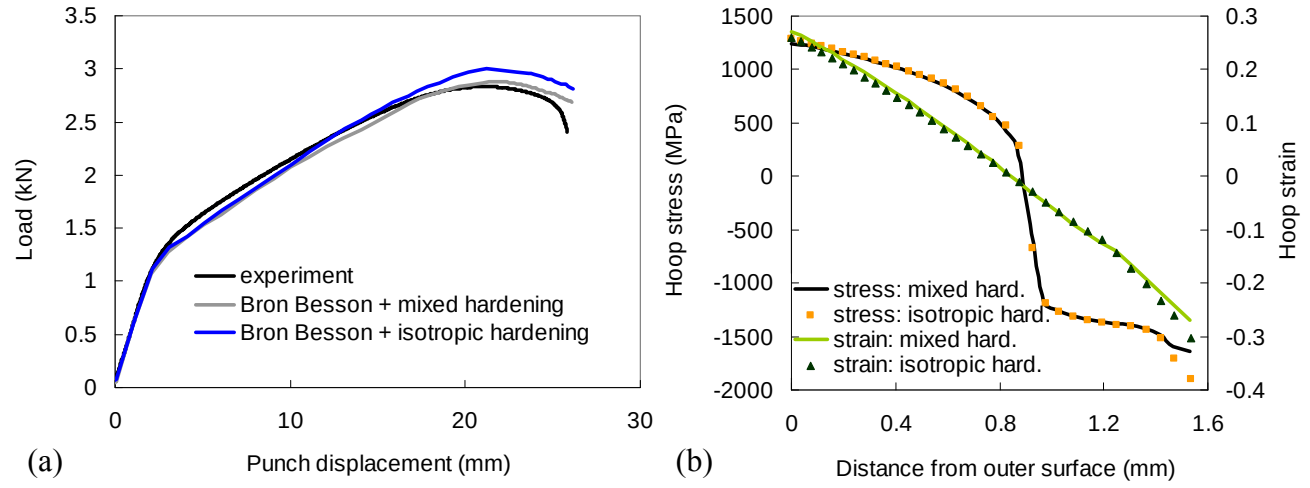

Figure II.17. (a) Load / displacement curves for the air-bending test. Black, grey and blue curves respectively correspond to experiment, model predictions with a mixed hardening law and a Bron Besson yield criterion (as in section I) and model predictions with an isotropic hardening law and a Bron Besson yield criterion. (b) Hoop stress and hoop strain distributions across the thickness both with a mixed hardening rule and a purely isotropic hardening rule at the end of the test (i.e. a punch displacement of 26mm).

III.D. Summary: influence of modelling conditions on air-bending test predictions

In this part, the influence of the air-bending modelling conditions was discussed. It was shown that the mesh has no influence on the global force / displacement curves but has an impact on the stress and strain fields. Therefore to get the best compromise between the accuracy of predictions and the number of elements, it was chosen to perform all air-bending simulations with 32 elements across the thickness. Then, the influence of the friction coefficient was considered. Regarding previous results, it was demonstrated that in this case, the friction coefficient between the punch and the sheet has no influence. This is in agreement with the fact that similar results were obtained with or without the punch. Finally, the choice of the constitutive equations was discussed. A Von Mises yield criterion combined with a mixed hardening rule as well as a Bron Besson yield criterion associated with a purely isotropic hardening rule were used to simulate the air-bending test. In terms of load / displacement curves, both results overestimate the experimental curve (especially at the end of the test). More accurate results were obtained with the association of a mixed kinematic + isotropic hardening and a Bron Besson yield criterion. Regarding the stress and strain distributions, similar results were obtained except for the nodes close to the inner surface which had lower values. A summary of all these results is given in Table 8.

	Load /displacement curve	**Hoop stress and hoop strain**
Meshing influence → 8 elements → 16 elements → 32 elements → 64 elements across the thickness	No influence	Slight influence → 8 elements: not enough accuracy → 16 elements: correct accuracy → 64 elements: too many elements → 32 elements is the best compromise between the accuracy and the number of elements and this number will be used in the following chapter when damage will be taken into account.
Friction coefficient → $\mu = 0.25$ → $\mu = 0.1$	No influence	No influence
Effect of the punch → with the punch → with prescribed nodes displacement	No influence	No influence
2D / 3D calculations	No influence	No influence
Yield criterion → Von Mises → Bron Besson	Better predictions with the Bron Besson yield criterion	Slight influence for nodes close to the inner surface both for hoop stress and hoop strain
Hardening rule → Purely isotropic → Mixed	Better predictions with the mixed isotropic / kinematic hardening	Slight influence for nodes close to the inner surface both for hoop stress and hoop strain

Table 8. Summary of the influence of air-bending modelling conditions on the load / displacement curve and the hoop stress and hoop strain distribution across the thickness.

IV. Summary of Chapter 2

In this chapter, a comprehensive experimental database including tensile tests on smooth and notched specimens and shear tests was established. All these experiments enable to determine the constitutive equations of Steel 1. The "reference" model chosen here account for anisotropic elasto-plastic behaviour (Bron Besson yield criterion) with a mixed kinematic + isotropic hardening rule. The possibility of using simplifying assumptions in the model (such as an isotropic Von Mises yield criterion or a purely isotropic hardening rule) was also discussed.

It was demonstrated that with a Von Mises yield criterion and a mixed hardening rule, the load is always overestimated and the reverse shear tests were not well simulated. With a Bron Besson yield criterion and a purely isotropic hardening rule, similar results were obtained than with a mixed hardening law except for the cyclic shear tests. As expected, without kinematic contribution in the hardening rule, the Bauschinger effect is not taken into account and thus shear tests are poorly modelled, whereas satisfactory agreement was obtained by using the "reference" model.

Using these "reference" constitutive equations allowed modelling the air-bending test. The simulation of this test showed that for the punch geometry, sheet thickness and sheet material considered here (Steel 1), the friction coefficient between the sheet and the punch has no influence. In addition, when using a very sharp punch (R=0.1mm in this study), the punch can be replaced by prescribing the displacement of the nodes located just below the punch. The meshing has no influence on the load / displacement curve but has one on the stress and strain distributions through the thickness. The final meshing chosen for the rest of the work has 32 elements in the thickness. In addition, it is interesting to underline that this modelling can be carried out in plane strain conditions. For thickness-reduced Steel 2, same conditions are used, i.e. 32 elements across the thickness, plane strain calculations and Bron Besson yield criterion associated with a mixed isotropic/kinematic hardening rule. However, in this case, the punch was not replaced by prescribed nodes displacement.

Regarding the role of the yield criterion, simulations of the air-bending tests with a Von Mises or with a Bron Besson criterion were carried out and simulation assuming a Bron Besson yield criterion fitted better with the experiment than the modelling with a Von Mises criterion. By using a Bron Besson yield criterion, a slight difference in load / displacement curves with mixed and purely isotropic hardening rules was noticed. Better predictions were obtained with a mixed hardening rule. The kinematic contribution was also discussed by studying its influence on a prestrained and bent specimen. In this case, it seems clear that when prestraining is performed before a air-bending test, a kinematic contribution is needed to satisfactorily predict the load/displacement curve during the bending.

Numerical simulation of the air-bending tests using the "reference" model revealed that the thickness of the sheet decreases inhomogeneously and this leads to a shift of the neutral fibre from the mid-thickness towards the compressive area. In addition, material points close to the mid-thickness undergo initial compression followed by tension suggesting that kinematic hardening is necessary to predict the strain path in the vicinity of the mid-thickness especially for very severe bending such as that of thickness-reduced Steel 2 until 180°.

Résumé du Chapitre 2

Dans ce chapitre, une base de données expérimentale détaillée a été établie incluant des tests de traction sur éprouvettes lisses et entaillées ainsi que des tests de cisaillement. Ces essais ont permis de déterminer la loi de comportement de l'acier 1. Le modèle de "référence" établi précédemment inclut un comportement élasto-plastique anisotrope (critère d'écoulement de Bron Besson) et un écrouissage mixte isotrope + cinématique. La possibilité d'utiliser des modèles plus simples tels qu'un modèle d'écoulement isotrope de Von Mises ou un écrouissage purement isotrope a également été envisagée.

Avec un critère de Von Mises et un écrouissage mixte, les efforts sont souvent surestimés. Avec le critère anisotrope de Bron Besson et un écrouissage purement isotrope, nous avons obtenu des résultats similaires à ceux obtenus avec un écrouissage mixte excepté pour les essais de cisaillement qui étaient mal prédits. Sans écrouissage cinématique, l'effet Bauschinger n'est pas pris en compte, et cela entraîne une mauvaise prédiction des essais de cisaillement alors qu'ils étaient correctement simulés avec le modèle de "référence".

Cette loi de comportement a permis de modéliser l'essai de pliage en V. La simulation numérique de ce test a montré que pour cette géométrie de poinçon, cette épaisseur de tôle et l'acier de l'étude (acier 1), le coefficient de frottement entre la tôle et le poinçon n'a pas d'influence. Lorsqu'un poinçon avec un rayon très fin est utilisé (R = 0.1mm dans cette étude), ce dernier peut être remplacé par le déplacement imposé des nœuds situés sous le poinçon. Le maillage n'a aucune influence sur les courbes force/déplacement mais en a une sur la distribution des contraintes et des déformations à travers l'épaisseur. Le maillage choisi pour toute l'étude a 32 éléments à travers l'épaisseur et les simulations numériques du pliage en V peuvent être effectuées en déformation plane. Pour l'acier 2 rectifié en épaisseur, les mêmes conditions que précédemment ont été appliquées, à savoir, 32 éléments dans l'épaisseur, l'hypothèse d'un calcul en déformation plane, un critère d'écoulement de Bron Besson et un écrouissage mixte. Néanmoins, dans ce cas là, le poinçon n'a pas été remplacé par le déplacement imposé des nœuds sous le poinçon.

La modélisation du pliage en V a été réalisée à la fois avec un critère d'écoulement de Von Mises, ainsi qu'avec Bron Besson. La simulation numérique utilisant le critère anisotrope de Bron Besson a donné des résultats plus proches de l'expérience que celle avec le critère de Von Mises. Utilisant un critère d'écoulement anisotrope de Bron Besson, nous avons montré que les courbes force/déplacement étaient mieux prédites avec un écrouissage mixte plutôt qu'avec un écrouissage purement isotrope. La contribution de l'écrouissage cinématique a été discutée en étudiant son influence sur un échantillon plié préalablement prédéformé en traction. Nous avons démontré que lorsqu'une prédéformation est appliquée avant un test de pliage, il est nécessaire de prendre en compte l'écrouissage cinématique pour prédire de manière satisfaisante le pliage.

La simulation numérique du pliage en V avec le modèle de "référence" a révélé que l'épaisseur de l'acier diminuait de manière inhomogène et cela entraînait un déplacement de la fibre neutre depuis la mi-épaisseur vers la zone en compression. De plus, nous avons montré que les points situés dans le voisinage de la mi-épaisseur subissaient d'abord une compression puis une tension, suggérant la nécessité d'inclure l'écrouissage cinématique dans le modèle pour prédire de manière précise le trajet de chargement des points proches de la mi-épaisseur.

Chapter 3

Investigation of damage mechanisms

In previous parts, it was shown that the microstructure has a key role in the bendability of steels. Hence, it is now necessary to precisely investigate damage mechanisms involved both in air-bending and in stretch bending tests.
In a first part, damage was characterized using scanning electron microscope and light microscope on air-bent, stretch bent and tensile specimens. Fractographic observations showed that fracture modes are ductile both in air and stretch bending tests. In addition, the influence of both central segregation and banded structures were investigated for the two bending tests.
Finally, in a second part, the role of the segregated bands depending on their locations through the thickness was investigated.

Table of contents

In this chapter, damage mechanisms are investigated for the four TRIP-aided steels under study. In stretch bending, first experiments were carried out with an hydraulic press. Then, in order to be able to interrupt the test just before fracture, a new device was designed enabling to perform tests with a lower displacement rate.
In order to investigate damage mechanisms in air-bending in more detail, Steel 1 and thickness-reduced Steel 2 were chosen (section 2). The first objective of these complementary investigations is to evidence the influence of the location of hard bands on bendability. A quantitative relationship between damage, band thickness and local strain is proposed at the end of this section.
Finally, in the second part of section 2, complementary observations of thickness-reduced Steel 2 are given.

I. Experimental characterization of damage mechanisms

I.A. Fractographic observations after air and stretch bending tests

In order to determine fracture modes of air-bending and stretch bending specimens, fractographic observations were carried out using scanning electron microscopy.
As air-bending specimens are not fully broken, it was very difficult to observe their fracture surfaces (Figure III.1). Nevertheless, dimples can be observed in some areas of the main microcrack (Figure III.2).

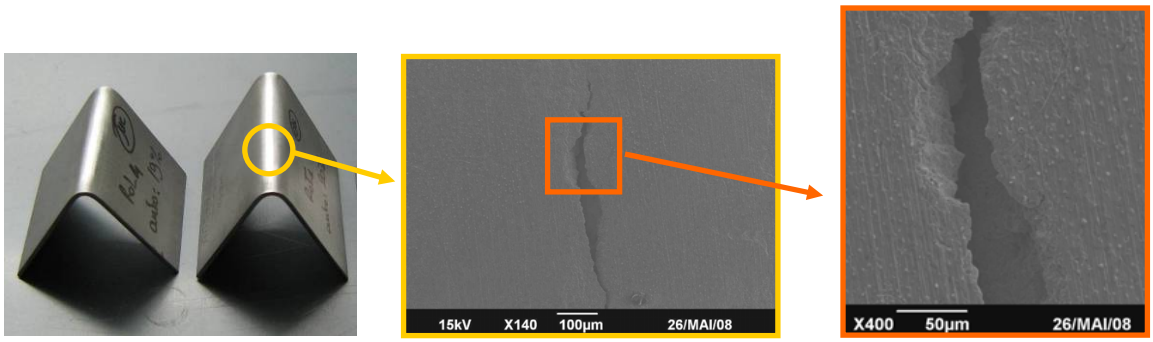

Figure III.1. Crack observed by SEM on Steel 1 after air-bending.

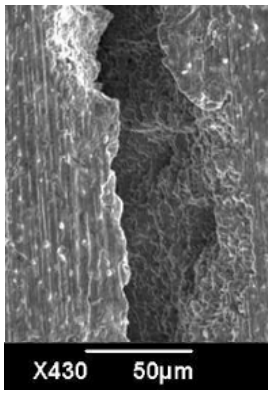

Figure III.2. Ductile failure of Steel 1 after air-bending.

In order to confirm the fracture mode, additional tests were carried out to open cracks initiated during air-bending. After performing air-bending test on Steel 1 specimens until

cracking (classifications will be given in section 2), the partially cracked specimens were then heat treated in a furnace at 300°C in air during 1 hour in order to oxidize the fracture surface induced by air-bending. The specimens were then dipped into liquid nitrogen during a few minutes and then quickly fractured in order to break them in a brittle manner and therefore to easily distinguish the initial microcrack from final (cleavage) fracture (Figure III.3). Figure III.4a shows the initial air-bending crack (in light grey) as well as the final fracture surface (in dark grey). The difference between the ductile fracture surface (due to air-bending) and the brittle fracture surface (cleavage after cooling) is clearly observed (Figure III.4b).

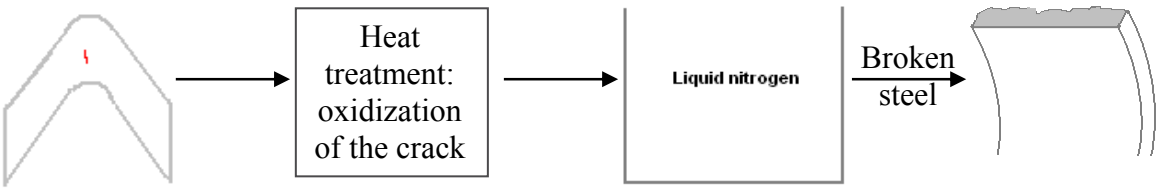

Figure III.3. Steps to mark the crack by oxidization.

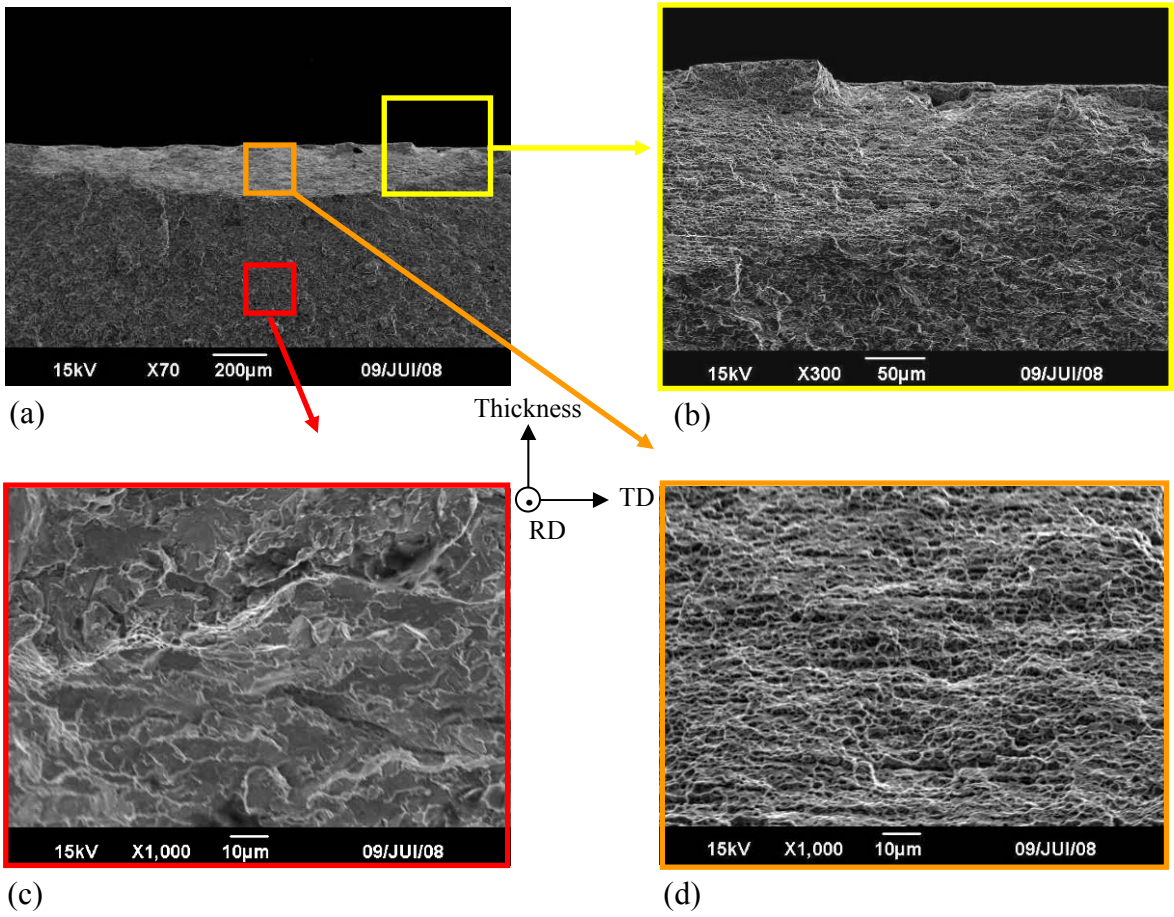

Figure III.4. SEM observations of a crack along RD (Steel 1), (a) general view of the crack induced by air-bending, (b) transition between the two cracks, (c) brittle cleavage fracture at low temperature, (d) ductile fracture with dimples occurred during air-bending.

In the particular case of Figure III.4, the crack due to bending has a width of about 1.6mm and a maximum depth of 200µm. Note that the crack has a smooth propagation front through the sheet thickness.
In order to check whether the fracture is also ductile during stretch bending tests, fractographic observations were carried out on Steel 1, Steel 3 and Steel 4. As fracture is unstable in the stretch bending tests, no particular sample preparation was carried out, the specimens being completely broken into two parts after the stretch bending tests. For the three steels, dimples were also observed, confirming the ductile nature of the fracture mechanism with this forming mode (Figure III.5, Figure III.6).

It is important to underline that the mid-thickness is readily observable in the fracture surfaces. In Figure III.5, two planes, which together form a V-shape, are distinguished. In Figure III.6, lines oriented along the rolling direction are noticed at mid-thickness, this could correspond to segregated bands or elongated inclusions. Thus, under stretch bending, the role of segregated bands on damage development was further investigated.

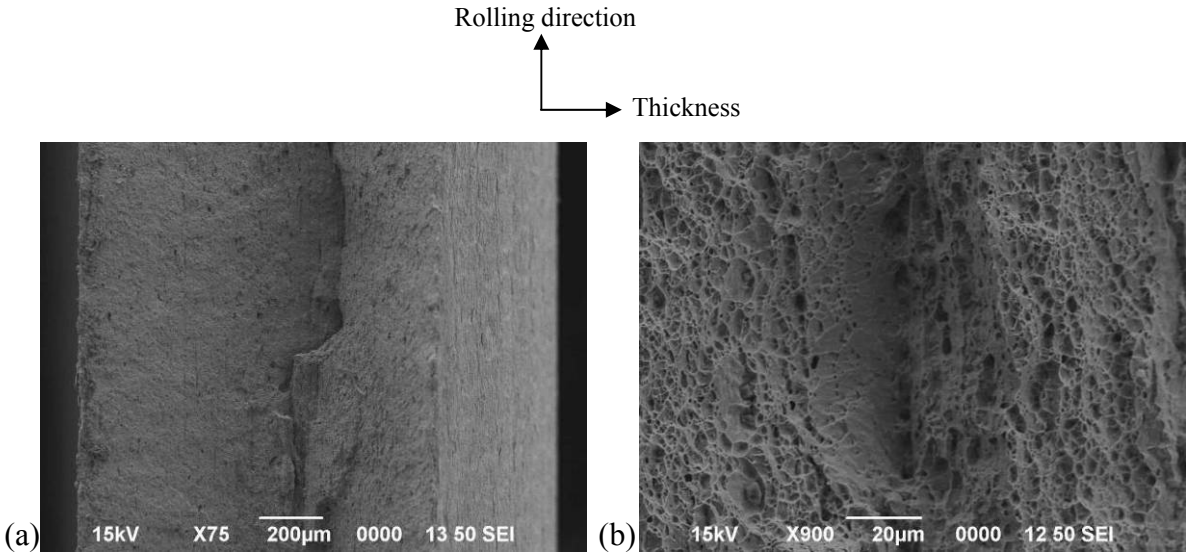

Figure III.5. Fractographic observations by SEM on Steel 3. (a) general view of the thickness, (b) close up view of the mid-thickness.

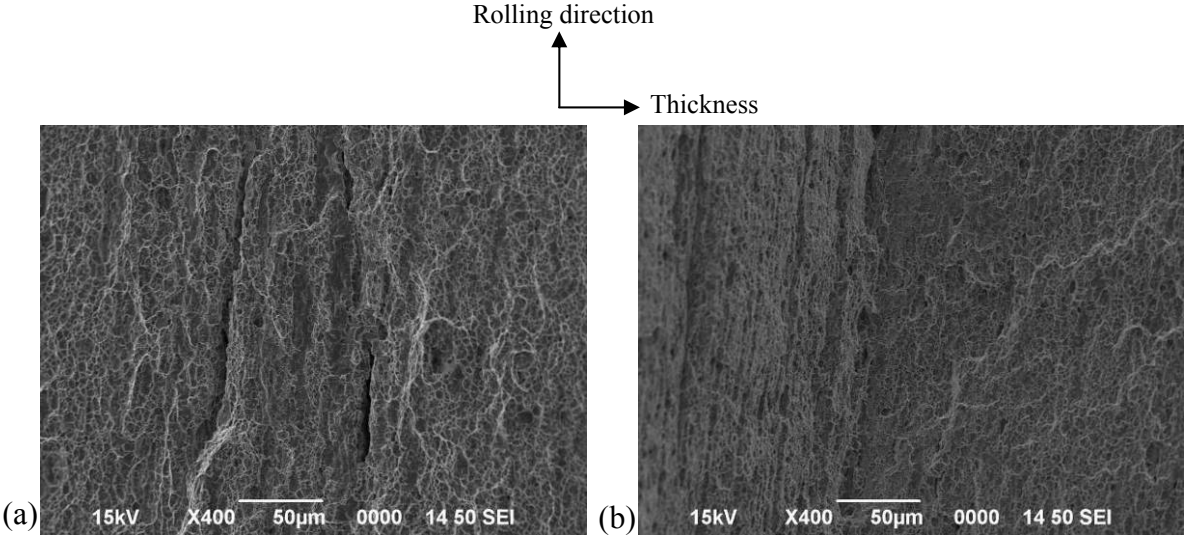

Figure III.6. Fractographic observations by SEM in the vicinity of the mid-thickness. (a) Steel 1, (b) Steel 4.

To summarize, the fracture modes are ductile both in air and stretch bending tests. Particular features such as marked lines oriented along the rolling direction (for stretch bending along TD) are probably linked to segregated bands.

I.B. Damage development during air and stretch bending tests

1. Air-bending test

To investigate damage mechanisms during air-bending, light and scanning electron microscopy were used. After bending of various specimens up to "microcracking" (which will be defined in section II), the cracks were first observed thanks to a binocular magnifier (Figure III.7). Then, through-thickness metallographic observations perpendicular to the crack were performed to investigate crack initiation.
The LePera colour etching reagent was used making it possible to reveal easily martensite/austenite islands (in white) and the ferritic matrix (in brown).

(a)  (b) 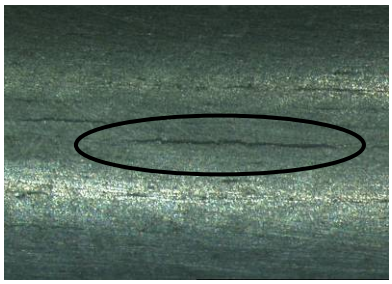

Figure III.7. (a) Bent sample with a crack on the bent apex surrounded with black line, (b) Crack observed with binocular magnifier. Crack surrounded with black line.

Figure III.8 and Figure III.9 illustrate microcracks after an air-bending test before and after LePera etching. Before etching, cavities (dark spots) are observed close to the microcrack, highlighting damage all around it.
The microcrack is of nearly 180µm in depth and makes an angle of about 45° with the outer surface. This confirms fracture mechanisms already observed in the past by Chien et al. (2004). At first sight, the microcrack seems to initiate from the outer surface. However, at about 50µm below the surface in tension, a slight discontinuity of the microcrack is noticed (Figure III.8d). This could also suggest crack initiation from just below the surface.

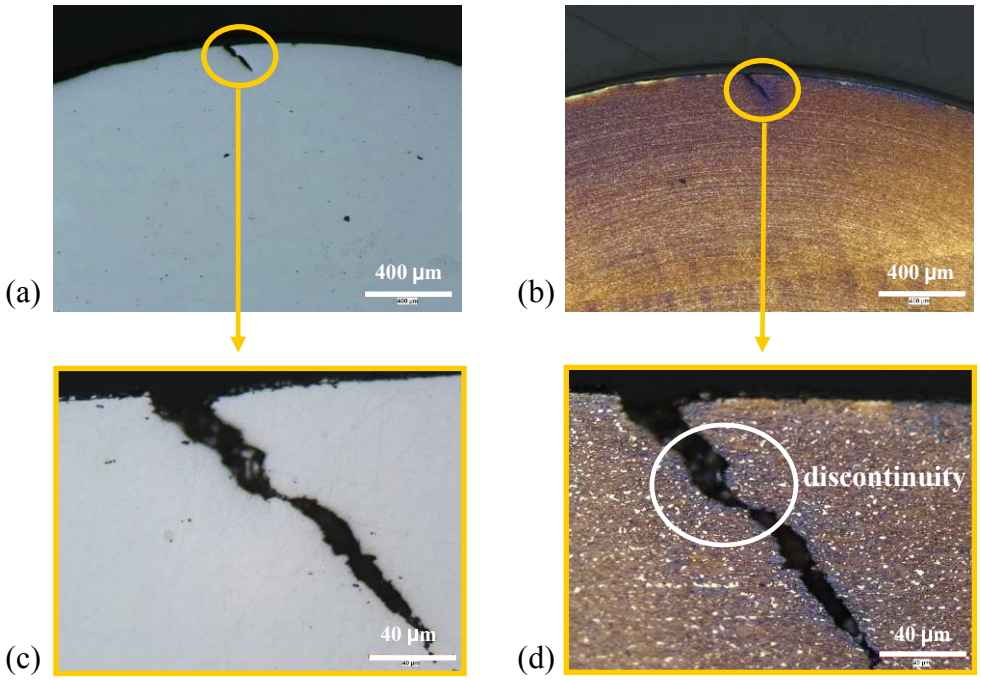

Figure III.8. Cross sectional observations using light microscopy on Steel 1 along the rolling direction. (a) General view of the crack before etching, (b) general view of the crack after LePera etching, (c) close up view of the crack before etching, (d) close-up view of the crack after LePera etching.

Figure III.9 shows another shape of microcrack for Steel 1 bent along the transverse direction. The microcrack makes a kink with a kind of (vertical) flat area below the outer surface suggesting two possibilities regarding crack initiation: either from the surface in tension or, just below that surface, from the flat area where a change in the direction of the microcrack is noticed. Here also, the microcrack develops with an angle of 45° with the outer surface.

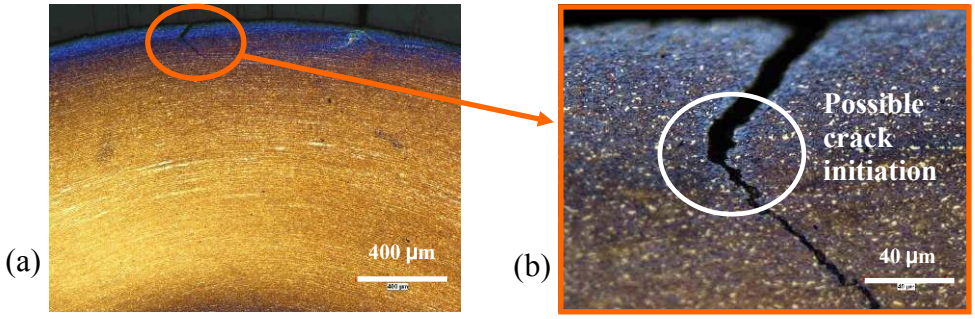

Figure III.9. Cross sectional observations using light microscopy on Steel 1 along the transverse direction, LePera etching. (a) General view, (b) close up view.

Damage (dark spots) at the central segregation band and a very small microcrack at the outer surface were also observed (Figure III.10) in another specimen. Moreover, there is a kind of local necking at the central segregation between cavities. In “pure” bending, we would not expect cavities at central segregation as this hard band would coincide with the neutral fibre (no deformation). However, in air-bending, as this neutral fibre is slightly shifted from the mid-thickness of the sheet, such events can be observed.

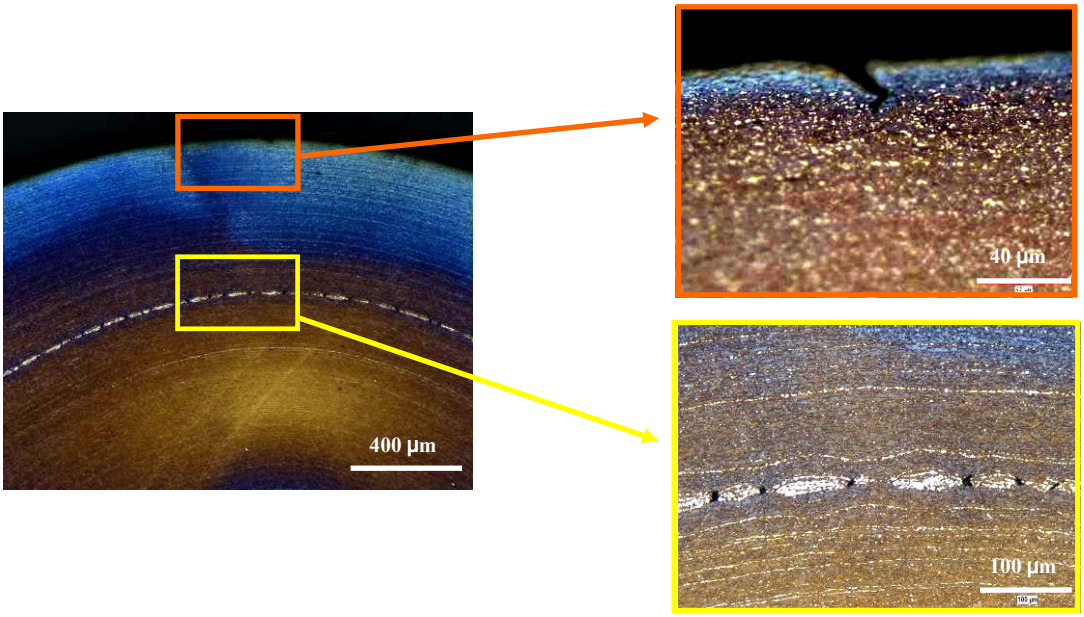

Figure III.10. Metallographic observations on Steel 1 along rolling direction (LePera etching).

No metallographic observations of Steel 3 and Steel 4 are given here, as these steels did not present any crack in air-bending.

In order to get more detail about the damage process in bending, scanning electron microscopy was used. Figure III.11 illustrates two air-bent microcracks after a slight Nital etching. The microcrack in Figure III.11a seems to have initiated from the outer surface. In addition, damage is clearly noticed all around the crack and seems to nucleate either by cleavage at martensite/austenite (M/A) islands, or by phase decohesion between M/A islands and softer ferrite. Poruks et al. (2006) and Avramovic-Cingara et al. (2009) noticed similar damage mechanisms after tensile tests, respectively on low-carbon bainitic steels and DP600 steels. During the preparation stage (before the polishing), the microcracks were filled with mounting resin. In the bent specimens, all microcracks were free from any particles before metallographic preparation.

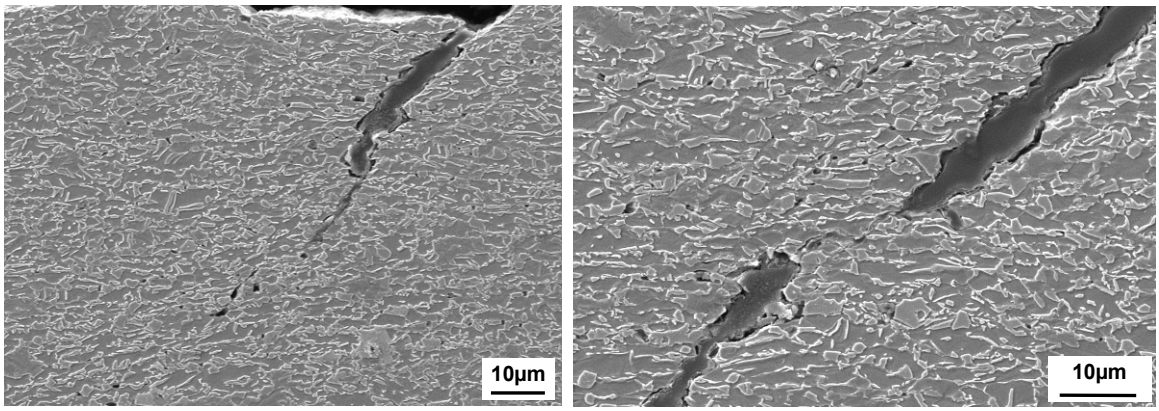

(a) (b)

Figure III.11. Two air-bent specimens of Steel 1 observed using scanning electron microscope. (a) Microcrack which has surely initiated from the surface, (b) propagation of a microcrack through the thickness. Damage is well noticed all around the microcrack.

2. Stretch bending test

Observations on stretch bent specimens were performed on both broken and unbroken specimens. As fracture during this test is very unstable, it was therefore very difficult to interrupt it before complete failure. Figure III.12 shows large cavities which have initiated at central segregation but no significant crack propagation from this damage area did occur. In fact, it seems very difficult to catch the stage between first damage development at central segregation and full propagation across the thickness.

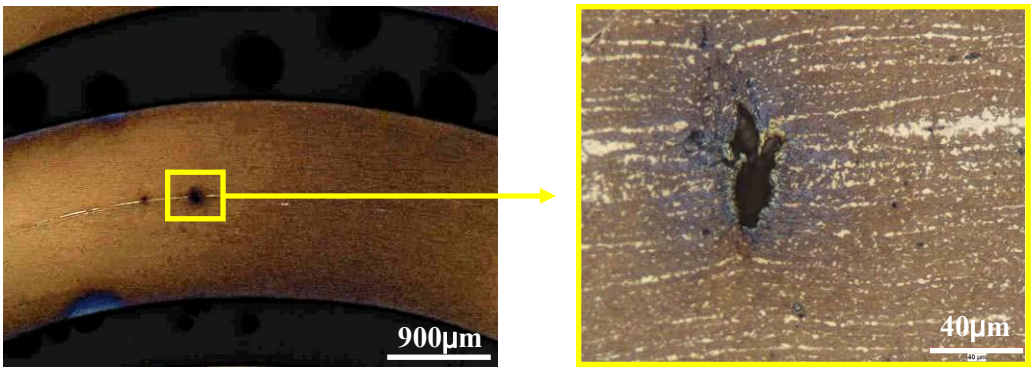

Figure III.12. Metallographic observations of stretch bent Steel 1 along the transverse direction.

Metallographic observations of broken samples are given in Figure III.13 to Figure III.15. In each picture, rather large cavities located at the central segregation band are observed whereas no crack is noticed close to the outer surface. Note that close to the mid-thickness, a "V" shape of the fracture surface is also noticed. From these observations, the central segregation seems to play a significant role during stretch bending as the crack apparently initiates from it. Moreover, a similar orientation for the crack propagation (~ 45° from the initial sheet plane) as for the air-bending test is observed.

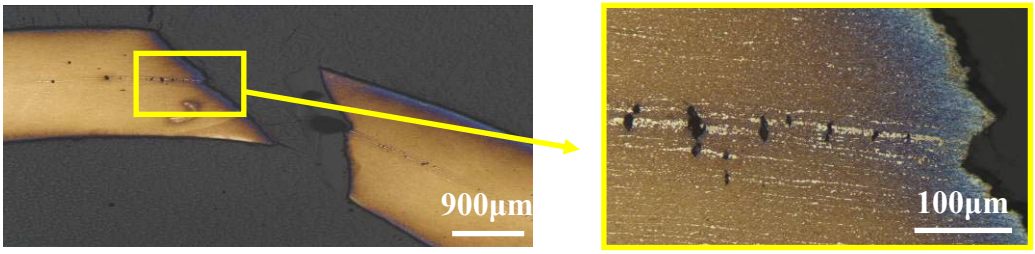

Figure III.13. Metallographic observations of Steel 1 stretch bent along the transverse direction.

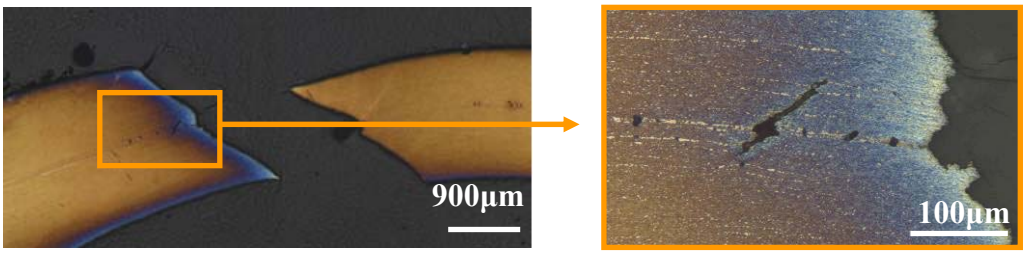

Figure III.14. Metallographic observations of Steel 3 stretch bent along the transverse direction.

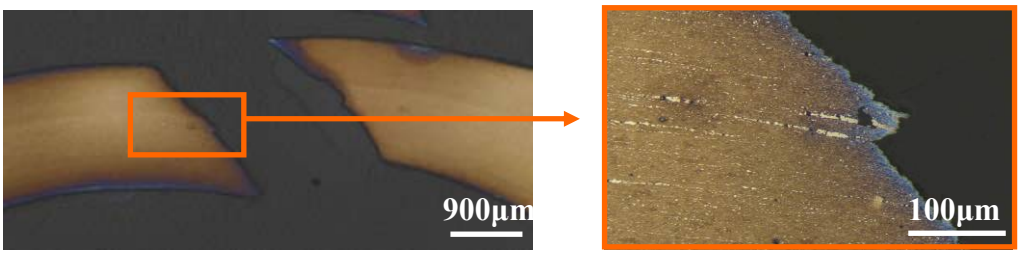

Figure III.15. Metallographic observations of Steel 4 stretch bent along the transverse direction.

As the stretch bent specimens are completely broken, it is, however, difficult to prove that cracks start from the central segregation region. Therefore, the device designed at Centre des Matériaux was used to carry out interrupted tests and to stop the test just before failure, as very low displacement rates can be reached with this device (0.05mm/s instead of 0.5mm/s with the hydraulic press).

As already mentioned, interrupting tests on this kind of device is still very difficult because the crack remains very unstable. In one case, however, we successfully stopped the test with an internal crack just before the failure (Figure III.16).

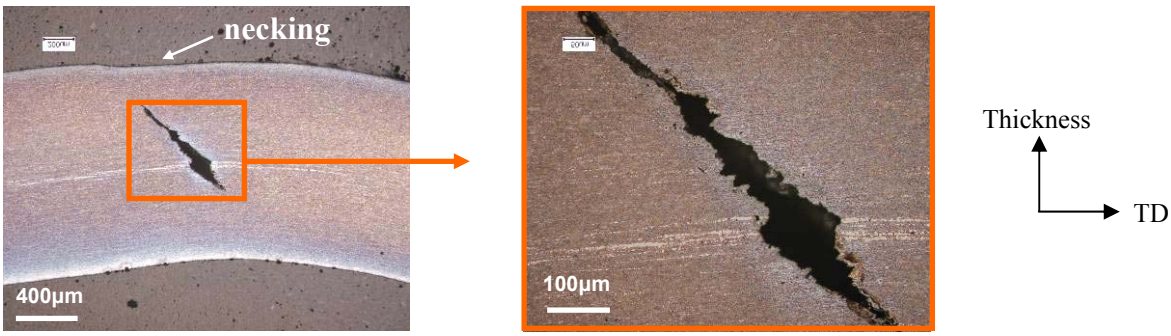

Figure III.16. Interrupted stretch bending test on Steel 1, LePera etching. Crack initiation from the central segregation region.

The shape of the crack clearly indicates that, in stretch bending, fracture initiates from the central segregation while, in air-bending, the crack initiates from the outer surface or from just underneath. Figure III.16 suggests the following mechanism: first, crack initiation close to central segregation and then, crack propagation with a 45° angle, probably linked to both mechanical fields and sensitivity of the material to strain localization.
In Figure III.16 we can also notice some necking of the sheet just above the crack, at the outer surface. Indeed, the initial thickness of the sample was 1.6mm (before the stretch bending) and after the stretch bending, just at the location of the crack, the thickness was about 1.35mm. Out of the necking, the thickness was nearly 1.45mm.

Then, to study damage mechanisms in stretch bending at a finer scale, scanning electron microscopy was used to observe metallographic sections after Nital etching (Figure III.17). The main hard band is clearly seen in Figure III.17c with a lot of cavities within it. It is also noticed that the thicker bands are more extensively damaged than the thinner ones. Similar damage mechanisms are observed as for the air-bending test, i.e., cavities originate either from decohesion between M/A islands and ferrite or from cleavage cracking of M/A

islands. In addition, at a macroscopic scale, as segregated bands are very hard (principally composed of austenite and martensite), they fail earlier than the softer matrix, which can sustain a higher amount of strain before to be damaged.

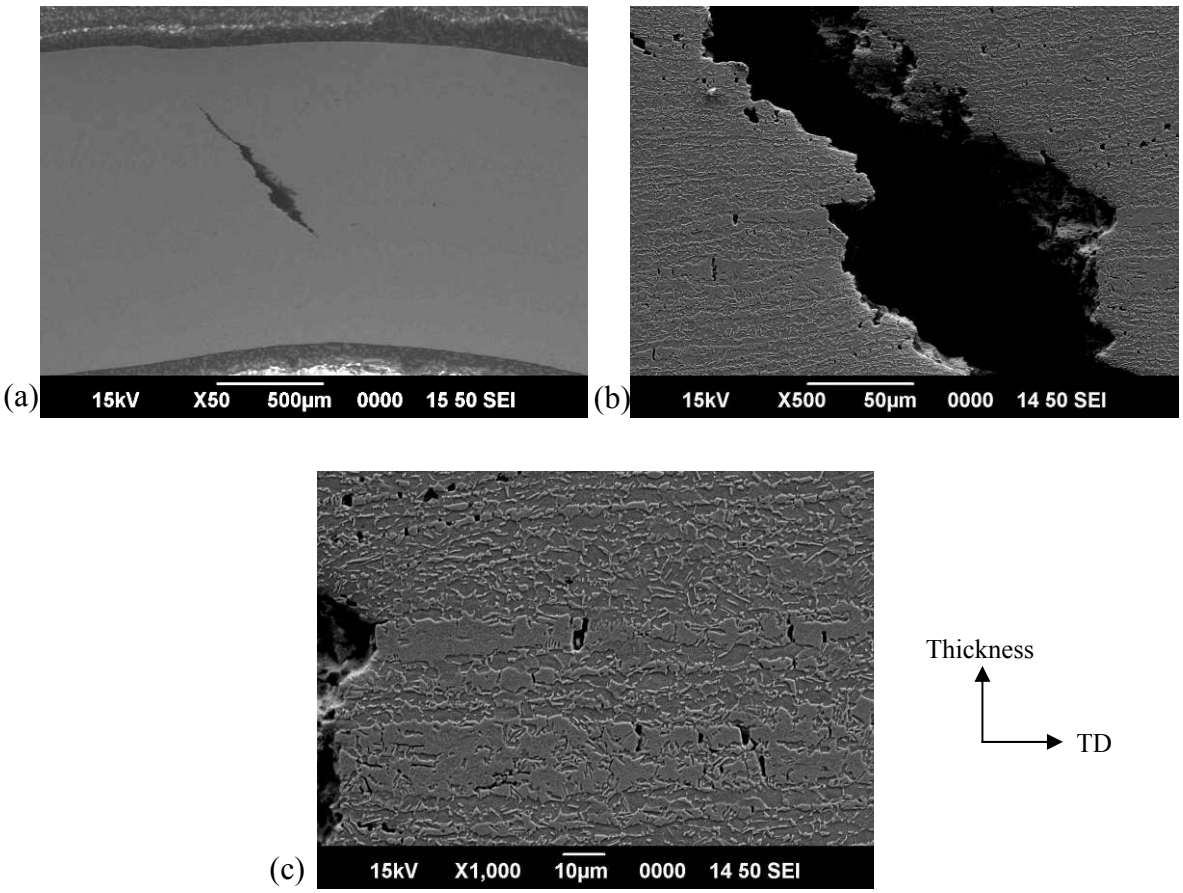

Figure III.17. Stretch bent specimen of Steel 1. Observation of damage mechanisms after a slight Nital etching using scanning electron microscopy. (a) General view of the crack, (b) close-up view of the crack at mid-thickness, (c) close-up view of damage close to mid-thickness at the right of the crack.

I.C. Investigation of damage development in segregated bands using tensile specimens

In order to determine the fracture strain of the segregation bands, several cross-section observations were performed: first, on a broken tensile specimen, then on several specimens deformed in uniaxial tension with various strain levels. SEM observations of the broken tensile specimen are reported in Figure III.18. A decrease in the amount of damage along the specimen axis (away from the fracture surface) is clearly observed.

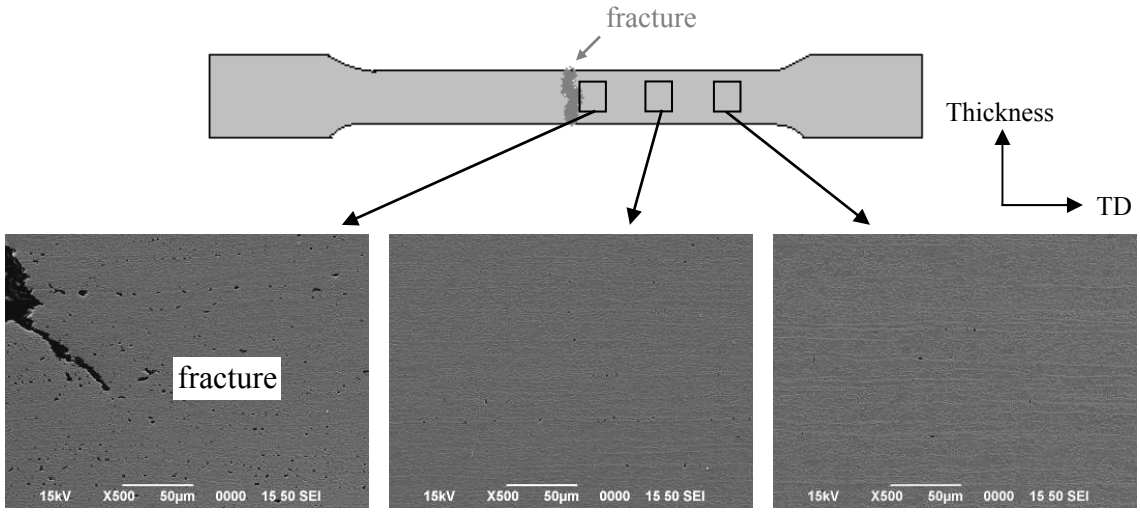

Figure III.18. SEM observations along a broken tensile specimen of Steel 1 (Nital etching).

Interrupted tensile tests were performed on 12.5x50mm smooth tensile specimens for various true strain levels (0.09 up to 0.21). These values of strain were measured with Aramis software [Aramis system]. This facility allows monitoring the evolution of strain during a test. For that purpose, a speckle has to be deposited on the surface of the studied material and then, thanks to two CCD cameras, strain fields are derived from digital image correlation. The values of strain are given for the regions where damage was actually quantified thanks to SEM observations.

The following damage features are noticed (Figure III.20):
- No damage is observed for $\varepsilon = 0.09$ for Steel 1 and only a few cavities are observed for Steel 4. Steel 3 is more severely damaged than the two other ones.
- For higher strains (0.11 up to 0.18), Steels 1 and 4 have similar amount of damage (cavity of maximum 1 µm in size, similar number density) while Steel 3 exhibits much more damage with larger cavities (up to 2 µm). The size of a cavity given here corresponds to its opening (Figure III.19).

Figure III.19. Schematics of damage quantification in a segregation band.

To summarize, for Steels 1 and 4, the first occurrence of damage in the microstructure is observed for an amount of true strain ranging from 0.09 up to 0.11 while for Steel 3, several larger cavities are noticed for a true strain of 0.09 meaning that they nucleated earlier. Therefore, the fracture strain of the segregation bands for these steels is roughly close to 0.10. In more detail, these results also show that the thicker segregated bands may experience earlier damage nucleation during deformation.

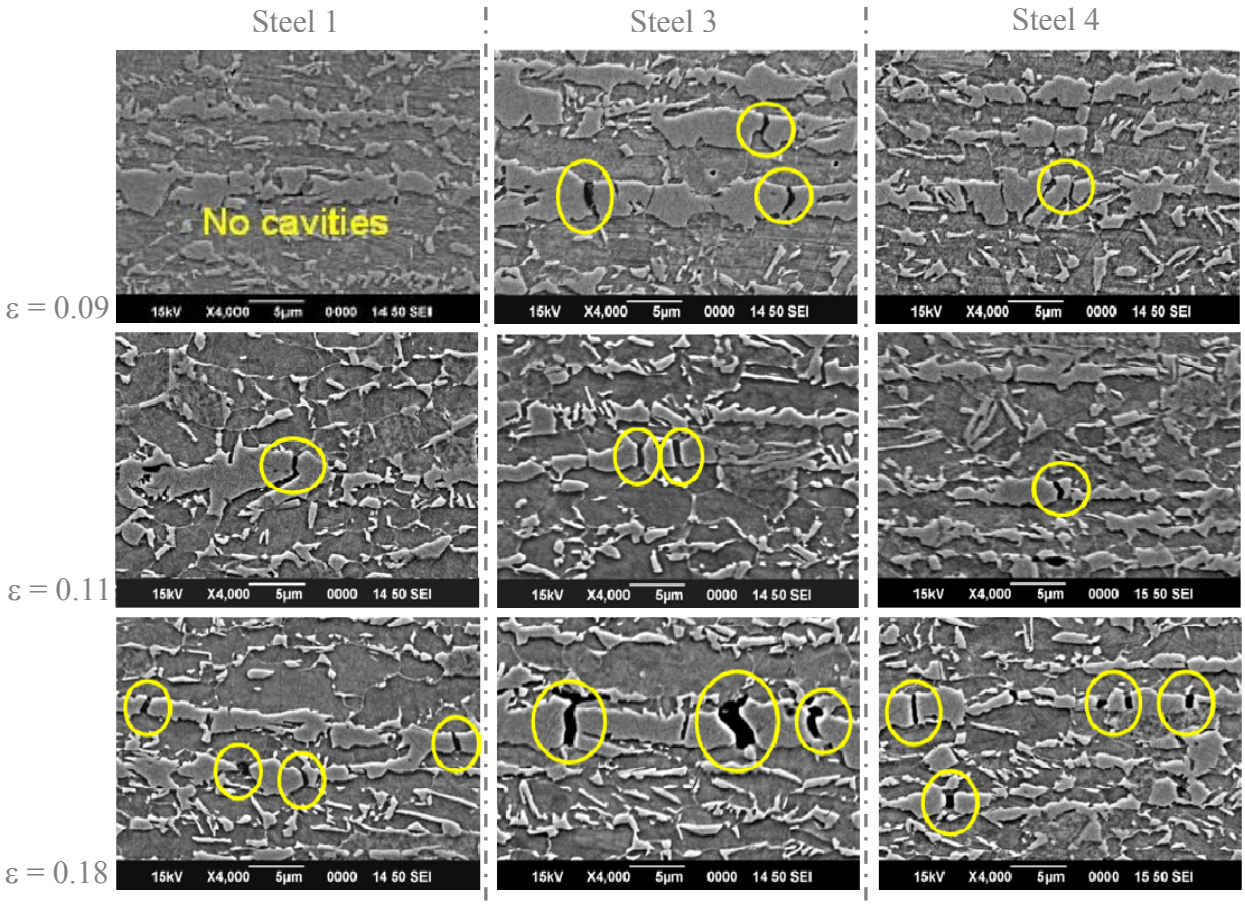

Figure III.20. SEM observations after Nital etching of the three TRIP steels (1.6mm in thickness) after a uniaxial tensile true strain of 0.09, 0.11 and 0.18."

As Steel 3 is the most sensitive one to damage, the rest of the study concentrated on this material. Figure III.21 shows damage at segregated bands for various tensile strain levels (0.09 up to 0.21). As expected, the size of cavities increases with increasing tensile strain.

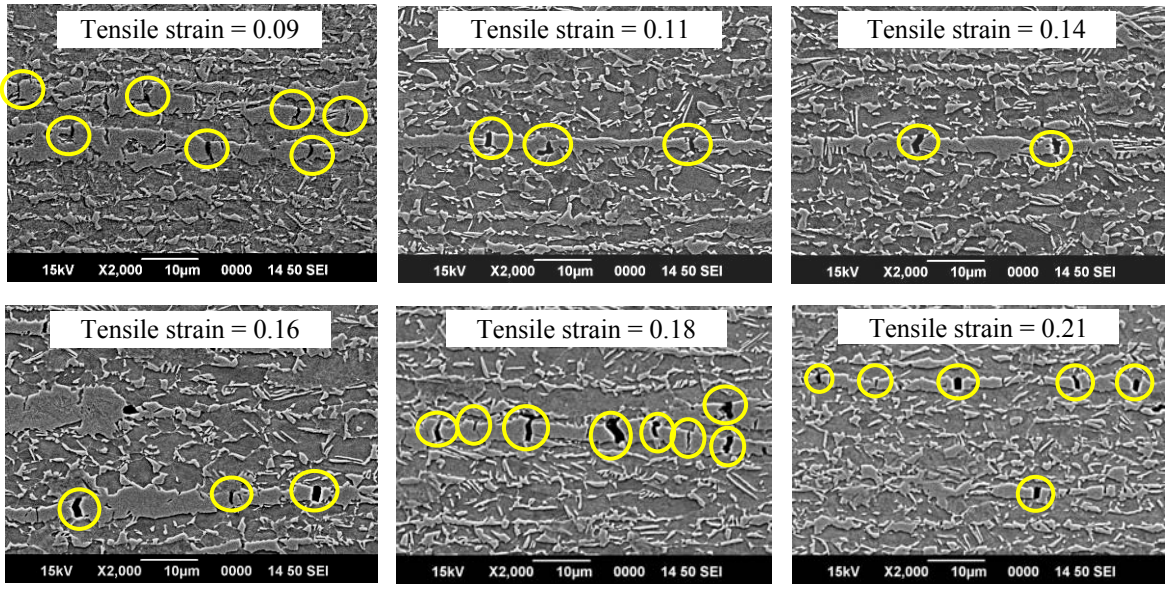

Figure III.21. Damage development during uniaxial tension of Steel 3 - various tensile true strain levels (from 0.09 up to 0.21) (Nital etching).

The spatial distribution of these cavities along the bands was also quantitatively studied. Figure III.22 presents the average number of cavities contained over a 10-micron-long segment along a segregated band. The standard deviation is very high, it is therefore very difficult to provide a tendency in this plot. However, it can be suggested that the number of cavities is relatively constant (~1cavity per 10µm in length) up to a strain of 0.16 and then, a slight increase is noticed.
It suggests that the damage process may follow the following steps:

i) nucleation of first cavities just before a true strain of 0.09.
ii) growth of cavities up to a true strain of 0.16.
iii) nucleation of new cavities above this limit.

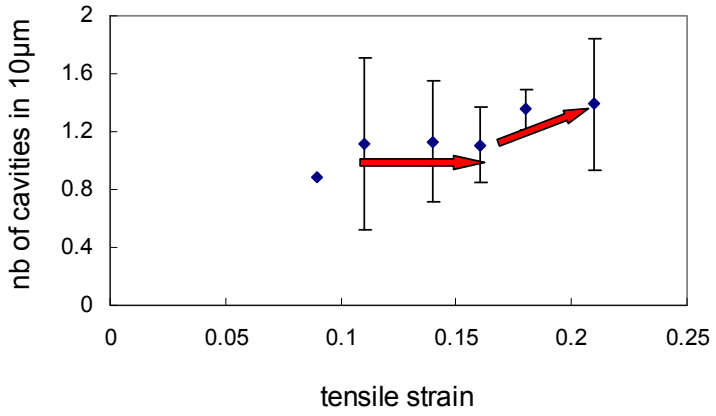

Figure III.22. Spacing of cavities along segregated bands as a function of the applied tensile strain.

To go further, the size distribution of cavities was determined for each strain level (Figure III.23). The largest cavities are observed for the highest strain levels. For example, for a true strain of 0.09, all cavities range between 0.2 and 0.8 µm in size. For higher strain levels, cavities grow but there are also smaller ones. This means that there is nucleation of new cavities during all steps of the tensile deformation. However, it is noticed that there are a big amount of small cavities (size < 0.3 µm) for the material strained up to 0.18 and 0.21. Therefore, although nucleation seems to act at all strain levels, the main steps of nucleation are for an amount of true strain close to 0.09 and from 0.18 and 0.21.

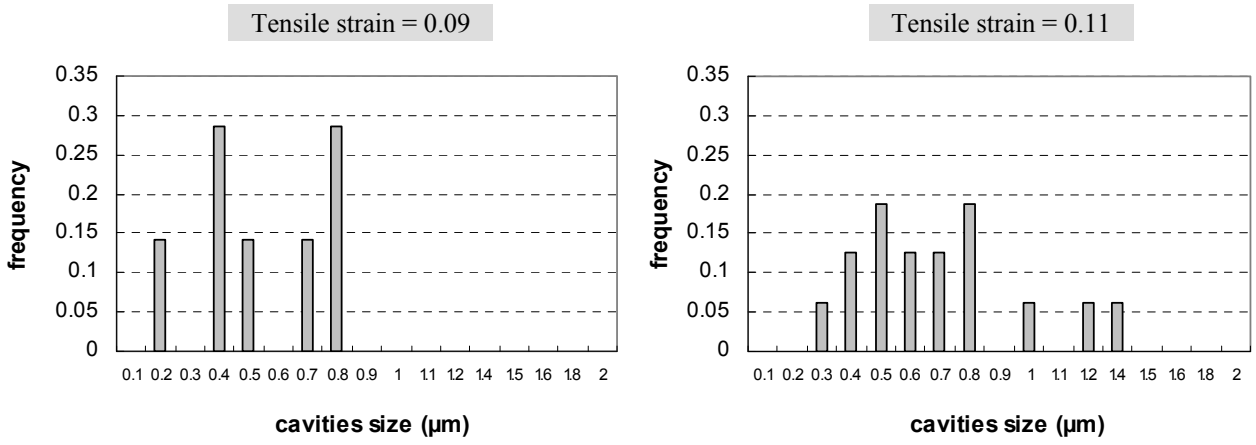

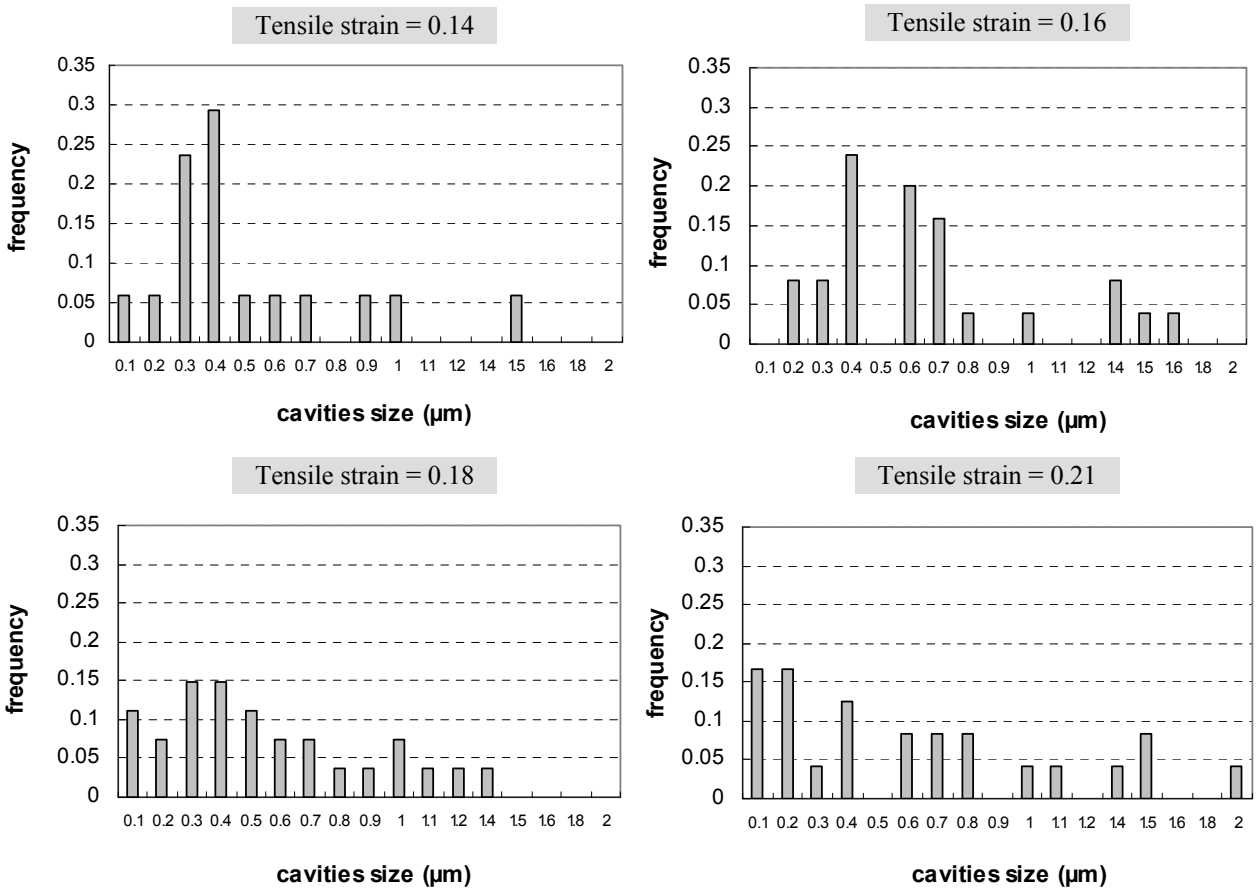

Figure III.23. Cavities size distribution for the various true strain levels (0.09 up to 0.21).

Figure III.24 illustrates this assumption where larger cavities and smaller ones are noticed. The big ones generally measure between 1 and 2 µm in width and are circled in red. The cavities circled in yellow represent the "newer ones" (opening width < 0.3 µm).

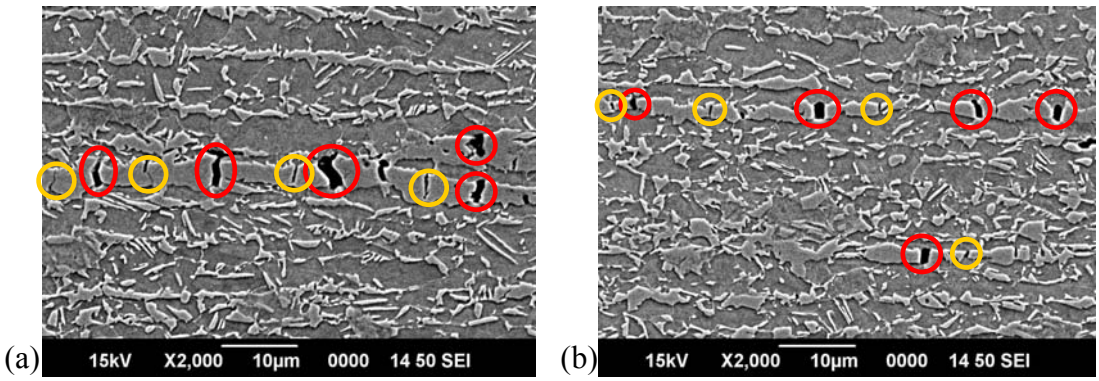

Figure III.24. SEM observation after Nital etching: spatial distribution of damage cavities along the band for a specimen deformed under uniaxial tension up to a true strain of (a) 0.18 and (b) 0.21. Red circles: big cavities (open at low strain), yellow circles: second generation of (i.e. newly nucleated) cavities.

I.D. Summary of section I

It was demonstrated that crack initiation mechanisms are different in air bending and in stretch bending. In fact, the two bending procedures do not test the same microstructural parameters. Stretch bending depends on the central segregation while air-bending is more sensitive to banded structures i.e. to segregation bands closer to the surface of the sheet.
Regarding damage in the microstructure after uniaxial tension, it was demonstrated that the amount of true strain needed to nucleate damage cavities at central segregation is about 0.10 for the three TRIP-aided steels studied. This value is strongly dependent on the band thickness. Cavities were only observed for higher fracture strains for very thin hard bands.

To further investigate the influence of banded structures in air-bending, the main hard band was shifted from the mid-thickness towards the outer surface in thickness-reduced Steel 2. This is the aim of section II. In the following part, it is also intended to quantitatively correlate band thickness and band sensitivity to damage nucleation during air-bending.

II. Influence of segregated bands on bendability

II.A. Investigation of damage mechanisms in air-bending

This part is based on a journal paper which has been accepted for publication to *Materials Science and Engineering A* in March 2011. The text of this article is reproduced below.

Damage development in low alloy TRIP-aided steels during air-bending

D. Rèche[a,b,*], T. Sturel[b], O. Bouaziz[a,b], A. Col[b], A.F. Gourgues-Lorenzon[a]

[a] MINES ParisTech, Centre des Matériaux, CNRS UMR 7633, BP 87, 91003 Evry Cedex, France
[b] ArcelorMittal Global R&D, Voie Romaine, BP 30320, 57283 Maizières-lès-Metz Cedex, France

ARTICLE INFO

Article history:
Received 3 August 2010
Received in revised form 5 March 2011
Accepted 7 March 2011
Available online 12 March 2011

Keywords:
Ultra high strength steels
Air-bending
Microstructure
Fracture mechanisms

ABSTRACT

In order to optimize the metallurgical quality of advanced high strength steels for automotive applications, the present study aims at understanding damage mechanisms involved in air-bending of two low alloy TRansformation Induced Plasticity (TRIP)-aided steels. Air-bending tests were performed together with metallographic investigations of damage development in bent specimens. In order to assess the role of hard bands induced by chemical segregations, air-bending tests on specimens with various locations of the main hard band (with respect to the neutral fibre) were performed. Cracking initiates from the outer surface or from just below, mainly by decohesion between ferrite and secondary (martensite) phases, at hard bands located close to the outer surface. From these examinations, together with a simple kinematics analysis of bending, a quantitative relationship between cracking, local thickness of hard band and local "mesoscopic" strain is proposed.

1. Introduction

In recent years, the automotive industry has made increased use of advanced high strength steels (AHSS) for weight and cost reduction as well as for crash performance improvement. These steels differ considerably in their strengthening mechanisms because of the presence of several phases in the microstructure. To enlarge the use of these steels in automotive body and structural parts, good knowledge and experience must be developed regarding their formability.

As TRIP-aided steels present a very high ductility, they are expected to be shaped into more complex automotive parts than those achievable with other AHSS. However, to be formed into complex shapes, the sheet has to undergo various loading modes such as bending, stretch bending, and stamping. It is therefore necessary to predict the forming behaviour of TRIP-aided steels in increasingly severe conditions. In particular, to improve the bendability of TRIP-aided steels, it is essential to get a better understanding of the damage mechanisms that might develop during bending. This is the aim of the present study.

The formability of metallic sheets generally refers to the limit strain or stress states up to which the forming process is accomplished without failure. The bending limit could be defined as the amount of strain that initiates a noticeable granulation (increase in roughness) at the outer surface of the bending zone, from which a minimum bending radius is deduced [1]. It is affected by many parameters such as the tool geometry, bending procedure, material properties, sheet thickness, surface and edge conditions of the blank.

Several authors demonstrated that refinement and homogenization of the microstructure would be the key to improve the bendability of steels [2,3]. Yamazaki et al. [2] evaluated the bendability of steels by forming a specimen in a 90° V-block and measuring the minimum bending radius at which the specimen did not crack. The Rockwell C scale hardness was measured at five points with 2 mm intervals on the surface of sheet specimens and its standard deviation was taken as a "microstructural homogeneity index". They found that the minimum bending radius better correlates with the "microstructural homogeneity index" than with total elongation measured under uniaxial tension. Nagataki et al. [3] investigated the bendability of fully martensitic steels having a tensile strength ranging from 1100 to 1650 MPa and they also showed that the microstructure of these steels should be refined and homogenized for the improvement of bendability.

In TRIP-aided steels, the transformation of retained austenite into martensite during deformation has been largely studied both in the past and more recently [4–7]. Several authors [7–13] showed that smaller austenite grains have higher carbon content compared to larger austenite islands. In addition to the effect of particle size, this induces a higher stability of smaller retained austenite islands than of larger ones. Hence, larger austenite islands are transformed into martensite at lower strains due to their lower stability and the spatial distribution of such islands might influence local events such as the initiation of damage cavities under mechanical loading.

* Corresponding author at: ArcelorMittal Global R&D, Voie Romaine, BP 30320, 57283 Maizières-lès-Metz Cedex, France. Tel.: +33 3 87 70 48 01; fax: +33 3 87 70 47 14.
E-mail address: delphine.reche@arcelormittal.com (D. Rèche).

0921-5093/$ – see front matter © 2011 Elsevier B.V. All rights reserved.
doi:10.1016/j.msea.2011.03.042

In order to well represent the mechanics of multiphase steels at the scale of individual microcracks or damage cavities, it is necessary to account for the properties of the constitutive phases. For example, the strain hardening ability of TRIP-aided steels strongly depends on interactions between harder and softer phases and on the mechanically induced phase transformation of retained austenite into martensite [7]. Jacques et al. [7] measured the true strain of each phase as a function of the macroscopic true strain under uniaxial tension. It was found that, for a macroscopic true strain of about 0.10, ferrite was nearly strained up to 0.12 while the amount of strain in austenite did not exceed about 0.07. Bouquerel et al. [14] also studied the behaviour of TRIP-aided steels by using a micromechanical model including the contributions of each microstructural constituent to the flow stress and the strain hardening of multiphase steel.

Various studies [6,7,15,16] demonstrated that the transformation rate of retained austenite depends on stress triaxiality. Thus, the flow behaviour of TRIP-aided steels strongly depends on the loading mode. Consequently, mechanical modelling of bending, even at the macroscopic scale considered in the present study, must be carried out using a material database that is relevant with respect to loading modes encountered during bending.

In the present study, the failure mode and damage mechanisms in air-bending conditions were experimentally investigated for two low alloy TRIP-aided steels. Besides the conventional characterization of sensitivity to cracking during bending and in order to provide guidelines to optimize the steel microstructure for bending purposes, damage was finely investigated by metallographic examinations. In particular, the role of hard bands of larger martensite/austenite islands and local hoop strain was investigated using thickness-reduced "model" specimens with various locations of those bands with respect to the neutral fibre. To derive a simple damage initiation criterion from instrumented air-bending tests, the strain field was determined at a "mesoscopic" scale (i.e., by considering the material as a homogeneous medium, as explained in the corresponding section) by using a simplified analysis of the air-bending test.

2. Materials and experimental methods

2.1. Materials

Two low alloy TRIP-aided steels of thickness 1.6 and 2 mm, from the same heat and thus with similar chemical composition (C ~0.2 wt%, Mn ~1.6 wt%, Al + Si ~1.5 wt%, Mo + P + Ti + Cr + Ni ~0.2 wt%) were considered in the study. Steel 1 was used to perform the global characterisation of damage after air-bending or tensile tests, while Steel 2 (with a lower amount of material available) was only used to investigate the influence of the hard band location on the air-bending ability. These materials were processed by hot and cold rolling followed by continuous annealing, i.e., after a soaking in the intercritical temperature range, the sheets were hold in the bainitic region (~460 °C) enabling to stabilize the austenite phase through its enrichment in carbon, during the formation of carbide-free bainite (due to the presence of Si and Al). In order to assess the possible influence of "hard" bands, rich in large martensite/retained austenite (M/A) islands, processing conditions were deliberately chosen to enhance such bands in the considered sheets.

The two steels exhibit similar room temperature mechanical properties (Table 1). Their microstructures are similar and that of Steel 1 is presented in Fig. 1. They consist of hard M/A islands in a softer ferritic matrix, which leads to an excellent combination of high strength and ductility. The third-thickness microstructure is rather homogeneous with austenite and martensite islands within ferrite, while in the mid-thickness microstructure, one can distinguish a central band of hard phases due to segregation of austenite forming elements. Hard phases are present as 1–5 μm islands linked by thin bands of smaller islands.

X-ray diffraction (XRD) measurements were carried out by using a Co tube (high voltage 40 kV, intensity 25 mA) to determine the amount of retained austenite from the integrated intensities of $\{200\}_\alpha$, $\{211\}_\alpha$, $\{220\}_\alpha$, $\{200\}_\gamma$, $\{220\}_\gamma$ and $\{311\}_\gamma$ diffraction peaks. Several measurements were carried out at third-thickness of the as-received sheets to be representative of the bulk materials and the amount of retained austenite was found to be close to 8% for Steel 1 (1.6 mm) and 10% for Steel 2 (2 mm). The sampling area was about 3 mm^2 for each material. From XRD measurements, both steels have similar carbon content (1.15%) in retained austenite. This value is consistent with literature data [17,18]. In addition, XRD measurements were also performed on full-thickness bent specimens a few micrometers under the surface in tension and no austenite was detected. This suggests that, due to the high amount of strain that was reached, most of the austenite located there transformed into martensite during the air-bending test.

From image analysis of optical micrographs, the amount of M/A islands for Steel 1 and Steel 2 were respectively evaluated to be equal to 18% and 17% at third-thickness (which is thought to be representative of the bulk material). By difference with the retained austenite content determined by XRD, Steel 1 and 2 respectively contain 10% and 7% of martensite in the as-received state. In addition, at mid-thickness, islands of hard phases were larger (up to 10 μm in size). Light optical microscopy observations after a sodium disulphite colour etching (8 g of sodium disulphite in 100 ml of distilled water) showed that most of these larger islands were martensitic even in the as-received state.

In order to evaluate the hardness of each phase, a nanohardness testing facility (Triboscope®, Hysitron SA) coupled with an Atomic Force Microscope (AFM) (Digital Instrument 3100) was used to perform nanoindentation measurements of Steel 1. After a loading/unloading cycle with a maximum applied load of 5 mN, indentation depths were measured in two cases: in M/A islands close to mid-thickness and in the ferritic matrix. From an average of five measurements for each of them, the ferritic matrix and the M/A islands in the vicinity of mid-thickness of the sheet show a nanohardness close to 4 GPa and 11 GPa, respectively. Please note that it was very difficult to differentiate martensite islands from retained austenite islands with the AFM. Therefore, only the nanohardness of M/A islands, instead of that of each phase respectively, is reported in the present study. Nevertheless, it is supposed that retained austenite islands have a lower hardness than martensite islands. The values found here are in agreement with the ones found by Jacques et al. [7] and Furnémont et al. [19] who reported a nanohardness of about 10 GPa and 17 GPa for retained austenite and martensite islands, respectively. This means that in the present study, the few islands considered for the nanohardness measurements were probably mainly composed of retained austenite.

2.2. Experimental methods

For the rest of the article, the "inner surface" and "outer surface" respectively denote the surface in contact with the punch and the surface that is pulled in tension during the air-bending test.

Bending tests were first performed on Steel 1 to understand crack initiation in conventional air-bending conditions.

To quantitatively investigate the relationship between damage development, local strain and local geometry of hard bands, it was intended to artificially vary the location of the hardest band (central segregation) in the thickness in order to obtain a "model material". To this aim, the thicker material (Steel 2) was used. By machining both sheet surfaces, it was possible to investigate the bending behaviour of various specimens (the central hard band being shifted

Table 1
Room temperature mechanical properties for Steels 1 and 2 along rolling (RD) and transverse (TD) directions (ISO 20 mm × 80 mm tensile specimens).

	Yield strength (MPa)	Tensile strength (MPa)	Maximum uniform elongation (%)	Fracture elongation (%)
Steel 1 (1.6 mm)				
RD	467	866	15.0	20.0
TD	546	851	15.0	19.2
Steel 2 (2 mm)				
RD	464	816	16.6	22.9
TD	521	834	13.6	17.0

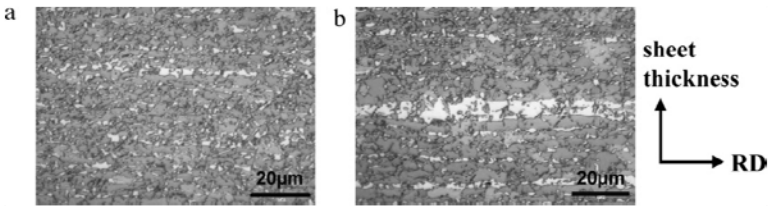

Fig. 1. Light optical micrographs of Steel 1, LePera etching. (a) Third-thickness microstructure and (b) mid-thickness microstructure. Hard phases (austenite + martensite) in white, ferrite in grey.

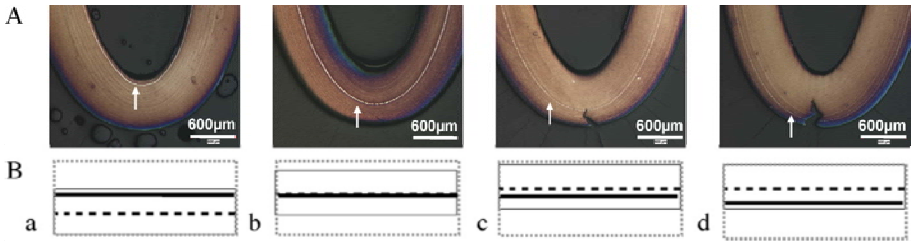

Fig. 2. (A) Light optical micrographs after a 180° bending and (B) schematic side view before bending of the four kinds of thickness-reduced specimens of Steel 2. (A) LePera etching with the main hard band in white (indicated by white arrows). (a) Case 1, (b) case 2, (c) case 3 and (d) case 4. The thick continuous black line in (B) represents the central hard band and the dashed black line represents the mid thickness of the thickness-reduced specimen. The initial (resp. final) shape of the specimen is drawn with grey, dotted (resp. continuous) lines. The outer surface is on the bottom.

away from the mid-thickness) by reducing the thickness from 2 mm down to 0.8 mm. In addition, in order to suppress any damage and residual stresses due to machining, the outer surface of all specimens was chemically polished (solution of hydrofluoric acid diluted in hydrogen peroxide) to remove a layer of about 0.05 mm in thickness. This procedure led to the same final thickness of 0.75 mm for all specimens (Fig. 2).

Several cases were considered, leading to various locations of the central hard band with respect to the mid-thickness and outer surface at the beginning of the test:

- case 1: hard band between mid-thickness and the inner surface (i.e., in the compressive region)
- case 2: hard band at mid thickness
- case 3: hard band between mid-thickness and the outer surface (i.e., in the tensile region)
- case 4: hard band just below the outer surface (i.e., in the tensile region)

Fig. 2A illustrates the four cases with specimens bent until 180°. The main hard band (in white) is readily visible at various locations through the thickness.

The following tests were performed on the considered Steels 1 and 2:

i) Air-bending tests on Steel 1 up to cracking to investigate the bendability of this steel in conventional conditions (including typical values of sheet thickness and bending radii).
ii) Interrupted tensile tests on Steel 1 to investigate damage initiation at hard band as a function of the average strain level (which is much more homogeneous and more easily determined in uniaxial tension than in bending).
iii) 180° bending tests on thickness-reduced Steel 2 in order to determine the influence of the location of the main hard band on bendability. This high value of the bending angle was chosen to enforce cracking in such thin specimens.
iv) Air-bending tests interrupted at various bending angles on thickness-reduced Steel 2 to investigate damage development mechanisms (with hard band located close to the outer surface).

2.2.1. Air-bending tests

To investigate the bendability of the prepared specimens, conventional air-bending tests (Fig. 3a) were performed without lubrication, at room temperature, on a universal tensile machine, with two rotary rolls and a punch radius of 0.1 mm (Fig. 3b). The punch displacement rate was set to 1 mm/s. These testing conditions are typical of those used to compare the bendability of various steels sheets for automotive applications. The punch had a thickness of 10 mm, a V-shaped tip with an angle of 30° and a tip radius of 0.1 mm. The edges of the specimens (size: 100 mm in length and 50 mm in width) were ground before testing to avoid cracks starting from them [20]. Five specimens of Steel 1 were bent along each of the rolling (RD) and transverse (TD) directions. The test was stopped once the first microcrack appeared (Fig. 4b and c). This corresponds to a load drop of about 5%. To compare the bendability of the various specimens, a qualitative evaluation of cracking was made. The bending angle (α in Fig. 3a) was then measured after specimen unloading using a protractor. Damage at the outer surface of the specimen was termed a "crack" if its width ranged between 1 and 5 mm, its depth between 0.18 and 0.3 mm and its

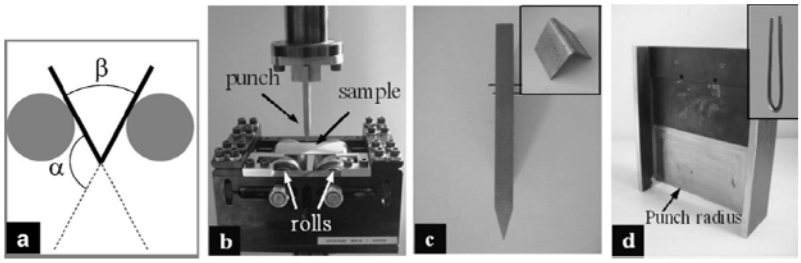

Fig. 3. (a) Schematics of air-bending test (with α the bending angle), bent specimen in black, rolls in grey, punch not represented, (b) air bending device, (c) classical punch with radius = 0.1 mm, bent specimen and (d) thinner punch with radius = 0.4 mm, side stiffeners and thickness-reduced specimen with a bending angle of 180°.

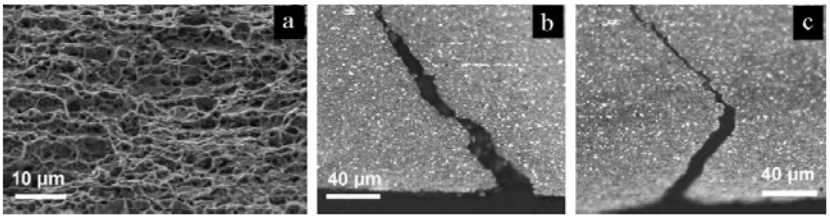

Fig. 4. (a) Fractographic observation by SEM after air-bending test of Steel 1. (b and c) Cross-sections of bent specimens of (full-thickness) Steel 1: two types of microcracks are detected at the outer surface. (a) Almost straight microcrack, with some crack deviation (or initiation) at about 50 μm from the outer surface, (b) V-shaped microcrack, possibly initiated at about 70 μm from the outer surface. Optical micrographs, LePera etching.

crack opening between 0.03 mm and 0.1 mm. This type of crack is observable by eye. "Macrocracks" are bigger (depth > 0.3 mm and crack opening > 0.1 mm) and "microcracks" are shallower and can only be observed using a magnifying glass (depth < 0.18 mm and crack opening < 0.03 mm).

Then, air-bending tests on thickness-reduced Steel 2 were performed in order to investigate the role of hard bands in more detail. A thinner punch was designed for these severe tests (thickness 0.8 mm with side stiffeners to prevent from punch buckling, round-shaped tip with a radius of 0.4 mm). As for Steel 1, the punch displacement rate was set to 1 mm/s and no lubrication was used. In order to compare the bendability of specimens with various locations of the main hard band, 180° bending was first performed for each case (1–4) (Fig. 3d). Then, to investigate damage development, additional tests were interrupted at various angles just before cracking or at microcracking for cases 3 and 4. For case 3 (main hard band in the tensile region), to get the first microcrack, air-bending was interrupted at 142°. For case 4 (hard band just under the outer surface), air-bending was interrupted at 110° to investigate internal damage, while no microcracking was still observed at the outer surface. Bent specimens are shown as inlets in Fig. 3c and d.

2.2.2. Tensile tests

Conventional uniaxial tensile tests were performed at room temperature on smooth specimens of Steel 1 (ISO 12.5 mm × 50 mm specimens cut along TD) using a Zwick tensile machine. These tests were interrupted after amounts of total strain ranging between 0.10 and 0.20. As highest values of average applied strain were larger than the maximum uniform elongation of these specimens (~16%), non-homogeneous strain developed all along some specimens. Therefore, in order to obtain accurate values of local strain, deformation was monitored using digital image correlation (Aramis software [21]) by using two CCD cameras focused on one side surface on which a speckle had previously been deposited.

2.2.3. Investigation of damage development

SEM observations of fracture surfaces of bent specimens showed ductile dimpled fracture (Fig. 4a), as commonly observed after bending of advanced high strength steels.

Damage cavities were investigated using optical and scanning electron microscopy both after bending and interrupted uniaxial tensile tests. Cross-section observations of uniaxial tension specimens enabled to determine the average fracture strain that corresponds to the onset of damage nucleation in the vicinity of mid-thickness (i.e., at the main hard band) and the location of damage with respect to the hard bands. Detailed investigations were carried out on all bent specimens to investigate damage development with respect to the microstructure (and in particular, of the local geometry of hard M/A islands). Hardness measurements were also carried out on cross-sections of bent specimens to assess the location of the less work-hardened area, which will be denoted as the "neutral fibre" in the following.

3. Results and discussion

3.1. Cross-sectional observations of damage development (Steel 1)

3.1.1. Damage development during air-bending tests

During air-bending of full-thickness specimens of Steel 1 (with the main hard band initially at mid-thickness), cracks seem to initiate from the outer surface (Fig. 4b) or, as suggested by the V shape of some of the microcracks (Fig. 4c), from just below the outer surface. In this last case, this could result from the detrimental combination of locally high tensile stress (or strain) and lower local damage resistance of a hard band located at the kink of the V-shaped microcracks. However, hard bands are generally thin close to the outer surface of full-thickness Steel 1 and they are thus difficult to detect by cross-section observations. Thus, from these first observations, it was not possible to fully conclude on this point. The only similar feature between the two crack configurations of Fig. 4 was the angle of about 45° between the microcrack and the outer surface. This phenomenon was already reported by Steninger and Melander [22] who worked on low carbon steels. Sarkar et al. [23] investigated damage development in bending of AA5754 aluminium alloys and showed also bending cracks making a 45° angle with the outer surface. As suggested by Chien et al. [24] for aluminium sheets, combined necking and shear localization analysis is probably needed to determine the failure strain on the stretch-

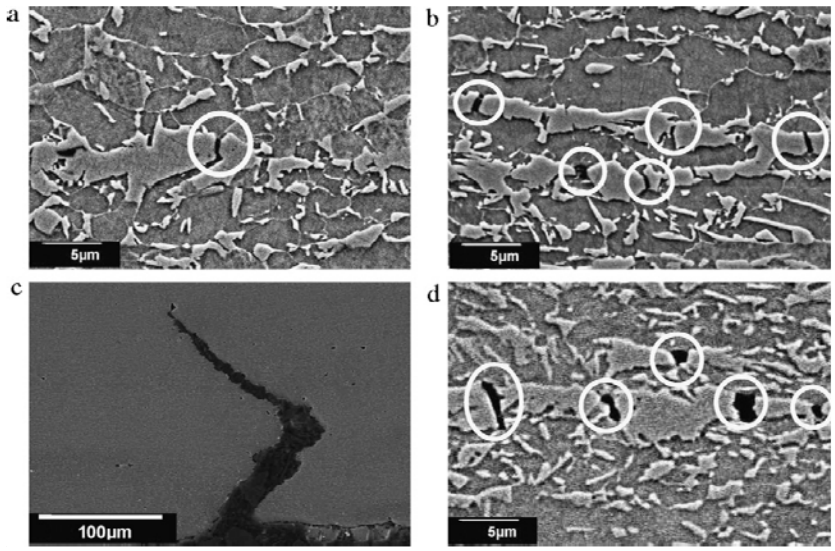

Fig. 5. (a and b) SEM observations of damage after interrupted uniaxial tensile tests of Steel 1 (Nital etching). Cavities (in white circles) are observed at hard bands. Average axial strain = 0.11 for (a) and 0.17 for (b). (c and d) SEM observations of damage after air-bending. (c) General view of a bending crack and (d) damage development at hard bands close to the outer surface (Steel 2, case 3).

ing side of the sheet. Thus, the sensitivity of the sheet material to shear localization, in particular close to the outer surface, should be considered to derive a local crack propagation criterion in bending.

3.1.2. *Damage development during interrupted uniaxial tensile and air-bending tests*

After uniaxial tensile tests, damage was detected at hard bands (Fig. 5), mainly as decohesion at ferrite/martensite interfaces and, occasionally, as cleavage microcracks within martensite islands. As illustrated by comparing Fig. 5b and d, similar damage mechanisms were observed after uniaxial tensile and air-bending tests. Thus, it seems reasonable to compare results of bending tests with those of tensile tests. Jacques et al. [6] and Avramovic-Cingara et al. [25] reported similar damage mechanisms respectively in TRIP-assisted multiphase steels and in DP600 dual-phase steels after a tensile test, i.e., void nucleation occurring either by localized cracking of martensite or by decohesion at the ferrite/martensite interface. As expected, the higher the average amount of strain, the more numerous the damage cavities (Fig. 5a and b). In the present study, cavities were observed at the central hard band for a uniaxial tensile strain of at least 0.11. Furthermore, damage cavities nucleated at thicker bands after lower amounts of strain than at thinner bands. Out of these bands, and far from the mid-thickness, i.e., where the M/A islands were more finely and more homogeneously distributed, cavities were observed to nucleate after a higher macroscopic strain of at least 0.2. This value is higher than the uniform elongation of the tensile specimens.

From these observations, damage cavities nucleate at thicker hard bands for an average strain that is much lower than the uniform elongation of the considered tensile specimens. As the band thickness is very small compared to the sheet thickness, and as TRIP steels strongly resist strain localisation, the tensile specimens could further deform and show work-hardening after nucleation of first damage cavities at hard bands. Thus, these voids did not lead to premature macroscopic necking in uniaxial tension.

To summarize, observation of tensile specimens suggested that damage nucleation in Steel 1 seems to be driven by the combination of a local poor resistance to damage (hard band) and a critical average tensile strain level.

As previously mentioned, even in the as-received state, hard bands at mid-thickness are mainly martensitic and it is well known [7–13] that larger islands of retained austenite tend to transform into martensite for lower strains. In addition, Radu et al. [26] and Sugimoto et al. [27] showed that for respectively a TRIP 800 steel and a TRIP-aided dual phase steel, most of the retained austenite transformed into martensite after low strains (i.e., after a uniaxial tensile strain of 0.10, only 7% and 1% of retained austenite was yet present respectively for the TRIP800 and the TRIP-aided dual phase steel). It seems therefore reasonable to consider that the retained austenite, which was still present at main hard bands in the as-received material, transformed almost entirely into martensite before nucleation of damage cavities (strain of 0.11 for the occurrence of first cavities in the hard bands). Out of the mid-thickness, M/A islands were smaller and retained austenite transformed into martensite for higher amounts of strain. This means that the main hard band was already martensitic before nucleation of the first damage cavities.

In addition, as shown by XRD measurements (Section 2.1), retained austenite close to the outer surface (in tension) was completely transformed into martensite at the end of the air-bending test (i.e., just before cracking), whatever the size of M/A islands located there, because a high amount of strain was reached (higher than 0.2, see below). Less deformed regions of the specimen surely still contain retained austenite which did not transform into martensite. In the present study, damage observations of bent specimens were only performed close to the outer surface. After such high amount of strain, the microstructure was locally composed of martensite islands dispersed in a ferritic matrix.

3.2. *Effect of the initial location of hard bands with respect to the specimen thickness on damage development (thickness-reduced Steel 2)*

After air-bending, the outer surface of all thickness-reduced Steel 2 specimens was observed and the amount of cracking was qualitatively determined for each specimen (Figs. 6 and 7):

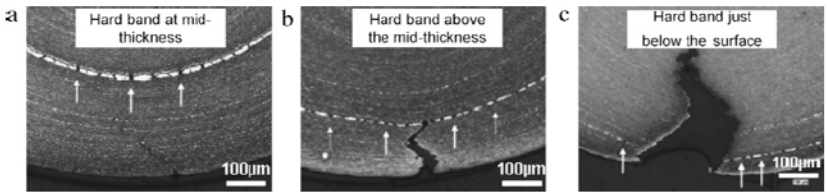

Fig. 6. Cross-section optical micrographs (LePera etching) after a 180° bending of thickness-reduced Steel 2. (a) Case 2, (b) case 3 and (c) case 4. White lines are thicker hard bands. White arrows illustrate some of the cavities that nucleated at hard bands.

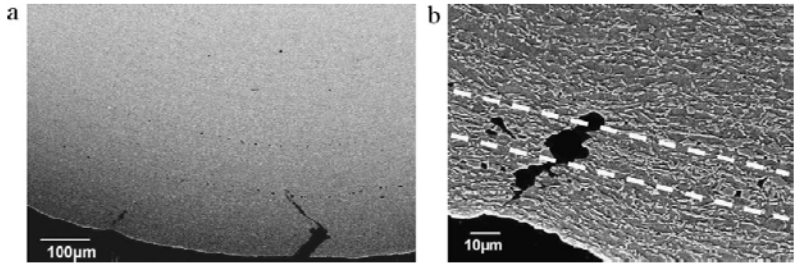

Fig. 7. Cross-section SEM observations of sub-surface microcracks of thickness reduced Steel 2 after bending with a 142° angle, case 3 (Nital etching). (a) General view: nucleation and propagation of two microcracks. (b) Close-up view of the bottom left microcrack in (a) which initiated at a hard band (located between white dotted lines). Necking is evidenced between this microcrack and the outer surface.

- For case 1 and 180° bending: no crack was observed at the outer surface.
- For case 2 and 180° bending: a "microcrack" was observed at the outer surface (Fig. 6a).
- For case 3 and 180° bending: a "crack" was observed at the outer surface (Fig. 6b).
- For case 3 and 142° bending: a "microcrack" was observed at the outer surface and a sub-surface (internal) microcrack was evidenced in cross-section (Fig. 7).
- For case 4 and 180° bending: a "macrocrack" was observed at the outer surface (Fig. 6c).
- For case 4 and 110° bending: no crack was observed at the outer surface but internal damage at hard bands was found in cross-section.

As expected, for all specimens bent up to 180°, cracking becomes more and more severe when shifting the hard band (located at mid-thickness before machining of the thickness-reduced specimens) toward the outer surface (i.e., from case 1 to case 4). As observed in Fig. 6, cavities nucleated at hard bands and bending cracks extended over directions inclined by 45° with respect to the local tensile direction. At a finer scale, nucleation of cavities in Steel 2 appears in a way similar to what was observed in Steel 1, i.e., mainly by decohesion at ferrite/martensite interfaces.

Fig. 7 shows sub-surface cracks observed after bending tests interrupted before macroscopic cracking. Just below the surface, at a distance of about 50 µm from the outer surface, internal "microcracks", which did not reach the surface, were observed, together with local necking. In the particular case of Fig. 7, no microcrack was observed with the magnifying glass, which strongly suggests that microcracks indeed nucleated from underneath the outer surface. This indicates that during air-bending, a microcrack might initiate from underneath the outer surface, provided that a critical combination of stress (or strain) and local sensitivity to damage (detrimental hard band) is reached. More precisely, even if the microcrack may have reached the outer surface somewhere in three dimensions (i.e., out of the plane of the polished cross-section), it may have developed preferentially at (and even have nucleated from) subsurface hard bands. Local necking has thus resulted from strain localisation between the nucleated damage cavities and the outer surface.

3.3. *Quantitative damage nucleation criterion (Steels 1 and 2)*

As the transformation of retained austenite into martensite in hard bands occurs well before nucleation of damage cavities, coupling between the austenite phase transformation and damage development can be assumed to be weak. In addition, in order to perform an accurate stress and strain analysis at the scale of individual phases, it would be necessary to assess the three-dimensional geometry of secondary phases in hard bands but this data is not readily available for all bands that were investigated in cross-section in the present study. As this data is a key parameter to any micromechanical modelling (see Section 3.4), it was chosen in the present study to derive a phenomenological, but quantitative damage nucleation criterion.

In order to derive a quantitative criterion for damage nucleation at hard bands, a relationship between the presence of damage cavities (or local interfacial decohesion), the local band thickness (as measured from two-dimensional cross-sections) and the local "mesoscopic" strain was determined for all bent specimens.

The local "mesoscopic" strain was defined as the average strain in the region of interest, i.e., without taking the heterogeneous local mechanical properties (i.e., soft matrix with harder bands) into account. In this simplified analysis, the material was thus considered to be homogeneous for the calculation of strain through the specimen thickness.

3.3.1. *Simplified analysis of the local "mesoscopic" strain through the thickness of an air-bent specimen*

The local "mesoscopic" strain at each band for all bent specimens (i.e., with various bending angles from 110 to 180°) was determined by using a simple analytical formula. Several formulae are available in literature to determine the local bending strain in a homogeneous medium [28,29]. As a first approximation the local "mesoscopic" strain was determined using a geometrical approach:

$$\varepsilon = \ln\left(1 + \frac{y}{R}\right) \quad (1)$$

where y is the distance between a hard band and the neutral fibre (along the thickness direction) and R is the bending radius at the neutral fibre. Marciniak et al. [28] used this formula in the case of

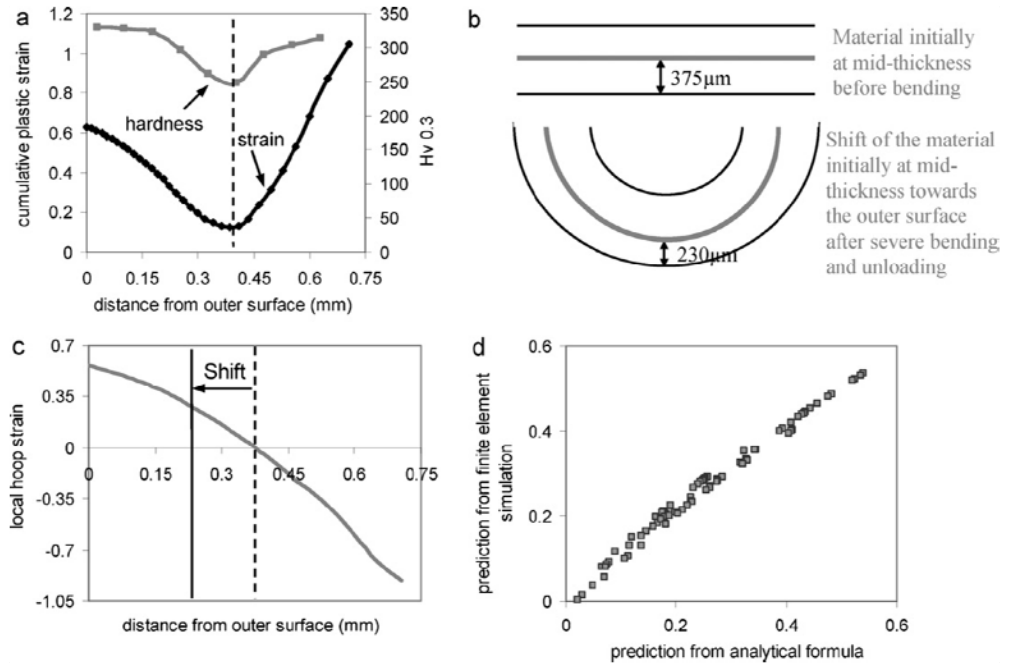

Fig. 8. (a) Evolution of cumulative plastic strain [36] and Vickers hardness (load 300 g) across the specimen thickness after bending up to 180° and then unloading (thickness-reduced Steel 2, case 2). The neutral fibre is represented by the vertical dashed line (0.38 mm from outer surface). (b) Schematic view of the region of the specimen which is closest to the punch. The shift of the material initially at mid-thickness (0.375 mm from the outer surface) toward the surface in tension (0.23 mm from the outer surface) is illustrated by thick grey lines. (c) Finite element estimate of local hoop strain along the specimen thickness after bending up to 180° and then unloading [36] (thickness-reduced specimen of Steel 2). The initial location of material initially at mid-thickness (i.e., before bending) is represented by the dashed vertical line (0.375 mm from outer surface) and its location after bending is represented by the continuous vertical line (0.23 mm from the outer surface). (d) Validation of calculation of the local hoop strain by the analytical formula (Eq. (2)) for all bent specimens.

a neutral fibre located at mid-thickness of the specimen (involving small strain assumption).

In the past, several studies [30–32] assumed that the sheet thickness remains constant during the bending process. However, this assumption is not realistic in the case of highly formable materials such as TRIP steels. In the severe bending conditions used here, the neutral fibre significantly moved apart from the mid-thickness: a high amount of strain is reached locally, so that the updated geometry of the bent specimens should be taken into account for the analysis of the effect of hard bands. Therefore, to avoid this shortcoming, the decrease in thickness and the shift of the neutral fibre from mid-thickness have to be considered as in [33–35] to accurately predict the bendability of sheets.

Therefore, Eq. (1) was modified by considering the updated location of the neutral fibre through the thickness after bending. It was derived as follows:

$$\varepsilon = \ln\left(1 + \frac{t/2 - d + y_0}{R}\right) \quad (2)$$

where t is the thickness of the sheet, d is the distance between the point under consideration and the outer surface, y_0 is the algebraic distance between the neutral fibre and the mid-thickness of the specimen ($y_0 > 0$: the neutral fibre was located between the mid-thickness and the inner surface) and R is the radius of curvature at the neutral fibre, all from the updated geometry. To use this formula, the location of the neutral fibre had to be determined.

3.3.2. Determination of the location of the neutral fibre

For thickness-reduced Steel 2, the location of the neutral fibre was first determined from Vickers hardness measurements on polished longitudinal cross-sections along the thickness of specimens bent up to 180° and then unloaded. For the load selected (i.e., 0.3 kg), hardness indents were about 45 µm in size. This value is much higher than both the size of M/A islands and width of hard bands. Therefore, these measurements are considered to be representative of both four "cases" considered here. In fact, the hardness of both as-received sheets, measured in the same conditions, was found to be constant through the sheet thickness. Due to the severe bending conditions used here, the significant reduction in thickness after bending (from 0.75 mm down to 0.7 mm) was taken into account in the following measurements. The region of minimum hardness after bending and unloading was located at 380 µm from the outer surface, i.e., 30 µm below the mid-thickness in the updated geometry (Fig. 8a).

This value was compared to finite element estimation of the location of the minimum cumulative plastic strain [36]. Finite element simulations were carried out considering a homogeneous material and assuming an anisotropic elastoplastic constitutive behaviour with mixed kinematic and isotropic hardening. The experimental load vs. punch displacement curves were well predicted by the numerical simulation. More details about these calculations are given in [36]. A good agreement was also obtained between the location of, respectively, the region with minimum hardness and that with minimum cumulative plastic strain (Fig. 8a).

3.3.3. Derivation of the local "mesoscopic" strain after air-bending and unloading

Once the location of the neutral fibre was determined, both the distance between the outer surface and each band, as well as the local radius of curvature of the neutral fibre were measured on cross-section micrographs of the (bent + unloaded) specimens. The local "mesoscopic" hoop strain was then determined by using Eq. (2) as a function of the distance from the outer surface. To confirm the validity of the analytical strain formula, the values of the local hoop strain predicted by finite element simulation [36] and by the geometrical model were plotted in Fig. 8d for all specimens (various

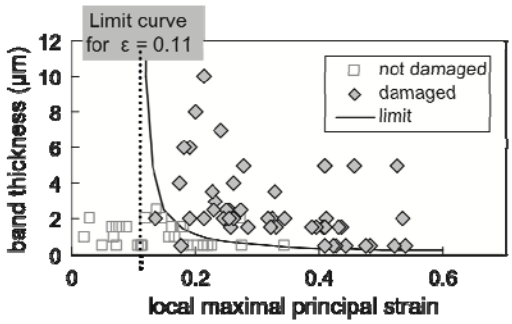

Fig. 9. Damage development criterion (Eq. (3)) at hard bands for all bent specimens (observed from 2D sections) as a function of the local band thickness and the local "mesoscopic" maximal principal strain calculated with the analytical formula.

initial locations of the main hard band and various bending angles). Very good agreement was observed between predictions from the two methods. Therefore, the analytical formula can be used to estimate local "mesoscopic" strains for the testing conditions used in the present study.

3.3.4. Investigation of damage at hard bands as a function of the local "mesoscopic" strain

In the following, the "mesoscopic strain" will be called "strain" for simplification. The relationship between nucleation of damage cavities, band thickness and local hoop strain is given in Fig. 9 for all bending angles, in the case of thickness reduced Steel 2 (i.e., from 110° to 180°). Despite bands were sometimes discontinuous (at least in two-dimensional sections), inducing scattering for the values of both band thickness and d (used in Eq. (2)), such uncertainties were evaluated to be of minor significance. Damage nucleation clearly depends on both the local thickness of the hard band and the local hoop strain. A limit curve between a "safe region" and a "damage region" is proposed in Fig. 9 according to Eq. (3). To determine a quantitative criterion for damage nucleation in bending, the left part of the limit curve (i.e., for lower values of strain) had to be assessed. As previously mentioned in Section 3.1.2, first damage cavities were observed at thickest hard bands for an average strain close to 0.11 in uniaxial tension for Steel 1. For lower amounts of strain, no cavity was observed. As damage mechanisms and microstructure were similar for both steels, a vertical "limit" straight line was plotted for a true strain of 0.11 by assuming that the critical strain is, in fact, a maximal principal strain. To derive a quantitative criterion for damage nucleation during air-bending, a simple heuristic equation of the limit curve was chosen as follows:

$$t_b = \frac{a}{\varepsilon_1 - b}, \quad \text{for } \varepsilon_1 > b \tag{3}$$

where t_b is the band thickness, ε_1 is the maximal "mesoscopic" principal strain at this band (hoop strain in air-bending, tensile strain in uniaxial tension) and a and b are two fitting material parameters. For the considered Steel 1 and Steel 2, $a = 0.1$ and $b = 0.11$. The value of a was determined by a trial-and-error method and the value of b was given by the vertical tangent curve for a strain of 0.11.

From Eq. (3), most of the bands thicker than 2 μm are actually damaged for any value of ε_1 at least equal to 0.11. After $\varepsilon_1 \sim 0.4$, all bands are damaged whatever their thickness. For intermediate values of strain: $\varepsilon_1 \sim 0.2$, most of the bands having a thickness ranging between 1 and 2 μm are damaged. This is in agreement with the metallographic cross-section observations: M/A islands (size ranging between 1 and 2 μm) were damaged far from the mid-thickness after a tensile strain of at least 0.2. Two experimental observations of "damaged" bands were predicted to be located in the "safe area" (yet, close to the limit curve). In these two bands, however, only a very low amount of cavities was observed.

The vertical limit straight line for a strain of 0.11 (Fig. 9) was set from uniaxial tension results. However, the strain path experienced during air-bending is an intermediate case between uniaxial tension and plane strain states, depending on the width-to-thickness ratio of the bent specimen. Yan et al. [37] studied the transformation behaviour of retained austenite into martensite for various deformation modes on a 1 mm-thick low alloy TRIP600 steel and they showed that retained austenite transformed into martensite earlier in plane strain conditions than in uniaxial tension. Numerical simulation of the bending tests considered here [36] showed that accurate modelling could actually be performed under a plane strain assumption. This means that the higher stress triaxiality undergone in bending (with respect to uniaxial tension), may lead to a shift toward lower values of the parameter b, and thus to a shift of this limit curve toward lower amounts of strain. Jacques et al. [6] already showed that such damage cavities can appear in TRIP-aided steels for very low amounts of strain. In their work, they performed tensile tests on notched specimens on two TRIP-aided steels (one with a high amount of silicon, another one with a lower silicon content) and damage was observed for average strains higher than 0.06 and 0.09, respectively. This difference between their and our results is probably due to the difference in stress triaxiality between smooth and notched specimens. Indeed, stress triaxiality might play a significant role in interfacial decohesion between harder and softer phases (as well as in the mechanically induced transformation of retained austenite) and should be included in the "mesoscopic" criterion. This requires quantitative evaluation of the effect of stress triaxiality on the nucleation of damage cavities by using a variety of mechanical tests on the same TRIP-aided steel.

3.4. Discussion

3.4.1. Effect of the (central) main hard band on the air-bending ability

To assess what happens to a central hard band during bending, it was necessary to experimentally determine the location, after a 180° bending followed by unloading, of the material initially located at mid-thickness. The hard band (in case 2) was used as a marker in cross-section observations of (bent + unloaded) specimens (Fig. 2b). In agreement with these observations, the abovementioned numerical simulations [36] showed that the material initially at mid-thickness (375 μm from the outer surface) was eventually located at 230 μm from the outer surface after bending (Fig. 8b and c). In the following, this is considered to be true for all four cases.

As the material initially at mid-thickness was shifted toward the outer surface during bending, the central hard band (initially at mid-thickness for Steel 2, case 2) was eventually loaded in tension during bending (here, up to a strain of about 0.3, see Fig. 8c) and could thus possibly be damaged during very severe bending. A band located at mid-thickness does not seem to directly impact the air-bending ability in more conventional bending conditions but hard bands closer to the surface have to be avoided, as they are more severely stretched during bending. The severe air-bending conditions chosen here are not representative of any automotive part, but such strain levels can more easily be reached in other forming processes where tension or stretching are involved in addition to bending. Therefore, it is important to underline that in the TRIP-aided steels investigated here, the central hard band has to be stretched by less than 0.1 to avoid damage cavity nucleation during forming. After (less severe) bending of Steel 1 (i.e., in more conventional bending conditions), the central hard band only undergoes a local "mesoscopic" strain of 0.06, which, by using the above cri-

terion, now explains why almost no damage was detected at the central hard band during the present tests on Steel 1.

3.4.2. Comparison of the present criterion with a micromechanical approach

The two phases that are present after significant strain, i.e., ferrite and martensite, strongly differ in strength and this plays an important role in the plastic flow behaviour of low alloy TRIP steels due to the interactions between harder and softer phases. However, the aim of this study was to propose a simple mechanical approach to derive a relationship between damage, local microstructural features of hard bands and local "mesoscopic" strain (averaged over the two phases). Using a micromechanical model would imply, in fact, use of two micromechanical models, one for the vicinity of the thickest hard bands, and one for the rest of the material (with thinner bands or even with more homogeneously dispersed M/A islands). Micromechanical models used for this purpose in open literature assumed a "homogeneous" microstructure at the macroscopic scale (i.e., only one micromechanical model throughout the thickness), which is not relevant to the case of this study. That is why micromechanical approaches such as in [14] or [38] were not used in this work.

Another advantage of the present approach is that detailed morphological and mechanical characteristics of hard bands are generally not available. Indeed, this requires the knowledge of both the strength of the interfaces between ferrite and secondary phases, as well as a fracture criterion of harder phases to be determined. Moreover, it also requires the determination, in three dimensions, of the geometry of phase distribution (major hard islands but also thin bands of matrix) within the bands. This was, however, not necessary in the simplified approach used in the present study. Here, coupling between the local strain, the transformation rate and the behaviour of each individual phase was not explicitly taken into account in the present criterion because the present work was conducted at a "mesoscopic" scale (i.e., at an intermediary scale between the size of individual phases and the sheet thickness).

The criterion defined in Eq. (3) being based on "mesoscopic" strains, i.e., the material being considered as a homogeneous medium, the present approach can be tentatively applied to any high strength steel, whatever its microstructure and phase stability, provided that strain plays a role in damage nucleation. At the scale of the microcracks, however, the strong contrast in strength between the various phases of high strength steels (ferrite, retained austenite, bainite, and martensite) has to be considered to derive a physically based damage initiation criterion. Together with local microstructural and mechanical data (that have to be collected for every steel considered), average values of "critical" strains determined as in the present study could serve as boundary conditions for such micromechanical models.

As an intermediate modelling step, for the case of low alloy TRIP-aided steels, as the main hard band at mid-thickness is principally composed of martensite in the as-received state and as the large part of retained austenite remaining is already transformed into martensite for the threshold level of average strain considered here (0.11), one could first consider a simpler two-phase ferrite + martensite microstructure in the micromechanical model.

In addition, as the final aim of the present study was to implement damage initiation criterion in finite element simulations of air-bending, it is not possible to use a micro-mechanical model for which characteristic length of phases is much finer than mesh sizes that are conventionally used in such finite element simulations. One could instead, in a simplified manner, consider the material close to the hard band to be more sensitive to damage nucleation (threshold strain of 0.11) than the rest of the sheet (threshold strain of 0.20) and then use these two criteria in the framework of continuum damage mechanics to predict damage nucleation and thus the critical bending angle of a "composite" sheet. This is currently in progress.

4. Conclusion

Air-bending failure mode and damage development were investigated on two low alloy TRIP-aided steels and led to the following results:

- Using an original procedure based on thickness-reduced specimens, providing various locations of the main hard band (induced by chemical segregations) along the specimen thickness, the sensitivity to cracking during severe bending was quantified as a function of the location of the hard band with respect to the surface pulled in tension.
- The failure mode of TRIP-aided steels during bending is fully ductile. Sub-surface cracks seem to initiate at damaged hard bands. They propagate through the thickness with an angle of about 45° with the outer surface, typical of a shear mode. During air-bending, a crack might initiate below the outer surface provided that a critical combination of hoop strain and band thickness is reached.
- To provide guidelines for metallurgical optimization of the steels under interest, a quantitative relationship between damage, band thickness and local "mesoscopic" hoop strain was derived for the considered TRIP steels.

Acknowledgements

The authors would like to thank ArcelorMittal Global R&D for financial support. The authors also thank Nicole De Dave – Fabrègue (MINES ParisTech) for nanohardness measurements, Grégory Leuillier (ArcelorMittal) for XRD measurements, Stéphane Douchamps (ArcelorMittal) for strain measurements with Aramis software and Nathalie Adelaide (ArcelorMittal) for metallographic investigation of M/A islands.

References

[1] D.K. Leu, J. Mater. Process. Technol. 66 (1997) 9–17.
[2] K. Yamazaki, M. Oka, H. Yasuda, Y. Mizuyama, H. Tsuchiya, Nippon steel technical report no. 64 (1995) 37–44.
[3] Y. Nagataki, S. Tsuyama, Y. Hosoya, T. Okita, High-Strength Steels for Automotive Symposium Proceedings, 1994, pp. 239–244.
[4] V.F. Zackay, E.R. Parker, D. Fahr, R. Bush, Trans. ASM 60 (1967) 252–259.
[5] E. Girault, A. Mertens, P. Jacques, Y. Houbaert, B. Verlinden, J.V. Humbeeck, Scripta Mater. 44 (2001) 885–892.
[6] P. Jacques, Q. Furnémont, T. Pardoen, F. Delannay, Acta Mater. 49 (2001) 139–152.
[7] P. Jacques, Q. Furnémont, F. Lani, T. Pardoen, F. Delannay, Acta Mater. 55 (2007) 3681–3693.
[8] G.B. Olson, M. Cohen, Metall. Trans. 7A (1976) 1897.
[9] I. Tsukatani, S. Hashimoto, T. Inoue, ISIJ Int. 31 (1991) 992.
[10] Y. Sakuma, O. Matsumura, H. Takechi, Metall. Trans. 22A (1991) 489–498.
[11] M. Lin, G.B. Olson, M. Cohen, Metall. Trans. 23A (1992) 2987–2998.
[12] H. Huang, O. Matsumura, T. Furukawa, Mater. Sci. Technol. 10 (1994) 621–626.
[13] G.N. Haidemenopoulos, A. Vasilakos, Steel Res. 67 (11) (1996) 513–519.
[14] J. Bouquerel, A. Verbeken, B.C. De Cooman, Acta Mater. 54 (2006) 1443–1456.
[15] J.R. Patel, M. Cohen, Acta Metall. 1 (1953) 531–538.
[16] S.S. Hecker, M.G. Stout, K.P. Staudhammer, J.L. Smith, Metall. Trans. 13A (1982) 619–626.
[17] E. Girault, A. Mertens, P. Jacques, Y. Houbaert, B. Verlinden, J. Van Humbeek, Scripta Mater. 44 (2001) 885–892.
[18] K.I. Sugimoto, R. Kikuchi, S.I. Hashimoto, Steel Res. 73 (2002) 253–258.
[19] Q. Furnémont, M. Kempf, P. Jacques, M. Göcken, F. Delannay, Mater. Sci. Eng. A328 (2002) 26–32.
[20] A. Dalloz, J. Besson, A.F. Gourgues-Lorenzon, A. Pineau, Eng. Fract. Mech. 76 (2009) 1411–1424.
[21] Aramis system, Optical 3D deformation analysis software developed by GOM GmbH. <http://www.gom.com/3d-software/aramis-software.html>.
[22] J. Steninger, A. Melander, Scand. J. Metall. 11 (2) (1982) 55–71.
[23] J. Sarkar, T.R.G. Kutty, K.T. Conlon, D.S. Wilkinson, J.D. Embury, D.J. Lloyd, Mater. Sci. Eng. A316 (2001) 52–59.
[24] W.Y. Chien, J. Pan, S.C. Tang, Int. J. Plast. 20 (1981) 1953–1981.

[25] G. Avramovic-Cingara, Y. Ososkov, M.K. Jain, D.S. Wilkinson, Mater. Sci. Eng. A516 (2009) 7–16.
[26] M. Radu, J. Valy, A.F. Gourgues, F. Le Strat, A. Pineau, Scripta Mater. 52 (2005) 525–530.
[27] K.I. Sugimoto, M.A. Misu, M. Kobayashi, H. Shirasawa, ISIJ Int. 33 (1993) 775–782.
[28] Z. Marciniak, J.L. Duncan, The Mechanics of Sheet Metal Forming, first ed., A. Arnold, Great-Britain, 1992, pp. 68–99.
[29] H. Livatyali, G.L. Kinzel, T. Altan, J. Mater. Process. Technol. 142 (2003) 532–543.
[30] Z.T. Zang, S.J. Hu, Int. J. Mech. Sci. 40 (1998) 533–543.
[31] W.M. Quach, J.G. Teng, K.F. Chung, Eng. Struct. 26 (2004) 1249–1259.
[32] W.M. Quach, J.G. Teng, K.F. Chung, J. Constr. Steel Res. 65 (2009) 1803–1815.
[33] C.T. Wang, G.L. Kinzel, T. Altan, J. Mater. Process. Technol. 39 (1993) 279–304.
[34] M. Ben Bettaieb, X. Lemoine, L. Duchêne, A.M. Habraken, Mater. Sci. Eng. A528 (2010) 434–441.
[35] M. Ben Bettaieb, X. Lemoine, L. Duchêne, A.M. Habraken, Mater. Sci. Eng. A528 (2010) 442–448.
[36] D. Rèche, T. Sturel, A.F. Gourgues-Lorenzon, J. Besson, Proceeding of European Conference of Fracture 18, Dresden, Germany, 2010, pp. 1–8.
[37] H.Y. Yan, G.Y. Kai, M.D. Jian, Mater. Sci. Eng. A441 (2006) 331–335.
[38] F. Lani, Q. Furnémont, T. Van Rompaey, F. Delannay, P. Jacques, T. Pardoen, Acta Mater. 55 (2007) 3695–3705.

II.B. Complementary observations

In this part, additional observations about bending of thickness-reduced Steel 2 with various locations of hard bands are reported.
Figure III.25 shows specimens bent up to 180° for four main hard band configurations. As expected, the severity of the test increases with the proximity of the central segregation with the outer surface.

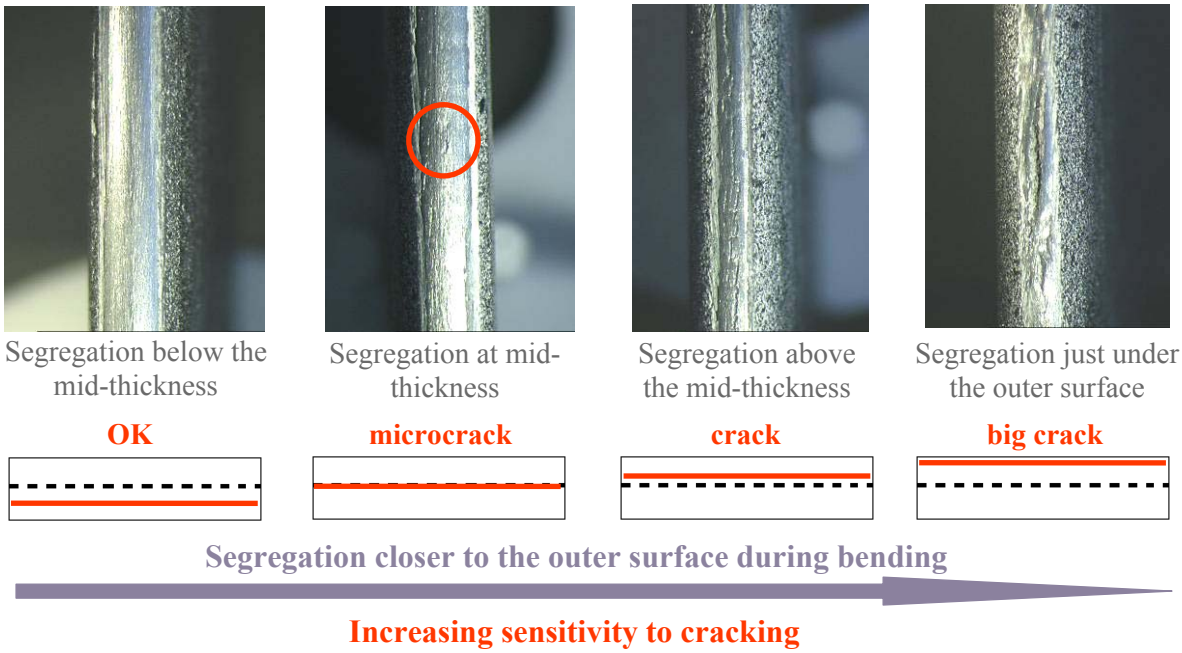

Figure III.25. Macrographic observations of four specimens of reduced-thickness Steel 2 bent along TD up to 180° with various locations of the main segregation band.

Figure III.26 illustrates cross-section optical microscopy observations for the four previous cases after a 180° bending and a LePera etching.

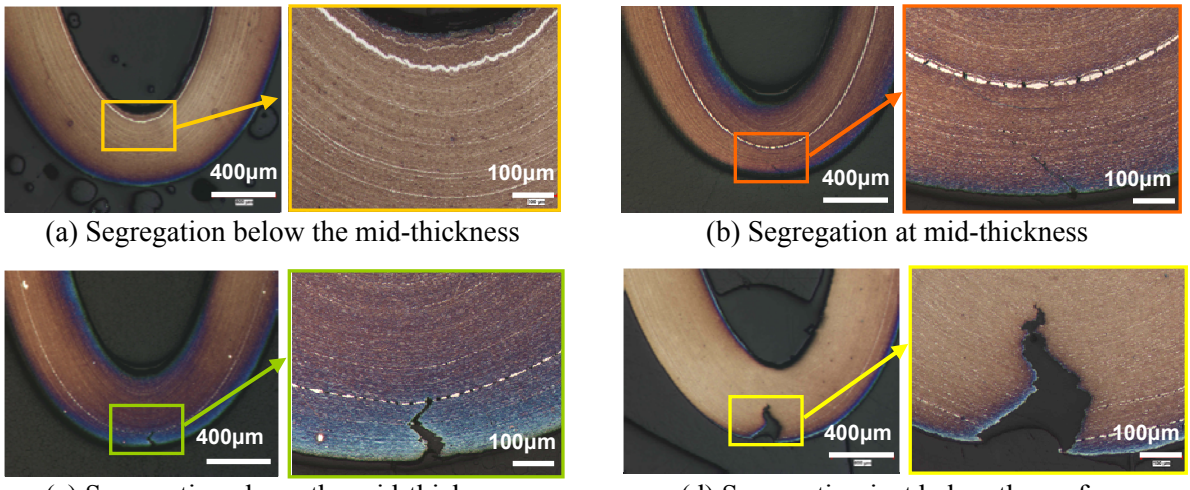

(a) Segregation below the mid-thickness (b) Segregation at mid-thickness

(c) Segregation above the mid-thickness (d) Segregation just below the surface

Figure III.26. Optical micrographs of thickness-reduced Steel 2 for various locations of the main hard segregation band with a general view and a close-up view, LePera etching. (a) Segregation below the mid-thickness, (b) segregation at mid-thickness, (c) segregation above the mid-thickness, (d) segregation just below the surface.

As observed in Figure III.25, cracking becomes more and more severe with a shift of the segregation towards the outer surface. Both the opening and the depth of crack increase with the proximity of the segregation with the surface.

In order to investigate crack initiation more precisely, additional air-bending tests were carried out with specimens having the segregation just below the outer surface. Air-bending tests were interrupted just before cracking by a trial and error procedure (bending angles 110°, 142° and 160°) followed by metallographic observations using light optical and scanning electron microscopy. Figure III.27 shows pictures obtained for two specimens with the segregation band below the outer surface: one with the segregation band close to the surface (~130µm) and the other one with the segregation band very close to the surface (~50µm). Damage at hard band is observed for the two specimens without any crack at the outer surface. As expected, damage at the segregation band is more intense for the specimen with the segregation just below the surface.

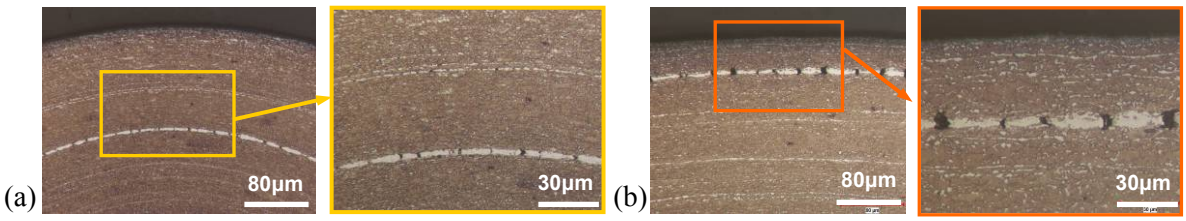

Figure III.27. Optical micrographs of thickness-reduced Steel 2 specimens bent without crack: (a) Segregation 130µm below the surface with a 160° bending angle, (b) segregation 50µm below the surface with a 110° bending angle. Air-bending along TD.

Then, additional tests were performed with a little more severe bending angle, in order to stop the test just before cracking at the outer surface. Figure III.28 and Figure III.29 show internal cracks at hard segregation bands with necking at the outer surface above each sub-surface crack, meaning that in air-bending, cracks could initiate from just below the surface, as already suggested in Part I of this chapter. It is also noticed in Figure III.29 that the crack propagates with a 45° angle as already observed in part I.B.

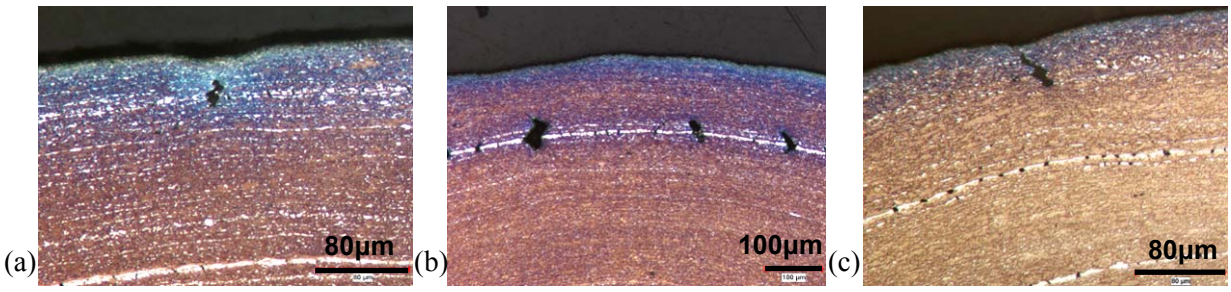

Figure III.28. Optical micrographs of sub-surface cracks for three air-bent thickness-reduced Steel 2 specimens with a 142° angle (LePera etching).

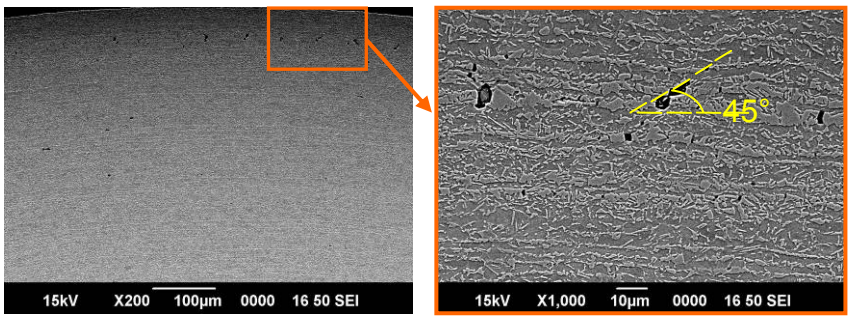

Figure III.29. SEM observations of damage at hard band located just under the outer surface (Nital etching). Bending up to 110° for thickness-reduced Steel 2.

Finally, Figure III.30 illustrates three cracks due to air-bending. The central crack does not give enough precise clues to determine the exact initiation point (maybe from the surface or maybe from just below where there is a change in the direction of propagation). But thanks to the two small cracks located at each side of the main microcrack, and being initiated below the outer surface at the same hard band, we assume that all three cracks initiated at that segregation band. There are also a lot of cavities or even of arrested microcracks along that segregation band (e.g. in the bottom left picture of Figure III.30).

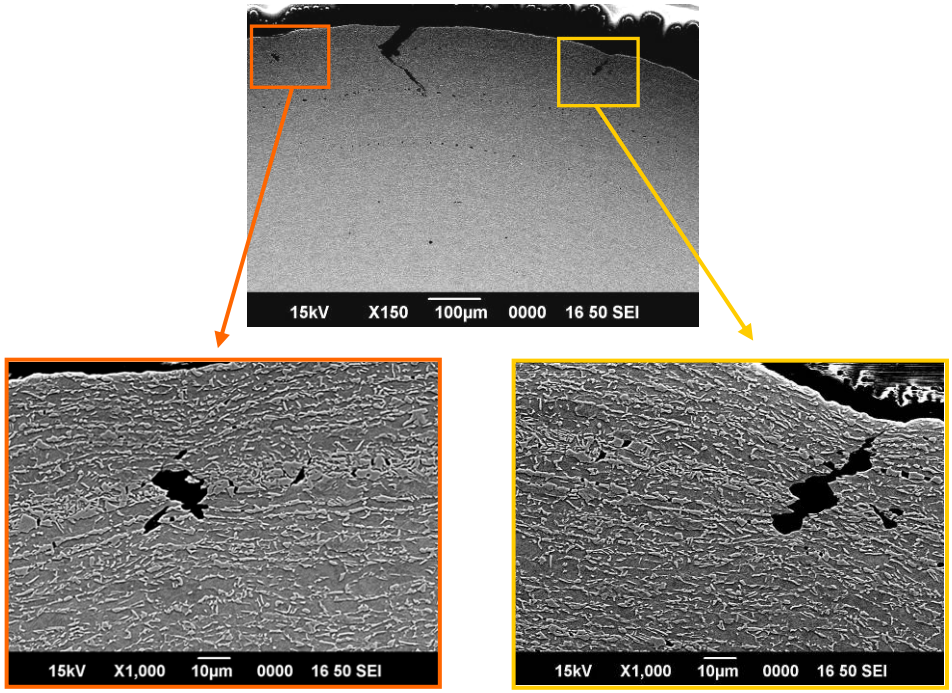

Figure III.30. SEM observations of sub-surface cracks of two thickness-reduced Steel 2 bent specimens (Nital etching), 142° bending angle.

It can be concluded that in air-bending, cracks may actually nucleate from segregation bands, provided that the combination of band thickness and local strain is favourable. A quantitative relationship was given by Equation (3) in the previous part with (for this steel) a = 0.1 and b = 0.11. However, this relationship is based on a very simplified analysis of the bending test.

III. Summary of Chapter 3

In this chapter, damage mechanisms were studied both in air-bending and stretch bending tests as well as in tensile tests with various true strain levels. In a second part, the influence of segregated bands as a function of their locations through the thickness was more particularly investigated using thickness-reduced specimens of Steel 2.
The investigation of damage mechanisms gave the following results:

- The fracture mode is ductile both in air-bending and in stretch bending. Using light and scanning electron microscopy, cracks were shown to propagate with a 45° angle with respect to the outer surface, indicating a strong sensitivity to strain localization.

- Damage was noticed at hard segregated bands with more cavities for the thickest bands for all bending tests. This suggests that segregation bands play a non-negligible role in fracture during bending. In fact, in air-bending, the closer the thicker segregation bands to the outer surface, the higher the severity of cracking.

- Cracks initiate from the outer surface or from just underneath (at a hard band) in air-bending while they initiate from the central segregation band in stretch bending.

- Thanks to tensile tests, it was revealed that the fracture strain of the main hard band is close to 0.10 for the three TRIP-aided steels studied. Based on this result and on the previous observations, a simple quantitative relationship between cavity nucleation, band thickness and local “mesoscopic” strain was proposed.

Résumé du Chapitre 3

Dans ce chapitre, les mécanismes d'endommagement ont été étudiés à la fois en pliage en V et sous traction, ainsi qu'en traction à différents taux de déformation. Dans une deuxième partie, l'influence des bandes de ségrégation en fonction de leurs positions à travers l'épaisseur a été plus particulièrement étudiée grâce aux échantillons de l'acier 2 rectifié.
L'étude des mécanismes d'endommagement a révélé les résultats suivants :

- *Le mode de rupture est ductile à la fois en pliage en V et en pliage sous traction. Grâce à la microscopie optique et à balayage, il a été observé que les fissures se propagent à 45°, indiquant une forte sensibilité à la localisation en déformation.*

- *L'endommagement a principalement été observé sur les bandes de ségrégation et nous avons montré que les bandes les plus épaisses étaient les plus endommagées. Ce résultat suggère le rôle non négligeable des structures en bandes sur la fissuration en pliage. De plus, en pliage en V, plus les bandes de ségrégation sont proches de la surface, plus les éprouvettes fissurent tôt.*

- *Les fissurent s'amorcent en surface ou juste en dessous (sur les bandes de ségrégation) en pliage en V, tandis qu'elles s'initient à partir de la ségrégation centrale en pliage sous traction.*

- *Grâce aux tests de traction interrompus, nous avons montré que la déformation à rupture des bandes de ségrégation était proche de 0.10 pour les trois aciers TRIP étudiés. Utilisant ce résultat et les précédentes observations, une simple relation quantitative entre la germination de cavités, l'épaisseur des bandes et la déformation locale mésoscopique a été proposée.*

Chapter 4

Mechanical analysis of fracture during air and stretch bending tests

In chapter 2, air-bending tests have been modelled thanks to finite-element simulation without taking damage development into account. In chapter 3, it was demonstrated that damage mechanisms are different in air and stretch bending tests and the role of the hard bands on damage development was experimentally investigated.

In this section, constitutive equations were associated to a Gurson-Tvergaard-Needleman yield potential for the mechanical analysis of damage development and failure during air and stretch bending tests. A comparison between both air and stretch bending tests was first carried out for Steel 1. A complementary parametric study including the effect of meshing, friction coefficient and 2D vs. 3D modelling is then presented for the stretch bending test. In the last part of this chapter, the influence of the location of the band within the sheet thickness is numerically investigated on Steel 1 tested in air-bending.

Table of contents

I. Mechanical analysis of the air and stretch bending tests

This part is based on a project journal paper which is to be submitted for publication to *Engineering Fracture Mechanics*. The text of this article is reproduced below.

Flow and fracture analysis of a ultrahigh strength steel during stretch bending and air-bending tests

D. Rèche [1), 2)], J. Besson [1)], T. Sturel [2)], A.F. Gourgues-Lorenzon [1)]

[1)] MINES ParisTech, Centre des Matériaux, CNRS UMR 7633, BP 87
91003 Evry Cedex, France
[2)] ArcelorMittal Global R&D, Voie Romaine, BP 30320,
57283 Maizières-lès-Metz Cedex, France

Abstract

In order to evaluate the bendability of a ultra high strength steel, air-bending and stretch bending tests were performed along rolling and transverse directions. A full analysis of these tests was given with both experimental and numerical data. To examine and understand damage mechanisms involved, cross section observations were carried out both after interrupted air-bent tests and after broken and interrupted stretch bent tests. Cracks initiate from central segregation bands (if any) in stretch bending while cracks initiate from the outer surface or from just below in air-bending. The two tests were then modelled thanks to finite element simulation including a damage criterion, in 2D for the air-bending test and in 3D for the stretch bending test. An extension of the Gurson-Tvergaard-Needleman (GTN) model was used in this simulation with damage development principally governed by nucleation of cavities. Good agreement was obtained between experimental data and model predictions.

Key words

Air-bending, stretch bending, ultra high strength steel, finite element simulation, damage mechanisms.

1. Introduction

Stamping is one of the most common methods in industry to give specified shapes to sheet metal. Many different deformation modes are used to obtain the desired shape of sheet steel during stamping, such as stretching, bending, deep drawing, embossing, and so on. In recent years, the demand to reduce the weight of automotive vehicles led to increasing use of Advanced High Strength Steels (AHSS). Thus, the forming behaviour of these steels

had to be quantified both experimentally and numerically. Therefore, the finite-element simulation of various forming modes is required to characterize the formability of these materials and to determine the limit to which the material can be formed without reaching failure.

The forming limit depends on processing conditions and on the shape of the part. Hence, it is necessary to find an adapted failure criterion to well predict the sheet formability. The forming limit curve (FLC) is the most widely used criterion in sheet metal forming analysis (Keeler and Backofen, 1964; Goodwin, 1968). However, Laukonis and Gosh (1978), Graf and Hosford (1993) showed that FLCs are only valid along proportional strain paths. During metal stamping, the stress/strain state changes continuously, so that the loading path is generally not proportional. Consequently, traditional FLCs cannot be used for accurate predictions of the behaviour during bending.

Only a few papers deal with the initiation of fracture in bending. For example, in bending without tension, cracks seem to initiate from the surface (Chien et al., 1981; Steninger and Melander, 1982; Sarkar et al., 2001) or from just below. In stretch bending, there are a lot of papers addressed the location of the crack along the bent sheet, i.e., at the punch nose or at a sidewall.
Among them, Demeri (1981), Damborg (1998), Sadagopan et al. (2003), Hudgins et al. (2007) and Kim et al. (2009) performed stretch bending tests on several steels and aluminium sheets to determine their stretch bendability. Typically, the height at failure as a function of the R/t (punch radius over sheet thickness) ratio was reported as a measure of formability under stretch bending conditions. The test was stopped once the first failure appeared and they noticed that failure occurred at the punch nose radius of the specimen for small R/t ratios. When R/t increased above some limit, $(R/t)_c$, failure moved from the punch nose to the sidewall. For example, Hudgins et al. (2007) found that TRIP steels have a high value of $(R/t)_c$ compared to other UHSS. However, there was no information concerning the location of crack initiation through the thickness in all these studies, although the microstructure of the sheet may be not fully homogeneous through the thickness. Therefore, a mechanical analysis across the thickness is necessary.

In order to predict fracture during forming processes, several fracture and damage criteria have been proposed in the past (Cockroft and Latham, 1968; McClintock, 1968; Rice and Tracey, 1969; Gosh, 1976; Gurson, 1977; Leroy et al., 1981; Lemaitre, 1985; etc.). The family of continuum damage mechanics models was widely used to model forming tests. In these models, damage evolution is coupled with elastoplastic constitutive equations and fracture is predicted to occur as soon as the damage variable reaches a critical value. Gurson (1977) developed a ductile damage macroscopic constitutive law based on microvoid growth. Its model was largely used and extended in literature (Tvergaard, 1982; Tvergaard and Needleman, 1984). Gurson's model is the first micromechanical model for ductile fracture introducing a strong coupling between deformation and damage.

Several models were used in the past to analysed bending tests. Among them, Date et al. (1999) and Gan and Wagoner (2004) studied the springback of bent sheets. To accurately predict both bendability and fracture, Brunet et al. (1996) used a modified Gurson model with a Hill anisotropic yield criterion to simulate square-cup deep drawing. Hambli et al. (2004) simulated the air-bending process in 3D by coupling a Von Mises yield criterion with a Lemaitre damage equation. They showed that the simulation of air-bending, respectively with and without damage in the model, led to similar load/punch displacement

curves up to the maximum in load. For higher values of punch displacement, the model including damage development predicted a faster decrease in load than the damage-free model. More recently, two studies reported numerical simulation of forming tests, both using a Von Mises yield criterion coupled with a damage evolution equation, respectively, the Gurson-Tvergaard-Needleman (GTN) model (Uthaisangsuk et al., 2008) and the Lemaitre approach (Bahloul et al., 2006). Uthaisangsuk et al. (2008) used a galvanized bake-hardening steel of 1mm in thickness to study the Nakazima test and showed that the GTN model offers an acceptable sheet metal failure criterion. Bahloul et al. (2006) obtained a good prediction of punch load and stress distribution during the wiping-die bending process of an high strength low alloy steel using a 3D finite element simulation. Ben Bettaieb et al. (2010) simulated a pure bending test on a dual phase steel using a mixed hardening rule, an anisotropic yield criterion and an extended Gurson model. In their study, Luo and Wierzbicki (2010) used Hill's yield criterion coupled with a Modified Mohr-Coulomb (MMC) ductile fracture criterion (Bai and Wierzbicki, 2010) to predict the failure during stretch bending of DP780 steels. They demonstrated that the 3D finite element simulations provided the best prediction in terms of fracture location, load/displacement curves and failure wall stress compared to shell or plane strain finite element simulations. Kim et al. (2009) simulated the draw bending test on a DP980 steel with a coupled thermo-mechanical, damage-free finite-element model. They demonstrated that their model accurately predicted failure location, maximum stress and displacement at failure by taking the change in temperature during fracture into account. To summarize, from these analyses, an anisotropic yield criterion is required to account for the anisotropic behaviour of most of steels and to accurately predict curves, stress and strain fields. A mixed hardening rule enables to account for the Bauschinger effect and is more reliable in case of non proportional loading, as in the case of a prestraining before a bending test (Rèche et al., 2011).
The aim of the present study being to predict failure conditions for two different bending tests, the local approach to ductile fracture was chosen to be used by including damage in the constitutive equations.

In this study, elastoplastic constitutive equations coupled with damage development were chosen to describe damage mechanisms leading to fracture on one low alloy TRIP-aided steel both in air and stretch bending. As stretch bending tests were carried out at a very low displacement rate in the present study, it is reasonable not to take the change in temperature into account in the model. Thus, no thermo-mechanical model as in Kim et al. (2009) was used in this study. A model based on the GTN equations was used in the in-house finite element software Zset (Besson and Foerch, 1997). First, air-bending tests, stretch bending tests and metallographic observations were performed to determine fracture initiation mechanisms. The damage criterion was then introduced into existing constitutive equations (Rèche et al., 2011) for the modelling of both bending tests.

2. Materials and testing procedures

2.1. Material

A cold rolled low alloy TRIP-aided steel with a thickness of 1.6mm (C~0.2 wt%, Mn~1.6 wt%, Al+Si~1.5 wt%) was investigated in this study. Its mechanical properties are shown in Table 1. This material has a multiphase microstructure with martensite/retained austenite islands in a softer ferritic matrix. The third-thickness microstructure (Figure 1a) was

homogeneous while the mid-thickness microstructure presented bands of hard phases principally composed of retained austenite and martensite (Figure 1b).

	0.2% proof stress (MPa)	Tensile strength (MPa)	Uniform elongation (%)	Fracture elongation (%)
RD	467	866	15.0	20.0
TD	546	851	15.0	19.2

Table 1: Room temperature mechanical properties along rolling (RD) and transverse (TD) directions (ISO 20x80mm tensile specimens).

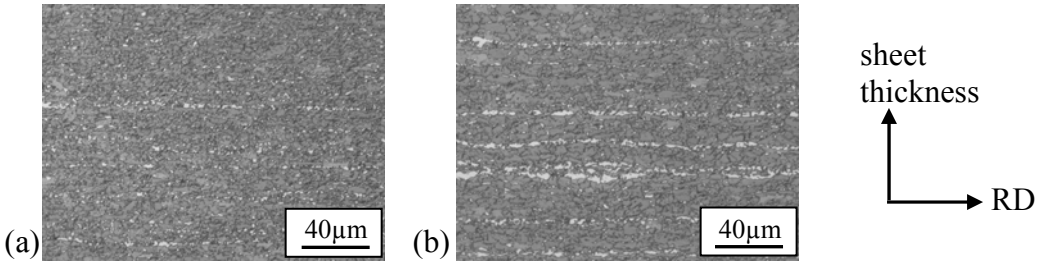

Figure 1: Light optical micrographs of the as-received steel sheet, LePera etching. (a) third-thickness microstructure, (b) mid-thickness microstructure. Hard phases (austenite + martensite) in white, ferrite in grey.

2.2. Air-bending tests

Air-bending tests were carried out at room temperature using a universal tensile machine on 50x100mm specimens (Figure 2). Air-bending tests were performed without lubrication. The sheet was laid on two rotary rolls and a very sharp punch (tip radius of 0.1mm) went down to bend specimens. Before the tests, the specimen edges were ground to avoid premature failure that could be due to cutting edge-induced damage effects sometimes encountered in AHSSs (Dalloz et al., 2009). Five specimens were tested along both rolling and transverse directions on as-received material until microcracking occurred (corresponding to a load drop of 5%) and a very good reproducibility was observed. Finally, the bending angle α (Figure 2b) was measured after unloading.

As in industrial stamping, bent areas are often already deformed when bending occurs, it seemed necessary to investigate the influence of prestraining before an air-bending test. In a previous study (Rèche et al., 2011), the influence of prestraining prior to air-bending and more particularly, the influence of the kinematic contribution to hardening was discussed but no damage was included in the model, leading to a good prediction of the load/displacement curve except at the end of the test. Tensile tests along TD with a prestraining of 10% were carried out on the as-received material and air-bending specimens were cut from tensile specimens and tested along TD until microcracking occurred.

(a) 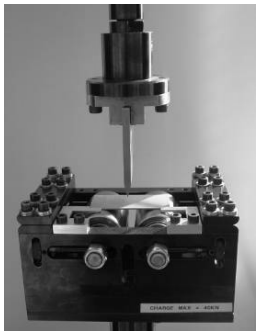

(b) 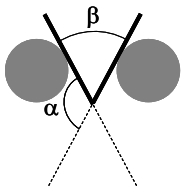

Figure 2: (a) Air-bending device (b) schematics of the air-bending test with α = bending angle.

2.3. Stretch bending tests

In order to investigate the formability of this steel, stretch bending tests were performed at room temperature. They were carried out on a conventional Instron servohydraulic testing machine designed and developed for that purpose making it possible to apply very low displacement rates (0.05mm/s) (Figure 3). As for an Erichsen test, the method consisted in clamping a 180mm x 40mm blank between a die and a blank-holder. In order to limit friction, lubrication was employed between the punch and the sheet. Grease was put on the punch radius and then a Teflon film was added on it. Specimen edges were ground before testing to avoid cracks starting from them. Five samples along both rolling and transverse directions were bent with three different punches (tip radii = 2mm, 4mm and 6mm, respectively) along the transverse direction. As expected, the higher the punch tip radius, the better was the bendability. Only results with the punch radius of 4mm will be given in the following. The test was stopped either once the sample was broken, or just before fracture to investigate interrupted stretch bent tests. Finally, the bending angle at fracture (α in Figure 3c) was given.

(a) 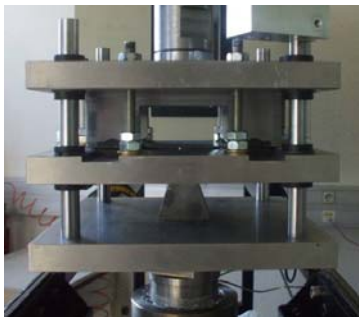

(b) 

(c) 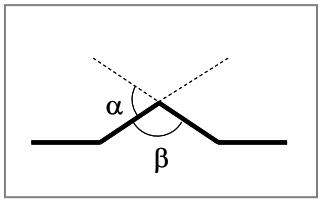

Figure 3: (a) stretch bending device, (b) stretch bending test in progress with specimen clamped between die and blank-holder and a punch radius of 4mm, (c) schematics of the stretch bent sheet (thick line) with α = bending angle.

3. Experimental results

3.1. Air-bending curves

Load vs. punch displacement curves are shown in Figure 4 both for as-received and prestrained specimens. The prestrained specimen was bent up to a lower value of the punch

displacement to get the first crack. Therefore, prestraining prior to air-bending affects the bendability of the sheet because cracking was observed earlier. This result is in agreement with the work of Friedman and Luckey (2002) and Sarkar at al. (2001).

The hoop strain reached at the outer surface at microcracking for the as-received material was evaluated to be 0.27 in Rèche et al. (2011). If the amount of elongation (10%) applied during prestraining is removed from this value, the punch displacement corresponding to a hoop strain of 0.175 at the outer surface was found to be equal to 20.5 mm. This value is in very good agreement with the punch displacement at microcracking of the prestrained specimen. Thus, as a first approximation, an additive rule on strain can be used to estimate the bendability, for tensile strains applied along the same direction during both prestraining and bending. However, this very simple rule may obviously not work for other prestraining conditions.

Regarding the as-received steel bent along both rolling and transverse directions, slight differences were observed between the two curves. Note that the maximum load reached for the bent specimen along RD is lower than the one along TD. In addition, specimens taken along RD were bent up to a higher punch displacement than for TD specimens, meaning than the transverse direction is less ductile than the rolling one. These differences are consistent with the slight anisotropy of this steel in uniaxial tension.

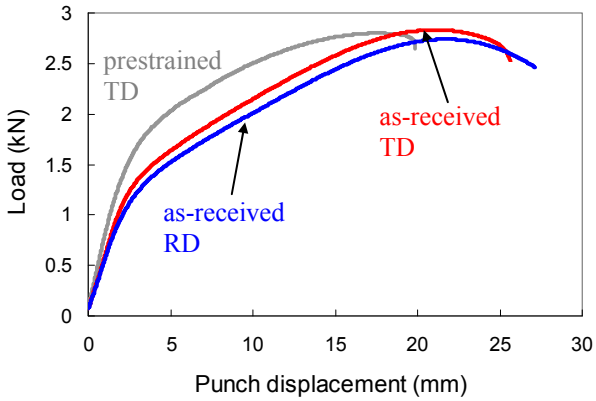

Figure 4: Air-bending test. Load vs. punch displacement curves both on as-received and on prestrained material.

3.2. Stretch bending curves

A stretch bending load vs. punch displacement curve is illustrated in Figure 5. In air and stretch bending, curves look very different. While in air-bending, the load decreased rather slowly after its maximum, in stretch bending, the load sharply decreased after its maximum due to unstable fracture. Note that in stretch bending, the load reached just before fracture was much higher than in air-bending test, this was due to the tension applied on the whole specimen in these bending conditions.

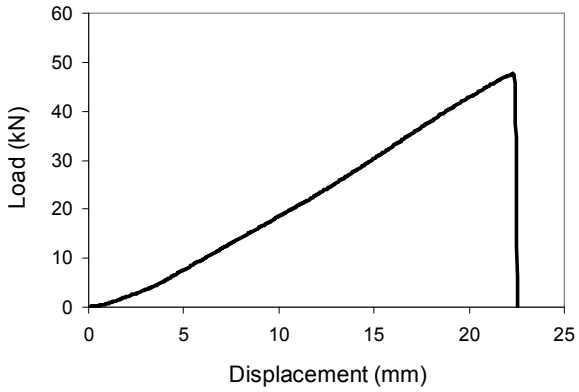

Figure 5: Stretch bending test along TD. Load / displacement curve.

3.3. Crack initiation both in air-bending and stretch bending

In order to investigate damage mechanisms, cross-sectional observations were carried out on one specimen after cracking in air-bending. As noticed in Figure 6, cracks generally initiated from the outer surface. In a recent study (Rèche et al, 2010), it was also noticed that cracks can initiate from just below the surface provided that there are thin hard bands underneath the outer surface.

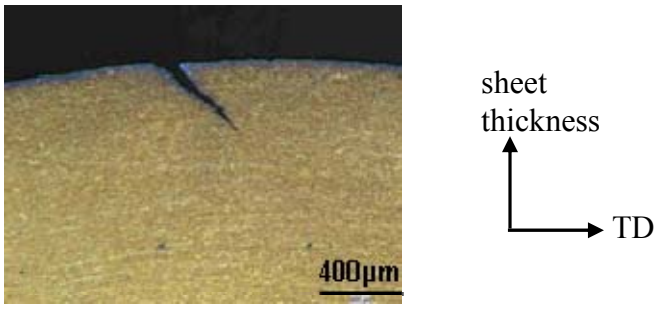

Figure 6: Cross-section of an air-bent specimen. Optical micrograph, LePera etching.

As stretch bending specimens broke suddenly, it was very difficult to interrupt stretch bending tests just before fracture even by using the device developed for this study. Stretch bent specimens appeared to be either safe or broken into two parts so it was difficult to stop the test with a crack inside the sheet thickness. In Figure 7, noticeable cavities located at the central hard band (in white) are seen in a broken specimen. In addition, a V-shaped kink was noticed in the cross-section of the fracture surface, close to the central hard band. Based on these observations, the central hard band seemed to play a significant role during stretch bending as a significant amount of damage initiated from it. In one case, however, the test was successfully stopped with an internal crack just before specimen failure (Figure 8). This figure suggests the following mechanism: first, cavity nucleation close to the central hard band, then, microcrack propagation with a 45° angle probably linked to both mechanical fields and sensitivity of the material to strain localization. In Figure 8a, necking of the sheet just above the crack was observed. The initial thickness of the as-received sample was 1.6mm and after stretch bending, just above the crack, the thickness was about 1.35mm. Out of the crack, the thickness was 1.45mm.

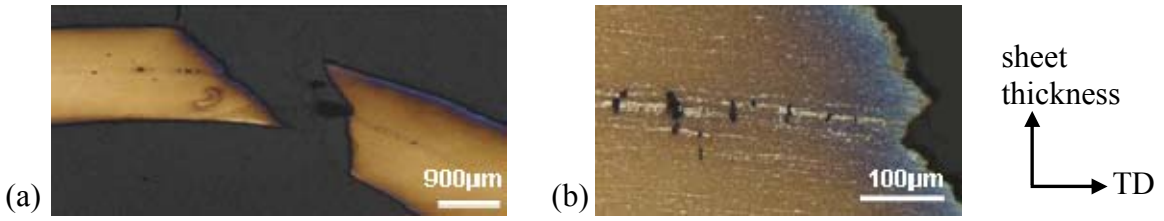

Figure 7: Optical micrographs after stretch bending. LePera etching. (a) General view of a broken sample, (b) close-up view of damage close to the central hard band.

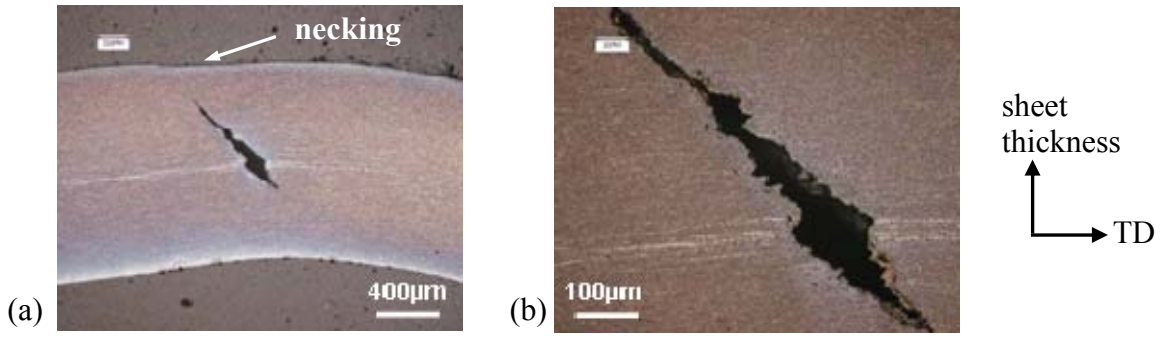

Figure 8: Optical micrographs after an interrupted stretch bending test. LePera etching. (a) General view of the cracked specimen, (b) close-up view of the crack which seems to have initiated from the central hard band.

Fractographic observations (Figure 9a, 9b, 9c) showed that in stretch bending, cracks propagated by a ductile mechanism, as dimples were observed on the fracture surface. In Figure 9a, the mid-thickness of the sheet was well visible (horizontal dark area). Figure 9b represents a close-up view of the mid-thickness part of the fracture surface. It seems that cleavage-like facets are observed in this area, contrary to Figure 9c where dimples were noticed everywhere out of this mid-thickness area. Damage was noticed with cavities located either at the martensite/ferrite interface or by cleavage of martensite islands (Figures 9d and 9e). In addition, damage was noticed to initiate first at hard bands and then in the softer matrix.

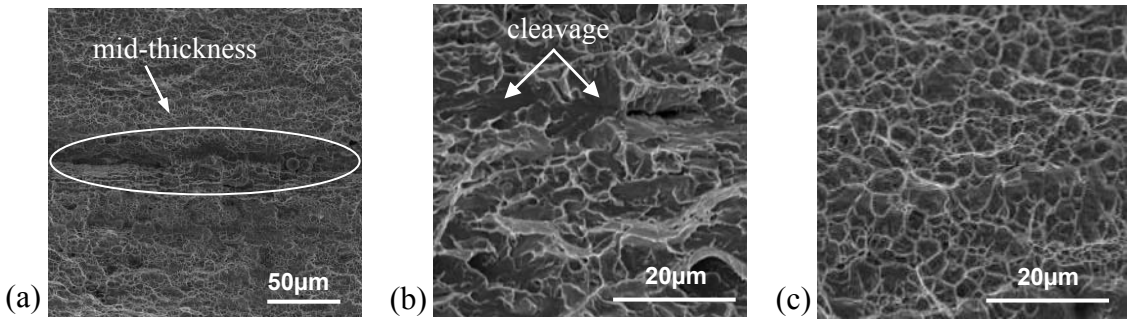

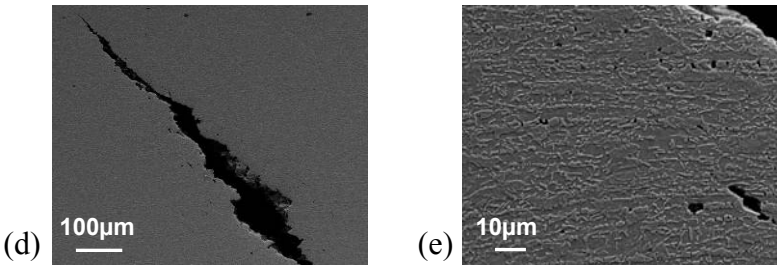

Figure 9: Fractographic observations by SEM of a broken sample after stretch bending. (a) General view with mid-thickness surrounded by a white ellipse, (b) close-up view of the mid-thickness with some of cleavage showed by white arrows, (c) close-up view of ductile failure with dimples far from the mid-thickness. (d, e) SEM observations after Nital etching of the crack and damage close to the crack at hard bands. The crack in the upper right corner of (e) is the one shown in (d).

Cross-sectional observations of cracking showed that crack initiation mechanisms are different for the two bending tests (initiation at the outer surface in air-bending vs. initiation from central hard band in stretch bending) so the key microstructural parameters controlling crack initiation might not be the same for the two investigated bending tests.

3.4. Investigation of cavity nucleation both at and out of hard bands

Uniaxial tensile tests interrupted after various strain levels were performed in previous work (Rèche et al., 2010) in order to investigate the beginning of damage cavity nucleation at hard bands. For this steel, cavities were first observed for an average true axial strain of 0.11 in uniaxial tension (Figure 10a). Then, it was also interesting to determine the beginning of nucleation in the rest of the steel ("softer matrix" composed of ferrite and austenite/martensite islands). Based on SEM observations performed on air-bent specimens (Figure 10b), cavities were observed in the tensile zone in the softer matrix. On the other hand, by using finite element analysis of the air-bending test (Rèche et al., 2011), the evolution of strain as a function of the thickness of the sheet was determined. Therefore, by coupling SEM observations and results of mechanical analysis, the nucleation of first damage cavities was observed in the softer matrix for a true strain close to 0.21.

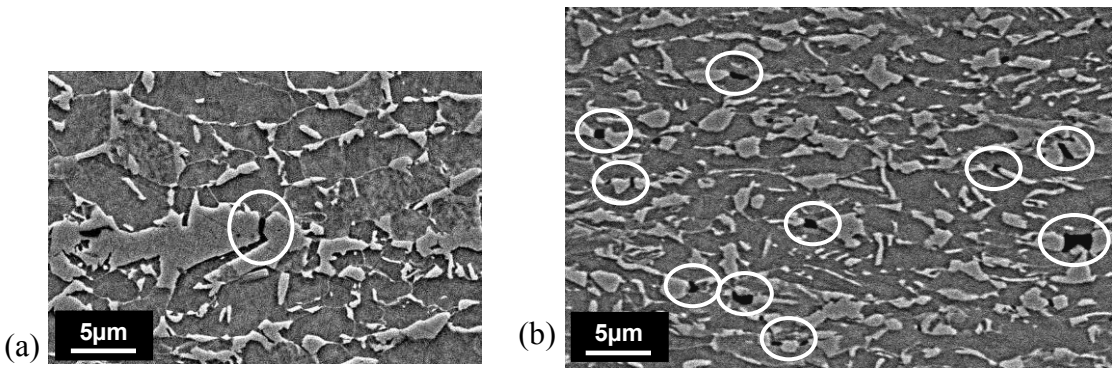

Figure 10: cross-section SEM observations of damage after a Nital etching. Damage cavities are surrounded with white circles. (a) Damage at hard band after an interrupted uniaxial tensile test ($\varepsilon = 0.11$), (b) damage in the softer matrix with either decohesion at martensite/ferrite interface or with cleavage at martensite islands (air-bent specimen).

4. Modelling

4.1. Constitutive equations

In a previous work, (Rèche et al., 2011), constitutive equations of this material were established thanks to an experimental database based on tensile tests on smooth and notched specimens and on shear tests. These constitutive equations included both isotropic and kinematic contributions to hardening with an anisotropic yield criterion (Bron and Besson, 2004). Other authors such as Eggertsen and Mattiasson (2009), Williams et al. (2010), Vladimirov et al. (2010) and Shinohara et al. (2010) also used a mixed hardening rule coupled with an anisotropic yield criterion.
To simulate both air-bending and stretch bending tests, the damage model used was based on extensions of the GTN model (Gurson, 1977; Tvergaard and Needleman, 1984). Thuillier et al. (2010) used similar method by predicting bending test on an aluminium thin sheet. In their study, they characterize the mechanical behaviour of the material using tensile tests on smooth and notched specimens and equibiaxial tests. The GTN model was used to predict the ductile rupture in bending but only a purely isotropic hardening rule and a Von Mises yield criterion was used in their work.

As in Shinohara et al. (2010), kinematic hardening is represented by a back stress $\underline{X}$ introduced by Chaboche (1989). The yield surface is defined by using the difference $\underline{B}$ between the Cauchy stress $\underline{\sigma}$ and the back stress: $\underline{B} = \underline{\sigma} - \underline{X}$. In order to account for anisotropic plasticity, it was necessary to use an anisotropic stress measure to define the yield surface. The model proposed in (Bron and Besson, 2004) was used in the following. It consists in a generalization of previously published models (Barlat et al., 1991; Karafillis and Boyce, 1993).

For any symmetric second order tensor, $\underline{T}$, the anisotropic scalar measure (T_E) of $\underline{T}$ is defined as:

$$T_E(\underline{T}) = \left(\sum_{k=1}^{K} \alpha_k \left(T_{Ek} \right)^a \right)^{1/a} \tag{1}$$

The function $T_E(\underline{T})$ is positive and homogeneous of degree 1. T_{Ek} are secondary anisotropic scalar measures and α_k are positive coefficients with a sum equal to 1. In practice, only two functions ($K = 2$) were used i.e. $\alpha_1 = \alpha$ and $\alpha_2 = 1 - \alpha$. One first defines two modified deviators:

$$\underline{T}_k = \underline{\underline{L}}_k : \underline{T} \tag{2}$$

where the fourth order tensor $\underline{\underline{L}}_k$ is expressed as follows using Voigt notations:

$$\underline{\underline{L}}_k = \begin{pmatrix} \frac{1}{3}\left(c^k_{LL}+c^k_{SS}\right) & -\frac{1}{3}c^k_{SS} & -\frac{1}{3}c^k_{LL} & 0 & 0 & 0 \\ -\frac{1}{3}c^k_{SS} & \frac{1}{3}\left(c^k_{SS}+c^k_{TT}\right) & -\frac{1}{3}c^k_{TT} & 0 & 0 & 0 \\ -\frac{1}{3}c^k_{LL} & -\frac{1}{3}c^k_{TT} & \frac{1}{3}\left(c^k_{LL}+c^k_{TT}\right) & 0 & 0 & 0 \\ 0 & 0 & 0 & c^k_{TL} & 0 & 0 \\ 0 & 0 & 0 & 0 & c^k_{LS} & 0 \\ 0 & 0 & 0 & 0 & 0 & c^k_{ST} \end{pmatrix} \tag{3}$$

The eigenvalues of $\underline{T}_k$ are then computed: $T_k^1 \geq T_k^2 \geq T_k^3$. T_{E1} and T_{E2} are respectively computed as :

$$T_{E1} = \left[\frac{1}{2}\left(\left|T_1^2 - T_1^3\right|^{b_1} + \left|T_1^3 - T_1^1\right|^{b_1} + \left|T_1^1 - T_1^2\right|^{b_1}\right)\right]^{1/b_1} \tag{4}$$

$$T_{E2} = \left[\frac{3^{b_2}}{2^{b_2}+2}\left(\left|T_2^1\right|^{b_2} + \left|T_2^2\right|^{b2} + \left|T_2^3\right|^{b_2}\right)\right]^{1/b_2} \tag{5}$$

a, b_1, b_2 and α are four material parameters that influence the shape of the yield surface and the model was simplified assuming $a = b_1 = b_2$. $c^{1,2}_{TT...ST}$ parameters control yield anisotropy. L, T and S respectively correspond to the longitudinal, the transverse and the thickness directions of the sheet. As mechanical tests were performed along in-plane directions, coefficients corresponding to shear in the thickness direction could not be determined. It was therefore assumed that $c^k_{ST} = c^k_{LS} = 1$.

Experimental observations led to define the void fraction as a damage indicator. Among the models using the void fraction as a damage parameter, the GTN model is the most widely adopted. It couples the void volume fraction, f, with material constitutive equations. For any symmetric second-order tensor, $\underline{T}$, the corresponding effective stress, $T_*(\underline{T}, f)$, is implicitly defined by:

$$\Psi(T_*, T_E, T_{kk}, f) = \left(\frac{T_E}{T_*}\right)^2 + 2q_1 f_* \cosh\left(\frac{q_2}{2}\frac{T_{kk}}{T_*}\right) - 1 - q_1{}^2 f_*{}^2 = 0 \tag{6}$$

In Equation (6), $T_E = T_E(\underline{T})$ is the anisotropic stress, T_{kk} is the trace of the stress tensor. Parameters q_1 and q_2 introduced by Tvergaard (1982) are assumed to be constant and respectively equal to 1.5 and 1. These q parameters can be used to correct the effect of void shape changes, of large strain hardening and of void interaction. f_* is a function introduced by Tvergaard and Needleman (1984) to represent the coalescence of damage cavities:

$$f_* \begin{cases} f_g + f_n \quad \text{for} \quad f_g < f_c \\ \\ f_c + f_n + \delta(f_g - f_c) \quad \text{for} \quad f_g > f_c \end{cases} \tag{7}$$

In Equation (7) f_c represents the critical growth void volume fraction for which coalescence starts, f_g represents the damage due to cavity growth and f_n corresponds to damage nucleation as in (Besson et al., 2000) . δ and f_c are material parameters.

The yield function is then expressed by:

$$\phi = B_*(\underline{B}, f) - R(p) \tag{8}$$

Here, p is the cumulative plastic strain and R is the flow stress. The normality rule applies and the strain rate tensor is given by:

$$\underline{\dot{\varepsilon}}_p = (1-f)\dot{p}\frac{\partial B_*}{\partial \underline{\sigma}} \tag{9}$$

Damage growth is both controlled by void nucleation and void growth. Therefore, the evolution law for damage is expressed as (Chu and Needleman, 1980):

$$\dot{f} = (1-f)tr(\underline{\dot{\varepsilon}}_p) + A_n\dot{p} \tag{10}$$

The first term corresponds to the evolution law for f_g given by mass conservation and the second term corresponds to the contribution of void nucleation. A_n is the nucleation rate parameter which may depend on the material state variables such as plastic strain and stress state.

Kinematic hardening is described using an intermediate tensor variable, $\underline{\alpha}$, for which the evolution equation is given following the standard expression for non linear kinematic hardening (Lemaitre and Chaboche, 1990) by:

$$\underline{\dot{\alpha}} = \underline{\dot{\varepsilon}}_p - \frac{3}{2}\frac{D}{C}\dot{p}\underline{X} \tag{11}$$

C and D are material parameters.

The equation ($\underline{X} = \frac{2}{3}C\underline{\alpha}$) used in the damage-free version of the model (Rèche et al., 2011) is not valid here. Therefore, an intermediate back stress, χ , is used. It represents the back stress at the microscopic level and is linked to α by: $\underline{\chi} = \frac{2}{3}C\underline{\alpha}$.

In practice, $\underline{\chi}_1 = \frac{2}{3}C_1\underline{\alpha_1}$ and $\underline{\chi}_2 = \frac{2}{3}C_2\underline{\alpha_2}$ and $\underline{X} = \underline{X}_1 + \underline{X}_2$

According to Besson and Guillemer-Néel (2003), the actual back-stress, $\underline{X}$, is defined implicitly by the following equation:

$$\underline{\chi_i} = \frac{2}{3}X_{i*}\frac{\partial X_{i*}}{\partial \underline{X_i}} \tag{12}$$

To solve this equation, X_* is defined as a solution of $\Psi(X_*, X_{eq}, X_{kk}, f) = 0$ where X_{eq} and X_{kk} are respectively the von Mises invariant of $\underline{X}$ and its trace.

Finally, the elastoplastic behaviour of the TRIP sheet has been identified thanks to tensile tests on smooth and notched specimens and to shear tests (Rèche et al., 2011). The evolution equation for isotropic hardening is given by the following:

$$R(p) = R_0 + Hp + Q\left(1 - \exp\left(-bp\right)\right) \tag{13}$$

p is the cumulative plastic strain, R is the flow stress and H, Q and b are material parameters.
In addition, note that while tensile and shearing tests were being carried out on the steel, retained austenite was transformed into martensite during deformation, meaning that the TRIP-effect was implicitly taken into account in the model. Hence, no micromechanical model was used here because it was well beyond the scope of this study.

4.2. Adjustment of material parameters

Adjustment of all model parameters yielded the values reported in Table 2. As a relatively high level for plastic strain has to be reached before damage occurs, it was therefore possible to adjust parameters related to plastic hardening and plastic anisotropy independently of damage parameters.
Consequently, plastic behaviour parameters were determined separately and their values were given in (Rèche et al., 2011). As already mentioned, they were determined using an experimental database based on tensile tests on smooth and notched specimens and shear tests.
To include the effect of stress triaxiality on the damage cavity nucleation rate as evidenced by (Kao et al., 1990), the void nucleation rate parameter A_n in Equation (10) was expressed as a function of the local stress triaxiality ratio, Tr, and of the cumulative plastic strain as:

$$A_n = \begin{cases} 0 & \forall Tr \in \left]-\infty;-1/3\right] \text{ or } p < p_n \\ \frac{3}{2} A_n^0 \left(Tr + \frac{1}{3}\right) & \forall Tr \in \left]-1/3;1/3\right[\text{ and } p > p_n \\ A_n^0 & \forall Tr \in \left[1/3;\infty\right[\text{ and } p > p_n \end{cases} \tag{14}$$

A_n^0 is the maximum value of the nucleation rate parameter. It is assumed to be constant. p_n is the cumulative plastic strain at which nucleation can start. This choice for the expression of A_n is dictated by the analysis of Bridgman's results (Bridgman, 1952) made in (Bao and Wierzbicki, 2005), which shows that failure does not occur in specimens where stress triaxiality is lower than -1/3. The above formula provides a continuous transition between $-1/3 < Tr < 1/3$. Above this value, nucleation is assumed to be triaxiality independent.

SEM observations performed on bent and tensile specimens (Paragraph 3.4) showed that cavity nucleation starts for a true strain close to 0.11 for the main hard band and close to 0.21 for the softer matrix. This implies that a given strain must be reached for nucleation to start. In this case, the true strain (ε) was not exactly equal to the cumulative plastic strain p. A true strain (ε) of respectively 0.11 and 0.21 corresponded to a cumulative plastic strain at nucleation (p_n) of respectively about 0.13 and 0.24. In the present model, the sheet specimen was divided into three parts: (i) the material within the fold, with hard bands (i.e. mixed ferrite + aligned second phases), with a value of $p_n = p_b = 0.13$, (ii) still

within the fold, the "softer matrix" material with a higher value $p_n = p_m = 0.24$ and (iii) the material far from the fold where no damage nucleation occurred. The corresponding nucleation rate parameters were respectively evaluated to be equal to $A_n = A_b = 2.3$ for the material with hard bands and $A_n = A_m = 1.15$ for the "softer matrix" material. The value of A_m was mainly adjusted using air bending simulation and that of A_b using stretch bending simulation.

Elastic properties	$E = 210GPa, \nu = 0.3$
Isotropic hardening	$R_0 = 499MPa, H = 110MPa$
	$b = 8.4, Q = 382MPa$
Kinematic hardening	$C_1 = 718MPa, D_1 = 9.4$
	$C_2 = 9900MPa, D_2 = 66.7$
Plastic anisotropy	$a = 6.1, \alpha = 0.55$
	$c_{TT}^1 = 0.99, c_{LL}^1 = 0.96, c_{SS}^1 = 0.92, c_{TL}^1 = 1.14, c_{LS}^1 = c_{ST}^1 = 1$
	$c_{TT}^2 = 0.99, c_{LL}^2 = 1.04, c_{SS}^2 = 1.17, c_{TL}^2 = 1.04, c_{LS}^2 = c_{ST}^2 = 1$
Damage	$q_1 = 1.5, q_2 = 1, f_c = 0.05, \delta = 4$
	$p_m = 0.24, p_b = 0.13$
	$A_m = 1.15, A_b = 2.3$
Size of finite elements	Through-thickness: 50µm Length: 50µm Width (3D calculation): 500µm

Table 2: Optimized constitutive equation parameters.

4.3. Finite-element simulation procedure

The in-house finite-element software Zset (Besson and Foerch, 1997) with a fully implicit integration scheme was used to simulate the two bending tests. All calculations were done using an updated Lagrangian formulation with linear brick elements using selective integration. The mesh used for the air-bending test is shown in Figure 11a and the one used for the stretch bending test modelling is illustrated in Figure 11b. Tools (punch, roll and die) were assumed to behave elastically with a Young's modulus and a Poisson ratio equal to 210 GPa and 0.3. To reduce the number of elements in the stretch bending calculations, the punch was modelled as a layer of elements to reduce the number of degrees of freedom. To ensure its stiffness, all displacements were prescribed inside the punch. The same method was used for the die as well as for the roll in air-bending.
As the model included damage-induced softening, there was a strong dependence of damage development on the mesh size (Besson et al., 2003). Therefore, it was decided to fix the mesh size in order to compare the two bending tests in a rigorous manner. Hence, smallest elements located close to the punch had a size of 50x50µm (corresponding to 32 elements across the thickness).

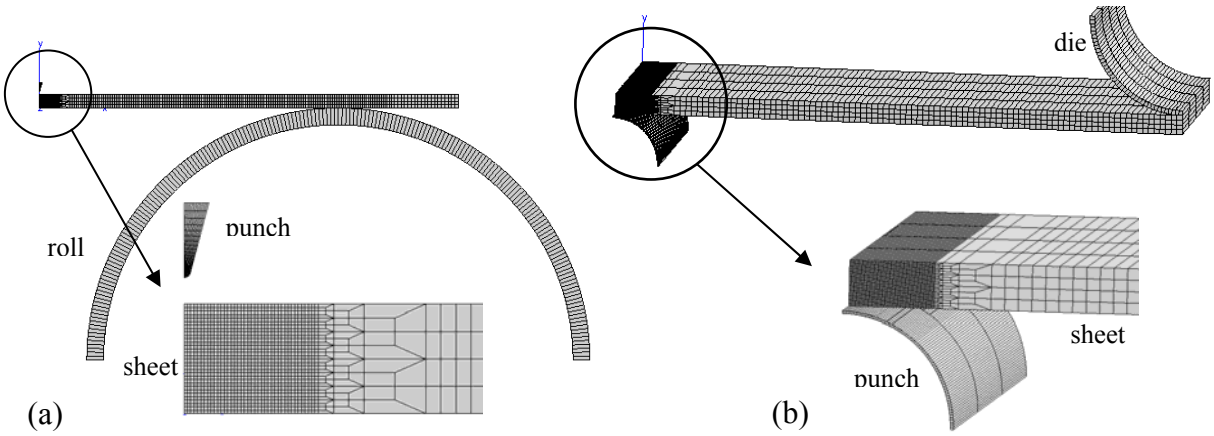

Figure 11: (a) Meshing of the air-bending test, (b) meshing of the stretch bending test.

The modelling of the air-bending test had been performed using the damage-free model in (Rèche et al., 2011). Identical numerical conditions were used here, i.e., plane strain elements were used, only a half of the specimen and punch and one roll were meshed due to symmetry conditions (Figure 11a). Two contact conditions were considered (Rèche et al., 2011):

- Between the sheet and the punch, as the friction coefficient was shown to have little influence on the results, it was fixed to 0.25.
- Between the sheet and the rolls, as rolls rotated freely during the test, friction was neglected. Here, the rolls were fixed and the friction coefficient was set to 0.

The simulation of stretch bending was carried out in 3D, so only one quarter of the specimen and punch and a half of one die were meshed due to symmetry conditions (Figure 11b). The size of the smallest element located just above the punch was 50x50x500 µm (i.e. there were 32 elements across the sheet thickness and 4 elements across the half-width). The punch and the die had respectively a radius of 4mm and 8mm. The nodes located just below the die were considered to be fixed to well represent the clamping of the sheet between the die and the blank-holder. Here, two contact conditions were considered:

- Between the sheet and the punch, lubrication consisted in grease and a Teflon film but the actual friction coefficient was not known. It was thus considered as a model parameter.
- Between the die and the sheet: the friction coefficient between them had no influence on stretch bending results due to its location far from the fold. Consequently, it was arbitrarily set to 0.1.

According to cross-sectional observations illustrated in Figure 1, the investigated steel exhibited at mid-thickness an area with hard bands and for simplification, it was considered that the region containing the wider bands can be represented within a thickness of 100µm in the meshing. The three parts of the sheet defined previously are illustrated in Figure 12.

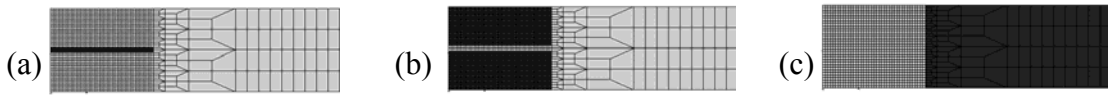

Figure 12: Closer view of the sheet thickness. Elements coloured in black are (a) material with hard bands (100µm in thickness), (b) the softer matrix and (c) the material far from the fold.

5. Finite element analysis, results and discussion

5.1. Air-bending

Numerical simulations were performed both with and without damage in the model (Figure13a). Calculation carried out without damage yielded rather good results but the load did not decrease enough at the end of the test, i.e. after the onset of cracking. By including damage in the model, the load decreased quicker and there was very good agreement between the experimental curve and model predictions. A prestrained sample was bent until cracking and Figure 13b illustrates both experimental and model predicted curves. A good agreement was obtained between the two curves except at the end of the test where the load decreased too early by including damage into the model. This could be due to the change in strain path: from tension during prestraining to plane strain during bending. The value of the plastic strain p is increased during prestraining so that damage starts earlier during subsequent bending thus explaining the reduced ductility of the pre-strained material. A better agreement with experiment could possibly be obtained by fitting p_m and A_m on experimental curves shown in Figure 13b. With the parameters used here, this model was very efficient to predict air-bending curves without prestraining, while being a little bit less accurate to predict air-bending curves after prestraining.

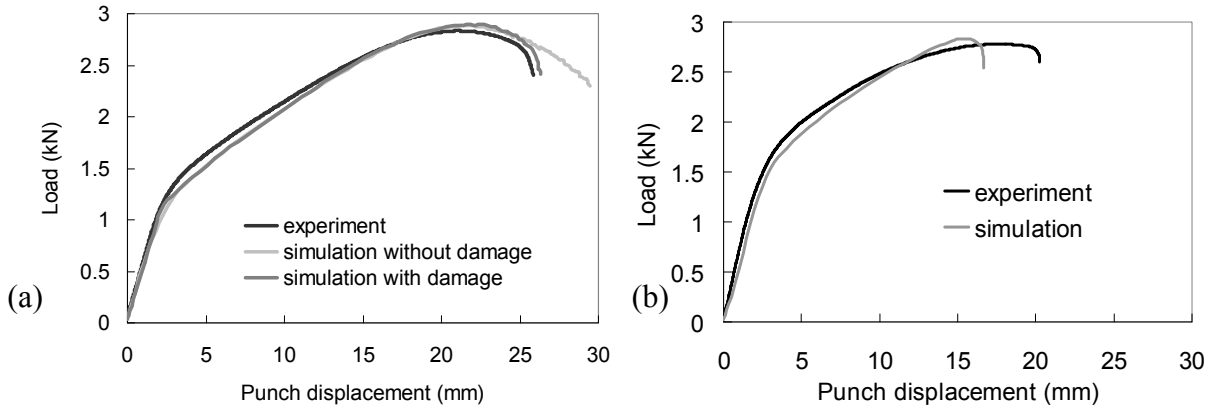

Figure 13: Air-bending tests (a) simple air-bending test, (b) air-bending test after 10% tensile prestraining.

The spatial distribution of damage is mapped in Figure 14b for the air-bent specimen without prestraining. A similar damage map was observed for the prestrained sample. There was very good agreement between simulation and experiments (Figure 14a) where similar crack propagation at 45° was observed. Although the central hard band was taken into account in the model, it had no effect on the global response because cracks initiated from the outer surface and not from the central hard band. This result is in agreement with experimental observations.

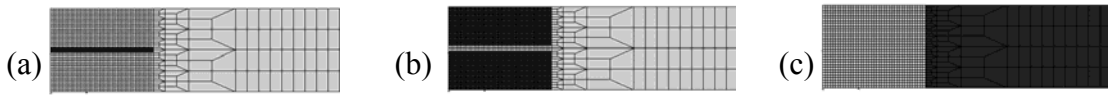

Figure 12: Closer view of the sheet thickness. Elements coloured in black are (a) material with hard bands (100µm in thickness), (b) the softer matrix and (c) the material far from the fold.

5. Finite element analysis, results and discussion

5.1. Air-bending

Numerical simulations were performed both with and without damage in the model (Figure13a). Calculation carried out without damage yielded rather good results but the load did not decrease enough at the end of the test, i.e. after the onset of cracking. By including damage in the model, the load decreased quicker and there was very good agreement between the experimental curve and model predictions. A prestrained sample was bent until cracking and Figure 13b illustrates both experimental and model predicted curves. A good agreement was obtained between the two curves except at the end of the test where the load decreased too early by including damage into the model. This could be due to the change in strain path: from tension during prestraining to plane strain during bending. The value of the plastic strain p is increased during prestraining so that damage starts earlier during subsequent bending thus explaining the reduced ductility of the pre-strained material. A better agreement with experiment could possibly be obtained by fitting p_m and A_m on experimental curves shown in Figure 13b. With the parameters used here, this model was very efficient to predict air-bending curves without prestraining, while being a little bit less accurate to predict air-bending curves after prestraining.

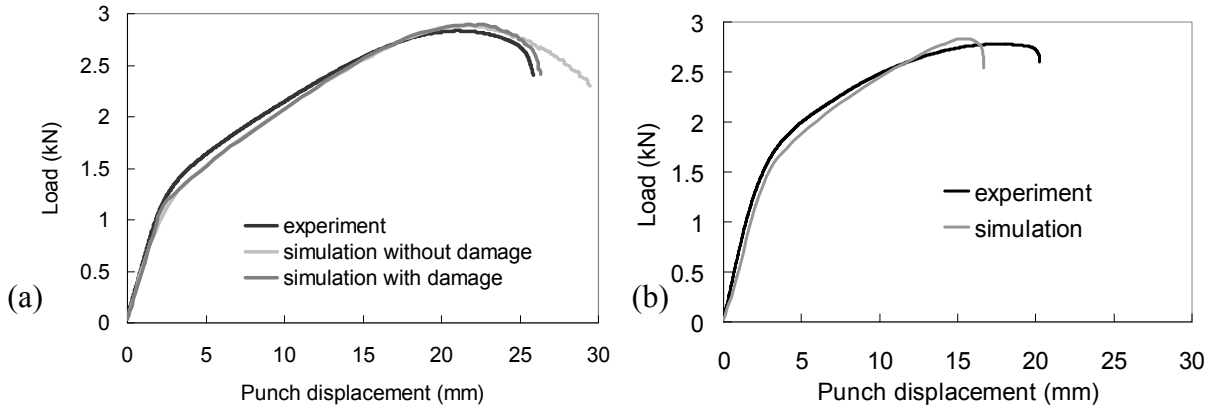

Figure 13: Air-bending tests (a) simple air-bending test, (b) air-bending test after 10% tensile prestraining.

The spatial distribution of damage is mapped in Figure 14b for the air-bent specimen without prestraining. A similar damage map was observed for the prestrained sample. There was very good agreement between simulation and experiments (Figure 14a) where similar crack propagation at 45° was observed. Although the central hard band was taken into account in the model, it had no effect on the global response because cracks initiated from the outer surface and not from the central hard band. This result is in agreement with experimental observations.

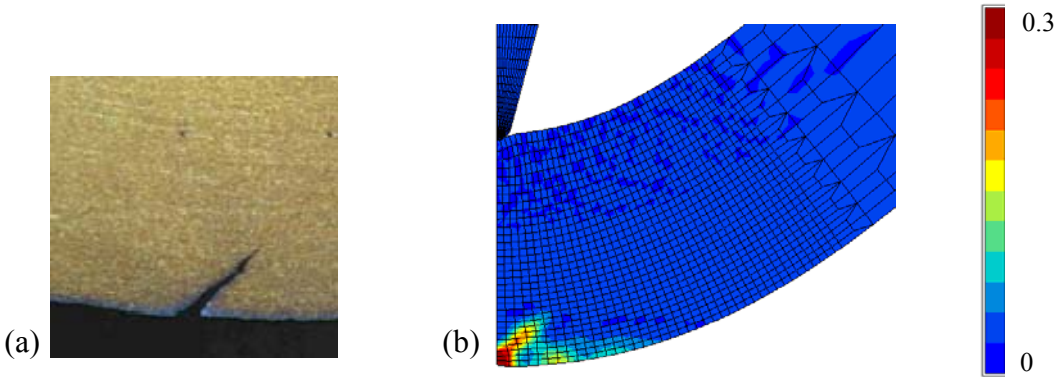

Figure 14: (a) crack on an air-bent specimen, (b) damage map at the end of the air-bending test.

5.2. Stretch bending

As the actual friction coefficient, μ, between the punch and the sheet was not known, the variation in width was measured along stretch bent specimens to give additional experimental information about this friction coefficient. Necking observed on samples corresponded to a mean decrease in width by 5.6% +/- 0.2. The numerical simulation gave a variation of 5.7% with $\mu = 0.1$ and 5.3% with $\mu = 0.15$. Therefore, for stretch bending modelling along the transverse direction, the friction coefficient between the sheet and the punch was set to 0.1.

Figure 15 illustrates the predicted curves obtained both without damage and with the set of damage parameters given in the previous part. Excellent agreement between experimental curve and 3D simulation was obtained. As seen in Figure 15, the load decreased very quickly just after its maximum. This observation confirmed that very unstable failure occurs in this test. Note that without damage in the model, the load did not decrease proving the necessity to include a damage criterion to fit well with experiment.

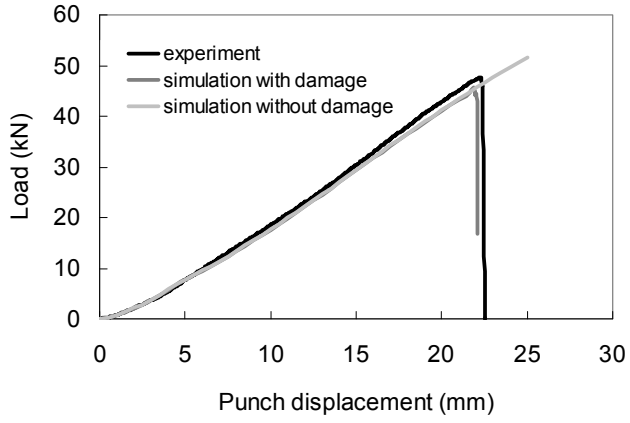

Figure 15: Experimental and predicted stretch bending load vs. punch displacement curves with and without damage in the model.

In addition, it was noticed that in this test, the neutral fibre was not at the mid-thickness. Very quickly, it moved towards the inner skin. In fact, from a punch displacement of 2mm, the compressive zone shrank toward the inner surface and reduced to a thickness of 0.5mm. For a punch displacement of 10mm, the compressive zone reduced to a thickness

of 0.15mm. Thus, the compression stress gradually decreased in that area and annihilated for a punch displacement of about 15mm. This result confirms that, in stretch bending, tension prevails over bending.

According to metallographic examinations of stretch bent samples (Figure 16a), cracks initiated from the central hard band and propagated along a 45° direction with local necking visible at the outer surface. Localization was clearly noticed within a 45° band (Figure 16b) and damage was concentrated at the mid-thickness with development along that band (Figure 16c). These results were in good agreement with experiment (Figure 16a). The model predicted that damage extended along the hard band at mid-thickness over a distance of about 2mm. From all metallographic cross-sectional observations carried out on various stretch bent specimens, damage at mid-thickness was observed to extend over a distance between 1 and 1.9mm. The thicker the hard band, the more extended of the damage at mid-thickness. In the present model, the "hard bands" containing material had a thickness of 100µm but in as-received materials, most of steels had thinner hard bands at mid-thickness. Therefore, there was good agreement between model predictions and experimental observations regarding the extent of damage at mid-thickness.

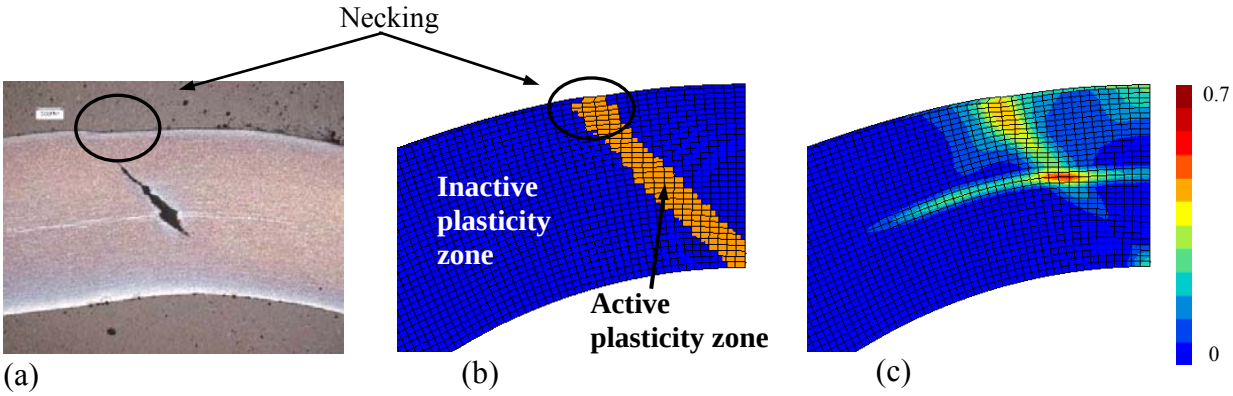

Figure 16: (a) cross-sectional observation of an internal crack during stretch bending (b) active and inactive plasticity zones: localization within a 45° band and (c) damage map taken at mid-width for a punch displacement of 22mm.

Conclusion

In this paper, analysis of rupture in air-bending and stretch bending tests was performed. Thanks to an existing comprehensive database, constitutive equations without damage were already determined for this material. In the present study, in order to predict fracture more precisely, a model based on the GTN approach has been used introducing (i) mixed isotropic and kinematic hardening, (ii) plastic anisotropy and (iii) damage evolution essentially based on the nucleation and growth of voids. Using this model allowed good predictions of both air and stretch bending behaviours. The key conclusions for this study are:

1) Fracture modes and damage mechanisms are different for both bending tests. In air-bending, cracks initiated from the surface or from just below while in stretch bending tests, cracks inclined by 45° initiated from the main hard band located at mid-thickness and propagated in an unstable manner leading to sudden fracture.

2) The Bron Besson yield criterion, together with mixed plastic hardening and ductile damage development allowed the load vs. punch displacement curve to be very well predicted as well as the propagation of a crack from the outer surface in air-bending.
3) The numerical response of an air-bending test after prestraining along the same direction also showed good agreement with experiment thanks to the kinematic contribution to hardening being taken into account in the model.
4) Load vs. punch displacement curves as well as internal crack initiation and propagation are well predicted for the stretch bending test.
5) Contrary to the air-bending test, a 3D simulation was required in stretch bending to fit well with experiment. In this case, the friction conditions between the sheet and the punch must be carefully modelled.

Acknowledgements

The authors would like to acknowledge ArcelorMittal Global R&D for financial support and material supply. Thanks also are due to Alain Col, Olivier Bouaziz and Xavier Lemoine for valuable discussions.

References

Bao, Y., Wierzbicki, T., 2005. On the cut-off value of negative triaxiality for fracture, Engineering Fracture Mechanics 72, 1049-1069.

Bai, Y., Wierzbicki, T., 2010. Application of extended Mohr-Coulomb criterion to ductile fracture, International Journal of Fracture 161, 1-20.

Besson, J., Foerch, R., 1997. Large scale object-oriented finite element code design, Computer methods in applied mechanics and engineering 142, 165-187.

Besson, J., Devilliers-Guerville, L., Pineau, A., 2000. Modelling of scatter and size effect in ductile fracture: Application to thermal embrittlement of duplex stainless steels, Engineering Fracture Mechanics 67, 169-190.

Besson, J., Steglich, D., Brocks, W., 2003. Modeling of plane strain ductile rupture, International Journal of Plasticity 19, 1517-1541.

Besson, J., Guillemer-Neel, C., 2003. An extension of the Green and Gurson models to kinematic hardening, Mechanics of Materials 35, 1-18.

Ben Bettaieb, M., Lemoine, X., Duchêne, L., Habraken, A.M., 2010. Simulation of the bending process of hardening metallic sheets using damage model. Part I: Theoretical development and numerical implementation, Materials Science and Engineering A528, 434-441.

Ben Bettaieb, M., Lemoine, X., Duchêne, L., Habraken, A.M., 2010. Simulation of the bending process of hardening metallic sheets using damage model. Part II: Numerical investigations, Materials Science and Engineering A528, 442-448.

Bridgman, P.W., 1952. Studies in large plastic flow and fracture: With special emphasis on the effects of hydrostatic pressure, McGraw-Hill.

Bron, F., Besson, J., 2004. A yield function for anisotropy materials. Application to aluminium alloys, International Journal of Plasticity 20, 937-963.

Chaboche, J.L., 1989. Constitutive equations for cyclic plasticity and cyclic viscoplasticity, International Journal of Plasticity 5, 247-302.

Chaboche, J.L., 2008. A review of some plasticity and viscoplasticity constitutive theories, International Journal of Plasticity 24, 1642–1693.

Charpentier, P.L., 1975. Influence of punch curvature on the stretching limits of sheet steel, Met. Trans. A, vol 6A, 1665-1669.

Chien, W.Y., Pan, J., Tang, S.C., 1981. A combined necking and shear localization analysis for aluminium sheets under biaxial stretching conditions, International Journal of Plasticity 20, 1953-1981.

Chu, C., Needleman, A., 1980. Void nucleation effects in biaxially stretched sheets, Journal of Engineering Materials and Technology 102, 249-256.

Cockroft, M.G., Latham, D.J., 1968. Ductility and workability of metals, Journal of the Institute of Metals 96, 33-39.

Dalloz, A., Besson, J., Gourgues-Lorenzon, A.F., Pineau, A., 2009. Effect of shear cutting on ductility of a dual phase steel, Engineering Fracture Mechanics 76, 1411-1424.

Damborg, D.D., 1998. Prediction of fracture in bending under tension, In: Proceeding of the 19th Riso International Symposium on Material Science: Modelling of Structure and Mechanics from Microscale to Product, Roskilde, Denmark, pp. 235-240.

Date, P.P., Narashima, K., Maiti, S.K., Singh, U.P., 1999. On the prediction of springback in V-bending of metallic sheets under plane strain condition. Proceeding of the International Conference on Sheet Metal, Earlangen, Germany, pp. 447-456

Demeri, M.Y., 1981. The stretch bend forming of sheet metal, J. Applied Metal Working 2, 3-10.

Eggertsen, P.A., Mattiasson, K., 2009. On the modelling of the bending-unbending behaviour for accurate springback predictions, International Journal of Mechanical Sciences 51, 547-563.

Faleskog, J., Gao, X., Shih, C., 1998. Cell model for nonlinear fracture analysis. I: Micromechanics calibration, International Journal of Fracture 89, 355-373

Friedman, P.A., Luckey, S.G., 2002. Failure of Al-Mg-Si alloys in bending, ASM International, Practical Failure Analysis 2, 33-42.

Gan, W., Wagoner, R.H., 2004. Die design method for sheet springback, International Journal of Mechanical Sciences 46, 1097-1113.

Goodwin, G.M., 1968. Application of strain analysis to sheet metal forming in the press shop, SAE paper 680093.

Ghosh, A.K., 1976. A criterion for ductile fracture in sheet under biaxial loading, Metallurgical Transactions A 7A, 523-533.

Graf, A., Hosford, W., 1993. Effect of changing strain paths on forming limit diagrams of AL2008-T4, Metallurgical Transactions 24A, 2503-2512.

Gurson, A.L., 1977. Continuum theory of ductile rupture by void nucleation and growth: part I-yield criteria and flow rules for porous ductile media, Journal of Engineering Materials and Technology 99, 2-15.

Hudgins, A., Matlock, D., Speer, J., Fekete, J., Walp, M., 2007. The susceptibility to shear fracture in bending of advanced high strength sheet steels, In: Proceedings from Materials Science and Technology (MS&T): Advanced High Strength and Other Specialty Sheet Steel Products for the Automotive Industry, Detroit, Michigan, pp. 145-157.

Kao, A., Kuhn, H., Richemond, O., Spitzig, W., 1990. Tensile fracture and fractographic analysis of 1045 spheroidized steel under hydrostatic pressure, Journal of Materials Research 5, 83-91.

Kim, J.H., Sung, J.H., Wagoner, R.H., 2009. Thermo-mechanical modelling of draw-bend formability tests, International Deep Drawing Research Group, International Conference, Golden, CO, USA, pp. 503-512.

Keeler, S.P. and Backofen, W.A., 1963. Plastic instability and fracture in sheets stretched over rigid punches. Transactions of the American Society for Metals 56, 25-48.

Laukonis, J.V., Ghosh, A.K., 1978. Effects of strain paths changes to the formability of sheet metals, Metallurgical Transactions 9A, 1849-1856.

Lemaitre, J., 1985. A continuum damage mechanics model for ductile fracture, Journal of Engineering Materials and Technology 107, 83-89.

Lemaitre, J., Chaboche, J.L., 1990. Mechanics of Solid Materials. Cambridge University Press.

Luo, M., Wierzbicki, T., 2010. Numerical failure analysis of a stretch bending test on dual-phase sheets using a phenomenological fracture model, International Journal of Solids and Structures 47, 3084-3102.

LeRoy, G., Embury, J.D., Edwards, G., Ashby, M.F., 1981. A model of ductile fracture between the nucleation and growth of voids, Acta Metallurgica 29, 1509-1522.

McClintock, F.A., 1968. A criterion of ductile fracture by growth of holes, Journal of Applied Mechanics 35, 363-371.

Perrin, G. and Leblond, J.B., 1990. Analytical study of a hollow sphere made of plastic porous material and subjected to hydrostatic tension-application to some problems in ductile fracture of metals, International Journal of Plasticity 6, 677-699.

Rèche, D., Sturel, T., Bouaziz, O., Col., A., Gourgues-Lorenzon, A.F., 2010. Damage development in low allow TRIP-aided steels during air-bending. Submitted to "Materials Science and Engineering A".

Rèche, D., Besson, J., Sturel, T., Lemoine, X., Gourgues-Lorenzon, A.F., 2011. Analysis of the air-bending test using finite-element simulation: Application to steel sheets. Submitted to "Journal of Materials Processing Technology".

Rice, J.R. and Tracey, D.M., 1969. On the ductile enlargement of voids in triaxial stress fields, Journal of the Mechanics and Physics of Solids 17, 201-217.

Sriram, S., Wong, C., Huang, M., Yan, B., 2003. Stretch bendability of advanced high strength steels, SAE International World Congress, Detroit, Michigan, pp. 107-115.

Sarkar, J., Kutty, T.R.G., Conlon, K.T., Wilkinson, D.S., Embury, J.D., Lloyd, D.J., 2001. Tensile and bending properties of AA5754 aluminium alloys, Materials Science and Engineering A316, 52-59.

Shinohara, Y., Madi, Y., Besson, J., 2010. A combined phenomenological model for the representation of anisotropic hardening behaviour in high strength steel line pipes, European Journal of Mechanics / A Solids 29, 917-927.

Steninger, J., Melander, A., 1982. The relation between bendability, tensile properties and particle structure of low-carbon steel, Scandinavian Journal of Metallurgy 11, no. 2, 55-71.

Thuillier, S., Le Maoût, N., Manach, P.Y., 2010. Bending limit prediction of an aluminium thin sheet, International Journal of Material Forming 3, 223-226.

Tvergaard, V. and Needleman, A., 1984. Analysis of the cup-cone fracture in a round tensile bar. Acta Metallurgica 32, 157-169.

Uthaisangsuk, V., Prahl, U., Münstermann, S., Bleck, W., 2008, Experimental and numerical failure criterion for formability prediction in sheet metal forming, Computational Materials Science 43, 43-50.

Vladimirov, I.N., Pietryga, M.P., Reese S., 2010. Anisotropic finite elastoplasticity with nonlinear kinematic and isotropic hardening and application to sheet metal forming, International Journal of Plasticity 26, 659-687.

Williams, B.W., Simha, C.H.M., Abedrabbo, N., Mayer, R., Worswick, M.J., 2010. Effect of anisotropy, kinematic hardening and strain-rate sensitivity on the predicted axial crush response of hydroformed aluminium alloy tubes, International Journal of Impact Engineering 37, 652-661.

II. Influence of simulation conditions on the stretch-bending test

II.A. Influence of meshing conditions

In order to determine the influence of the mesh, four calculations in the same conditions as for the air-bending test (Chapter 2) were performed, i.e. with various numbers of elements across the thickness close to the punch, i.e. over 3mm (this value was set regarding the stress and strain fields). As the GTN model is sensitive to the mesh size, all calculations were performed without damage in the model and we chose to keep the same length element size, i.e. 50µm. The four cases studied were:

(i) 8 elements across the sheet thickness (i.e. 200µm thick elements)
(ii) 16 elements across the sheet thickness (i.e. 100µm thick elements)
(iii) 32 elements across the sheet thickness (i.e. 50µm thick elements)
(iv) 64 elements across the sheet thickness (i.e. 25µm thick elements)

In agreement with section I, this parametric study was carried out in 3D, with the Bron Besson yield criterion, mixed isotropic/kinematic hardening rules but no damage was included in the model. These calculations were carried out with a friction coefficient of 0.1 between the punch and the sheet. The corresponding meshes are illustrated in Figure IV.1.

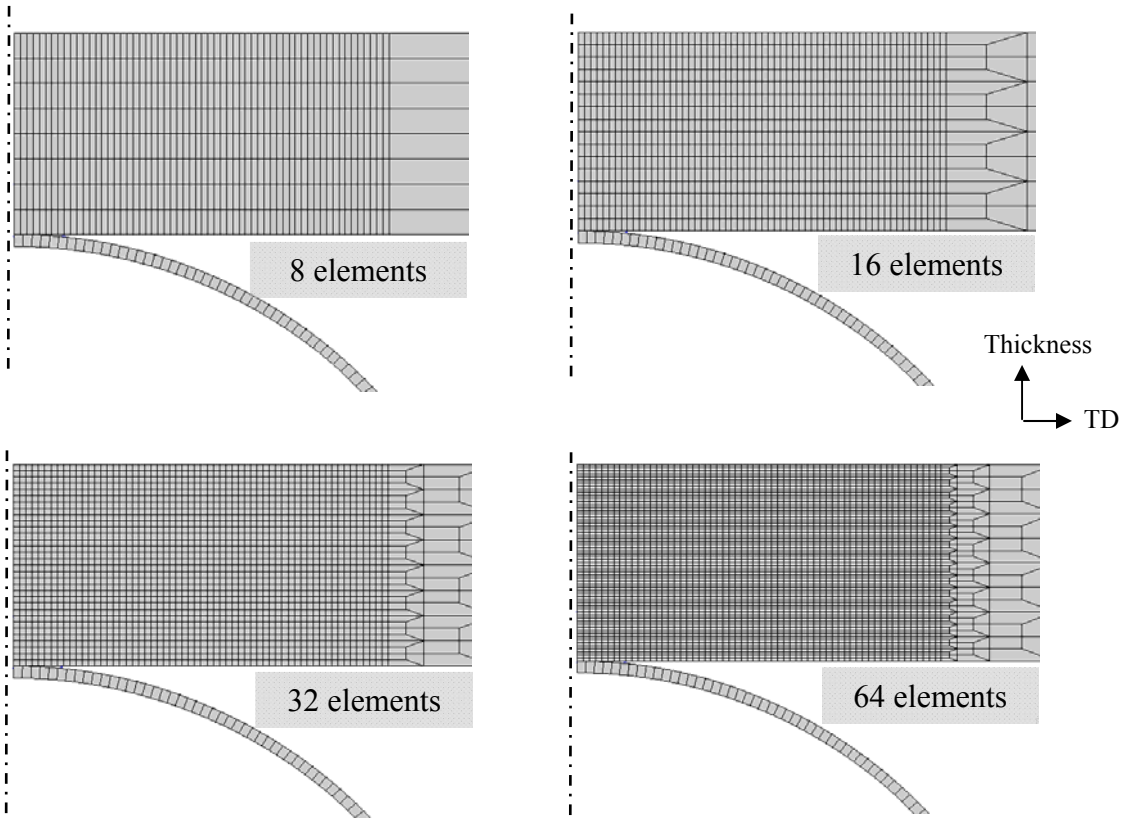

Figure IV.1. Four meshes with various numbers of elements across the thickness. Total thickness = 1.6mm.

Figure IV.2a illustrates load vs. punch displacement curves for the four meshing conditions. Similar curves are obtained for the four simulations, meaning that the number

of elements across the thickness does not change the global response in the range investigated here. Hoop stress and hoop strain distributions across the thickness at mid-width are illustrated in Figure IV.2b. Here also, similar curves are obtained for the four meshing conditions. Stress and strain fields calculated using each of the four meshes across the sheet thickness are respectively given in Figure IV.3 and Figure IV.4.

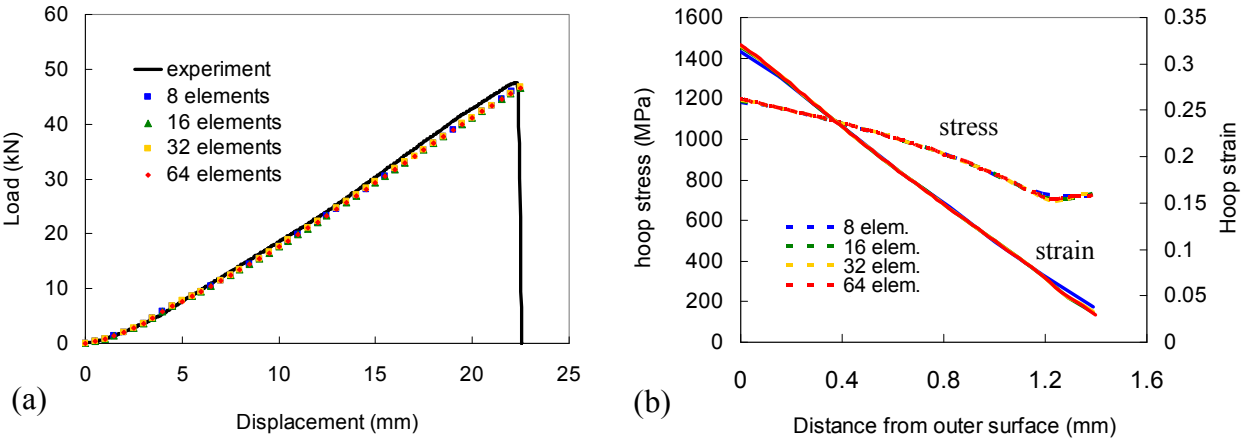

Figure IV.2. (a) Influence of the mesh on the load / displacement curves. Calculations with the Bron Besson yield criterion, mixed isotropic/kinematic hardening rule and no damage. (b) Influence of the mesh on the hoop stress and hoop strain distributions across the thickness for a punch displacement of 22mm at mid-width.

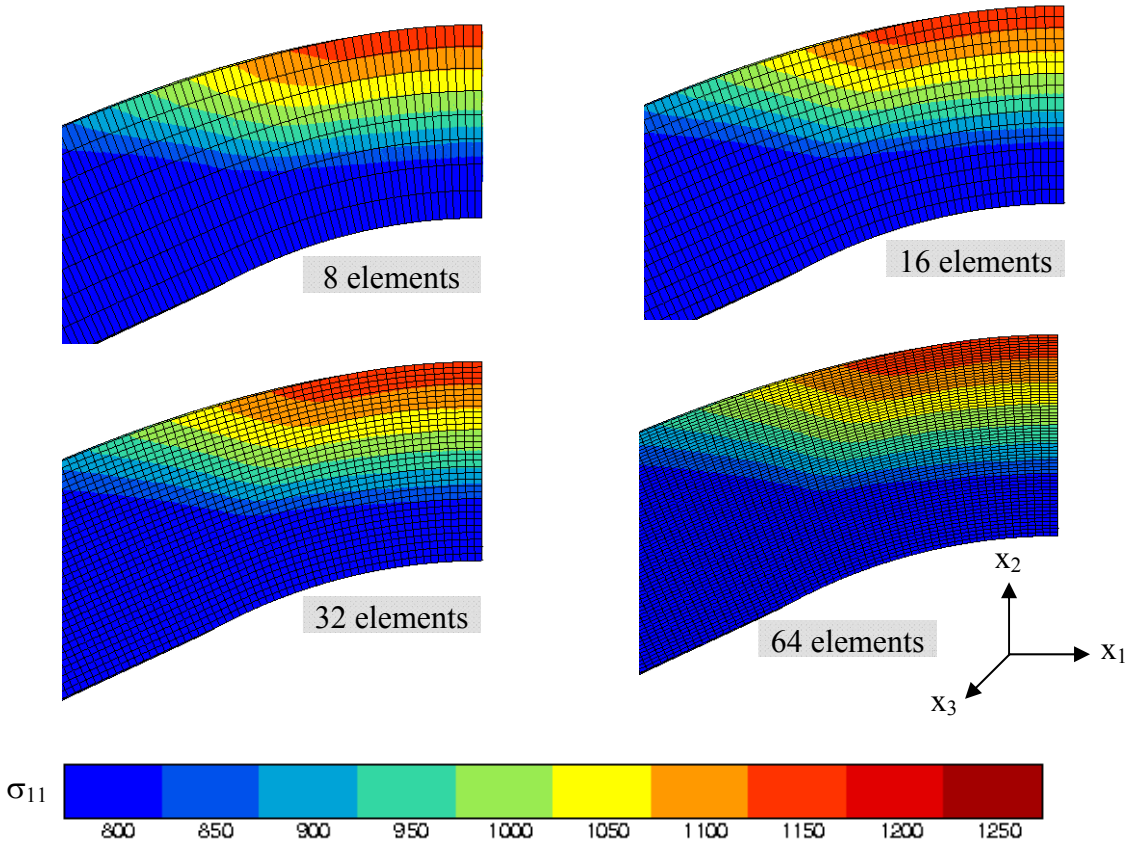

Figure IV.3. σ_{11} field (in MPa) after stretch bending up to a punch displacement of 22mm (8 to 64 elements across the thickness) at mid-width.

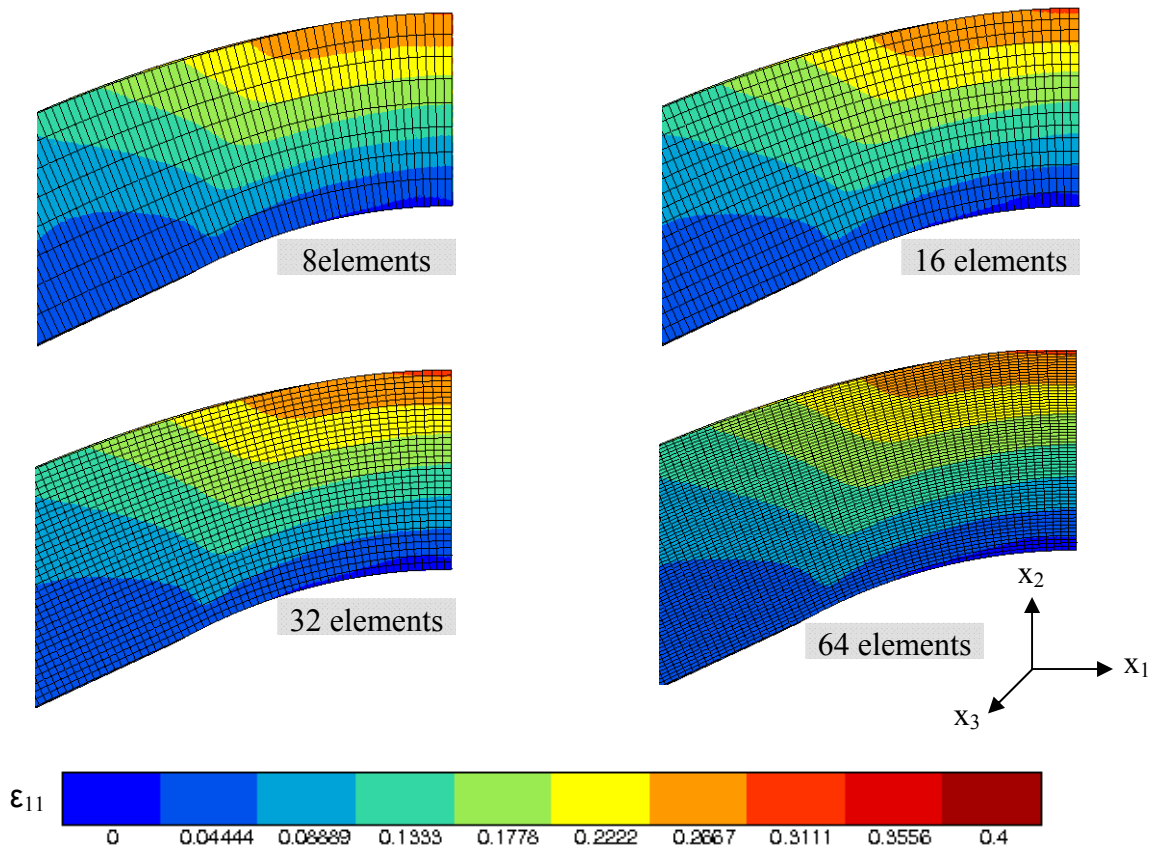

Figure IV.4. ε_{11} field after stretch bending up to a punch displacement of 22mm (8 to 64 elements across the thickness) at mid-width.

Regarding stress and strain fields as a function of the local meshing size, similar maps are obtained for the four calculations. However, as damage criterion has to be included into constitutive equations, it is necessary to use a quite thin mesh. With 64 elements across the thickness, calculations lasted a very long time. At the end, the mesh size is determined by the best compromise between computation time and accuracy of damage prediction. Therefore, all calculations were performed with 32 elements across the thickness i.e. for a mesh size of 50 µm along the specimen thickness.

II.B. Influence of boundary conditions

1. Abnormal sensitivity to the friction coefficient in 2D

Stretch bending test simulations were first carried out in 2D with a plane strain state hypothesis, as for the air-bending test. As the actual friction coefficient between the sheet and the punch was not known, a parametric study was conducted. Several calculations were launched with various values of the friction coefficient (μ = 0.2, 0.3, 0.4 and 0.5).
For these calculations, the Bron Besson yield criterion associated with mixed isotropic/kinematic hardening was used as in section I but no damage was included in the constitutive equations to only investigate the influence of the friction coefficient on the flow curve.

A surprising result was obtained (Figure IV.5). The slope of the load vs. punch displacement curves is similar for all calculations but the load drops at various values of the punch displacement corresponding to the various values of the friction coefficient. In fact, the higher the friction coefficient, the later the load drops. Necking in the thickness was observed earlier with a lower friction coefficient (Figure IV.6). To be in accordance with experiments, a very high friction coefficient should be used, i.e. close to 0.4. However, this value of the friction coefficient is not realistic for this kind of test, and the load does not drop as quickly as observed experimentally. This discrepancy could stem from two phenomena:
(i) only strain localisation (and no damage) was involved in this model
(ii) the strong influence of the friction coefficient influences the ability for specimen to shrink i.e. to be strained along the thickness direction.
Figure IV.6 illustrates ε_{11} field for two values of the friction coefficient (μ = 0.2 and μ = 0.4). Premature necking of the sheet thickness is clearly observed especially for the lowest value of the friction coefficient, explaining the early drop of the load. These results explicitly show that the 2D calculations are not correct (besides this abnormal influence of the friction coefficient, stress and strain fields are not correct and the sheet does not shrink as much experimentally). It is therefore necessary to perform all stretch bending calculations in three dimensions to accurately predict the load vs. punch displacement curves, stress and strain fields and the location of fracture.

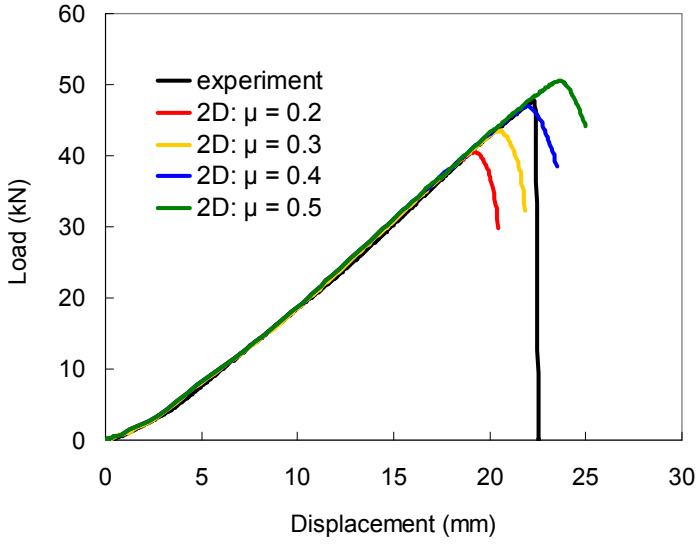

Figure IV.5. Load /displacement curves in stretch bending. Influence of the friction coefficient in 2D.

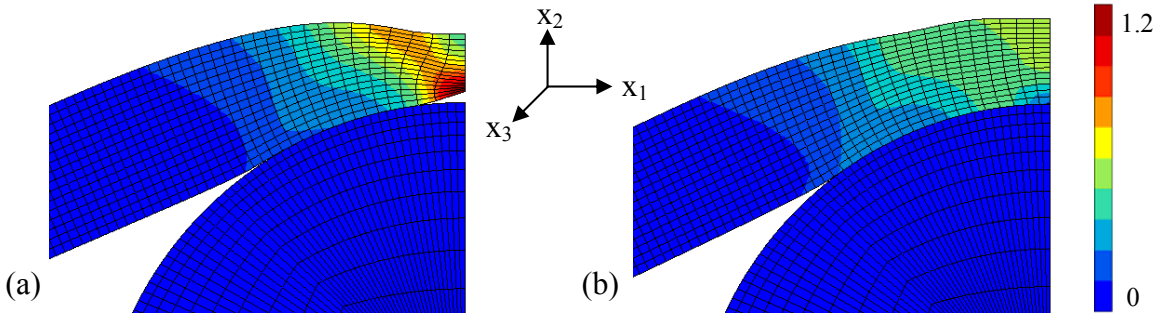

Figure IV.6. ε_{11} field after stretch bending in 2D. Abnormal necking along the sheet thickness due to the friction coefficient (a) μ = 0.2, (b) μ = 0.4.

2. Influence of the friction coefficient in 3D

Here it is checked that the abnormal effect reported in the previous section was actually an artefact due to the plane strain assumption. As the actual friction coefficient of this sheet with the bending tool was not known, various "reasonable" values of the friction coefficient were tested: $\mu = 0.05$, 0.1 and 0.15. In this case, the constitutive equations included damage with parameters defined in section I. Corresponding load vs. punch displacement curves are shown in Figure IV.7. The curves have similar slopes but different load drops. As in 2D modelling, the lower the friction coefficient, the earlier the load decreases. Here, the best fit was obtained with $\mu = 0.1$, which is a reasonable value for the lubrication conditions used experimentally. These curves confirm that the predicted load drop is due to the introduction of damage in the model. In 2D, the load drop was a calculation artefact due to abnormal necking along the sheet thickness.

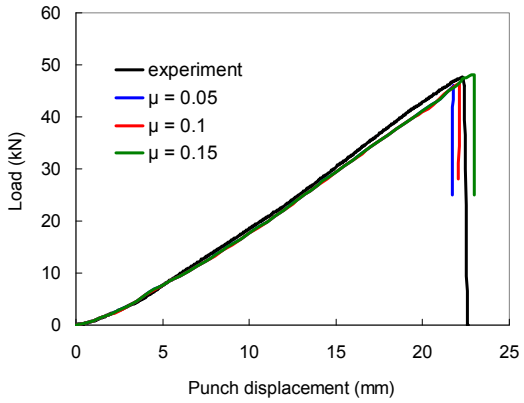

Figure IV.7. Load / displacement curves for various friction coefficients ($\mu = 0.05$, $\mu = 0.1$ and $\mu = 0.15$) in 3D simulation with damage in the model.

The value of μ was further checked by measuring the variation in width along stretch bent specimens (Figure IV.8). Necking observed along the specimen width corresponded to a mean decrease in width by 5.6% +/- 0.2. The numerical simulation yielded a variation in width by 5.7% with $\mu = 0.1$ and by 5.3% with $\mu = 0.15$. Thus, the value of $\mu = 0.1$ leads to global response and local strain that are consistent with experimental measurements, therefore, this value was chosen for all stretch bending test simulations (see previous part). Note that this observation was in agreement with the study of Luo and Wierzbicki (2010). In fact, in their work, they showed that localized width necking was noticed in the vicinity of the punch nose, that could not be simulated by a 2D calculation with a plane strain assumption.

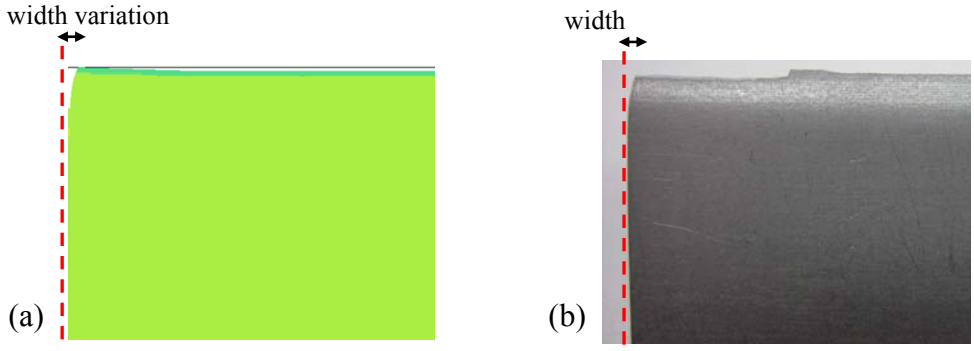

Figure IV.8. (a) Part of the stretch bent specimen geometry predicted by the model, with necking along the width. (b) real stretch bent specimen with necking along the width.

II.C. Summary: influence of modelling conditions on stretch-bending test predictions

In this part, the influence of the stretch-bending modelling conditions was discussed. It was shown that until damage begins to develop, the 3D mesh size has an influence neither on the global load vs. displacement curve nor on the hoop stress and hoop strain distributions across the sheet thickness. In order to be able to simulate a realistic thickness of the damaged hard band, it was chosen to perform all stretch-bending simulations with 32 elements across the thickness. Then, it was demonstrated that 3D element model provided much better agreement with experiments than with a plane strain assumption. The influence of the friction coefficient was also considered. It was demonstrated that a friction coefficient of 0.1 should be used in this case between the sheet and the punch. A summary of all these results is given in Table 9.

	2D	**3D**
Influence of meshing → 8 elements → 16 elements → 32 elements → 64 elements across the thickness before damage develops	/	No influence on hoop stress and hoop strain distributions and on the load/displacement curve → 32 elements across the thickness has been chosen to get the best compromise between time computation and accuracy of damage prediction
Friction coefficient	Abnormal results: a very high friction coefficient (μ=0.4) has to be used to fit reasonably with experiment. The load drop is a function of the necking along the sheet thickness depending of the friction coefficient.	The best fit friction coefficient in 3D is μ = 0.1. This value was adjusted using the experimental variation in width along the bent specimen
Type of elements	Plane strain elements (2D calculations) induce artefacts and are not adapted due to unrealistic premature necking of the specimen along the thickness direction. A three-dimensional calculation is required in stretch bending	

Table 9. Summary of the influence of stretch-bending modelling conditions in 2D and 3D.

III. Parametric study: effect of the location of the hard band on failure during air-bending

In section I, modelling was performed by assuming a hard band at mid-thickness which had the highest sensitivity to damage. In chapter 3, we demonstrated that a hard band close to the outer surface had a deleterious effect on the bendability because cracking appeared earlier with the proximity of the band with the outer surface. Experiments investigating the influence of the location of the band were carried out on thickness-reduced Steel 2 and the

simulation of air-bending of this material was performed in Chapter 2. A good agreement was observed at the beginning of the test (i.e. good prediction of the load / displacement curve) but not at the end, where the load was underestimated by the model. Therefore, it seemed inappropriate to model the air-bending test on thickness-reduced Steel 2 with various locations of the band because the model should first be improved.

One aim of the study was to quantitatively investigate the influence of banded structures (see Figure IV.9) on bendability. In this case, the banded structure is assimilated to a continuous hard band as for the central segregation. Therefore, air-bending simulations with various locations of hard band across the thickness were carried out on Steel 1 (classical thickness for automotive products, i.e. 1.6mm) because calculations were much simpler than for thickness-reduced Steel 2, leading to more reliable predictions. A row of elements with the highest sensitivity to damage (representing a banded structure) was located at various distances from the mid-thickness towards the outer surface. Each set has a thickness of 50µm corresponding to the thickness of one element.

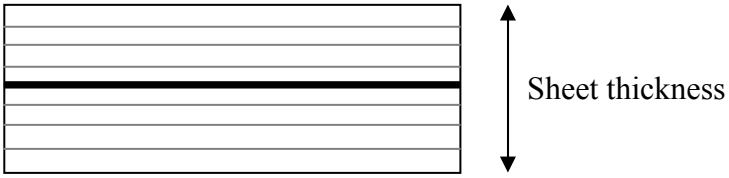

Figure IV.9. Schematics of a cross-section along the sheet thickness with the central segregation as a thick black line at mid-thickness and banded structures across the thickness as thin grey lines.

Several cases were investigated:

(i) at 150 µm from the outer surface
(ii) at 200 µm from the outer surface
(iii) at 250 µm from the outer surface
(iv) at 300 µm from the outer surface
(v) at 350 µm from the outer surface
(vi) at 400 µm from the outer surface

Note that the distances between the outer surface and the band were measured in the undeformed state. After air-bending, as the thickness of the sheet had decreased, all the bands were located at a smaller distance from the outer surface.
As in section I, the Bron Besson yield criterion, a mixed isotropic / kinematic hardening rule and damage were included in the model for all these calculations. The same damage parameters as previously were kept both for the hard band and for the softer matrix.

Experimentally, in chapter 3, it was noticed that sub-surface cracks could appear with a hard band located at 50µm from the outer surface after air-bending of thickness-reduced Steel 2 (Figure IV.10).

Regarding damage maps given by the various calculations (Figure IV.11, air-bending test of Steel 1), it is difficult to affirm whether cracks initiate from the surface or from just below. However, it seems reasonable to say that as soon as bands are located as far as 250µm from the outer surface, cracks initiate from the surface even if hard bands are also damaged. For the band located at 200µm from the surface, it is not possible to exactly determine the exact initiation of the crack. For a band located between the outer surface

and 150µm below it, it seems that a sub-surface crack is noticed. Regarding this result, it seems that sub-surface cracks can appear with bands farther from the outer surface than for thickness-reduced Steel 2 (Figure IV.10) for which the critical distance was evaluated to 50µm. This difference can be due to various factors: (i) the sheet thickness (0.75mm for thickness-reduced Steel 2 and 1.6mm for Steel 1), (ii) the hard band thickness (a few microns for thickness reduced Steel 2 and 50µm for the modelling of Steel 1), etc.

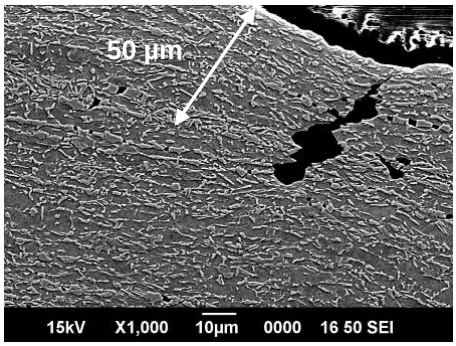

Figure IV.10. Sub-surface crack at 50µm from the outer surface after air-bending of thickness-reduced Steel 2.

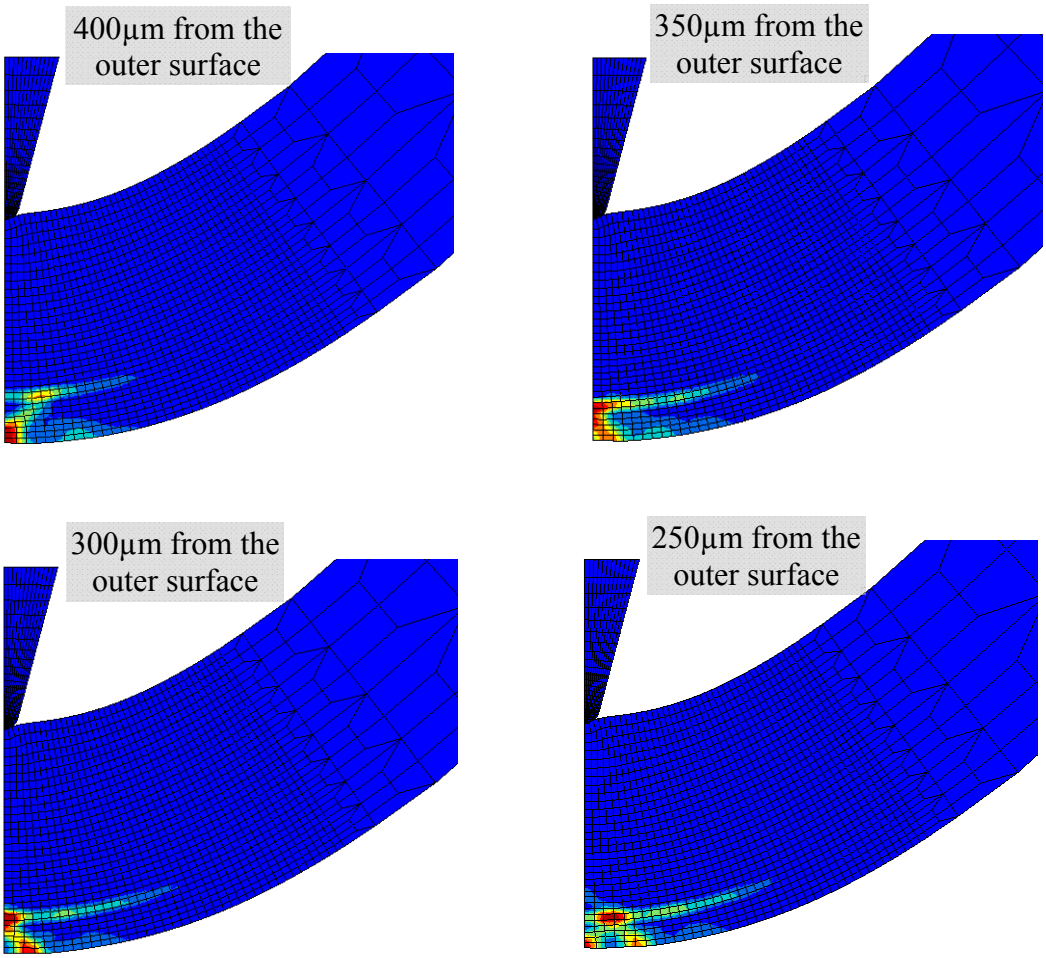

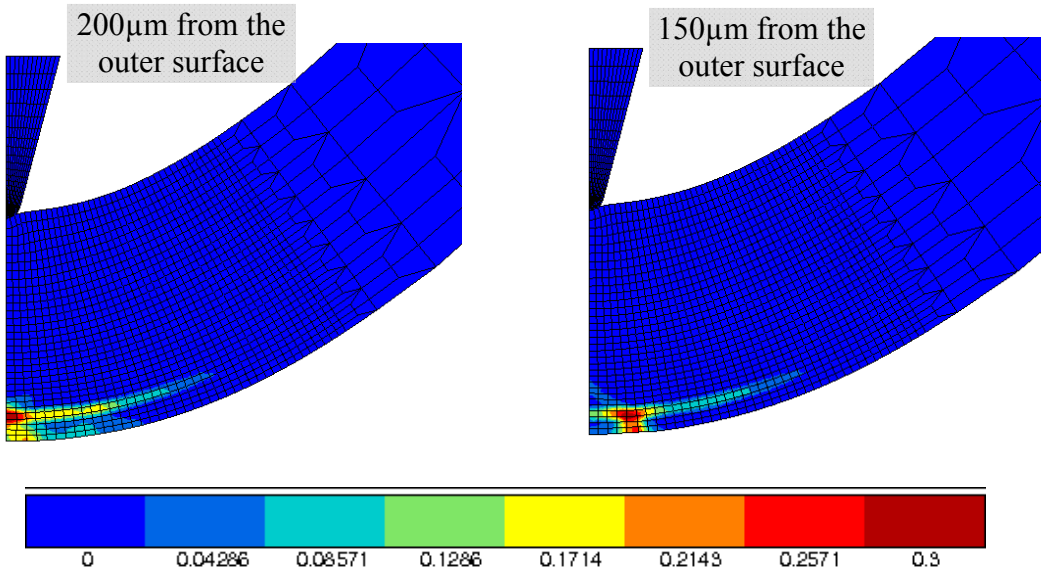

Figure IV.11. Damage map for six initial locations of the band across the thickness. Damage initiates internally as soon as the hard band is initially at 150µm or less from the outer surface.

The corresponding load / displacement curves are given in Figure IV.12. Note that the load decreases earlier with the closer proximity of the band to the outer surface. This is in agreement with the fact that cracks appeared earlier with bands located closer to the surface.

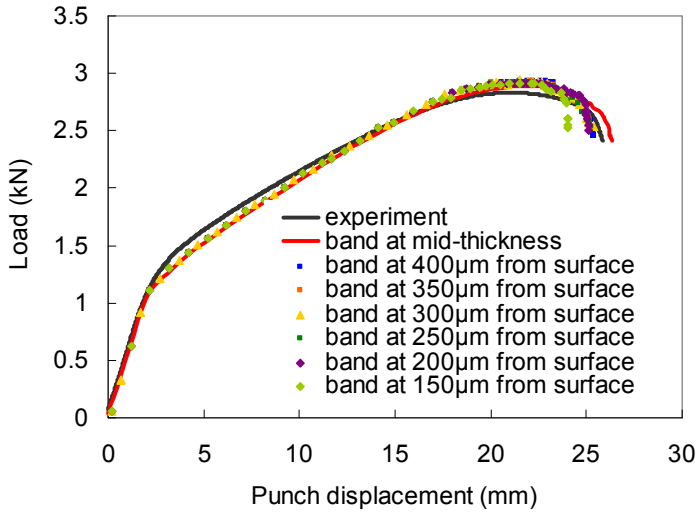

Figure IV.12. Load / displacement curves for various locations of the band across the thickness.

As cracks initiate from the central hard band in stretch-bending tests, it was not necessary to perform these same calculations with various locations of hard band for the stretch bending test. It is expected that by shifting the hard band close to the outer surface in stretch bending, cracks would also initiate from this band and fracture would appear earlier.

IV. Summary of Chapter 4

In this chapter, the mechanical analysis of both air and stretch bending tests was conducted by finite-element calculations taking damage into account. Damage-free constitutive equations were first determined in chapter 2 thanks to an experimental database based on tensile tests on smooth and notched specimens and to shear tests. In this chapter, the "reference" constitutive equations included mixed isotropic/kinematic hardening, a Bron Besson yield criterion and ductile damage development.

Using such a model made it possible to predict air bending as well as stretch bending tests very accurately both as load vs. punch displacement curves and as fracture initiation location. To represent the microstructure heterogeneity of the material along the sheet thickness, a band with a higher sensitivity to damage was included in the model at mid-thickness of the sheet. Using this meshing enabled to obtain a kind of "composite" model of the sheet representative of the as-received material. This model is thus able to represent the two bending tests and to help to predict the beginning of fracture.

In air-bending, cracks initiated from the outer surface when the hard band was located at mid-thickness. Additional air-bending calculations carried out on Steel 1 to investigate the influence of band location across the thickness demonstrated that cracks can initiate from just below the surface when hard bands were initially located at 150µm or less from the outer surface. In stretch bending, cracks initiated from the main hard band located at mid-thickness and this was also well predicted by the model.

Regarding the stretch bending test, the 3D mesh size has no influence both of the load vs. displacement curve and on the hoop stress and strain distributions through the thickness. As a "composite" material had to be used to investigate the influence of hard band on both bending tests, a thin mesh was required. Therefore, a mesh with 32 elements across the thickness was chosen to get a good compromise between good accuracy and a limited number of elements.

3D calculations are required to simulate stretch bending test while 2D modelling with plane strain elements was satisfactory for air-bending. This was explained by the fact that necking along the sample width occurs during the stretch bending test. The friction coefficient required for the modelling of the stretch bending test was adjusted by width reduction measurements on stretch bent specimens and was set to 0.1 between the punch and the sheet.

Résumé du Chapitre 4

Dans ce chapitre, une analyse mécanique à la fois du pliage en V et du pliage sous traction a été effectuée par la méthode des éléments finis en prenant en compte l'endommagement dans le modèle. La loi de comportement sans endommagement a été déterminée dans le chapitre 2 grâce à une base de données expérimentale incluant des tests de traction et de cisaillement. Dans cette partie, le nouveau modèle de "référence" inclut un écrouissage mixte, un critère d'écoulement anisotrope Bron Besson ainsi qu'une prise en compte de l'endommagement.

Grâce à cette loi de comportement, nous avons été capables de prédire aussi bien les courbes force/déplacement que la localisation de la rupture à la fois pour le test de pliage en V et pour le pliage sous traction. Pour représenter l'hétérogénéité de la microstructure à travers l'épaisseur dans le matériau, une bande possédant une plus grande sensibilité à l'endommagement a été incluse à mi-épaisseur dans le modèle. Ceci a permis d'obtenir un matériau "composite" modèle, représentatif du matériau de l'étude. Ce modèle est donc capable de représenter deux essais de pliage différents et de prédire l'apparition de la rupture.

En pliage en V, les fissures s'amorcent en surface quand les bandes de ségrégation sont situées à mi-épaisseur. Des calculs supplémentaires réalisés sur l'acier 1 pour déterminer l'influence de la position des bandes ont permis de montrer que les fissures peuvent s'initier sous la surface lorsque des bandes de ségrégation se trouvent à moins de 150µm de la surface de l'acier. En pliage sous traction, les fissures s'amorcent à partir de la ségrégation centrale et ce résultat a été correctement prédit par le modèle.

En pliage sous traction, le maillage 3D n'a aucune influence sur les courbes force/déplacement ou sur la distribution des déformations et des contraintes à travers l'épaisseur. Comme nous souhaitions modéliser un matériau "composite" pour déterminer l'influence des bandes de ségrégation (structures en bandes, ségrégation centrale) sur les deux tests de pliage, un maillage fin était nécessaire. Dans le but de garder un bon compromis entre un nombre limité d'éléments et une bonne précision, un maillage avec 32 éléments dans l'épaisseur a été choisi.

Un calcul 3D est nécessaire pour modéliser le test de pliage sous traction alors qu'une simulation numérique en 2D avec l'hypothèse des déformations planes est suffisante pour simuler le test de pliage en V. Ceci provient du fait qu'une striction dans la largeur apparait pendant le pliage sous traction. Le coefficient de frottement requis pour la modélisation du pliage sous traction a été ajusté grâce aux mesures de réduction de largeur sur les éprouvettes de pliage sous traction et a été évalué à 0.1 entre la tôle et le poinçon.

General conclusions and proposals for future work

In order to reduce both vehicle weight and fuel consumption, steelworkers need to develop and propose new steel grades such as Ultra High Strength Steels (UHSS). Among them, TRIP-aided steels, composed of hard retained austenite/martensite and bainite islands dispersed in a soft ferritic matrix, exhibit a very good compromise between strength and formability. However, as TRIP steels are used to perform very complex parts, formability issues can be encountered on these materials. On new TRIP steel grades with increasing mechanical properties, cracking can occur on radii during part stamping and it is difficult to directly connect steel formability with standard mechanical properties. It is therefore necessary to take the complex microstructures of these steels into account to accurately investigate their bendability.

This study aimed at understanding the relationships between microstructure and bendability of Ultra High Strength Steels for automotive applications. The approach used during this Ph.D. project was based on coupling experimental and numerical analyses. Four TRIP-aided steels, exhibiting both various bending performances and microstructures, were investigated through air and stretch bending tests.

Main results

The first chapter of this manuscript was devoted to a literature survey describing bendability, TRIP-aided steels and the origin of micro and macrosegregations. It was shown that several parameters such as mechanical properties, microstructure, tools, etc…can influence steel bendability, making it difficult to understand formability issues.
Regarding simulation of bending tests, various models have already been used, including (or not) an anisotropic yield criterion as well as a purely isotropic or mixed hardening rule. However, no detailed mechanical analysis of what happens through the specimen thickness was performed except with simplified models.
The aim of the present study was therefore to develop an experimental and numerical approach to quantitatively assess the effect of microstructural inhomogeneities on the bendability of ultrahigh strength steels. To introduce the study, this first chapter also provided both microstructural and general mechanical characterization (including standard bending tests) of the four selected TRIP-aided steels.
Among the four materials studied here, Steel 1 and Steel 2 exhibited the lowest bendability compared to the two other ones and they were selected for the remaining of the study. This result was in agreement with their tensile strength but no clear relationship with their microstructures could be determined. From these preliminary tests, it was thus not possible to determine the influence of microstructural inhomogeneities such as central segregation and banded structures on both air and stretch bending tests.

In chapter 2, an experimental database, including tensile smooth and notched specimens, as well as reverse shear tests was established. All these results made it possible to determine constitutive equations of Steel 1 in order to model the two bending tests. These constitutive equations included the anisotropic Bron Besson yield criterion associated with a mixed isotropic/kinematic hardening rule. They were included in a finite element model. The possibility to use “simplified models”, by assuming an isotropic von Mises yield criterion and/or a purely isotropic hardening rule was also discussed. Using a von Mises yield criterion, the experimental database was satisfactorily modelled even if the load was systematically always overestimated. Using purely isotropic hardening, reverse shear tests were not well predicted, as the Bauschinger effect was not taken into account.

Regarding the air-bending test, better predictions were obtained using a Bron Besson yield criterion and a mixed isotropic/kinematic hardening rule than with simplified models. In addition, when prestraining is carried out prior to air-bending, kinematic hardening is required to obtain a good prediction of the load. Moreover, the reduction in thickness during air-bending led to a shift of the neutral fibre toward the inner radius of the fold. Indeed, a change in the strain path in the elements located in the vicinity of the mid-thickness was observed as these nodes underwent initial compression followed by tension.
To investigate the effect of the central hard band on bendability, a specific air-bending facility was set up to test specimens of Steel 2 that were reduced in thickness, to locate this band at various distances from the outer radius of the fold. Model predictions of air-bending of thickness-reduced Steel 2 were in very good agreement at the beginning of the test but not at its end, possibly due to contact and/or very high strain issues. In addition, although higher strains were reached after 180° bending of thickness-reduced Steel 2 than with Steel 1, the former specimens did not crack with the central segregation at mid-thickness. Damage developed inside the specimens but did not lead to microcracking at the outer surface.

The third chapter dealt with the investigation of damage mechanisms in three tests: interrupted tensile tests, air and stretch bending tests. Metallographic observations of damage were performed using light and scanning electron microscopy. Ductile (dimple) fracture modes were found in both air and stretch bending tests. Cracks initiated from the outer surface or from just below in air-bending while cracks initiated from the central segregation in stretch bending; in both cases, cracks propagated along a band at 45° from the loading direction. Damage mainly nucleated by interfacial decohesion between martensite/austenite (M/A) islands and softer ferrite and occasionally by cleavage of M/A islands. Using tensile tests interrupted at various strain levels, the fracture strain of hard bands was determined to be about 0.10 for the studied TRIP-aided steels. Thicker hard bands promoted earlier damage nucleation than thinner ones and nucleation of new cavities further occurred all along the tests.
Using thickness-reduced specimens of Steel 2 showed that the closer the hard band to the outer surface, the higher the severity of cracking in air-bending. In fact, sub-surface cracks initiated from these hard bands. A quantitative relationship between damage, band thickness and local “mesoscopic” strain was eventually derived.

In chapter 4, a comparison between the two bending tests was presented. The constitutive equations established in chapter 2 were used and associated with an extension of the Gurson-Tvergaard-Needleman (GTN) model to well predict the fracture in both air and stretch bending tests. Scanning electron microscopy observations coupled with numerical results made it possible to determine the damage parameters for both “hard bands” material and “softer matrix” material. Using a “composite” representation of the sheet specimens, modelling of the two bending tests was carried out by assuming a hard band at mid-thickness exhibiting higher sensitivity to damage development. Using such a model allowed quantitative prediction of the load/displacement curves as well as of fracture location for two different tests: air and stretch bending. In addition, because of necking along the specimen width, 3D modelling was required for stretch bending simulations while 2D calculations with a plane strain assumption were shown to be accurate enough in the case of air-bending.

For the low alloy TRIP-aided steels studied here, hard bands do not have the same influence in both air and stretch bending tests. Regarding air-bending, banded structures

have a potentially deleterious effect on bendability while the central segregation does not lead to earlier cracking. Nevertheless, in one case, damage was observed at the central segregation after air-bending. In that particular case, the central segregation band was particularly thick but was still not responsible for microcracking at the outer surface. It was demonstrated that sub-surface cracks can occur when banded structures are located in the vicinity of the outer surface. Under the conditions described by the parametric numerical study carried out at the end of chapter 4 (air-bending with various locations of the hard band through the thickness for Steel 1), this critical distance was evaluated to about 150μm. It is worth noting that the potentially deleterious influence of a banded structure will depend on a combination of several parameters such as its ability to deform without damage, which will be a function of its average thickness, its location (distance from the outer surface of the fold), the strain generated during bending and probably on other parameters such as its hardness and so on. The higher the thickness and the amount of strain, the lower this critical distance will be.
The most deleterious metallurgical feature in stretch bending tests is the central segregation band, as fracture clearly initiates from this band. Therefore, when dealing with complex forming paths involving a tensile contribution to loading, it may be important to control and even to optimize the microstructure of those steels.
As shown in the first chapter, different steel processing parameters have to be used to act on banded structures and central segregation, respectively. Usually, a low coiling temperature is recommended to decrease the severity of the banded structure. In addition, as banded structures too close to the outer surface are deleterious in air-bending, it will be better to perform high superheat in the steelmaking process to concentrate bands towards the mid-thickness. This has to be balanced, however, with stretch bending properties, which strongly depend on the microstructure at mid-thickness. Regarding the central segregation, one actuator to reduce it, is to use the soft reduction process.

Proposals for future work

To go further in the understanding of the link between microstructure and bendability, it would be necessary to apply the methods developed in this study to other steel families such as Dual Phase (DP) and Multiphase (MP) steels. In these materials, other parameters such as inclusions, etc. can possibly play an important role on the bendability.

In this Ph.D. project, we only focused on two forming modes: air-bending and stretch bending. It would be interesting to determine the influence of microstructure in other formability tests such as stamping or expansion. For example, during stamping, some parts of the specimen are in tension, and therefore, central segregation band could also have a significant impact on formability.

Outputs of this work are mainly methodological and partly qualitative regarding microstructural data. Regarding the air-bending test, banded structures are the most important parameters to be controlled in order to improve the steel bendability.
It will be interesting to perform complementary experiments linking the band thickness, the amount of strain reached during bending and the sensitivity to damage in air-bending, to more precisely determine a critical thickness for banded structures and a minimum distance from the sheet surface to avoid premature failure in bending. It would also be important to include stress triaxiality effects in the phenomenological relationship

established here between the critical band thickness and the critical amount of strain, to more accurately apply this equation to other forming cases.
Finally, in order to improve steel bendability, heat treatments could be used to homogenize sheet microstructure and obtain “model” materials.

In this study, the damage initiation criterion was set at a macro or mesoscopic scale. A more detailed analysis of the mechanical behaviour of each phase could be helpful to determine the stress at the interface between harder and softer phases. The nanohardness of each phase was given and it is now essential to provide information about the shape and size of individual phases to perform a comprehensive micromechanical study of ductile damage void nucleation during bending. In addition, to get more information about damage mechanisms, it would be interesting to use tomography experiments. With all this data, it would then be possible to use a micromechanical model to more accurately determine a microstructure-based ductile damage initiation criterion.

The finite element method proved to be a good tool to investigate the bendability of a sheet material. With accurate constitutive equations and by reliably taking damage into account, the model can predict ductile fracture during bending. In view of the present results, it seems necessary to continue the parametric study of the air-bending test with various locations of the hard band across the specimen thickness. The present study was carried out with a “numerical” band exhibiting a thickness of 50μm. In the four steels under study, the central hard band was always thinner and the region containing such hard bands could only occasionally reach this thickness. To use more realistic assumptions, it would be necessary to use finer meshes and to again perform calculations with various locations of the band along the specimen thickness. It would be also interesting to investigate interactions between two hard bands (in particular, the effect of the distance between them) with respect to damage initiation.
Similar parametric studies could also be performed in stretch bending to determine a critical thickness that the central segregation should not exceed to avoid premature failure. By using such a damage initiation map together with predicted load/displacement curves, it will thus be possible to assess the bendability of a given steel sheet material.

Dans le but de réduire à la fois le poids des véhicules et leur consommation, les aciéristes doivent développer et proposer des nouveaux grades d'aciers comme les aciers Très Haute Résistance (THR). Parmi eux, les aciers TRIP, composés d'ilots durs d'austénite résiduelle, de martensite et de bainite dans une matrice ductile ferritique, présentent un bon compromis entre résistance et mise en forme. Cependant, comme les aciers TRIP sont utilisés pour réaliser des pièces complexes, ils peuvent présenter des problèmes de mise en forme. Sur les nouveaux grades d'aciers TRIP avec des propriétés mécaniques de plus en plus élevées, des fissures peuvent apparaître sur les rayons pendant l'emboutissage et il est difficile de directement relier la capacité de mise en forme d'un acier avec ses propriétés mécaniques classiques. Il est donc nécessaire de prendre en compte la microstructure complexe de ces aciers pour prédire d'une manière précise leur capacité à se plier.

Le but de cette étude était de comprendre les relations entre microstructure et capacité en pliage des aciers THR pour application automobile. L'approche qui a été utilisée pendant ce projet de thèse était basée à la fois sur des essais expérimentaux mais également sur une analyse de simulation numérique. Quatre aciers TRIP possédant des capacités en pliage différentes et des microstructures variées ont été étudiés à la fois en pliage en V et en pliage sous traction.

Principaux résultats

Le premier chapitre de ce manuscrit a été consacré à une étude bibliographique décrivant le pliage, les aciers TRIP et l'origine des micro et macroségrégations. Il a été montré que divers paramètres tels que les propriétés mécaniques, la microstructure, les outils, etc. peuvent avoir une influence sur la capacité en pliage, rendant difficile la compréhension des problèmes de mise en forme.
D'après la simulation numérique du test de pliage en V, différents modèles ont été utilisés, incluant (ou non) un critère d'écoulement anisotrope, un écrouissage purement isotrope ou mixte. Cependant, aucune étude détaillée de ce qui se produit dans l'épaisseur n'a été effectuée, mis à part sur des modèles simples.
Le but de cette étude était donc de développer une approche à la fois expérimentale et numérique pour évaluer l'effet d'une microstructure inhomogène sur la capacité en pliage des aciers THR. Pour introduire cette étude, une caractérisation à la fois mécanique et microstructurale a été effectuée sur les quatre aciers TRIP dans le premier chapitre.
Parmi les quatre matériaux étudiés ici, l'acier 1 et l'acier 2 présentaient une capacité en pliage faible comparé aux deux autres aciers et ils ont été choisis pour la suite de l'étude. Ce résultat était en accord avec leur résistance en traction mais aucune relation claire avec leurs microstructures n'a pu être déterminée. Ainsi, à partir de ces premiers essais, il n'a pas été possible de déterminer l'influence des inhomogénéités microstructurales comme la ségrégation centrale et les structures en bandes tant sur le test de pliage en V que sur le test de pliage sous traction.

Dans le chapitre 2, une base de données expérimentale, incluant des tests de traction sur éprouvettes lisses et entaillées, ainsi que des tests de cisaillement a été établie. Tous ces résultats ont permis de déterminer la loi de comportement de l'acier 1, destinée à modéliser les deux tests de pliage. Ce modèle inclut un critère d'écoulement anisotrope de Bron Besson ainsi qu'un écrouissage mixte isotrope/cinématique. Cette loi a été incluse dans un modèle de simulation numérique par éléments finis. La possibilité d'utiliser des

modèles simplifiés, tels qu'un critère d'écoulement isotrope de von Mises et/ou un écrouissage purement isotrope a aussi été envisagée. Avec un critère d'écoulement de von Mises, la base de données expérimentale a été prédite de manière satisfaisante même si les efforts étaient toujours surestimés. Avec un écrouissage purement isotrope, les essais de cisaillement réversibles n'ont pas été bien prédits, car l'effet Bauschinger n'était pas été pris en compte.
Quant aux essais de pliage en V, de meilleures prédictions ont été obtenues en utilisant un critère d'écoulement de Bron Besson et un écrouissage mixte isotrope/cinématique qu'avec des modèles simplifiés. De plus, quand une prédéformation est effectuée avant un pliage en V, un écrouissage cinématique est nécessaire pour prédire de manière satisfaisante les courbes force/déplacement. La réduction de l'épaisseur apparaissant pendant le pliage en V a mené à un déplacement de la fibre neutre vers le rayon intérieur du pli. En effet, les éléments situés proches de la mi-épaisseur ont subi un changement de trajet (compression initiale suivi par une tension).
Pour déterminer l'effet d'une bande de ségrégation sur le pliage, un essai spécifique du pliage en V a été utilisé sur l'acier 2 rectifié en épaisseur, sur lequel cette bande dure a été placée à différentes positions par rapport à la surface externe du pli. Les prédictions données par le modèle du pliage en V de l'acier 2 rectifié étaient en accord au début du test, mais pas à la fin. Ceci pourrait être dû à des problèmes de contact et/ou de déformations atteintes très importante. De plus, bien que des déformations plus élevées aient été atteintes après un pliage de l'acier 2 rectifié à 180° qu'avec l'acier 1, ces échantillons n'ont pas fissuré avec la ségrégation centrale à mi-épaisseur. L'endommagement s'est développé dans l'épaisseur mais n'a pas entraîné une microfissuration sur la surface extérieure.

Le troisième chapitre a traité des mécanismes d'endommagement au cours de trois essais : des tests de traction interrompus, du pliage en V et du pliage sous traction. Des observations métallographiques de l'endommagement ont été effectuées en utilisant la microcopie optique et celle à balayage. Les ruptures sont ductiles (avec cupules) aussi bien en pliage en V qu'en pliage sous traction. Les fissures s'amorcent à partir de la surface extérieure ou juste en-dessous en pliage en V alors qu'elles s'initient à partir de la ségrégation centrale en pliage sous traction; dans les deux cas, les fissures se propageaient à 45°. L'endommagement apparaît principalement par décohésion entre les îlots martensite/austénite et la ferrite et de temps en temps par clivage des îlots M/A. En utilisant des tests de traction interrompus à différents niveaux de déformation, la déformation à rupture des bandes de ségrégation a été évaluée à environ 0.10 pour les aciers TRIP étudiés. Les bandes de ségrégation les plus épaisses ont été endommagées plus rapidement que les plus minces et la germination de nouvelles cavités est apparue durant tout l'essai.
L'utilisation des échantillons de l'acier 2 rectifié en épaisseur a mis en évidence que plus les bandes de ségrégation étaient proches de la surface extérieure, plus les éprouvettes fissuraient tôt en pliage en V. De plus, des fissures en sous cutané se sont initiées sur ces bandes. Une relation quantitative entre l'endommagement, l'épaisseur des bandes et la déformation locale "mésoscopique" a été proposée.

Dans le chapitre 4, une comparaison entre les deux tests de pliage a été présentée. La loi de comportement établie dans le chapitre 2 a été utilisée et associée à une extension du modèle de Gurson-Tvergaard-Needleman (GTN) pour bien prédire la rupture à la fois en pliage en V et en pliage sous traction. Des observations au microscope électronique à balayage couplées à des résultats de simulation numérique ont permis de déterminer les

paramètres d'endommagement à la fois pour "les bandes de ségrégation" et pour "la matrice ductile". En utilisant ce matériau "composite" représentatif de l'échantillon, une modélisation des deux tests de pliage a été effectuée en mettant une bande dure à mi-épaisseur possédant la plus grande sensibilité à l'endommagement. L'utilisation d'un tel modèle a permis la prédiction des courbes de force/déplacement aussi bien que la localisation de la rupture pour deux tests différents : le pliage en V et le pliage sous traction. De plus, en raison de la striction apparaissant dans la largeur de l'échantillon, une simulation en 3D a été nécessaire en pliage sous traction alors que des calculs 2D étaient suffisamment précis pour la modélisation du pliage sous traction.

Pour les aciers TRIP étudiés, les bandes dures n'ont pas la même influence en pliage en V ou en pliage sous traction. En pliage en V, les structures en bandes ont un effet néfaste sur le pliage tandis que la ségrégation centrale n'entraîne pas une fissuration prématurée. Néanmoins, dans un cas, nous avons observé de l'endommagement au niveau de la ségrégation centrale en pliage en V. Dans ce cas particulier, la bande de ségrégation centrale était particulièrement épaisse, mais n'était pas responsable de la microfissure de la surface extérieure. Nous avons montré que des fissures sous-cutanées peuvent apparaître quand les bandes de ségrégation sont placées proches de la surface extérieure. Dans les conditions décrites par l'étude paramétrique effectuée à la fin du chapitre 4 (pliage en V de l'acier 1 avec différentes positions des bandes à travers l'épaisseur), nous avons évalué cette distance critique à environ 150µm.
Il faut noter que l'influence néfaste d'une structure en bande dépendra d'une combinaison de plusieurs paramètres comme sa capacité de se déformer sans endommagement, qui dépendra de son épaisseur moyenne, son emplacement (distance par rapport à la surface extérieure), la déformation atteinte en pliage et probablement d'autres paramètres comme sa dureté, etc. Plus l'épaisseur de la bande et la déformation seront élevées, plus cette distance critique sera faible.
Le paramètre métallurgique le plus néfaste en pliage sous traction est la ségrégation centrale, étant donné que les fissures s'amorcent à partir de celle-ci. Lorsque des trajets de chargement impliquant une contribution en traction sont appliqués, il est important de contrôler et même d'optimiser la microstructure de ces aciers.
Comme indiqué dans le premier chapitre, différents procédés doivent être utilisés pour agir sur les structures en bandes et sur la ségrégation centrale. Habituellement, une température de bobinage basse est recommandée pour diminuer la sévérité de ces bandes. De plus, comme des structures en bandes trop proches de la surface extérieure sont néfastes en pliage en V, il sera préférable d'effectuer une surchauffe haute dans le processus sidérurgique pour concentrer les structures en bandes vers la mi-épaisseur. Cela doit être équilibré, cependant, avec les propriétés en pliage sous traction, qui dépendent fortement de la microstructure à mi-épaisseur. Quant à la ségrégation centrale, un remède pour la diminuer pourrait être d'utiliser le processus de réduction douce.

Perspectives

Pour aller plus loin dans la compréhension des liens entre microstructure et pliage, il serait nécessaire d'appliquer les méthodes développées dans cette étude à d'autres familles d'aciers comme les aciers Dual Phase (DP) ou Multiphasés (MP). Dans ces matériaux,

d'autres paramètres comme les inclusions, les éléments d'alliage, etc. pourraient peut être jouer un rôle important sur le pliage.

Au cours de ce projet de thèse, nous nous sommes concentrés sur deux essais de mise en forme : le pliage en V et le pliage sous traction. Il serait intéressant de déterminer l'influence de la microstructure dans d'autres tests de mise en forme comme lors d'un emboutissage ou d'un test d'expansion. Par exemple, pendant l'emboutissage, comme certaines parties de la pièce sont en traction, la bande de ségrégation centrale pourrait aussi avoir un impact pendant la mise en forme.

Les données de ce travail sont principalement méthodologiques et qualitatives quant aux données microstructurales. En pliage en V, les structures en bandes sont les paramètres les plus importants qui doivent être contrôlés pour améliorer le pliage des aciers.
Il sera intéressant d'effectuer des essais supplémentaires reliant l'épaisseur d'une bande, sa déformation atteinte en pliage ainsi que sa sensibilité à l'endommagement, pour déterminer précisément une épaisseur critique pour les structures en bandes ainsi que la distance minimum par rapport à la surface à éviter pour limiter les fissures prématurées en pliage. Il serait aussi important d'inclure les effets de la triaxialité des contraintes dans la relation phénoménologique établie dans le chapitre 3 entre l'épaisseur critique d'une bande et la déformation critique, pour appliquer de manière plus précise cette équation à d'autres cas de mise en forme.
En pliage sous traction, la ségrégation centrale devrait être réduite et il sera essentiel d'éviter des bandes dures continues.
Enfin, pour améliorer le pliage des aciers, des traitements thermiques pourraient être utilisés pour homogénéiser la microstructure des tôles et ainsi obtenir des matériaux "modèles".

Dans cette étude, le critère d'endommagement a été établi à une échelle macro ou mésoscopique. Une analyse plus détaillée du comportement mécanique de chaque phase pourrait être utile pour déterminer la contrainte à l'interface entre les phases dures et les phases plus ductiles. La nanodureté de chaque phase a été donnée et il est maintenant essentiel de fournir des informations sur la forme et la taille de ces phases pour effectuer une étude micromécanique complète des mécanismes ductile d'endommagement pendant le pliage. De plus, pour obtenir plus d'informations sur des mécanismes d'endommagement, il serait intéressant d'utiliser la tomographie. Avec toutes ces données, il serait alors possible d'utiliser un modèle micromécanique pour déterminer précisément un critère d'endommagement.

La méthode des éléments finis s'est avérée être un bon outil pour étudier le pliage des aciers. Avec une loi de comportement précise et en prenant en compte l'endommagement de façon fiable, le modèle peut prévoir la rupture en pliage. Au vu des résultats, il semble nécessaire de continuer l'étude paramétrique du test de pliage en V avec différentes positions de la bande de ségrégation à travers l'épaisseur. L'étude actuelle a été effectuée avec une bande de ségrégation "numérique" ayant une épaisseur de 50µm. Dans les quatre aciers étudiés, la bande de ségrégation centrale était toujours plus mince et la zone contenant de telles bandes dures pouvaient parfois atteindre cette épaisseur. Pour utiliser des hypothèses plus réalistes, il serait nécessaire d'utiliser des maillages plus fins et de refaire des calculs avec différentes positions de la bande à travers l'épaisseur. Il serait également intéressant d'étudier les interactions entre deux bandes dures (particulièrement l'effet de la distance entre elles) et leurs rôles sur l'endommagement.

Des études paramétriques semblables pourraient aussi être effectuées sur le pliage sous traction afin de déterminer l'épaisseur critique que la ségrégation centrale ne devrait pas excéder pour éviter des ruptures prématurées. En utilisant les cartes d'endommagement et les courbes force/déplacement prédites par le modèle, il sera ainsi possible d'évaluer la capacité en pliage d'un acier donné.

Bibliography

Bibliography

Andrews, K.W., **1965**, Empirical formulae for the calculation of some transformation temperatures, Journal of the Iron and Steel Institute, 203, p. 721-727.

Aramis system, Optical 3D deformation analysis software developed by GOM GmbH, http://www.gom.com/3d-software/Aramis-software.html

Avramovic-Cingara, G., Ososkov, Y., Jain, M.K., Wilkinson, D.S., **2009**, Effect of martensite distribution on damage behaviour in DP600 dual phase steels, Materials Science and Engineering A, 516, p. 7-16.

Bach, M., Broll, N., Cornet, A., Gaide, L., **1996**, Diffraction X en traitements thermiques : dosage de l'austénite résiduelle par diffraction des rayons X, Journal de physique IV, 6, p. C4-887/C4-895.

Bahloul, R., Mkaddem, A., Dal Santo, Ph., Potiron, A., **2006**, Sheet metal bending optimisation using response surface method, numerical simulation and design of experiments, International Journal of Mechanical Sciences, 48, p. 991-1003.

Bai, D.Q., Di Chiro, A., Yue, S., **1998**, Stability of retained austenite in a Nb microalloyed Mn-Si TRIP steel, Materials Science Forum, 284-286, p. 253-260.

Bai, Y., Wierzbicki, T., **2010**, Application of extended Mohr-Coulomb criterion to ductile fracture, International Journal of Fracture, 161, p. 1-20.

Baik, S.C., Kim, S., Jin, Y.S., Kwon, O., **2001**, Effects of alloying elements on mechanical properties and phase transformation of cold rolled TRIP steel sheets, ISIJ International, 41, p. 290-297.

Bao, Y., Wierzbicki, T., **2005**, On the cut-off value of negative triaxiality for fracture, Engineering Fracture Mechanics, 72, p. 1049-1069.

Barbel, L., Tosal-Martinez, L., De Cooman, B., **2002**, Effect of phosphorus on the properties of a cold rolled and intercritically annealed TRIP-aided steel, in : Int. Conf. on TRIP-Aided high strength ferrous alloys, Ghent, Belgium, p. 147-152.

Barlat, F., Lege, D.J., Brem, J.C., **1991**, A six component yield function for anisotropic materials, International Journal of Plasticity, 7, p. 693-712.

Barlat, F., Brem, J.C., Yoon, J.W., Chung, K., Dick, R.E., Lege, D.J., Pourboghrat, F., Choi, S.H., Chu, E., **2003**, Plane stress yield function for aluminum alloy sheets - Part 1: theory, International Journal of Plasticity, 19, p. 1297-1319.

Bastien, P.G., **1957**, The Mechanism of formation of banded structure, ISIJ, p. 281-291.

Ben Bettaieb, M., Lemoine, X., Duchêne, L., Habraken, A.M., **2010**, Simulation of the bending process of hardening metallic sheets using damage model. Part I: Theoretical development and numerical implementation, Material Science and Engineering A, 528, p. 434-441.

Ben Bettaieb, M., Lemoine, X., Duchêne, L., Habraken, A.M., **2010**, Simulation of the bending process of hardening metallic sheets using damage model. Part II: Numerical investigations, Materials Science and Engineering A, 528, p. 442-448.

Béranger, G., Henry, G., Sanz, G., **1994**, Le livre de l'acier, Lavoisier

Besson, J., Foerch, R., **1997**, Large scale object-oriented finite element code design, Computer methods in applied mechanics and engineering, 142, p. 165-187.

Besson, J., Devillers-Guerville, L., Pineau, A., **2000**, Modeling of scatter and size effect in ductile fracture: application to thermal embrittlement of duplex stainless steels, Engineering Fracture Mechanics, 67, p. 169-190.

Besson, J., Steglich, D., Brocks, W., **2003**, Modeling of plane strain ductile rupture, International Journal of Plasticity, 19, p. 1517-1541.

Besson, J., Guillemer-Neel, C., **2003**, An extension of the Green and Gurson models to kinematic hardening, Mechanics of Materials, 35, p. 1-18.

Bleck, W., **2002**, Using the TRIP effect –The Dawn of a promising group of cold formable steels, in : Int. Conf. on TRIP-aided high strength ferrous alloys, Ghent, Belgium, p. 13.

Bobadilla, M., **2003**, Microsegregation in steels, ArcelorMittal internal document.

Bobadilla, M., **2008**, Solidification in continuous casting, ArcelorMittal internal document.

Bobadilla, M., Theyssier, M.C., Jolivet, J.M., Bonnet, F., Sturel, T., **2009**, Macrosegregations and microsegregations control in AHSS grades. Key actuators, ArcelorMittal internal document.

Bouquerel, J., Verbeken, K., De Cooman, B.C., **2006**, Microstructure-based model for the static mechanical behaviour of multiphase steels**,** Acta Materialia, 54, p. 1443-1456.

Bridgman, P.W., **1952**, Studies in large plastic flow and fracture: With special emphasis on the effects of hydrostatic pressure, McGraw-Hill.

Bron, F., Besson, J., **2004**, A yield function for anisotropic materials. Application to aluminium alloys, International Journal of Plasticity, 20, p. 937-963.

Brunet, M., Sabourin, F., Mguil-Touchal, S., **1996**, The prediction of necking and failure in 3D sheet forming analysis using damage variable, Journal de Physique III, 6, p. C6-473/C6-482.

Chaboche, J.L., **1989**, Constitutive equations for cyclic plasticity and cyclic viscoplasticity. International Journal of Plasticity, 5, p. 247-302.

Chaboche, J.L., **2008**, A review of some plasticity and viscoplasticity constitutive theories, International Journal of Plasticity, 24, p. 1642-1693.

Chakrabarty, J., Lee, W.B., Chan, K.C., **2000**, An analysis of the plane-strain bending of an orthotropic sheet in the elastic/plastic range, Journal of Materials Processing Technology, 104, p. 48-52.

Chakrabarty, J., Lee, W.B., Chan, K.C., **2001**, An exact solution for the elastic/plastic bending of anisotropic sheet metal under conditions of plane strain, International Journal of Mechanical Sciences, 43, p. 1871-1880.

Charpentier, P.L., **1975**, Influence of punch curvature on the stretching limits of sheet steel, Metallurgical Transactions A, 6, p. 1665-1669.

Chen, H.C., Era, H., Shimizu, M., **1989**, Effect of phosphorus on the formation of retained austenite and mechanical properties in Si-containing low-carbon steel sheet, Metallurgical Transactions A, 20, p. 437-445.

Cheng, L., Böttger, A., De Keijser, T.H., Mittemeijer, E.J., **1990**, Lattice parameters of iron-carbon and iron-nitrogen martensites and austenites, Scripta Metallurgica, 24, p. 509-514.

Chien, W.Y., Pan, J., Tang, S.C., **2004**, A combined necking and shear localization analysis for aluminum sheets under biaxial stretching conditions, International Journal of Plasticity, 20, p. 1953-1981.

Chu, C.C., Needleman, A., **1980**, Void nucleation effects in biaxially stretched sheets, Journal of Engineering Materials and Technology, 102, p. 249-256.

Cockroft, M.G., Latham, D.J., **1968**, Ductility and workability of metals, Journal of the Institute of Metals, 96, p. 33-39.

Col, A., **2010**, L'emboutissage des aciers, L'Usine Nouvelle, Dunod, p. 273.

Dalloz, A., **2007**, Etude de l'endommagement par découpe des aciers Dual Phase pour application automobile, thèse, Ecole des Mines de Paris.

Dalloz, A., Besson, J., Gourgues-Lorenzon, A.F., Sturel T., Pineau, A., **2009**, Effect of shear cutting on ductility of a dual phase steel, Engineering Fracture Mechanics, 76, p.1411-1424.

Damborg, D.D., **1998**, Prediction of fracture in bending under tension, in : Proceeding of the 19th Riso International Symposium on Material Science: Modelling of Structure and Mechanics from Microscale to Product, Roskilde, Denmark, p. 235-240.

Date, P.P., Narashima, K., Maiti, S.K., Singh, U.P., **1999**, On the prediction of springback in V-bending of metallic sheets under plane strain condition, in : Proceeding of the International Conference on Sheet Metal, Erlangen, Germany, p. 447-456.

Datsko, J., Yang, C.T., **1960**, Correlation of bendability of materials with their tensile properties, Journal of Engineering for Industry, , p. 309-314.

Demeri, M.Y., **1981**, The stretch bend forming of sheet metal, Journal of Applied Metalworking, 2, p. 3-10.

De Meyer, M., Vanderschueren, D., De Cooman, B.C., **1999**, The influence of the substitution of Si by Al on the properties of cold rolled C-Mn-Si TRIP steels, ISIJ International, 39, p. 813-822.

Determe, H., **1998**, Cétim, Formation: Influence des caractéristiques de la tôle sur les opérations de pliage, emboutissage et découpage.

Didier, M., Bobadilla, M., **2008**, Solidification and casting. Microsegregation and macrosegregation, ArcelorMittal internal document.

Eggertsen, P.A., Mattiasson, K., **2009**, On the modelling of the bending-unbending behaviour for accurate springback predictions, International Journal of Mechanical Sciences, 51, p. 547-563.

Eggertsen, P.A., Mattiasson, K., **2010**, On constitutive modelling for springback analysis, International Journal of Mechanical Sciences, 52, p. 804-818.

Faleskog, J., Gao, X., Shih, C., **1998**, Cell model for nonlinear fracture analysis. I: Micromechanics calibration, International Journal of Fracture, 89, p. 355-373

Falkinger, G., Andrieux, F., Helm, D., Riedel, H., **2010**, Finite-element modelling of Nakajima tests in due consideration of anisotropic ductile damage, in : IDDRG, June 2010, Graz, Autriche.

Friedman, P.A., Luckey, S.G., **2002**, Failure of Al-Mg-Si alloys in bending, Journal of Failure Analysis, 1, p. 33-42.

Furnémont, Q., Kempf, M., Jacques, P.J., Göcken, M., Delannay, F., **2002**, On the measurement of the nanohardness of the constitutive phases of TRIP-assisted multiphase steels, Materials Science and Engineering A, 328, p. 26-32.

Gallagher, M.F., Speer, J.G., Matlock, D.K., Fonstein, N.M., **2002**, Microstructure development in TRIP-sheet steels containing Si, Al and P, in : Proceedings of the 44th Mechanical Working and Steel Processing Conference and the 8th International Rolling Conference and International Symposium on Zinc-Coated Steels, Orlando, 2002, p.153-172.

Gan, W., Wagoner, R.H., **2004**, Die design method for sheet springback, International Journal of Mechanical Sciences, 46, p. 1097-1113.

Geng, L., Wagoner, R.H., **2002**, Role of plastic anisotropy and its evolution on springback, International Journal of Mechanical Sciences, 44, p. 123-148.

Gieck, K., **1997**, Formulaire technique, 10th ed., Dunod.

Girault, E., Mertens, A., Jacques, P., Houbaert, Y., Verlinden, B., Van Humbeek, J., **2001**, Comparison of the effects of silicon and aluminium on the tensile behaviour of multiphase TRIP-Assisted steels, Scripta Materialia, 44, p. 885-892.

Goodwin, G.M., **1968**, Application of strain analysis to sheet metal forming in the press shop, SAE paper 680093

Ghosh, A.K., **1976**, A criterion for ductile fracture in sheets under biaxial loading, Metallurgical Transactions A, 7, p. 523-533.

Graf, A., Hosford, W., **1993**, Effect of changing strain paths on forming limit diagrams of Al2008-T4, Metallurgical Transactions A, 24, p. 2503-2512.

Gurson, A.L., **1977**, Continuum theory of ductile rupture by void nucleation and growth: part I-yield criteria and flow rules for porous ductile media, Journal of Engineering Materials and Technology, 99, p. 2-15.

Haidemenopoulos, G.N., Olson, G.B., Cohen, M., Tsuzaki, K., **1989**, Transformation plasticity of retained austenite in stage-I tempered martensitic steels, Scripta Metallurgica, 23, p. 207-212.

Hambli, R., Mkaddem, A., Potiron, A., **2004**, Finite element damage modeling in bending processes, Journal of Materials Processing Technology, 147, p. 302-310.

Hecker, S.S., Stout, M.G., Staudhammer, K.P., Smith, J.L., **1982**, Effects of strain state and strain rate on deformation-induced transformation in 304 stainless steel: Part I. Magnetic measurements and mechanical behaviour, Metallurgical Transactions A, 13, p. 619-626.

Hill, R., **1948**, A theory of the yielding and plastic flow of anisotropic metals, Proceedings of the Royal Society of London, A193, p. 281-297.

Huang, J., Hammond, R.P., Conlon, K., Poole, W.J., **2002**, An experimental study of the ferrite austenite two phase regions in a Fe-C-Mn-Si steel using neutron diffraction, in : Proc. Int. Conf. on TRIP aided high strength ferrous alloys, Ghent, Belgium, 2002, p.187.

Hudgins, A., Matlock, D., Speer, J., Fekete, J., Walp, M., **2007**, The susceptibility to shear fracture in bending of advanced high strength sheet steels, in: Proceedings from Materials Science and Technology (MS&T): Advanced High Strength and Other Specialty Sheet Steel Products for the Automotive Industry, Detroit, Michigan, 2007, p. 145-157.

Jacques, P., **1998**, On the physics and mechanics of phase transformations in TRIP-assisted multiphase steels, Thèse de doctorat, Université Catholique de Louvain, Belgium.

Jacques, P., Furnemont, Q., Pardoen, T., Delannay, F., **2001**, On the role of martensitic transformation on damage and cracking resistance in TRIP-assisted multiphase steels, Acta Materialia, 49, p. 139-152.

Jacques, P.J., Petein, A., Harlet, P., **2002**, Improvement of mechanical properties through concurrent deformation and transformation : new steels for 21st century, in : Proc. Int. Conf. on TRIP-Aided high strength ferrous alloys, Ghent, Belgium, 2002, p. 281.

Jacques, P.J., Furnémont, Q., Lani, F., Pardoen, T., Delannay, F., **2007**, Multiscale mechanics of TRIP-assisted multiphase steels: I. Characterization and mechanical testing, Acta Materialia, 55, p. 3681-3693.

Jacques, P., Allain, S., Bouaziz, O., De, A., Gourgues, A.F., Hance, B.M., Houbaert, Y., Huang, J., Iza-Mendia, A., Kruger, S.E., Radu, M., Samek, L., Speer, J., Zhao, L., Van der Zwaag, S., **2009**, On measurement of retained austenite in multiphase TRIP steels – results of blind round robin test involving six different techniques, Materials Science and Technology, 25, p. 567-574.

Kao, A.S., Kuhn, H.A., Richemond, O., Spitzig, W.A., **1990**, Tensile fracture and fractographic analysis of 1045 spheroidized steel under hydrostatic pressure, Journal of Materials Research, 5, p. 83-91.

Karafillis, A.P., Boyce, M.C., **1993**, A general anisotropic yield criterion using bounds and a transformation weighting tensor, Journal of the Mechanics and Physics of Solids, 41, p. 1859-1886.

Keeler, S.P. and Backofen, W.A., **1963**, Plastic instability and fracture in sheets stretched over rigid punches, Transactions of the American Society for Metals, 56, p. 25-48.

Kim, S.J., Lee, C.G., Choi, I., Lee, S., **2001**, Effects of heat treatment and alloying elements on the microstructures and mechanical properties of 0.15 wt pct C TRIP-Aided cold rolled steel sheets, Metallurgical and Materials Transactions A, 32, p. 505-514.

Kim, S.J., Lee, C.G., Jeong, W.C., Park, I., **2002**, Microstructure and mechanical properties of the 0.15%C TRIP-Aided cold rolled steels containing Cu, Ni and Cr, in : Proc. Int. Conf. on TRIP-Aided high strength ferrous alloys, Ghent, Belgium, 2002, p. 165.

Kim, D., Barlat, F., Bouvier, S., Rabahallah, M., Balan, T., Chung, K., **2007**, Nonquadratic anisotropic potentials based on linear transformation of plastic strain rate, International Journal of Plasticity, 23, p. 1380-1399.

Kim, J.H., Sung, J.H., Wagoner, R.H., **2009**, Thermo-mechanical modelling of draw-bend formability tests, in : International conference, International Deep Drawing Research Group, Golden, CO, USA, 2009, p. 503-512.

Ladriere, J.H., He, X.J., **1986**, Mössbauer study on retained austenite in a Fe-Mn-C dual phase steel, Materials Science and Engineering A, 77, p.133-138.

Lani, F., Furnémont, Q., Van Rompaey, T., Delannay, F., Jacques, P.J., Pardoen, T., **2007**, Multiscale mechanics of TRIP-assisted multiphase steels: II. Micromechanical modelling, Acta Materialia, 55, p. 3695-3705.

Laukonis, J.V., Ghosh, A.K., **1978**, Effects of strain paths changes on the formability of sheet metals, Metallurgical Transactions A, 9, p. 1849-1856.

Lee, C.G., Kim, S.J., Oh, C.S., Lee, S., **2002**, Effects of heat treatment and Si addition on the mechanical properties of 0.1 wt% C TRIP-Aided cold rolled steel, ISIJ International, 42, p. 1162-1168.

Lee, C.G., Kim, S.J., Lee, T.H., Lee, S., **2004**, Effects of volume fraction and stability of retained austenite on formability in a 0.1C-1.5Si-1.5Mn-0.5Cu TRIP-aided cold rolled steel sheet, Materials Science and Engineering A, 371, p.16-23.

Lemaitre, J., **1985**, A continuous damage mechanics model for ductile fracture, Journal of Engineering Materials and Technology, 107, p. 83-89.

Lemaitre, J., Chaboche, J.L., **1990**, Mechanics of Solid Materials, Cambridge University Press.

Lemoine, X., Bettaieb, M.B., Goncalves, J., **2009,** Bibliography about bending process in particular formability criteria, ArcelorMittal internal document, p. 1-31.

LeRoy, G., Embury, J.D., Edwards, G., Ashby, M.F., **1981**, A model of ductile fracture based on the nucleation and growth of voids, Acta Metallurgica, 29, p. 1509-1522.

Leu, D.K., **1997**, A simplified approach for evaluating bendability and springback in plastic bending of anisotropic sheet metals, Journal of Materials Processing Technology, 66, p. 9-17.

Li, X., Yang, Y., Wang, Y., Bao, J., Li, S., **2002**, Effect of the material hardening mode on the springback simulation accuracy of V-free bending, Journal of Materials Processing Technology, 123, p. 209-211.

Lin, M., Olson, G.B., Cohen, M., **1992**, Distributed-activation kinetics of heterogeneous martensitic nucleation, Metallurgical Transactions 23A, p. 2987-2998.

Livatyali, H., Kinzel, G.L., Altan, T., **2003**, Computer aided die design of straight flanging using approximate numerical analysis, Journal of Materials Processing and Technology, 142, p. 532-543.

Luo, M., Wierzbicki, T., **2010**, Numerical failure analysis of a stretch bending test on dual-phase steel sheets using a phenomenological fracture model, International Journal of Solids and Structures, 47, p. 3084-3102.

Mahieu, J., Van Dooren, D., Barbé, L., De Cooman, B.C., **2002**, Influence of Al, Si and P on the kinetics of intercritical annealing of TRIP-Aided steels: Thermodynamical prediction and experimental verification, in : Proc. Int. Conf. on TRIP-Aided high strength ferrous alloys, Ghent, Belgium, 2002, p. 159.

Maki, J. Mahieu, J., De Cooman, B.C., Claessens, S., **2003**, Galvanisability of silicon free CMnAl TRIP steels, Material Science and Technology, 19, p. 125-131.

Marciniak, Z., Duncan, J.L., **1992**, Bending. The mechanics of sheet metal forming, E. Arnold, p.68-99.

Matsumura, O., Sakuma, Y., Takechi, H., **1987**, Enhancement of elongation by retained austenite in intercritical annealed 0.4C-1.5Si-0.8Mn steel, Transactions of the Iron and steel institute of Japan, 27, p. 570-579.

McClintock, F.A., **1968**, A criterion of ductile fracture by growth of holes, Journal of Applied Mechanics, 35, p. 363-371.

Mintz, B., **2001**, Hot dip galvanising of transformation induced plasticity and other intercritically annealed steels, International Materials Reviews, 46, 4, p. 169-197.

Moran, B., Ortiz, M., Shih, C.F., **1990**, Formulation of implicit finite-element methods for multiplicative finite deformation plasticity, International Journal for Numerical Methods in Engineering, 29, p. 483-514.

Muller, J., **2000**. Formulaire de mécanique générale, 17th ed, Paillart, p.147.

Nagataki, Y., Tsuyama, S., Hosoya, Y., Okita, T., **1994**, Effect of microstructure on bendability of ultra-high strength steel sheet, in : High-strength steels for automotive symposium proceedings, p. 239-244.

Nilsson, A., Melin, L., Magnusson, C., **1997**, Finite-element simulation of V-die bending: a comparison with experimental results, Journal of Materials Processing Technology, 65, p. 52-58.

Ohlert, J., Bleck, W., Hulka, K., **2002**, Control of microstructure on TRIP steels by niobium, in : Proc. Int. Conf. on TRIP-Aided High Strength Ferrous Alloys, Ghent, Belgium, 2002, p. 199.

Patel, J.R., Cohen, M., **1953**, Criterion for the action of applied stress in the martensitic transformation, Acta Metallurgica, 1, p. 531-538.

Pereloma, E.V., Timokhina, I.B., Hodgson, P.D., **1999**, Transformation behaviour in thermomechanically processed C-Mn-Si TRIP steels with and without Nb, Materials Science and Engineering A, 273-275, p. 448-452.

Perrin, G. and Leblond, J.B., **1990**, Analytical study of a hollow sphere made of plastic porous material and subjected to hydrostatic tension-application to some problems in ductile fracture of metals, International Journal of Plasticity, 6, p. 677-699.

Pichler, A., Stiaszny, P., **1999**, TRIP steel with reduced silicon content, Steel Research, 70, p. 459-465.

Pickering, F.B., **1992**, Constitution and properties of steels, Materials science and technology : a comprehensive treatment, 7, p. 272-284.

Poruks, P., Yakubtsov, I., Boyd, J.D., **2006**, Martensite-ferrite interface strength in a low-carbon bainitic steel, Scripta Materialia, 54, p. 41-45.

Quach, W.M., Teng, J.G., Chung, K.F., **2004**, Residual stresses in steel sheets due to coiling and uncoiling: a closed-form analytical solution, Engineering Structures, 26, p. 1249-1259.

Quach, W.M., Teng, J.G., Chung, K.F, **2009**, Residual stresses in press-braked stainless steel sections - I: Coiling and uncoiling of sheets, Journal of Constructional Steel Research, 65, p. 1803-1815.

Ragab, A.R., Saleh, C.A., **2005**, Evaluation of bendability of sheet metals using void coalescence models, Materials Science and Engineering A, 395, p.102-109.

Rèche, D., Sturel, T., Bouaziz, O., Gourgues-Lorenzon, A.F, **2011**, Damage development in low alloy TRIP-aided steels during air-bending, Materials Science and Engineering A, 528, p. 5241-5250.

Rèche, D., Besson, J., Sturel, T., Lemoine, X., Gourgues-Lorenzon, A.F., **2011**, Analysis of the air-bending tests using finite element simulation: Application to steel sheets, submitted to International Journal of Mechanical Sciences, May 2011.

Reed, R.C., Akbay, T., Shen, Z., Robinson, J.M., Root, J.H., **1998**, Determination of reaustenitisation kinetics in a Fe-0.4C steels using dilatometry and neutron diffraction, Material Science and Engineering A, 256, p. 152-165.

Rice, J.R. and Tracey, D.M., **1969**, On the ductile enlargement of voids in triaxial stress fields, Journal of the Mechanics and Physics of Solids, 17, p. 201-217.

Ridley, N., Stuart, H., Zwell, L., **1969**, Lattice parameters of Fe-C austenites at room temperature, Trans. Met. Soc. AIME, 245, p. 1834-1836.

Rigsbee, J.M., Van der Arend, P.J., **1977**, Laboratory studies of microstructures and structure-property relationships in dual phase steels, ed. A.T. Davenport, in : Proc. Conf. Formable HSLA and Dual Phase steels, Chicago, AIME, p. 56-86.

Roberts, C.S., **1953**, Effect of carbon on the volume fractions and lattice parameters of retained austenite and martensite, Trans. AIME, 197, p. 203-204.

Saanouni, K., Badreddine, H., **2007**, Damage prediction in sheet metal forming: theory, numerics and application, in : Numiform'07, Proceedings of the 9th International Conference on Numerical Methods in Industrial Forming Processes, Porto, Portugal, AIP Conference proceedings, p. 105-110.

Sriram, S., Wong, C., Huang, M., Yan, B., **2003**, Stretch bendability of advanced high strength steels, SAE technical paper, n° 2003-01-1151.

Sakuma, Y., Matsumura, O., Takechi, H., **1991**, Mechanical properties and retained austenite in intercritically heat treated bainite transformed steel and their variation with Si and Mn additions, Metallurgical Transactions A, 22, 1991, p. 489-498.

Sarkar, J., Kutty, T.R.G., Conlon, K.T., Wilkinson, D.S., Embury, J.D., Lloyd, D.J., Tensile and bending properties of AA5754 aluminum alloys, **2001**, Materials Science and Engineering A, 316, p. 52-59.

Shinohara, Y., Madi, Y., Besson, **2010**, J., A combined phenomenological model for the representation of anisotropic hardening behaviour in high strength steel line pipes, European Journal of Mechanics / A Solids, 29, p. 917-927.

Speich, G.R., Miller, R.L., **1979**, Mechanical properties of ferrite-martensite steels, in : Proc. Conf. Structure and Properties of Dual Phase Steels, New Orleans, TMS AIME, p. 145-182.

Sriram, S., Wong, C., Huang, M., Yan, B., **2003**, Stretch bendability of advanced high strength steels, in : SAE International World Congress, Detroit, Michigan, p. 107-115.

Srivastava, A.K., Bhattacharjee, D., Jha, G., Gope, N., Singh, S.B., **2007**, Microstructural and mechanical characterization of C-Mn-Al-Si cold-rolled TRIP-aided steel, Materials Science and Engineering A, 445-446, p. 549-557.

Steninger, J., Melander, A., **1982**, The Relation between bendability, tensile properties and particle structure of low-carbon steel, Scandinavian Journal of Metallurgy, 11, p. 55-71.

Stöcker, H., Jundt, F., Guillaume, G., **2007**. Physique, 2nd ed., Dunod, p. 253.

Sugimoto, K.I., Kikuchi, R., Hashimoto, S.I., **2002**, Development of high strength low alloy TRIP-aided steels with annealed martensite matrix, Steel research, 73, p. 253-258.

Tharrett, M.R., Stoughton, T.B., **2003**, Stretch-bend forming limits of 1008 Ak steel, in : SAE paper, n° 2003-01-1157, p.1-7.

Thompson, S.W., Howell, P.R., **1992**, Factors influencing ferrite/pearlite banding and origin of large pearlite nodules in a hypoeutectoid plate steel, Materials Science and Technology, 8, p. 777-784.

Thuillier, S., Le Maoût, N., Manach, P.Y., **2010,** Bending limit prediction of an aluminium thin sheet, International Journal of Material Forming, 3, p. 223-226.

Thuillier, S., Le Maoût, N., Manach, P.Y., **2011**, Influence of ductile damage on the bending behaviour of aluminium alloy thin sheets, Materials and Design, 32, p. 2049-2057.

Traint, S., Pichler, A., Hauzenberger, K., Stiaszny, P., Werner, E., **2002**, Influence of silicon, aluminium, phosphorus and copper on the phase transformations of low alloyed TRIP steels, in : Proc. Int. Conf. on TRIP-Aided high strength ferrous alloys, Ghent, Belgium, 2002, p. 121.

Tsukatani, I., Hashimoto, S., Inoue, T., **1991**, Effects of silicon and manganese addition on mechanical properties of high-strength hot rolled sheet steel containing retained austenite, ISIJ International, 31, p. 992-1000.

Tvergaard, V. and Needleman, A., **1984**, Analysis of the cup-cone fracture in a round tensile bar. Acta Metallurgica, 32, p. 157-169.

Tvergaard, V., **1989**, Material failure by void growth to coalescence, Advances in Applied Mechanics, 27, p. 83-151.

Uthaisangsuk, V., Prahl, U., Münstermann, S., Bleck, W., **2008**, Experimental and numerical failure criterion for formability prediction in sheet metal forming, Computational Materials Science, 43, p. 43-50.

Vallellano, C., Morales, D., Garcia-Lomas, F.J., **2008**, On the study of the effect of metal sheets, in : Conference Numisheet, Interlaken, Switzerland, September 2008.

Vladimirov, I.N., Pietryga, M.P., Reese S., **2010**, Anisotropic finite elastoplasticity with nonlinear kinematic and isotropic hardening and application to sheet metal forming, International Journal of Plasticity, 26, p. 659-687.

Wang, C., Kinzel, G., Altan, T., **1993**, Mathematical modeling of plane strain bending of sheet and plate, Journal of Materials Processing Technology, 39, p. 279-304.

Williams, B.W., Simha, C.H.M., Abedrabbo, N., Mayer, R., Worswick, M.J., **2010**, Effect of anisotropy, kinematic hardening and strain-rate sensitivity on the predicted axial crush response of hydroformed aluminium alloy tubes, International Journal of Impact Engineering, 37, p. 652-661.

Wu, J., Zhou, D., Zhang, L., Zhou, Y.J., Du, C.Q., Shi, M.F., **2006**, A failure criterion for stretch bendability of advanced high strength steels, SAE Technical Paper, n° 2006-01-0349.

Yamazaki, K., Oka, M., Yasuda, H., Mizuyama, Y., Tsuchiya, H., **1995**, Recent Advances in UHSS for automotive structural use, Nippon steel technical report, n°64, p. 37-44.

Yamazaki, K., Mizuyama, Y., Oka, M., Tokunaga, Y., **1995**, Influence of microstructure on bendability of ultrahigh-strength steel sheet, Journal of the Japan Society for Technology of Plasticity, 36, p. 973 – 978.

Yan, H.Y., Kai, G.Y., Jian, M.D., **2006**, Transformation behaviour of retained austenite under different deformation modes for low alloyed TRIP-assisted steels, Material Science and Engineering A, 441, p. 331-335.

Yoon, J., Barlat, F., Dick, R.E., Chung, K., Kang, T.J., **2004**, Plane stress yield function for aluminum alloy sheets - Part II : FE formulation and its implementation, International Journal of Plasticity, 20, p. 495-522.

Zackay, V.F., Parker, E.R., Fahr, D., Bush, R., **1967**, The enhancement of ductility in high strength steels, ASM Transactions Quarterly, 60, p. 252-259.

Zhang, Z.T., Hu, S.J., **1998**, Stress and residual stress distributions in plane strain bending, International Journal of Mechanical Sciences, 40, p. 533-543.

Zhao, K.M., Lee, J.K., **2002**, Finite element analysis of the three-point bending of sheet metals, Journal of Material Processing Technology, 122, p. 6-11.

Appendix

Appendix 1: Microstructural characterization procedures

Appendix 2: Mechanical characterization procedures

Appendix 1: Microstructural characterization procedures

A1.1. Light microscopy

Light optical microscopy was performed on each TRIP steel to characterize their microstructures and to conduct a quantitative analysis of phase components. Samples were mounted in resin and polished down to 1µm.

For these steels, a colorant etching is used to reveal the microstructure. The LePera etching makes it possible to reveal hard phases (martensite + retained austenite) in white and the soft ferrite in brown. This etching is composed of:

- Sodium disulfite (Sodium metabisulfite $Na_2 S_2 O_5$)
- Picric acid ($C_6 H_3 N_3 O_7$)
- Ethanol ($C_2 H_6 O$)

1) Dilute 1g of sodium disulfite in 100ml of distilled water → solution (A)
2) Dilute 4g of picric acid in 100ml ethanol → solution (B)

Just before using, mix these two solutions with identical proportions. Polished samples have to be etched during 5 to 10s.

In order to quantify the M/A islands content in each steel, light microscopy was carried out after a Klemm colorant etching. This etching enables to colour in white the M/A islands. This etching is composed of:

- 2g of potassium disulfite in 100mL of solution (A)
- Solution (A): 1kg of sodium thiosulfate in 300mL of water (warm this solution to help the dissolution).

A1.2. Scanning electron microscopy

The scanning electron microscope was used to observe damage more precisely and to perform fractographic observations. To carry out fractographic observations, specimens were directly put inside the microscope chamber and their fracture surfaces were observed using secondary electron imaging.

Observations of damage mechanisms required polished and electrically conductive specimens. In this case, samples were etched with 4% Nital.

Analysis conditions used for the study:
- acceleration tension: 15kV
- working distance close to 15mm
- secondary electron mode

A1.3. X-ray diffraction measurements

The amount of retained austenite contained in these TRIP steels was determined thanks to X-Ray Diffraction (XRD). These measurements have been performed, for each steel, on as-received material (without bending) and on bent samples which were first polished down to 1µm using diamond pastes and then with OPS (colloidal silica suspension) to avoid surface hardening and polishing-induced austenite transformation. Note that, with XRD, the measurements are localized at the first few microns just below the prepared sample surface. These measurements were carried out with a D500 Brucker diffractometer and with a cobalt tube (λ = 1.8 Å), under 40kV and 25mA. The angle domain in 2θ is between 30° and 130° with a step every 0.032° and 1second/step.

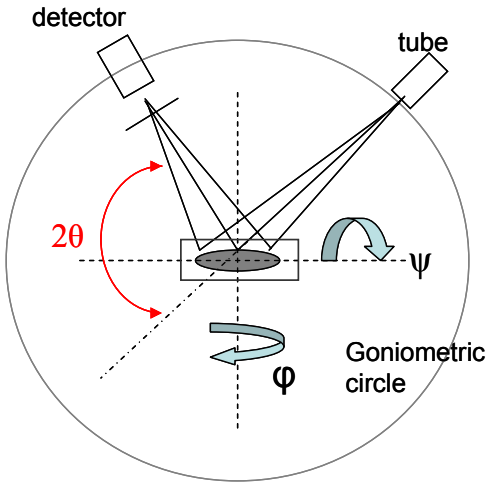

Figure A1.1. X-ray diffraction scheme.

To determine the amount of retained austenite in each sample, it is necessary to use the intensities of 6 peaks:

- austenite (γ): 200, 220, 311
- ferrite (α): 200, 211, 220

The amount of retained austenite is given by these formulas (Bach et al., 1996):

$\frac{C_\gamma}{C_\alpha} = \frac{\sum K_\alpha}{\sum K_\gamma} \cdot \frac{\sum I_\gamma}{\sum I_\alpha}$ and $C_\alpha + C_\gamma = 1$ where K_α and K_γ are correction coefficients and I_α, I_γ are the intensities of each peak.

A1.4. Magnetic measurements

The amount of retained austenite has also been measured by sigmametry for the three 1.6mm thickness steels, both on as-received material (without bending) and on bent samples. This technique consists in measuring the saturation magnetization of specimens with and without austenite. To perform this experiment, the magnetization is first measured on as-received samples (i.e. with retained austenite) and then, heat treatment at 500°C for two hours is carried out to decompose austenite contained in the material into ferrite and carbides.

Therefore, the content of retained austenite can be deduced by the difference between the two magnetizations by using the following equation:

$$V_\gamma = \frac{J_{s2} - J_{s1}}{J_{s2}}$$

Where J_{s1} is the saturation magnetization of the specimen with austenite and J_{s2} is the saturation magnetization of the specimen without austenite and V_γ is the volume content of retained austenite.

A1.5. Vickers microhardness measurements

Hardness measurements through the thickness of as-received and air-bent specimens were performed. The device used is a Emco microhardness testing. In the present case, two load values were tested: 300g for thin sheet specimens (0.75mm) and 500g for the other ones (1.6mm). Measurements were carried out in staggered rows on each specimen to get more points through the thickness. In addition, samples were polished before testing to have good reliability of measurements.

A1.6. Nanohardness measurements

The nanoindentation is a technique making possible to determine the nanohardness of various phases and to access at their Young modulus. This technique consists in indenting the material with a slight depth and to follow the penetration evolution as a function of the applied load. For these measurements, specimens were polished and a slight Nital etching was performed on each specimen. Analysis of experimental curves allows deducing mechanical properties of the surface of the material. The applied load (in µN) and the depth are stored all along the test. From these curves, the hardness (H in GPa) is determined by the ratio between the maximal applied load (P) and the indentation area (A).

Hence: $H = \frac{P}{A}$

The unloading curve depends on the elastic behaviour of the material. The Young modulus is then calculated by taking the tangent on the unloading curve. For these measurements, a loading/unloading cycle was used with a maximum applied load of 5000µN following by holding for about one second at this maximum load. The loading rate is about 1660µN/s both for the loading and the unloading.

Nanohardness measurements were carried out in the Evry's University with a nanohardness testing (Triboscope®, Hysitron SA) coupled with an atomic force microscope-AFM (Digital Instrument 3100). The AFM helps to locate the area to indent before testing, even if the resolution is poor due to non-optimized observation conditions.

In the present study, five nanohardness measurements were carried out both on the ferritic matrix and the M/A islands in the vicinity of the mid-thickness. Note that, due to the small size of the M/A islands, it was very difficult to be sure to have made an indentation on

these islands. Hence, when an indentation was performed at the interface between an M/A island and the ferritic matrix, another measurement was carried out.

Appendix 2: Mechanical characterization procedures

A2.1. Tensile tests

First, ISO tensile specimens of 80 mm in gauge length and 20 mm in width were tested according to the European standard EN 10002-1 (Figure A2.1). Load/line displacement of 0.5mm/min was prescribed with an initial strain rate of $2{,}5.10^{-4}$ s^{-1}. The engineering stress-strain curves for the four steels were determined both along rolling and transverse directions. The mechanical properties are characterized by means of the proof stress ($Rp_{0.2\%}$), the ultimate tensile strength (TS) and the uniform elongation (Ue%).

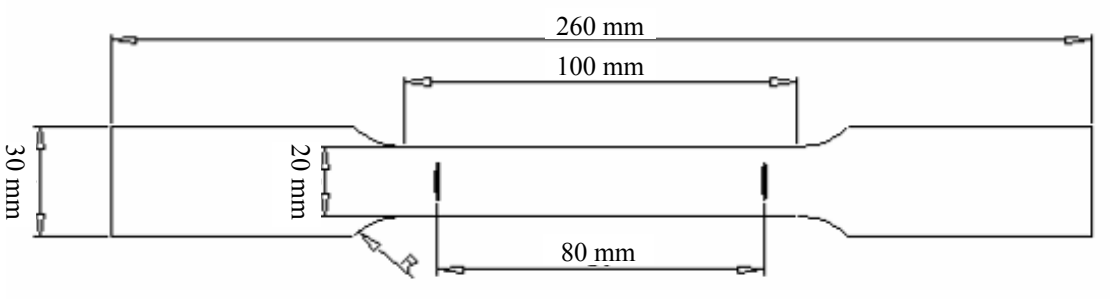

Figure A2.1. Scheme of tensile specimen (ISO 20x80 mm).

Secondly, tensile tests on smooth specimens with another dimension were performed for Steel 1 only (Figure A2.2). In the present case, tests were conducted with an initial elongation rate of 10^{-4} s^{-1}.

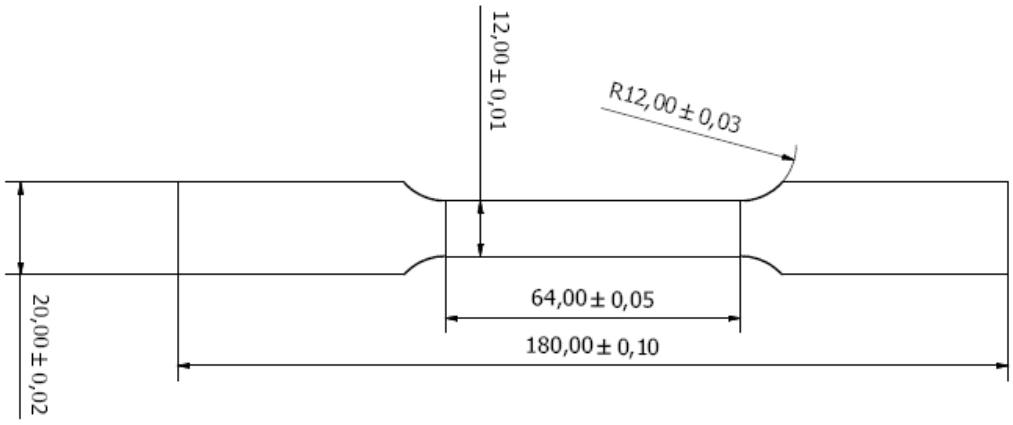

Figure A2.2. Additional tensile specimen used for Steel 1.

Tensile tests were also carried out on notched specimens. These specimens have a notch radius of 2mm with a distance between them of 10mm (Figure A2.3). The prescribed notch opening rate is 0.5 $mm.min^{-1}$.

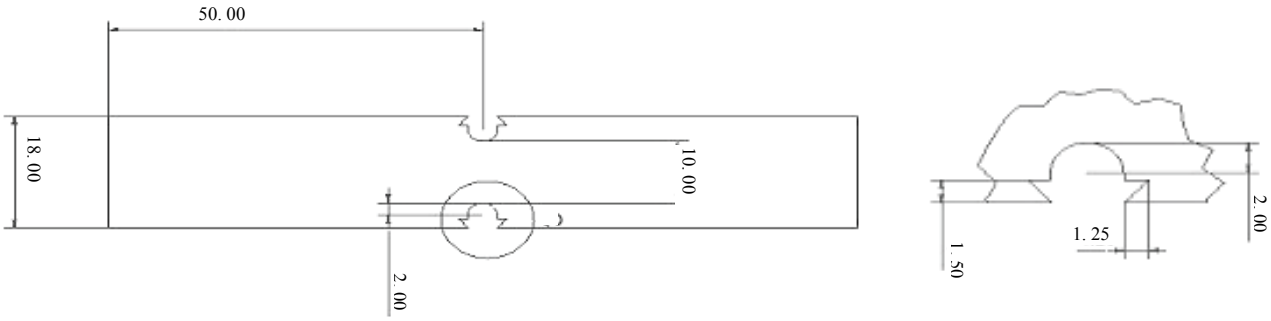

Figure A2.3. Scheme of notch tensile (NT) specimen and close-up view of a notch.

A2.2. Shear tests

Shear tests were performed on a shearing device and σ_{12} vs γ curves were stored for reverse shear tests. The cyclic shear tests were carried out along the rolling direction for $\gamma = 10$, $\gamma = 20$ and $\gamma = 30$ with a prescribed loading rate of 0.05 $kN.s^{-1}$. The scheme of reverse shear specimen is given in Figure A2.4.

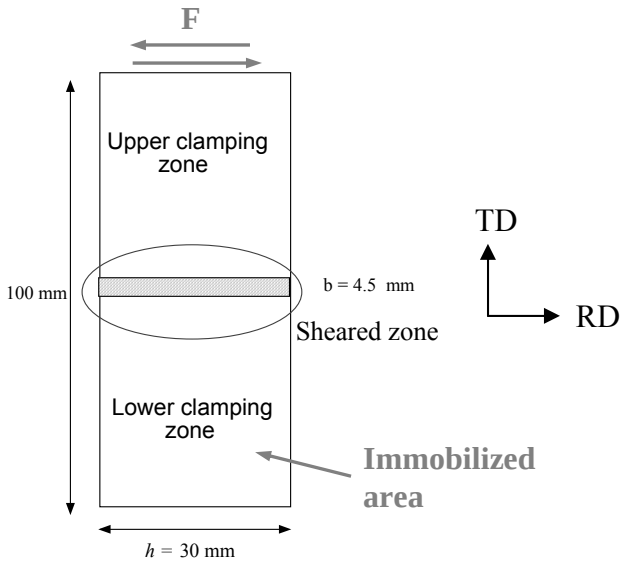

Figure A2.4. Reverse shear specimen.

A2.3. Air-bending tests

Air-bending specimens with a size of 50x100mm (Figure A2.6) were first edge ground to avoid premature failure starting from the cut-edge side surfaces. Air-bending device is shown in Figure A2.5.

The device was used on a Zwick universal tensile machine. The two rotary rolls have a diameter of 60mm. Two punches are used in this study. The first one is used to bend sheet with thickness of 1.6mm. This punch has a width of 10 mm and a radius close to 0mm (Figure A2.7a). The second one is used to bent sheet with a thickness of 0.75mm. It has a width of 0.8mm and a radius of 0.4mm (Figure A2.7b). All tests were conducted without lubrication.

For this test, a load/line displacement rate of 1mm.s^{-1} is used. The test is automatically stopped after a load drop between 5 and 10%. Finally the bending angle is given as a measurement to compare steels.

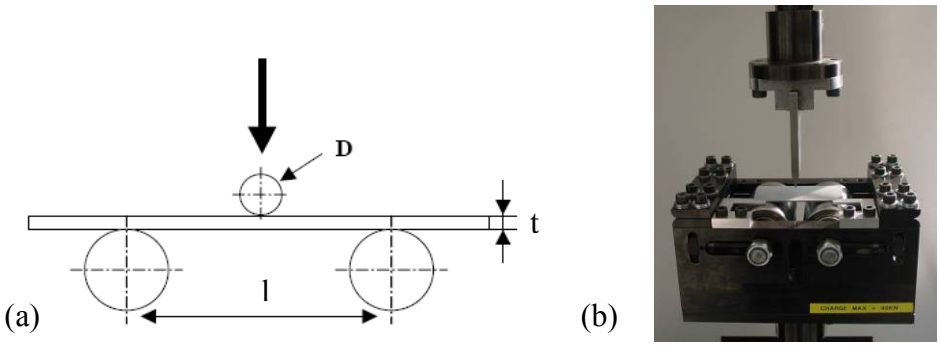

Figure A2.5. (a) Air-bending test scheme, (b) air-bending device used for the study.

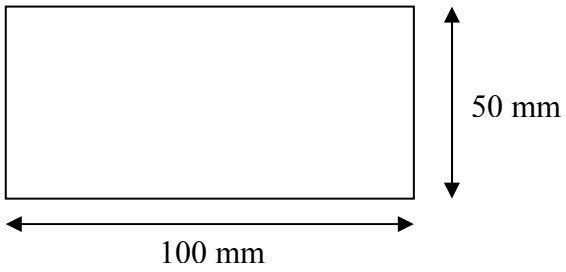

Figure A2.6. Air-bending specimen

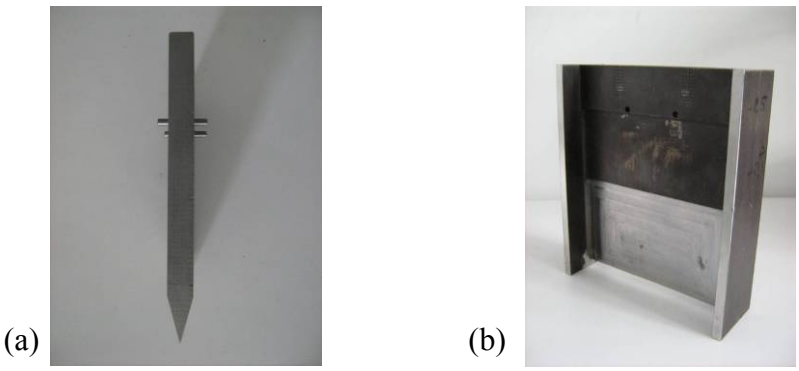

Figure A2.7. Air-bending punches. (a) punch with radius close to 0mm, (b) thin punch with radius of 0.4mm and side stiffeners.

A2.4. Stretch bending tests

a. With the hydraulic press

50x250mm specimens with ground edges (Figure A2.8) were stretch bent on a hydraulic press (BUP1000) (Figure A2.9). This press has a die and a blank-holder with respectively a

diameter of 85mm and 76mm. In addition, the die has a radius of 8mm and the draw-beads have a radius of 10mm. The blank-holder force on this press is set at 480 kN and the punch velocity is about 0.5mm.s^{-1}. Several punches with different radii are available (2, 4, 6, 8, 10 and 15 mm, Figure A2.10). In the present case, only three punch radii were used: 2, 4 and 6mm.

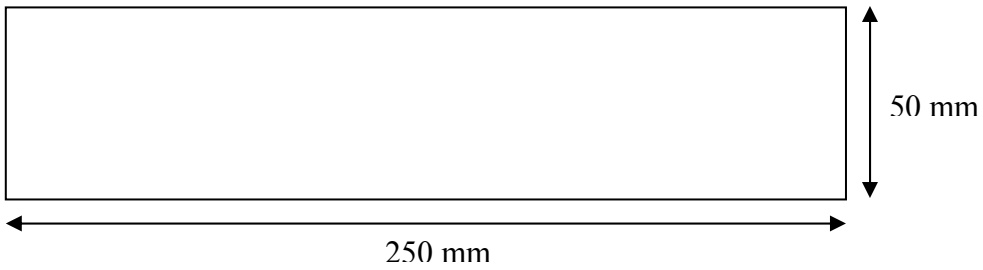

Figure A2.8. Stretch bending specimen (R = 2 to 15 mm).

(a) 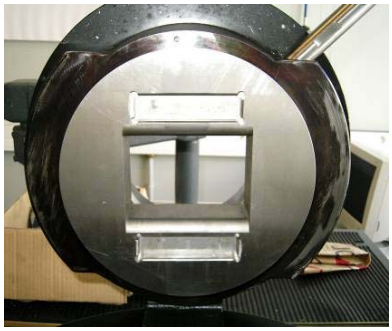 (b) 

Figure A2.9. Hydraulic press. (a) die, (b) blank-holder with draw-beads and punch.

Figure A2.10. Various punches (R = 2 to 15 mm).

b. With the servohydraulic tensile machine

In order to be able to interrupt the test just before fracture, a new device was designed at Centre des Matériaux making it possible to access at lower rate (0.05mm.s^{-1}) (Figure A2.11). Samples are a little bit smaller by using the new device. The dimensions of stretch bent specimens are 40x180mm. Here also, cut-edges have to be ground to avoid fracture starting from them. In the present case, only the punch with the radius of 4mm is used. Detailed scheme of the entire device is given in Figure A2.12.

This device is composed of:

- Three main parts (upper, lower and middle).
- One punch with a radius of 4 mm.
- Four rods sliding through the eight bronze rings in the three main parts used for the guiding during the test.
- Two blank-holders making it possible to clamp the sheet during the test thanks to 8 screws.

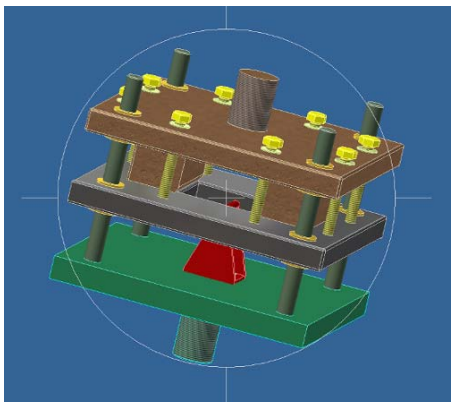

Figure A2.11. Designing of the tool with Inventor software.

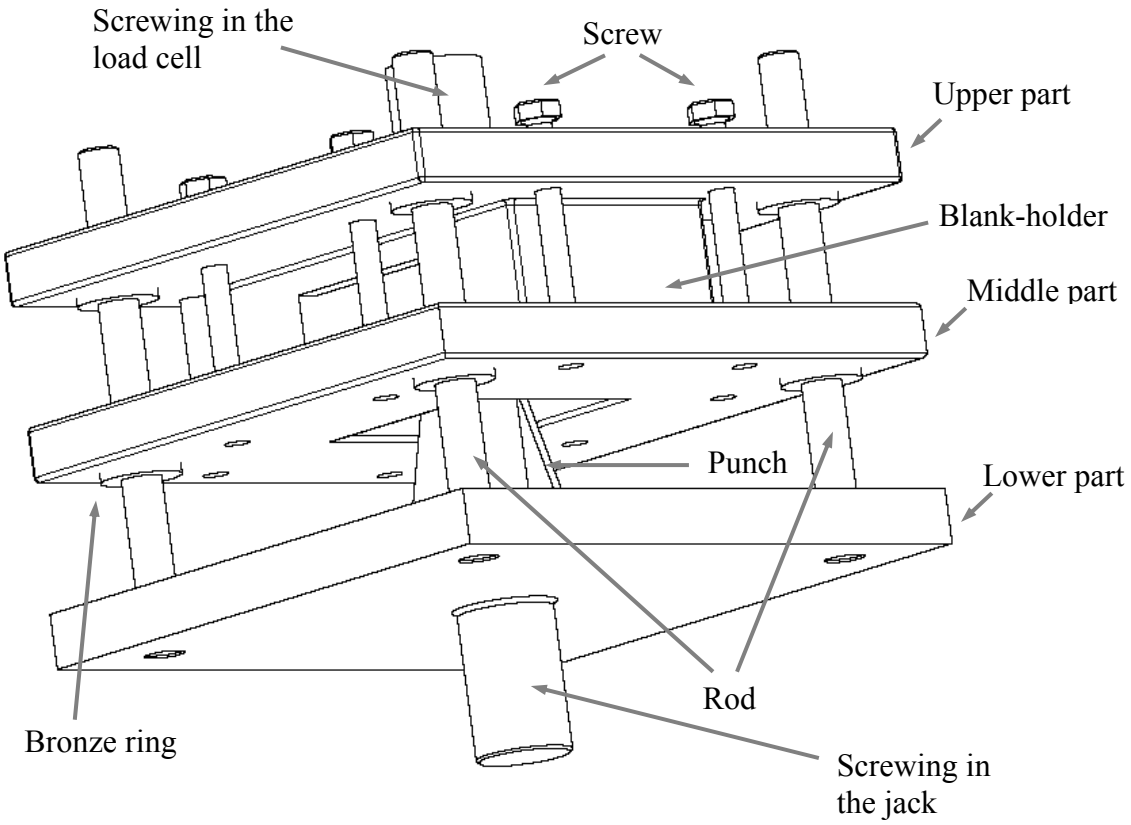

Figure A2.12. General view of the stretch bending device.

A.2.5. Strain measurement

In order to get the evolution of the strain during both bending and interrupted tensile tests, optical measuring system with Aramis software was used. This system used for optical 3D deformation analysis is developed by GOM GmbH. It is available to measure a maximum strain of 100%. This system is equipped with two CCD cameras allowing monitoring surface deformation thanks to a speckle deposited on the surface of the specimen.
It is then possible to obtained strain fields of the sheet. For bending experiments, the acquisition frequency was 2 images per mm of punch displacement.

Relations between microstructure and bendability on TRIP-aided steels for automotive products

Abstract
In order to limit fuel consumption, automotive industries push the steelmakers to develop thinner sheets with higher strength. Ultra High Strength Steels (UHSS) such as low alloy TRIP (TRansformation Induced Plasticity)-aided steels enable to get complex shapes for automotive parts. However, understanding the formability of these steels appears to be complex and involves a detailed study of failure mechanisms during forming tests. Therefore, links between microstructural features, in particularly banded structures, and formability were investigated in order to better predict the bending ability of steels as a function of their microstructure. In this study, four low alloy TRIP-aided steels exhibiting different bending performances were characterized using both air and stretch bending tests. From scanning electron and light microscopy observations, cracks initiate from the outer surface or from just below in air-bending, but from the central segregation bands in stretch bending. Fracture surfaces after bending tests are ductile and damage mainly appears by ferrite/martensite interface decohesion and occasionally as microcracks within martensite islands. An original procedure based on thickness-reduced specimens, with various locations of the main hard band within the specimen thickness, was set up. It enabled to propose a relationship between cracking, local thickness of hard band and local strain during air-bending. In order to develop a local fracture criterion that could be used for any bending test, stress and strain fields were computed by numerical simulation of the two bending tests. For that purpose, an experimental database including tensile tests on smooth and notched samples as well as shear tests was established. Material parameters of constitutive equations, accounting for anisotropic elasto-plastic behaviour with mixed hardening, were determined from this database. Finite element simulation of both bending tests associated with a ductile damage criterion made it possible to satisfactorily predict strain fields, bending load-displacement curves and fracture angle. The possibility of using simplifying assumptions in the model (such as an isotropic flow criterion, pure isotropic hardening, two-dimensional assumptions and simplified boundary conditions) is also discussed.

Keywords: Ultra High Strength Steels, TRIP-aided steels, microstructure, damage mechanisms, air-bending test, stretch bending test, finite-element simulation.

Relation entre microstructure et aptitude au pliage des aciers à effet TRIP pour application automobile

Résumé

Pour limiter la consommation des véhicules, les industries automobiles demandent aux aciéristes de développer des aciers de plus en plus fins avec des hautes résistances. Les aciers très haute résistance (THR) comme les aciers TRIP (TRansformation Induced Plasticity) permettent d'effectuer des pièces automobiles aux formes complexes. Néanmoins, le compréhension des mécanismes de mise en forme de ces aciers n'est pas simple et implique une étude détaillée des mécanismes de rupture apparaissant durant la mise en forme. Ainsi, les liens entre les paramètres microstructuraux, en particulier les structures en bandes, et la mise en forme ont été étudiés pour obtenir une meilleure prédiction de la capacité en pliage des aciers en fonction de leur microstructure. Dans cette étude, quatre aciers TRIP présentant des performances en pliage différentes ont été caractérisés à la fois en pliage en V et en pliage sous traction. A partir d'observations au microscope optique et à balayage, nous avons démontré que les fissures s'initiaient à partir de la surface ou juste en dessous en pliage en V alors qu'elles s'initiaient au niveau de la ségrégation centrale en pliage sous traction. Les surfaces de rupture après pliage sont ductiles et l'endommagement apparait principalement par décohésion de l'interface ferrite/martensite et occasionnellement par rupture des ilots martensitiques. Une procédure originale basée sur des échantillons rectifiés présentant la bande de ségrégation à différents endroits dans l'épaisseur a été établi. Ce travail a permis de proposer une relation entre l'épaisseur d'une bande, son endommagement et sa déformation locale atteinte pendant un test de pliage en V. Pour développer un critère de rupture pour ces tests de pliage, les champs de contrainte et déformation ont été calculés par simulation numérique pour ces deux tests. Pour ce faire, une base de données expérimentale incluant des tests de traction sur éprouvettes lisses et entaillées et des tests de cisaillement a été établie. La loi de comportement du matériau a été déterminée à partir de cette base expérimentale et présente un comportement élasto-plastique anisotrope avec écrouissage mixte. La simulation numérique des deux essais de pliage associée à un critère d'endommagement a permis de prédire de manière satisfaisante les champs de déformation, les courbes force/déplacement ainsi les angles de rupture. La possibilité d'utiliser des modèles simplifiés (tels qu' un critère d'écoulement isotrope, un écrouissage purement isotrope, des calculs en 2D et des conditions aux limites simplifiées) a également été discuté.

Mots clés: Aciers Très Haute Résistance, aciers TRIP, microstructure, mécanismes d'endommagement, test de pliage en V, test de pliage sous traction, simulation numérique par éléments-finis.

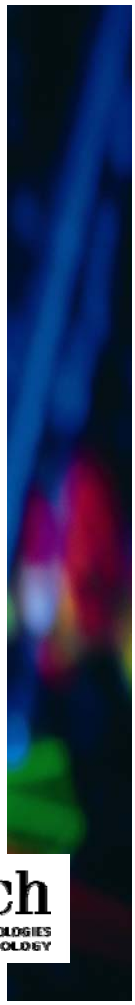

MINES ParisTech

ParisTech
INSTITUT DES SCIENCES ET TECHNOLOGIES
PARIS INSTITUTE OF TECHNOLOGY